Esmaeil Ghahremani

Contribution to Wide Area Control of Power Systems

Thèse présentée
à la Faculté des études supérieures et postdoctorales de l'Université Laval
dans le cadre du programme de doctorat en génie électrique
pour l'obtention du grade de Philosophiae Doctor (Ph.D.)

FACULTÉ DES SCIENCES ET DE GÉNIE
UNIVERSITÉ LAVAL
QUÉBEC

2013

Résumé

L'objectif principal des réseaux électriques est de convertir l'énergie d'une forme naturelle à la forme électrique et aussi de la distribuer aux clients avec la meilleure qualité. L'énergie électrique est une des formes d'énergie les plus utilisées dans l'industrie, dans les résidences, aux bureaux et dans le transport. Présentement, la complexité des réseaux électriques augmente continuellement en raison de la croissance des interconnexions et de l'utilisation des nouvelles technologies. Également, la croissance de la demande d'énergie électrique a forcé l'utilisation des réseaux électriques à leur capacité maximale et donc près de la limite de stabilité. Dans ces conditions, si le système est soumis à une perturbation, la chute de la tension ou celle de la fréquence serait très probable. Par conséquent, les équipements de contrôle, qui constituent une structure avec plusieurs niveaux de contrôle, peuvent aider les réseaux électriques à surmonter les événements imprévus. Les récentes pannes dans les réseaux électriques démontrent le besoin urgent d'une structure de contrôles multi-nivéaux basés sur une technologie avec très rapide réponse appelée en anglais Wide Area Measurement and Control system (WAMAC). Présentement, le Wide Area Measurement System (WAMS) qui utilise le Global Positioning System (GPS) et la technologie satellite, joue un rôle important dans différentes parties du système de contrôle des réseaux électriques pour empêcher les pannes globales ou locales du système. Les informations transférées par cette technologie seraient employées dans un contrôleur global appelé Wide Area Controller en anglais pour améliorer la performance dynamique des réseaux électriques pendant et après les perturbations.

Donc, pour implémenter un Wide-Area Controller dans cette thèse, nous présenterons un plan multi-étapes pour l'amélioration de la stabilité du système et l'amortissement des oscillations du réseau. La première étape de ce plan serait l'estimation d'état dynamique des réseaux électriques en utilisant des phaseurs qui sont accessibles de Phasor Measurement Unit (PMU). Les angles des machines synchrones estimés à la première étape, qui pourrait nous montrer l'état des oscillations du réseau, seront utilisés comme des signaux d'entrée pour le contrôleur. La deuxième étape de notre plan est de trouver les meilleurs eplacements des dispositifs FACTS sur le réseau électrique pour augmenter la puissance transmise dans le réseau, maximiser la chargeabilité et minimiser les pertes. Après le placement optimal des dispositifs FACTS, la troisième étape consiste à implémenter le Wide-Area Controller. Ce contrôleur reçoit les états estimés, qui sont disponibles à partir des résultats de la première étape, et d'autres informations de partout dans le réseau en utilisant des PMUs. Après la vérification des signaux reçus, le contrôleur commande des contrôleurs locaux, tels que les contrôleurs des dispositifs FACTS qui ont été placés de façon optimale à la deuxième étape. Le contrôleur implémenté modifie les signaux de référence des éléments locaux pour améliorer la performance dynamique du système et amortir les oscillations du réseau.

Abstract

The main goal of power system is to convert the energy from one of its natural forms to the electrical form and deliver it to the costumers with the best quality. So far, the complexity of power system is continually increasing because of the growth in interconnections and use of new technologies. Also, the growth of electrical energy demand has forced the power networks to work with the maximum possible capacity and in turn near the stability limits. In this condition, if the system is subjected to a disturbance, the voltage or frequency collapse events would be more probable. Therefore the control equipments, which constitute a multi level control structure, can help the power system to overcome the contingencies. Recent collapse events in the power system networks show the urgent need for such a multi level control structure based on a rapid response technology such as Wide Area Measurement and Control (WAMAC). Nowadays, the wide area measurement and monitoring, which uses the Global Positioning System (GPS) and satellite technology, plays an important role in different parts of power system control strategies to prevent from global or local collapses. The information transferred by this technology would be employed in a master central controller, called wide area controller, to improve the power system dynamic performance during and after disturbances.

From this point of view, in this thesis we will present a multi-step plan for system stability improvement and network oscillations damping by implementing a FACTS-based wide-area power oscillation damper (WA-POD) controller. The first step of this plan would be the dynamic state estimation of power system using the phasor measurements signals accessible from Phasor Measurement Units (PMUs). The estimated rotor angles of the synchronous machines from the first step, which could show us the network oscillations condition, will be used as the input signals of the wide-area controller. The second step of this plan is to find the best locations of FACTS devices to increase the power transmitted by network, maximize the system loadability and minimize the transmission line losses. After optimal placement of FACTS controllers, the third step is to implement a wide-area damping controller which receives the estimated rotor angles, available from the results of step one, and other information from all over the network, and then modifies the set points of optimized local control utilities such as FACTS device controllers. The implemented wide area controller, which acts as a master controller, sends the reference signals and set-points to the local FACTS controllers such as UPFC to improve the oscillations damping performance. This result in higher transfer limits across major transmission interfaces and less blackouts in terms of frequency, duration and consequences.

Acknowledgements

I would like to express my profound gratitude, and sincere thanks to my supervisor, professor Innocent Kamwa for his guidance, support, invaluable advice and continuous encouragements throughout these years of my Ph.D. study in Laval University. I learned priceless lessons from his vision, personality, and professionalism. It was a great honor to work with him.

My appreciation is also extended to my doctoral committee members, prof. Hoang Le-Huy and prof. Jérôme Cros from the electrical and computer engineering eepartment of Laval University, prof. Louis-A. Dessaint from École de Technologie Supérieure (ETS) and Dr. Serge Lefebvre from Institut de Recherche d'Hydro-Québec (IREQ).

Also, I would like to acknowledge the great services provided by the department of electrical and eomputer engineering, more specifically, the personnel of the departmental graduate office, Mrs. Lise Brais, Mrs. Nancy Duchesneau and Mrs. Louise Bussiéres. I will always remember their helps with my secretary problems in the department during my Ph.D. studying.

I would also like to offer my appreciation to my professors during my bachelor and master studies, specially prof. Mehrdad Abedi and prof. Mehdi Karrari. I have learned so much from them. Professor Abedi had a great influence on my visions respect to the life and education.

Special thanks to my officemates at LEEPCI lab for everything they did to make our lab a friendly place to work in: Loicq Serge Bakay, Mehdi Taghizadeh, Maxim Bergeron, Nicolas Dehlinger, Jean Longchamps, Mohamed Chakir and Geraldo Sincero.

I also extend my special thanks to my great friends Mr. Hamidreza Alvandi, Mr. Alireza Alvandi and Mrs. Shaghayegh Rahmatian who helped me so much since my first days of arrival to Québec city and during my Ph.D. studies.

My warmest thanks and appreciation to my parents who have undergone all the hardships in bringing me up and have offered me their support, encouragement, and love during the long years of my studies. I am extremely thankful of them to helping their son from the first steps of my studying until now. Also, my endless thanks to my sisters, my brother and my brothers-in-law for their support and kindness.

At the end, thank all the people who made this possible.

Esmaeil Ghahremani, January 2013

Dedication

To my beloved parents that without them I would not be the person who I am.

To my mother who taught me the love and the kindness, the two true meanings of life.

To my father who offered me the wisdom and the perseverance, the two wings that you would need to achieve your goals.

Table of Contents

List of Tables

List of Figures

List of Terms

AGC	Automatic Generation Control
AI	Artificial Intelligence-Based
AVR	Automatic Voltage Regulator
ADPOD	Adaptive phasor Power Oscillation Damping controller
CPF	Continuation Power Flow
DFT	Discrete Fourier Transform
EKF	Extended Kalman Filter
EKF-UI	Extended Kalman Filter with Unknown Inputs
EMS	Energy Management Systems
FACTS	Flexible Alternating-Current Transmission System
GA	Genetic Algorithm
GPS	Global Positioning System
GUI	Graphical User Interfaces
HVDC	High Voltage Direct Current
IEEE	Institute of Electrical and Electronics Engineers
MRAS	Model Reference Adaptive System
OPF	Optimal Power Flow
PDC	Phasor Data Concentrator
PMU	Phasor Measurements Unit

POD	Power Oscillation Damper
PSS	Power System Stabilizer
PSAT	Power System Analysis Toolbox
PF	Power Flow
SCADA	Supervisory Control and Data Acquisition
SMIB	Single Machine Infinite Bus
SMES	Superconducting Magnetic Energy Storage
SPC	System Protection Center
SPSS	Supervisory Power System Stabilizer
STATCOM	Static Synchronous Compensator
SSSC	Static Synchronous Series Compensator
SVC	Static Var Compensator
TCSC	Thyristor Controlled Series Compensator
TCVR	Thyristor Controlled Voltage Regulator
TCPST	Thyristor Controlled Phase Shifting Transformer
UPFC	Unified Power Flow Controller
UKF	Unscented Kalman Filter
UT	Unscented Transformation
WACS	Wide Area Control System
WAMAC	Wide Area Measurements and Control System
WAMS	Wide Area Measurements System
WACAP	Wide Area Control and Protection System
WADC	Wide Area Damping Controller
WA-POD	Wide Area Power Oscillation Damper
WSCC	Western Systems Coordinating Council

List of Symbols

Synchronous Generator

δ	Rotor angle with respect to the machine terminals (Load angle)
ω_0	Nominal synchronous speed
ω	Per unit rotor speed
J	Inertia constant per unit
T_m	Mechanical input torque
T_e	Electrical torque
D	Damping factor per unit
x_d	Direct axis reactance
x_q	Quadratic axis reactance
x'_d	Direct axis transient reactance
x'_q	Quadratic axis transient reactance
e_d	Direct axis voltage
e_q	Quadratic axis voltage
i_q	Quadratic axis current
i_d	Direct axis current
e'_d	Direct axis transient voltage

e'_q	Quadratic axis transient voltage
T'_{do}	Direct axis transient open circuit time constant
T'_{qo}	Quadratic axis transient open circuit time constant
E_{fd}	Steady state Internal voltage of armature
R_a	Stator resistance
P_t	Terminal active Power
Q_t	Terminal reactive Power
V_t	Terminal bus voltage
I_t	Terminal bus current
Φ	Power factor angle

Dynamic State Estimation

$\mathbf{x}_k$	System state vector
$\mathbf{y}_k$	System measured variable (output) vector
$\mathbf{f}_{k-1}$	System function
$\mathbf{h}_k$	System output function
$\mathbf{u}_{k-1}$	System known input vector
$\mathbf{u}^*_{k-1}$	System unknown input vector
$\mathbf{w}_{k-1}$	Process (random state) noise
$\mathbf{v}_k$	Measurement noise
$\mathbf{Q}_k$	Covariance matrix for state noise
$\mathbf{R}_k$	Covariance matrix for measurement noise
$\mathbf{P}_k$	Covariance matrix of the state estimation error
$\mathbf{K}_k$	Kalman filter gain matrix

E	Expected value
$\mathbf{F}_{k-1}$	Partial derivation of $\mathbf{f}_{k-1}$ with respect to the states
$\mathbf{L}_{k-1}$	Partial derivation of $\mathbf{w}_{k-1}$ with respect to the states
$\mathbf{H}_k$	Partial derivation of $\mathbf{h}_k$ with respect to the states
$\mathbf{M}_k$	Partial derivation of $\mathbf{v}_k$ with respect to the states
$\mathbf{B}^*_{k-1}$	Partial derivation of $\mathbf{f}_{k-1}$ with respect to the unknown inputs
$\mathbf{J}_k$	Objective function of the summed square error
$\mathbf{W}_k$	Weighting matrix defined as the inverse of the covariance matrix
Δ_k	Output error matrix
$\mathbf{X}_{e,k}$	Unknown extended state vector
$\mathbf{S}_{\mathbf{u}^*,k}$	Unknown input gain factor
$\mathbf{x}^{(i)}$	Sigma points of state variable
$\mathbf{y}^{(i)}$	Transformed points of sigma points $\mathbf{x}^{(i)}$
$\mathbf{P}_y^{\mathrm{UKF}}$	UKF Covariance of a given random variable such $\mathbf{y}$
$\bar{\mathbf{y}}^{\mathrm{UKF}}$	UKF Mean of a given random variable such as $\mathbf{y}$
$\mathbf{P}_{\mathbf{xy}}$	Cross covariance
$\mathbf{W}^{(i)}$	Weighting coefficients

FACTS Devices Placement

P_i^F	Equivalent injected active power at bus i
Q_i^F	Equivalent injected reactive power at bus i
P_{ik}	Transmitted active power in the line without FACTS devices

Q_{ik}	Transmitted reactive power in the line without FACTS devices
P_{ik}^{F}	Transmitted active power with FACTS devices in the line
Q_{ik}^{F}	Transmitted reactive power with FACTS devices in the line
Y	Admittance matrix
y_{ik}	Line admittance
r_{ik}	Line resistance
x_{ik}	Line reactance
y_c	Shunt admittance
b_c	Charging capacitance
Q_{SVC}	Injected or absorbed reactive power by SVC
V_n	Nominal voltage of bus
y_{SVC}	SVC admittance
z_{ik}	Line impedance
z'_{ik}	Modified value of line impedance
r'_{ik}	Modified value of line resistance
x'_{ik}	Modified value of line reactance
y'_c	Modified value of shunt admittance
b'_c	Modified value of charging capacitance
$Q_{STATCOM}$	Injected or absorbed reactive power by STATCOM
$y_{STATCOM}$	STATCOM admittance
y_{SMES}	SMES admittance
P_{SMES}	Injected or absorbed active power by SMES
X_L	Variable inductive reactance
X_{TCSC}	TCSC reactance
k_{TCSC}	TCSC coefficient

τ	Tap ratio
θ_{shift}	Phase shift angle
k_{TCVR}	TCVR coefficient
α_{TCPST}	Angle of TCPST
V_{SE}	Voltage magnitude of controllable series voltage for the series part of UPFC
Φ_{SE}	Phase of controllable series voltage for the series part of UPFC
I_{SH}	Controllable Current source for modeling the shunt part of UPFC
P_{12}	Active power transmitted in a line between two buses 1 and 2
Q_{12}	Reactive power transmitted in a line between two buses 1 and 2
V_1	Voltage magnitude of bus 1
V_2	Voltage magnitude of bus 2
δ_{12}	Difference angle between phasors $\underline{V}_1$ and $\underline{V}_2$
OVL	First term of fitness function: penalize Over loaded lines
VBL	Second term of fitness function: penalize over- or under- voltage buses
J	Objective function of optimization process
S_l	Current apparent power of the line l
S_{lmax}	Reactive power transmitted in a line between two buses 1 and 2
V_{bn}	Nominal voltage of bus i
V_{bi}	Current voltage of bus i
ΔV_{bi}	Difference between nominal and current voltage of bus i
μ	Constant coefficient
n_{Branch}	Number of total buses
n_{Bus}	Number of total branches
n_{FACTS}	Number of selected FACTS devices
n_{Location}	Number of total locations

$n_{\text{Individual}}$	Number of slots of each individual in genetic algorithm
v_{real}	Real value of FACTS devices
$v_{\min}$	Minimum value of the ranges of each FACTS device
$v_{\max}$	Maximum value of the ranges of each FACTS device
$v_{\text{normalized}}$	Minimum value of FACTS device
v_{real}	Real value of FACTS devices
Fit	Fitness function for security constraints
ρ	Power system loadability
λ	Power system load factor
λ_{max}	Maximum load factor
λ_{LRI}	Load factor related to Loss Reduction Improvement (LRI)
P_{G0i}	Initial power generation at bus i
P_{Gi}	Modified power generation at bus i
P_{L0i}	Initial active load power at bus i
P_{Li}	Modified active load power at bus i
Q_{L0i}	Initial reactive load power at bus i
Q_{Li}	Modified reactive load power at bus i
P_{gi}	Generation at bus i
P_{gi}^{min}	Minimum bound on generation at bus i
P_{gi}^{max}	Maximum bound on generation at bus i
TVD	Total Voltage Deviation for all buses of power system

Wide-Area Power Oscillation Damper

$\mathbf{x}$	Vector of the state variable, dynamic states of the generators and loads

$\mathbf{y}$	Vector of algebraic variables(e.g., bus voltage magnitudes and phase angles
$\mathbf{u}$	Set of controllable parameters (e.g., controller reference signals
$\mathbf{w}$	Set of output variable (e.g., line current flows
$\mathbf{f}$	Set of differential equations: represents system and controller dynamics
$\mathbf{g}$	Set of algebraic equations: represent the transmission network power flows
$\mathbf{h}$	Set of equations that represent output variables
$\mathbf{A}$	State or plant matrix
$\mathbf{B}$	Control or input matrix
$\mathbf{C}$	Output matrix
$\mathbf{D}$	Feedforward matrix
K_{PSS}	Gain of Power System Stabilizer (PSS)
K_{POD}	Gain of Power Oscillation Damper (POD)
T_w	Time constant of wash-out block of PSS
T_{wf}	Time constant of wash-out block of POD
T_r	Time constant of an anti-windup limiter of PSS
T_{rf}	Time constant of an anti-windup limiter of POD
T_i	T_1, T_2, T_3 and T_4: Time constants of two lead-lag blocks of PSS
T_{if}	T_{1f}, T_{2f}, T_{3f} and T_{4f}: Time constants of two lead-lag blocks of POD
J	Objective function of genetic algorithm
$\Delta\omega_i$	Speed deviation of generator i
δ_i	Rotor angle of generator i
V_i	Voltage magnitudes of bus i
P_{ij}	Power flows of the branch between buses i and j
u_{POD}	Input signal of POD
v_{PSS}	Output signal of PSS
v_{POD}	Output signal of POD

Chapter 1

Introduction

The function of electric power system is to convert energy from one of the naturally available forms to the electrical form and to transport it to the points of consumption to be used in other forms such as heat, light, and mechanical energy. The advantage of the electrical form of energy relies in the flexibility of its transport and control with a high degree of efficiency and reliability [1]. As a result, power system networks have become so important for the entire society and large efforts must be made to prevent them from collapse and instability scenarios.

Recent collapse events all over the world show the urgent need for stabilizing power systems beyond the classic technologies such as Supervisory Control and Data Acquisition system (SCADA). Increasing demands on the power system, forces the system to work near its stability limits and it will increase further the system problems such as instabilities and collapses. One promising way is to provide a system wide protection and control complementary to the conventional local equipment which could be named as Wide Area Measurement and Control system (WAMAC). The mentioned technology is used to save the system from a partial or total blackout in operational situations when equipment is faulted or operated outside its limitations [2, 3].

1.1 Research Motivation

The duty of the power system control is to design and operate the power system in acceptable ranges for the voltage and as well for the frequency. In addition, the control utilities are developed for some other fundamental requirements like providing continually the load demand for active and reactive power and energy production at minimum cost. These control units, need several levels of controls involving a complex array of devices which could be categorized as:

- **Generation Unit Controllers** such as: Governor, AGC, AVR and PSS.
- **Transmission System Controllers** such as: FACTS devices.

The above described control scheme, which can be named as local control units, are designed and used for a specific duty on an individual component in power systems. They contribute to the satisfactory operation of the power system by maintaining system voltage and frequency and other system variables within their acceptable limits.

The above mentioned local control utilities are cited in the lower layer of a hierarchical structure. In top of this multi-level structure, there is a master control which coordinates the local control utilities set-points. Such a master control center, which could be names as SCADA, provides information to indicate the system status. In SCADA, state estimation programs filter monitored data and provide an accurate picture of the system's condition. The human operator is an important link at various levels in this control hierarchy. The primary function of the operator is to monitor system performance and manage resources to ensure about health of operation system [1].

The wide use of SCADA in power system enables the dispatcher to supervise and

modulate the operation conditions of power system in time and ensures the operation safely and reliably. However, with rapid development of economics and supply shortage of power electricity, power system often operates near the edge of its stability limits. In this case the present SCADA and the applications based on it are not sufficient to support power systems to operate stably and safely, the blackout of North American and Canada in 2003 is such kind an example. Because SCADA can only provides steady, low sampling density, and non synchronous information of the network, the dispatching center would not have accurate information about the dynamic operation states of the system. Therefore, Wide Area Measurements System (WAMS) enables us to observe power system synchronously in more elaborate time scale, and analyze the power system with new methods [4].

The WAMS is based on the synchronized phasor measurements using the best synchronizing clock provided by Global Positioning System (GPS). This type of measurements, which is truly dynamic and deterministic in contrast to SCADA based measurements, can enable real-time monitoring of the operating state of power system [2].

In Wide Area Control System (WACS), when the network is subjected to disturbances, an operation control center will send the modified set-points signals to the local utilities and individual protection tools such as circuit breakers to clear the fault and disconnect the fault equipment [5]. This technology performs as a multi-level control structure that receives synchronized information from critical points of network using Wide Area Measurement System (WAMS) which is the basic element for implementing the wide area control of power system. Therefore the wide area controller, which has an accurate picture of system status using the information received from PMUs, could save the system from blackout in critical operational situations.

1.2 Wide Area Measurements System

Wide Area Measurements and Control System (WAMAC), which pertain to the control of a large interconnected power system throughout the synchronized phasor measurements at different points of the network, includes two principle parts: Wide Area Measurements System (WAMS) and Wide Area Control System (WACS). Wide area measurement systems can monitor the health of power system on-line. It consists of three main parts: data acquisition using PMUs, data transmitting to Phasor Data Concentrator (PDC) and data processing procedure. In WAMS applications a number of PMUs, which are connected to the data concentrator as a mass storage, are accessible from the control center. A schematic of relationship between PDC and PMUs is shown in Figure 1.1 [3, 5].

As it is shown in Figure 1.1 the common applications of WAMS take place in several layer. The basic layer should aim at achieving the monitoring capability. This could be used to improve the state estimation, post fault analysis, and operator information.

In wide area measurement system, for control process facility, the system uses GPS synchronized phasor measurement units for the measurement of current and voltage phasors at certain locations of the power system. Phasors measurements including both magnitude and angle are sampled by PMUs with a sample time by an accuracy of down to 1 μs. The

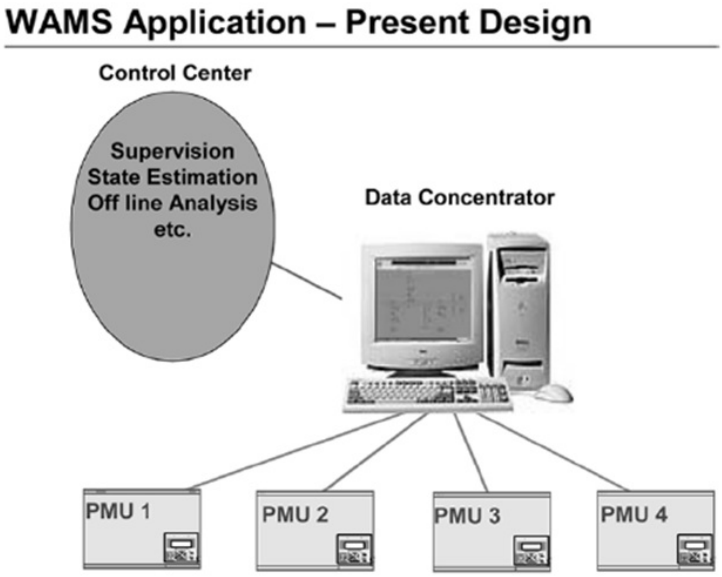

Figure 1.1: A schematic of control center: Phasor Data Concentrator (PDC).

time synchronization provided by GPS signals in PMU measurement technique assures that the measurements from entire of the power system are taken at precisely the same instant. Furthermore phasors are obtained directly from secondary of voltage and current transformers. As such they are minimize any other errors that may be introduced by traditional transducers. These two features assure that the state of power system estimated with synchronized phasor measurements is an accurate representation of the condition prevailing on the power network [6].

In addition, for example in the power system oscillations which are caused to due periodic interchange of kinetic energy between the rotors of various generators, WAMS enables monitoring not only of slow phenomena such as voltage and load evolution dynamics, but also faster phenomena such as oscillatory, transient and frequency dynamics. To detect the oscillations, PMUs are employed and the measured data are transmitted via communication channels to a central computer (PDC) for running the applications [7, 8]. Since the instability can originate anywhere on the network, depending on the system conditions, equipment outages and generation dispatch, therefore the PMUs should be installed at the key points throughout the power network [6].

Finally, it should be mentioned that in theory the WAMS could completely replaces the SCADA , but it is not practical with the technique nowadays because of some difficulties in the WAMS with the communication, storage and management. As a result we can predict that both SCADA and WAMS will exist in power system networks. In such a system in which SCADA and WAMS are complementing each other and can be integrated together, they can provide a guarantee for the steady and safe operation of power system [4].

1.3 Wide Area Control and Protection System

The lack of coordination among the local control utilities such as AVR, AGC and PSS may cause serious problems, such as inter-area oscillations. In order to overcome these problems a centralized wide area control system (WACS), which is encountered in a distributed power network control, could be employed. The WACS coordinated the actions of the distributed agents using wide area dynamic information gathered by PMUs. The WACS receives information and data of different areas in power system and based on some predefined objective functions sends appropriate control/feedback signals to the local distributed agents in the power network to enhance the system dynamic performance [9].

On the other hand, wide area control and protection system is used to save and protect the system from black- or brown-out in the operational situations such as very severe disturbance or after an extreme load growth [3].

Also, as it was mentioned before the basic idea of the WACS is the centralized processing of the data to evaluate the actual power system operation conditions with respect to its stability limits. Although the particular application range of WACS is quite wide, depending on the addressed phenomena, the fundamental structure remains the same. The hardware can be explained based on the data handling in WACS, as shown in Figure 1.2 [2].

Figure 1.2 shows more details of a WAMAC system architecture including the interfaces to SCADA/EMS and substation automation as well as the closed control loops back to the network controllers such as FACTS-devices [10]. For protection the system against the fault contingencies, the local control actions would help the networks. Meanwhile, the functions of the master control, the old one SCADA/EMS or the developed one WAMAC, are tools that assist the power grid operator to control and optimize the power system operations with sending the control set points to local control utilities. These local controls include the operations on generation or transmission devices [11].

As it is illustrated in Figure 1.2, the WACS is divided into two hierarchical levels: (a) system protection center incorporating the wide area applications and (b) field level equipment for data acquisition and the local control utilities. Communication links can be established between operational center and control systems to allow the optimum data sharing and implement the control philosophy. For actual implementation, thorough investigations must be made concerning location of the PMUs which send measurement to the System Protection Center (SPC) in the power system [10].

The central computer contains services for preprocessing the incoming phasor measurements and basic services. An interface to the SCADA/EMS system allows receiving topology information and device parameters. Based on this synchronized information, wide area control and protection system modifies the set points of the FACTS devices, generator exciters and other control equipments. The control signals are going back either directly to local controllers for specific devices or to substation automation systems [3].

While it is not possible to predict or prevent all contingencies that may lead to power system collapse, a wide area monitoring and control system provides a reliable security

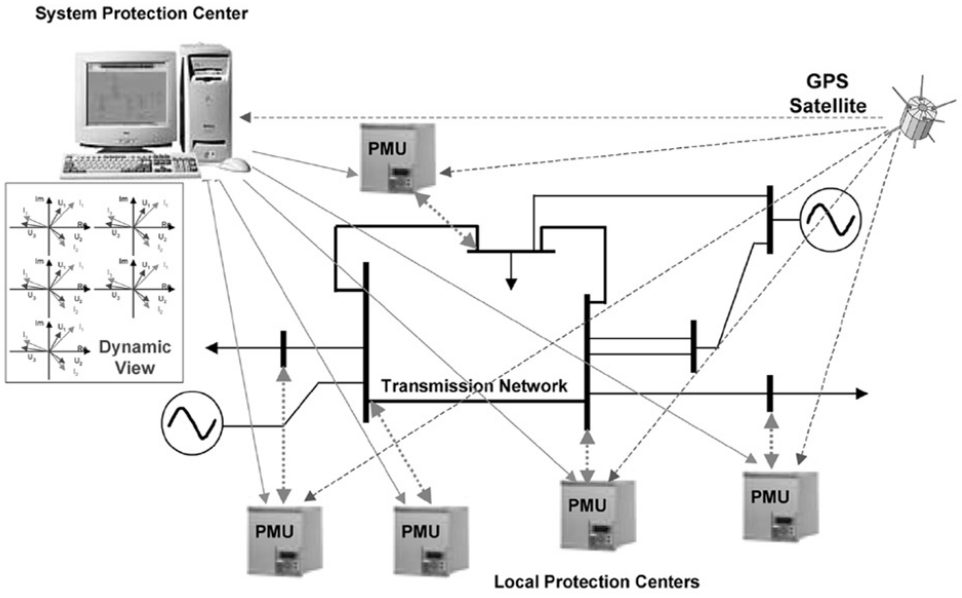

Figure 1.2: Architecture of a wide area monitoring, control and protection system.

prediction and optimized coordinated actions. This technology, which is able to mitigate or prevent large area disturbances, is constituted of two main parts: wide area measurement system and wide area control system. The first one is acquisition and receiving data and information from all critical points of network and delivering them to the control center and the second part is analyzing the data in order to send control set points to the local control equipments.

1.4 Outline of the Thesis

In this thesis we will implement a FACTS-based wide-area damping controller such as a master controller which improves the transient stability using the signals measured by PMUs. While we have a disturbance in the power system, this wide-area controller receives the data and information from entire network and sends the set-point reference signals to the local FACTS controllers for damping the power system oscillations. The thesis will be performed in a multi-step plan as presented in Figure 1.3.

The first step of this plan is the dynamic state estimation of power system using the phasor measurements signals accessible from Phasor Measurement Units (PMUs). In this step different approaches such as traditional Extended Kalman Filtering (EKF), Unscented Kalman Filtering (UKF) and EKF with Unknown Inputs (referred as EKF-UI) are applied for states estimation of synchronous machines. The estimated rotor angles of the synchronous machines from the first step that show the network oscillations condition, will be used as the input signals of the FACTS-based wide-area controller. The location of the mentioned FACTS device will be determined using a generic method in step two. In this

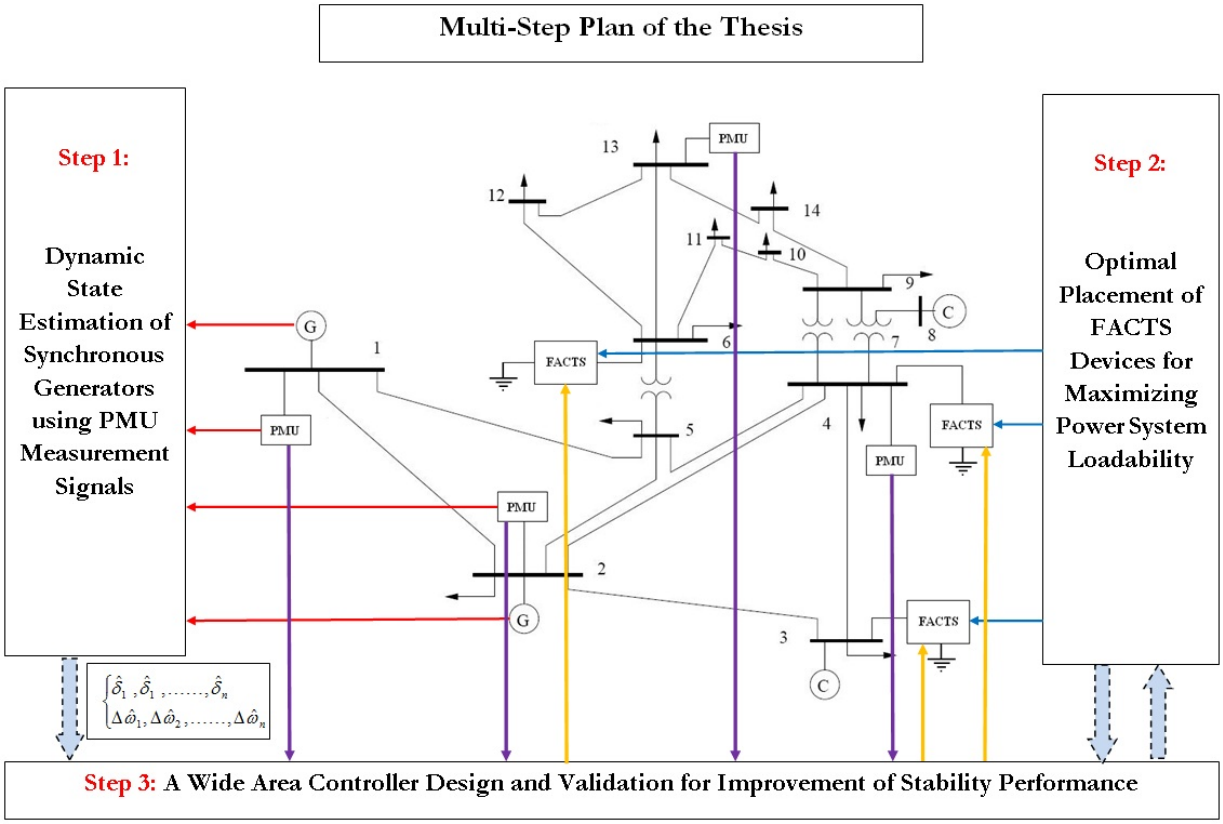

Figure 1.3: An overall schematic of different steps of thesis.

step, the optimal process of FACTS placement to maximize the power system loadability and minimize the transmission line losses is presented. After determining the optimal location of FACTS device in step two, the third step is to implement the wide-area damping controller. This controller receives the estimated rotor angles, available from the results of step one and other information from all over the network, and then modifies the set points of FACTS device controller to improve the oscillations damping performance.

The chapters of the thesis are organized as follows:

Chapter 1 the current chapter, provided a brief description of fundamental concepts related to Wide Area Measurements System (WAMS) and Wide Area Control and Protection system (WACAP).

Chapter 2 presents the dynamic state estimation of power system using phasor measurements which would be available from PMUs supposed to be installed at terminal bus of a synchronous machine. In this chapter, at first the Extended Kalman Filter (EKF) technique is developed for dynamic state estimation of a synchronous machine using phasor

measured signals. In the case of without using the linearization in the state estimation process in the classic EKF method, the Unscented Kalman Filter (UKF) is developed. Finally, for the case of no possibility of measuring the exciter output voltage E_{fd}, the Extended Kalman Filter with Unknown Inputs, referred to as EKF-UI, is applied for identifying and estimating the states and the unknown inputs of the synchronous machine simultaneously.

Chapter 3 presents the optimal placement of FACTS devices for maximizing the power system loadability and minimizing losses of transmission lines. In order to find the suitable locations of FACTS device, a Graphical User Interface (GUI) based on a genetic algorithm (GA) is presented to find the optimal locations and sizing parameters of multi-type FACTS devices in large power systems. This user-friendly tool, called the FACTS Placement Toolbox, allows the user to pick a power system network, determine the GA settings and select the number and types of FACTS devices to be allocated in the network. The GA-based optimization process is then applied to obtain optimal locations and ratings of the selected FACTS to maximize the system static loadability. Six different FACTS devices are implemented: SVC, TCSC, TCVR, TCPST, UPFC and STATCOM with SMES. The simulation results on IEEE test networks with up to 300-buses and also Hydro-Québec network show that the FACTS placement toolbox is effective and flexible enough for analyzing a large number of scenarios with mixed types of FACTS to be optimally sited at multiple locations simultaneously.

Chapter 4 presents a multi-step plan developed to implement a Wide-Area Power Oscillation Damping (WA-POD) controller of a UPFC in 14-bus test system. The first step of this plan is to find the optimal location for the UPFC to maximize power system loadability; the second step is to estimate the dynamic states of the generators; and the third step is to implement the WA-POD controller using the states estimated in step two. The estimated rotor angles are used to provide the input signal of the WA-POD controller while the estimated rotor speed deviations will be used for an off-line parameter tuning of both PSS and WA-POD using the genetic algorithm. Different types of faults are applied synchronous to the network to compare the performance of the traditional PSS and the WA-POD controller in the 14-bus test system. Simulation results show the effectiveness of the implemented WA-POD controller in damping

low-frequency oscillations and improving the dynamic performance of the system.

Chapter 5 summarizes the work presented in the thesis. The main contributions of the thesis are highlighted, and a list of potential research directions to study further is given.

Chapter 2

Dynamic State Estimation in Power System Networks

In first step of this thesis, the dynamic state estimation of power system is developed using the phasor measurements signals measured by Phasor Measurement Units (PMUs). In this step different approaches are applied to phasor signals for states estimation of synchronous machines. In step 3, the estimated rotor angles of the synchronous machines in this step, will be used as the input signals of the FACTS-based wide-area controller.

Availability of the synchronous machine angle and speed variables give us an accurate picture of the overall condition of power networks leading therefore to an improved situational awareness by system operators. In addition, they would be essential in developing local and global control schemes aimed at enhancing system stability and reliability. In this chapter, the Extended Kalman Filter (EKF) technique for dynamic state estimation of a synchronous machine using Phasor Measurement Unit (PMU) quantities is developed. The simulation results of the EKF approach show the accuracy of the resulting state estimates.

However, in the EKF classic state estimation technique, the linear approximations of the system at a given moment in time may introduce errors in the states. In order to overcome the drawbacks of the EKF, the Unscented Kalman Filter (UKF) is used for estimating the states of a synchronous machine, including rotor angle and rotor speed, using Phasor Measurement Unit (PMU) quantities. The UKF algorithm propagates the probability density function (pdf) of a random variable in a simple and effective way and is accurate up to the second order in estimating the mean and covariance. The overall impression is that the performance of the UKF is better than the EKF in terms of robustness, speed of convergence and, also in different levels of noise. Simulation results including saturation effects and grid faults show the accuracy and efficiency of the UKF method in state estimation of the system, especially at higher noise ratios.

Also, the traditional EKF method requires that all its externally observed variables, including input signals be measured or available, which may not always be the case. In synchronous machines, for example, the exciter output voltage E_{fd}, may not be available for measuring in all cases. As a result, the Extended Kalman Filter with Unknown Inputs, referred to as EKF-UI, is proposed for identifying and estimating the states and the unknown inputs of the synchronous machine simultaneously. Simulation results demonstrate the efficiency and accuracy of the EKF-UI method under noisy or fault conditions, compared to the classic EKF approach and confirms its great potential in cases where there is no access to the input signals of the system.

2.1 Literature Review

In order to increase power system stability and reliability during and after disturbances, new strategies for enhancing operator situational awareness and power grid global and local controllers must be developed [1, 12, 4]. But high-performance monitoring and control schemes can hardly be built on the existing SCADA system which provides only steady, low-sampling density and non-synchronous information about the network. SCADA measurements are too infrequent and non-synchronous to capture information about the system dynamics. It is to remove these limitations that Wide Area Measurements and Control

systems (WAMAC) using Phasor Measurement Units (PMUs) are being rapidly adopted worldwide. These systems enable synchronous power system dynamics to be monitored on a more refined time scale.

Building on the ability of WAMAC systems to capture dynamic system information, the state estimators of a power system can generate dynamic states, e.g., generator rotor angles and generator speed, instead of (or in addition to) the static states of voltage magnitudes and phase angles [13]. From this point of view, this paper presents a dynamic state estimation process based on Kalman filtering techniques to estimate the dynamic states of the power system.

A number of papers and studies have focused on just one dynamic state of the power system at a time, typically the rotor angle or speed which was estimated using artificial intelligence (AI) methods such as neural networks [14, 15]. These AI-based model-free estimators generate the estimated rotor angle or rotor speed signal without requiring a mathematical model or any machine parameters [14]. In the large-scale power system stability analysis, it is often preferable to have an exact model for all elements of the power network including lines, transformers, induction motors, FACTS, and also synchronous machines. Therefore, the physical model-based state estimator of the generator including voltage states in addition to rotor angle and speed would be more interesting in system monitoring and control.

Use of the term *dynamic state estimation* can be traced back to the 1970s [16] when Kalman filtering techniques were first applied to improve the computational performance of the traditional steady-state estimation process in power system applications. Since then, there have been several studies in this area which have used different approaches to capture dynamic states of the power system [17, 18, 19]. However, very few papers on state estimators have set their focus on the synchronous generator which is at the heart of the power system. For example, a gain-scheduling scheme was used in [13] for state observer design in a single-machine infinite-bus (SMIB) system while constant voltages were assumed in the dynamic modeling, which significantly reduces the ability to represent the full dynamics of a power system. In [20], a dynamic state estimation method was proposed for the second-order synchronous machine which could be extended to a multi-machine system. The accuracy of the proposed method was examined in terms of measurement noise levels. But the problem lies in not including the field voltage dynamic equations in the second-order system model of a synchronous machine. Also reported in [21], is dynamic state estimation scheme for a sixth-order power system with a third order for synchronous machine. However, they assumed the exciter output voltage E_{fd} and rotor angle δ to be two measurable signals, following on this respect, other papers in this area [22]. More specifically, the latter proposed a parameter estimation procedure based on the Unscented Kalman Filter (UKF) was presented for the third-order model of a synchronous generator assuming the output power Pe as one of the states with the E_{fd} and the constant T_m as input signals of the machine [22]. A third-order model was also assumed in [23] and algebraic equations were used to derive the quasi-steady states of the generator, assuming the field current i_{fd} was available in addition to the terminal quantities.

A methodology for real-time dynamic monitoring of the electric power systems using optimal state estimators is presented in [24] and [25], whereby the system state vector is extended to include generator internal dynamic states (rotor speed ω and angle δ), in addition to algebraic states (e.g. terminal voltage, generator internal voltage, output electric power and so on). The measurement set in [24] and [25] consists of V_t, I_t (both with magnitude and phase), P_t, Q_t and the generator speed and acceleration (frequency and rate of change of frequency at the substation).

In contrast with the above approaches, in this chapter we proposed a dynamic state estimator method based on Extended Kalman Filtering (EKF) applied to signals obtained from a Phasor Measurement Unit (PMU) which is assumed to be installed in the substation of a power plant. The synchronous machine model is a fourth-order, nonlinear state-space model with E_{fd}, T_m and V_t as inputs and P_t and Q_t as outputs. In the case of not using linearization in the state estimation process, the Unscented Kalman Filter (UKF) algorithm is applied to generate the estimated states from the available signals obtained from a PMU. In situations where the E_{fd} signal is not accessible for measuring, a novel method is applied based on Extended Kalman Filtering with Unknown Inputs (EKF-UI). From experimental test considerations, it could become a critical factor since measuring the field current and voltage is not easily applicable to brushless excitation systems. In any event, it will involve additional wiring and labor costs using existing technologies.

This chapter is organized as follows. The fourth-order nonlinear model structure considered for modeling the synchronous machine is given in section 2.2. In section 2.3, assuming that the E_{fd} signal is accessible, dynamic state estimation of the power system will be presented using the EKF method. Section 2.4 describes the UKF mathematical algorithm and the simulation results of the UKF state estimator. Section 2.5 includes an extended version of EKF, the EKF-UI method for an inaccessible or unknown E_{fd} signal. To demonstrate the robustness of the EKF-UI method, detailed simulation studies are also presented in Section 2.5. Section 2.6 presents a summary of the chapter.

2.2 Single-Machine Infinite-Bus Test System

Compared with higher-order nonlinear structures, the effect of damper windings and stator dynamics are neglected in the fourth-order nonlinear model of a synchronous machine. This is possible when very fast dynamic (sub-transient) are not of interest. However, the effect of damper windings is considered approximately in the rotor damping factor [1]. The single-machine infinite-bus (SMIB) power system, shown in Figure 2.1, is considered here as the benchmark system.

Giving a classical model for the synchronous generator and neglecting the transmission line resistance (R_e=0), all the active power produced by generator P_t, is delivered to the infinite-bus (P_t=P_B). Also, δ is the angle by which e'_q, the q-axis component of the voltage behind transient reactance x'_d, leads the terminal bus of machine E_t (or V_t). Assuming V_t as the reference phasor, the single-machine infinite-bus power system in Figure 2.1, can be

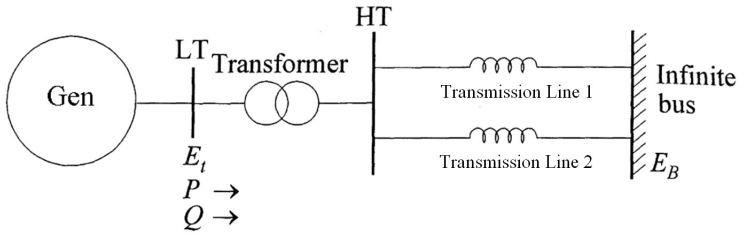

Figure 2.1: Synchronous machine connected to infinite-bus via the transmission lines.

represented in per unit (pu) by the fourth-order nonlinear equations as (2.1):

$$\begin{aligned}
\dot{\delta} &= \omega_0 \Delta\omega \\
\Delta\dot{\omega} &= \frac{1}{J}(T_m - T_e - D\Delta\omega) \\
\dot{e}'_q &= \frac{1}{T'_{do}}(E_{fd} - e'_q - (x_d - x'_d)i_d) \\
\dot{e}'_d &= \frac{1}{T'_{qo}}(-e'_d - (x_q - x'_q)i_q).
\end{aligned} \tag{2.1}$$

The SMIB system in above set of equations is presented with $V_t(=E_t)$ as the reference phasor. For this system, there is a second presentation by assuming the $V_B(=E_B)$ as the reference phasor. This second presentation, which has its own weaknesses and strengths, with related explanations is given in Appendix 5.2. By determining the state variables and inputs in the form of (2.2):

$$\begin{aligned}
\mathbf{x} &= [\delta \quad \Delta\omega \quad e'_q \quad e'_d] = [x_1 \quad x_2 \quad x_3 \quad x_4] \\
\mathbf{u} &= [T_m \quad E_{fd}] = [u_1 \quad u_2].
\end{aligned} \tag{2.2}$$

equation (2.1) can be rewritten in the following form as presented in (2.3):

$$\begin{aligned}
\dot{x}_1 &= \omega_0 x_2 \\
\dot{x}_2 &= \frac{1}{J}(u_1 - T_e - Dx_2) \\
\dot{x}_3 &= \frac{1}{T'_{do}}(u_2 - x_3 - (x_d - x'_d)i_d) \\
\dot{x}_4 &= \frac{1}{T'_{qo}}(-x_4 - (x_q - x'_q)i_q)
\end{aligned} \tag{2.3}$$

where ω_0=$2\pi f_0$ is the nominal synchronous speed (elec. rad/s), ω the rotor speed (pu), T_m the mechanical input torque (pu), T_e the air-gap torque or electrical output power (pu), E_{fd} the exciter output voltage or the field voltage as seen from the armature (pu) and δ the rotor angle in (elec.rad). Other variables and constants are defined in List of Symbols

in front-pages. Based on the system equations of Figure 2.1, the air-gap torque T_e will be equal to the terminal electrical power P_t (or P_e=$\omega_r\, T_e$) neglecting the stator resistance (R_a=0)and assuming ω_r=1.0 (pu):

$$T_e = P_t + R_a I_t^2 \quad \overset{R_a=0}{\rightarrow} \quad T_e \cong P_t = e_d i_d + e_q i_q \tag{2.4}$$

where the d-and q-axis voltages (e_d,e_q) can be expressed as:

$$\begin{aligned} e_d &= V_t sin\delta \\ e_q &= V_t cos\delta \end{aligned} \tag{2.5}$$

and as a result the terminal bus voltage equation is presented as (2.6):

$$E_t = V_t = \sqrt{e_d^2 + e_q^2}. \tag{2.6}$$

Also, the d-and q-axis currents (i_d,i_q) are:

$$\begin{aligned} i_d &= I_t sin(\delta + \Phi) = \frac{e'_q - V_t cos\delta}{x'_d} \\ i_q &= I_t cos(\delta + \Phi) = \frac{V_t sin\delta}{x_q} \end{aligned} \tag{2.7}$$

and consequently for the terminal current we will have:

$$I_t = \sqrt{i_d^2 + i_q^2}. \tag{2.8}$$

Replacing the variables δ and e'_q by the state variables x_1 and x_3, we will have:

$$\begin{aligned} i_d &= \frac{x_3 - V_t cosx_1}{x'_d} \\ i_q &= \frac{V_t sinx_1}{x_q}. \end{aligned} \tag{2.9}$$

Using (2.5) and (2.9) in (2.4) and after mathematical simplification, the electrical output power P_e at the terminal bus (P_e= P_t) can be presented as (2.10):

$$y_1 = P_e = \frac{V_t}{x'_d} e'_q sin\delta + \frac{V_t^2}{2}(\frac{1}{x_q} - \frac{1}{x'_d}) sin2\delta \tag{2.10}$$

and in terms of states x_1 and x_3 we will have:

$$y_1 = P_e = \frac{V_t}{x'_d} x_3 sinx_1 + \frac{V_t^2}{2}(\frac{1}{x_q} - \frac{1}{x'_d}) sin2x_1. \tag{2.11}$$

To summarize, using (2.11) and (2.9) in (2.3), the fourth-order nonlinear synchronous machine state space model is rewritten as (2.12) in a form suitable for state estimation purposes, with the electrical output power P_t as the single measurable system output. Since the modified equations in (2.12) include the terminal voltage V_t, it appears that the vector $\mathbf{u}$ in (2.3) now needs to be modified as well in order to add V_t as the third input as it is done in (2.12).

$$\begin{aligned}
&\mathbf{x} = [\delta \quad \Delta\omega \quad e'_q \quad e'_d] = [x_1 \quad x_2 \quad x_3 \quad x_4] \\
&\mathbf{u} = [T_m \quad E_{fd} \quad V_t] = [u_1 \quad u_2 \quad u_3] \\
&\dot{x}_1 = \omega_0 x_2 \\
&\dot{x}_2 = \frac{1}{J}(T_m - (\frac{V_t}{x'_d}x_3 sinx_1 + \frac{V_t^2}{2}(\frac{1}{x_q} - \frac{1}{x'_d})sin2x_1) - Dx_2) \\
&\dot{x}_3 = \frac{1}{T'_{do}}(E_{fd} - x_3 - (x_d - x'_d)(\frac{x_3 - V_t cosx_1}{x'_d})) \\
&\dot{x}_4 = \frac{1}{T'_{qo}}(-x_4 - (x_q - x'_q)(\frac{V_t sinx_1}{x_q})) \\
&y_1 = \frac{V_t}{x'_d}x_3 sinx_1 + \frac{V_t^2}{2}(\frac{1}{x_q} - \frac{1}{x'_d})sin2x_1
\end{aligned} \tag{2.12}$$

where all the parameters and quantities other than state variables are (or assumed to be) known and measurable. We can therefore represent (2.12) in a global structure as (2.13):

$$\begin{aligned}
\dot{\mathbf{x}} &= \mathbf{f}(\mathbf{x}, \mathbf{u}, \mathbf{w}) \\
\mathbf{y} &= \mathbf{h}(\mathbf{x}, \mathbf{u}, \mathbf{v})
\end{aligned} \tag{2.13}$$

where $\mathbf{x}$ is the state variable vector defined in (2.2) (1), $\mathbf{w}$ the process (state) noise, $\mathbf{v}$ the measurement noise, $\mathbf{f}$ the system function, $\mathbf{h}$ the output function, $\mathbf{u}$ the input signals defined in (2.12) and $\mathbf{y}$ the measurable output.

In the nonlinear state space model (2.12), the terminal bus signals V_t, P_t and Q_t are accessible from a PMU device which is assumed to be installed at the generator terminal bus. The PMU is a power system device that samples input voltage V_{abc} and current I_{abc} waveforms using a common synchronizing signal from the GPS, and calculates the phasors (magnitude and angle) using the Discrete Fourier Transform (DFT) [26, 27, 28].

The overall plan of the estimation process is illustrated in Figure 2.2. The dotted line of E_{fd} shows that one of the approaches in this chapter, the EKF-UI state estimator, does not need the E_{fd} signal which is estimated with the states. The classic EKF based state estimator will first be developed for the case where the E_{fd} signal is measurable. This assumption may be defendable for machines on which the field voltage is accessible or for the next generation of synchronous machines with embedded smart sensors. Then, in the case of not using linearization in the state estimation process, the UKF approach will be employed. Finally, in cases where the E_{fd} signal is not available or measurable, the new

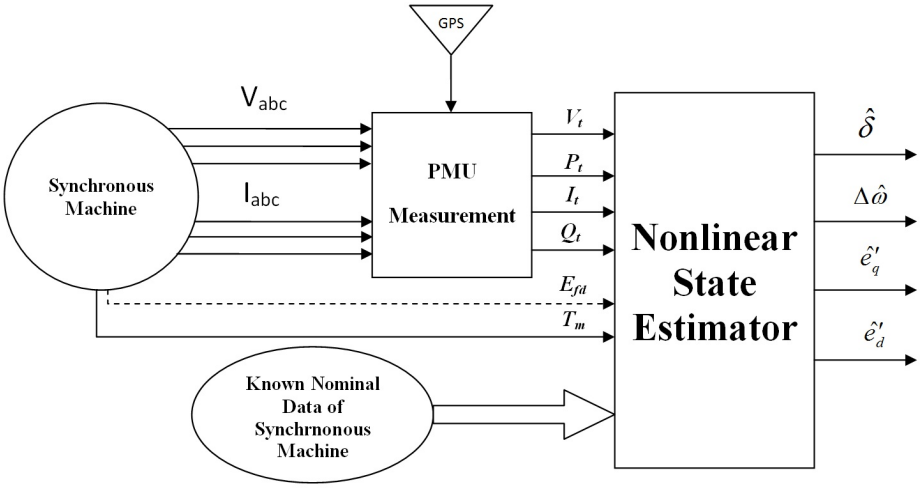

Figure 2.2: Overview of the dynamic state estimator for a synchronous machine.

extended version of EKF known as the Extended Kalman Filter with Unknown Inputs (EKF-UI) will be employed.

2.3 The Extended Kalman Filter (EKF)

2.3.1 Algorithm Description

To derive the discrete-time EKF algorithm, we start from the basic definition of time derivation of a variable $\mathbf{x}$:

$$\dot{\mathbf{x}} = \frac{\mathbf{x}(k) - \mathbf{x}(k-1)}{\Delta t} \quad \Rightarrow \quad \mathbf{x}(k) = \dot{\mathbf{x}}.\Delta t + \mathbf{x}(k-1) \tag{2.14}$$

where Δt is the time step, k and k-1 is used to indicate t=$k.\Delta t$ and t=(k-1).Δt respectively. Replacing (2.13) in (2.14), we easily obtain (2.15):

$$\mathbf{x}(k) = \mathbf{x}(k-1) + \Delta t.\mathbf{f}(\mathbf{x}, \mathbf{u}, \mathbf{w}) \tag{2.15}$$

and in turn (2.16):

$$\mathbf{x}_k = \Delta t \times \mathbf{f}(\mathbf{x}, \mathbf{u}, \mathbf{w}) + \mathbf{x}_{k-1}. \tag{2.16}$$

If rewritten properly, equation (2.16) gives us the discrete-time system equations pre-

sented in (2.17):

$$\begin{aligned} \mathbf{x}_k &= \mathbf{f}_{k-1}(\mathbf{x}_{k-1}, \mathbf{u}_{k-1}, \mathbf{w}_{k-1}) \\ \mathbf{y}_k &= \mathbf{h}_k(\mathbf{x}_k, \mathbf{u}_k, \mathbf{v}_k) \end{aligned} \tag{2.17}$$

where $\mathbf{x}_k$ is the system state vector, $\mathbf{u}_k$ is the known input vector of the system, $\mathbf{w}_k$ is either the process (random state) noise or represents inaccuracies in the system model, $\mathbf{y}_k$ is the noisy observation or measured variable (output) vector and $\mathbf{v}_k$ is the measurement noise. It is assumed that measurements are made at by the PMUs, at discrete sampling time instants $k.T$ (k=0,1,...,n). The noises sequences $\{\mathbf{v}_k\}$ and $\{\mathbf{w}_k\}$ are supposed to be white, Gaussian, and independent of each other as presented in (2.18)-(2.21):

$$\begin{aligned} &\{\mathbf{w}_k\} \sim (0, \mathbf{Q}_k) \\ &E[\mathbf{w}_k] = 0 \\ &E[\mathbf{w}_k \mathbf{w}_k^T] = \mathbf{Q}_k \end{aligned} \tag{2.18}$$

$$\begin{aligned} &\{\mathbf{v}_k\} \sim (0, \mathbf{R}_k) \\ &E[\mathbf{v}_k] = 0 \\ &E[\mathbf{v}_k \mathbf{v}_k^T] = \mathbf{R}_k \end{aligned} \tag{2.19}$$

$$\begin{aligned} &E[\mathbf{w}_k \mathbf{w}_j^T] = 0 \\ &E[\mathbf{v}_k \mathbf{v}_j^T] = 0 \end{aligned} \tag{2.20}$$

$$E[\mathbf{v}_k \mathbf{w}_j^T] = 0 \tag{2.21}$$

Equations (2.18) and (2.19) imply that $\{\mathbf{v}_k\}$ and $\{\mathbf{w}_k\}$ have a zero mean, with covariance matrices $\mathbf{Q}_k$ and $\mathbf{R}_k$ respectively. Equation (2.20) implies that the values of $\{\mathbf{v}_k\}$ (respectively $\{\mathbf{w}_k\}$), at different times instants, are not correlated while equation (2.21) shows that the process (state) and measurement (observation) noises are not cross-correlated [29].

Starting from these initial considerations, the discrete-time EKF algorithm for state estimation consists of two steps [29]:

Step I: Initialization of the filter at k=0:

$$\begin{aligned} \hat{\mathbf{x}}_0^+ &= E[\mathbf{x}_0] \\ \mathbf{P}_0^+ &= E[(\mathbf{x}_0 - \hat{\mathbf{x}}_0^+)(\mathbf{x}_0 - \hat{\mathbf{x}}_0^+)^T] \end{aligned} \tag{2.22}$$

where E indicates the expected value and the sign + in superscript denotes that the estimate is an *a posteriori* estimate.

Step II: For k=1, 2, ... perform the following:

(a) Compute the following partial-derivation matrices:

$$\begin{aligned}\mathbf{F}_{k-1} &= \left.\frac{\partial \mathbf{f}_{k-1}}{\partial \mathbf{x}}\right|_{\hat{\mathbf{x}}_{k-1}^{+}} \\ \mathbf{L}_{k-1} &= \left.\frac{\partial \mathbf{f}_{k-1}}{\partial \mathbf{w}}\right|_{\hat{\mathbf{x}}_{k-1}^{+}}\end{aligned} \tag{2.23}$$

(b) Perform the time update of the state estimate and estimation-error co-variance as follows:

$$\begin{aligned}\mathbf{P}_{k}^{-} &= \mathbf{F}_{k-1}\mathbf{P}_{k-1}^{+}\mathbf{F}_{k-1}^{T} + \mathbf{L}_{k-1}\mathbf{Q}_{k-1}\mathbf{L}_{k-1}^{T} \\ \hat{\mathbf{x}}_{k}^{-} &= \mathbf{f}_{k-1}(\hat{\mathbf{x}}_{k-1}^{+}, \mathbf{u}_{k-1}, 0)\end{aligned} \tag{2.24}$$

(c) Compute the following partial-derivative matrices:

$$\begin{aligned}\mathbf{H}_{k} &= \left.\frac{\partial \mathbf{h}_{k}}{\partial \mathbf{x}}\right|_{\hat{\mathbf{x}}_{k}^{-}} \\ \mathbf{M}_{k} &= \left.\frac{\partial \mathbf{h}_{k}}{\partial \mathbf{v}}\right|_{\hat{\mathbf{x}}_{k}^{-}}\end{aligned} \tag{2.25}$$

(d) Perform the measurement update of the state estimate and estimation-error co-variance as follows:

$$\begin{aligned}\mathbf{K}_{k} &= \mathbf{P}_{k}^{-}\mathbf{H}_{k}^{T}(\mathbf{H}_{k}\mathbf{P}_{k}^{-}\mathbf{H}_{k}^{T} + \mathbf{M}_{k}\mathbf{R}_{k}\mathbf{M}_{k}^{T})^{-1} \\ \hat{\mathbf{x}}_{k}^{+} &= \hat{\mathbf{x}}_{k}^{-} + \mathbf{K}_{k}\left[\mathbf{y}_{k} - \mathbf{h}(\hat{\mathbf{x}}_{k}^{-}, 0)\right] \\ \mathbf{P}_{k}^{+} &= (\mathbf{I} - \mathbf{K}_{k}\mathbf{H}_{k})\mathbf{P}_{k}^{-}\end{aligned} \tag{2.26}$$

2.3.2 Simulation Results

The discrete-time EKF algorithm has been implemented in Matlab/Simulink using the embedded function programming feature of Simulink as presented in Figure 2.3. The simulation of the generator nonlinear model is performed while including saturation assuming a two-factor d-q saturation model [1, 12] with the parameters presented in Appendix 5.2. On the other hand, the EKF-based estimation of the dynamic states is carried out in parallel with the simulation, in a single run without any assumption about saturation of the underlying generator.

In the embedded Matlab function block, the input signals in equation (2.12) T_m, E_{fd} and V_t and the system observation signal P_e (as y_1) are used as inputs for the EKF. The EKF block has access to the values of these signals (T_m, E_{fd}, V_t and P_e) and known machine parameters at each iteration. The embedded block then generates the state estimate based on its inside algorithm which is described in the previous section, while using the time step set through the Simulink configuration panel (T=500 μs). The initial values for

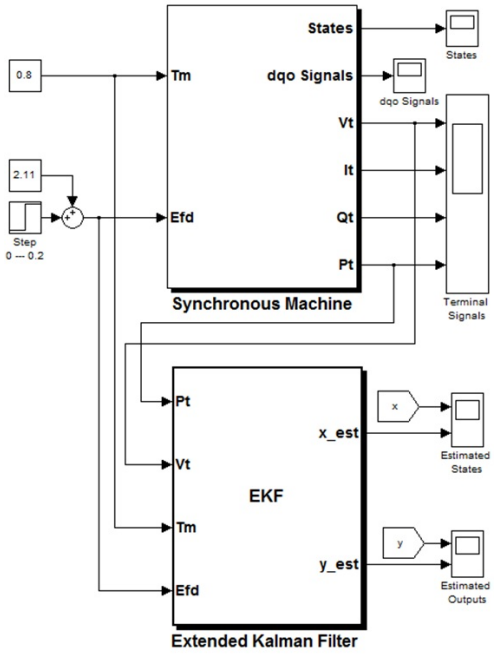

Figure 2.3: Implementation of EKF algorithm: Using the embedded Matlab function block which uses T_m, E_{fd}, V_t and P_t as its input signals.

states and state covariance matrix are $\mathbf{x}_0 = [0.6; 0; 0; 0]$ and $\mathbf{P}_0 = diag([10^2, 10^2, 10^2, 10^2])$ respectively. The noise-free results are presented in Figure 2.4(a).

Also, the process and measurement noise covariance matrices are set as $\mathbf{w}_k \sim(0,\mathbf{Q}_k) = (0, 0.08^2 \times \mathbf{I}_{4\times4})$ and $\mathbf{v}_k \sim(0,\mathbf{R}_k)=(0, 0.02^2 \times \mathbf{I})$. The size of matrix $\mathbf{I}_{4\times4}$ arises from the fact that there are four states. For simulation near real system conditions, white-noise sequences with covariance $(0,0.001^2)$ and $(0,0.01^2)$ were added to the state process and output measurement respectively.

The results in the presence of noise are presented in Figure 2.4(b). Near the estimated states, the estimated output signal $\hat{y}_k = \mathbf{h}(\hat{\mathbf{x}}_k^-, 0)$ compared with the real output signal y_k is also shown in Figure 2.4(b).

2.4 The Unscented Kalman Filter (UKF)

2.4.1 Background

The Extended Kalman Filter is probably the most widely used estimation algorithm for nonlinear systems. However, previous experience in the estimation community has shown that the EKF is often difficult to implement, difficult to tune, and reliable only for systems that are almost linear on the time scale of the updates. Many of these difficulties arise from its use of linearization. To overcome this limitation, unscented transformation (UT) was applied to propagate mean and covariance information by nonlinear transformation. It is

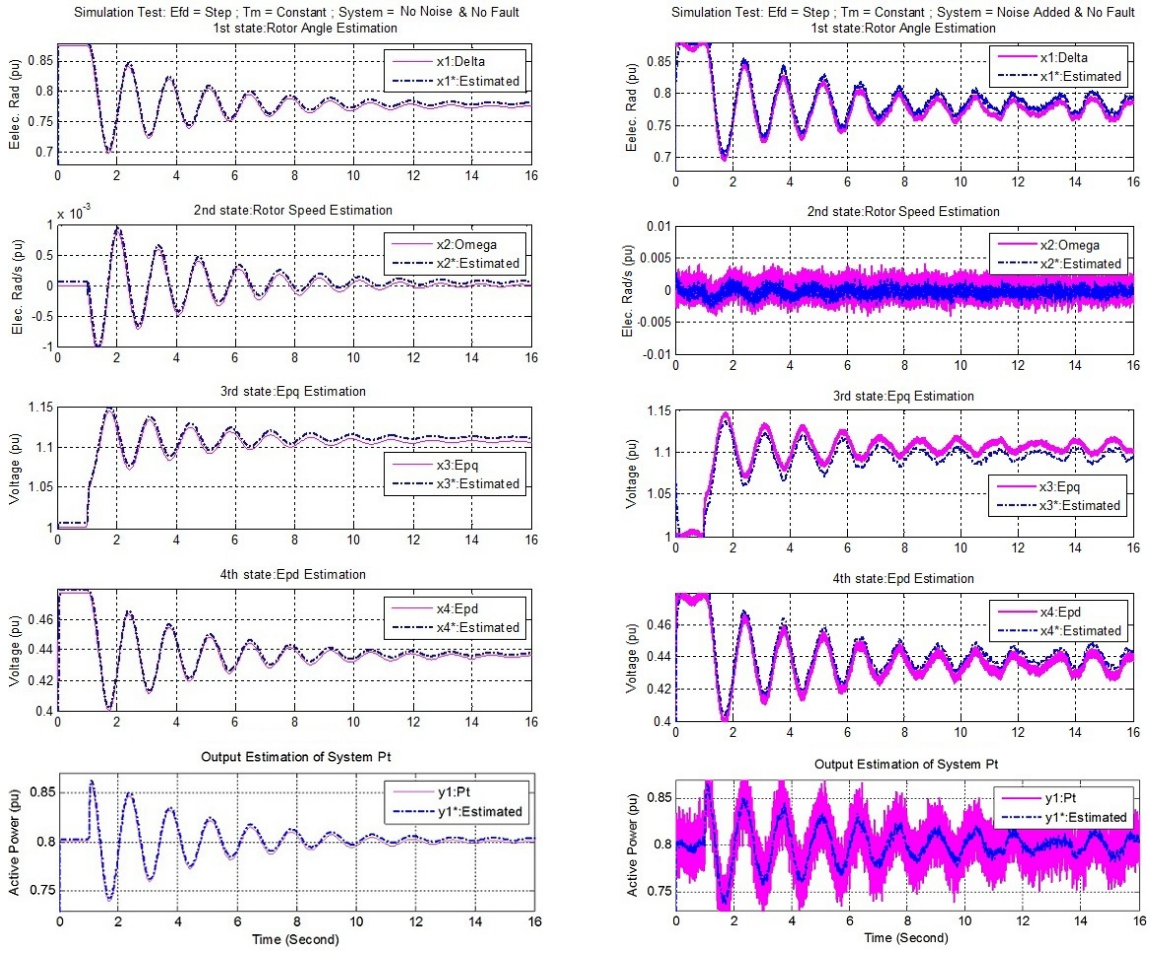

(a) (b)

Figure 2.4: EKF estimation results for states and output signals in two condition: (a) Noise-free results. (b) Noise-added results.

more accurate, easier to implement, and uses the same order of calculations as linearization [18, 29].

In this section, the state estimation of the system will be presented using the UKF algorithm. Considering a system in the form of $\mathbf{y}=\mathbf{g}(\mathbf{x})$, the question is, given the pdf of $\mathbf{x}$, how the UKF computes the mean ($\bar{\mathbf{y}}^{\mathrm{UKF}}$) and covariance ($\mathbf{P}_y{}^{\mathrm{UKF}}$) of a random variable ($\mathbf{y}$). The Unscented Transformation is founded on the intuition that *it is easier to approximate a probability distribution than it is to approximate an arbitrary nonlinear function or transformation* [30]. The basic idea of the UKF approach is illustrated in Figure 2.5.

In Figure 2.5, a set of points $\mathbf{x}^{(i)}$ ($i = 1, 2, ..., 2n+1$), termed sigma points, are chosen so that their mean and covariance are $\bar{\mathbf{y}}^{\mathrm{UKF}}$ and $\mathbf{P}_y{}^{\mathrm{UKF}}$. The nonlinear function is applied to each point, in turn, to yield a cloud of transformed points. The statistics of the transformed

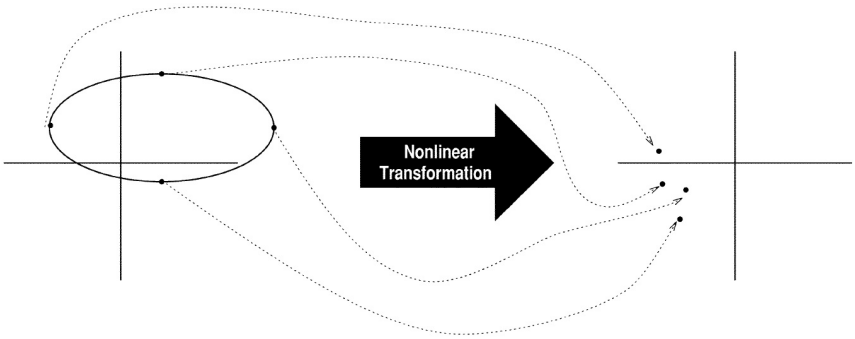

Figure 2.5: Principle of the Unscented Transformation (UT).

points can then be calculated to form an estimate of the nonlinearly transformed mean and covariance [30]. In Unscented Transformation, each sigma point is associated with a weight $\mathbf{W}^{(i)}$. The following steps are then involved in approximating the mean and covariance in the UKF algorithm [31]:

(i) Propagate each sigma point through the nonlinear function:

$$\mathbf{y}^{(i)} = \mathbf{g}(\mathbf{x}^{(i)}). \tag{2.27}$$

(ii) The mean is approximated by the weighted average of the transformed points:

$$\bar{\mathbf{y}}^{\text{UKF}} = \sum_{i=0}^{p} \mathbf{W}^{(i)} \mathbf{y}^{(i)} \tag{2.28}$$

where the weighting coefficients $\mathbf{W}^{(i)}$ are defined as follows:

$$\sum_{i=0}^{p} \mathbf{W}^{(i)} = 1. \tag{2.29}$$

(iii) The covariance is computed from the weighted outer product of the transformed points:

$$\mathbf{P}_y{}^{\text{UKF}} = \sum_{i=0}^{p} \mathbf{W}^{(i)} (\mathbf{y}^{(i)} - \bar{\mathbf{y}})(\mathbf{y}^{(i)} - \bar{\mathbf{y}})^T. \tag{2.30}$$

Both the sigma points and the weights are computed deterministically using a set of conditions given in [30]. The UKF algorithm is presented briefly below. For more details and the background theory, readers are referred to [30].

2.4.2 Algorithm Description

Let the n-state discrete-time nonlinear system be represented by (2.31):

$$\begin{aligned} \mathbf{x}_{k+1} &= \mathbf{f}(\mathbf{x}_k, \mathbf{u}_k, \mathbf{t}_k) + \mathbf{w}_k \\ \mathbf{y}_k &= \mathbf{h}(\mathbf{x}_k, \mathbf{u}_k, \mathbf{t}_k) + \mathbf{v}_k \\ \{\mathbf{w}_k\} &\sim (0, \mathbf{Q}_k) \\ \{\mathbf{v}_k\} &\sim (0, \mathbf{R}_k) \end{aligned} \tag{2.31}$$

where all variables are defined in (2.17). The UKF algorithm for this system can be expressed in following steps [29]:

Step I: Initialization of the filter at k=0 as follows:

$$\begin{aligned} \hat{\mathbf{x}}_0^+ &= E[\mathbf{x}_0] \\ \mathbf{P}_0^+ &= E[(\mathbf{x}_0 - \hat{\mathbf{x}}_0^+)(\mathbf{x}_0 - \hat{\mathbf{x}}_0^+)^T] \end{aligned} \tag{2.32}$$

where E indicates the expected value and the sign + in superscript denotes that the estimate is an *a posteriori* estimate.

Step II: The following time update equations are used to propagate the state estimate and covariance from one measurement time to the next.

(a) To propagate from time step (k-1) to k, first choose sigma points $\mathbf{x}_{k-1}^{(i)}$ as specified in (2.33), with appropriate changes since the current best guesses for the mean and covariance of $\mathbf{x}_k$ are $\hat{\mathbf{x}}_{k-1}^+$ and $\mathbf{P}_{k-1}^+$:

$$\begin{aligned} \hat{\mathbf{x}}_{k-1}^{(i)} &= \hat{\mathbf{x}}_{k-1}^+ + \tilde{\mathbf{x}}^{(i)} && i = 1, ..., 2n \\ \tilde{\mathbf{x}}^{(i)} &= \left(\sqrt{n\mathbf{P}_{k-1}^+}\right)^T && i = 1, ..., n \\ \tilde{\mathbf{x}}^{(n+i)} &= -\left(\sqrt{n\mathbf{P}_{k-1}^+}\right)_i^T && i = 1, ..., n \end{aligned} \tag{2.33}$$

(b) Use the known nonlinear system equation **f(.)** to transform the sigma points into $\hat{\mathbf{x}}_{k-1}^{(i)}$ vectors as shown in (2.27), with appropriate changes since the nonlinear transformation is **f(.)**:

$$\hat{\mathbf{x}}_k^{(i)} = \mathbf{f}(\hat{\mathbf{x}}_{k-1}^{(i)}, \mathbf{u}_k, \mathbf{t}_k). \tag{2.34}$$

(c) Combine the $\hat{\mathbf{x}}_{k-1}^{(i)}$ vectors to obtain the *a priori* state estimate at time k. This is based on (2.28):

$$\mathbf{x}_k^- = \frac{1}{2n} \sum_{i=1}^{2n} \mathbf{x}_k^{(i)}. \tag{2.35}$$

(d) Estimate the *a priori* error covariance as shown in (2.30). However, we should add $\mathbf{Q}_{k-1}$ to the end of the equation to take the process noise into account:

$$\mathbf{P}_k^- = \frac{1}{2n}\sum_{i=1}^{2n}(\hat{\mathbf{x}}_k^{(i)} - \hat{\mathbf{x}}_k^-)(\hat{\mathbf{x}}_k^{(i)} - \hat{\mathbf{x}}_k^-)^T + \mathbf{Q}_{k-1}. \tag{2.36}$$

Step III: Now that the time update equations are done, we implement the measurement-update equations in following steps:

(a) Choose sigma points $\hat{\mathbf{x}}_{k-1}^-$ as specified in (2.33), with appropriate changes since the current best guess for the mean and covariance of $\mathbf{x}_k$ are $\hat{\mathbf{x}}_k^-$ and $\mathbf{P}_k^-$:

$$\begin{aligned}
\hat{\mathbf{x}}_k^{(i)} &= \hat{\mathbf{x}}_k^- + \tilde{\mathbf{x}}^{(i)} && i = 1, ..., 2n \\
\tilde{\mathbf{x}}^{(i)} &= \left(\sqrt{n\mathbf{P}_k^-}\right)^T && i = 1, ..., n \\
\tilde{\mathbf{x}}^{(n+i)} &= -\left(\sqrt{n\mathbf{P}_k^-}\right)_i^T && i = 1, ..., n.
\end{aligned} \tag{2.37}$$

This step can be omitted if desired. Instead of generating new sigma points, we can reuse the sigma points that were obtained from the time update. This will save computational effort if we are willing to sacrifice performance.

(b) Use the known nonlinear measurement equation $\mathbf{h(.)}$ to transform the sigma points into $\hat{\mathbf{y}}_k^{(i)}$ vectors (predicted measurements) as shown in (2.27):

$$\hat{\mathbf{y}}_k^{(i)} = \mathbf{f}(\hat{\mathbf{x}}_k^{(i)}, \mathbf{t}_k). \tag{2.38}$$

(c) Combine the $\hat{\mathbf{y}}_k^{(i)}$ vectors to obtain the predicted measurement at time k. This is based on (2.28):

$$\mathbf{y}_k = \frac{1}{2n}\sum_{i=1}^{2n}\mathbf{y}_k^{(i)}. \tag{2.39}$$

(d) Estimate the covariance of the predicted measurement as shown in (2.30). However, we should add $\mathbf{R}_k$ to the end of the equation to take the measurement noise into account:

$$\mathbf{P}_k = \frac{1}{2n}\sum_{i=1}^{2n}(\hat{\mathbf{y}}_k^{(i)} - \hat{\mathbf{x}}_k)(\hat{\mathbf{y}}_k^{(i)} - \hat{\mathbf{y}}_k)^T + \mathbf{R}_k. \tag{2.40}$$

(e) Estimate the cross covariance between $\hat{\mathbf{x}}_k^-$ and $\hat{\mathbf{y}}_k$:

$$\mathbf{P}_{xy} = \frac{1}{2n}\sum_{i=1}^{2n}(\hat{\mathbf{x}}_k^{(i)} - \hat{\mathbf{x}}_k^-)(\hat{\mathbf{y}}_k^{(i)} - \hat{\mathbf{y}}_k)^T. \tag{2.41}$$

(f) The measurement update of the state estimate can be performed using the normal Kalman filter equations:

$$\begin{aligned}\mathbf{K}_k &= \mathbf{P}_{xy}\mathbf{P}_y^{-1}\\ \hat{\mathbf{x}}_k^+ &= \hat{\mathbf{x}}_k^- + \mathbf{K}_k\left[\mathbf{y}_k - \hat{\mathbf{y}}_k\right]\\ \mathbf{P}_k^+ &= \mathbf{P}_k^- - \mathbf{K}_k\mathbf{P}_y\mathbf{K}_k^T.\end{aligned} \tag{2.42}$$

The algorithm above assumes that the process and measurement equations are linear with respect to the noise, as shown in (2.31). In general, the process and measurement equations may have noise that enters the process and measurement equations nonlinearly. That is,

$$\begin{aligned}\mathbf{x}_{k+1} &= \mathbf{f}(\mathbf{x}_k, \mathbf{u}_k, \mathbf{w}_k, \mathbf{t}_k)\\ \mathbf{y}_k &= \mathbf{h}(\mathbf{x}_k, \mathbf{u}_k, \mathbf{v}_k, \mathbf{t}_k).\end{aligned} \tag{2.43}$$

In this case, the UKF algorithm presented above is not rigorous because it treats the noise as additive, as seen in (2.36) and (2.40). To handle this situation, we augment the noise on the state vector as shown in (2.45):

$$\mathbf{x}_k^{a+} = \begin{bmatrix}\mathbf{x}_k & \mathbf{w}_k & \mathbf{v}_k\end{bmatrix}^T. \tag{2.44}$$

We then use the UKF to estimate the augmented state $\mathbf{x}_k^{a+}$. The UKF is initialized as:

$$\begin{aligned}\mathbf{x}_0^{a+} &= \begin{bmatrix}E(\mathbf{x}_0) & 0 & 0\end{bmatrix}^T\\ \mathbf{P}_0^{a+} &= diag(E[(\mathbf{x}_0 - \hat{\mathbf{x}}_0)(\mathbf{x}_0 - \hat{\mathbf{x}}_0)], \mathbf{Q}_0, \mathbf{R}_0).\end{aligned} \tag{2.45}$$

Then we use the UKF algorithm presented above but, since we are estimating the augmented state with mean and covariance, we can remove $\mathbf{Q}_{k-1}$ and $\mathbf{R}_k$ from (2.36) and (2.40).

2.4.3 Simulation Results

The overall structure of the Matlab implementation based on the Simulink embedded function block is presented in Figure 2.6. In terms of Simulink implementation, we replaced the EKF block in Figure 2.3 by an equivalent UKF block, implemented according to the algorithm presented in previous section [29].

The embedded Matlab function was used to implement the UKF algorithm,as we have done for EKF state estimator, because this block enables us to predict the dynamic state (bottom of Figure 2.6) while simulating the synchronous machine (top of Figure 2.6). The embedded function block creates an m-file page in the Simulink model, which means we can easily set and run more or less complicated algorithms in the Simulink file.

As shown in Figure 2.6, in the embedded Matlab function block, the signals T_m, E_{fd} and

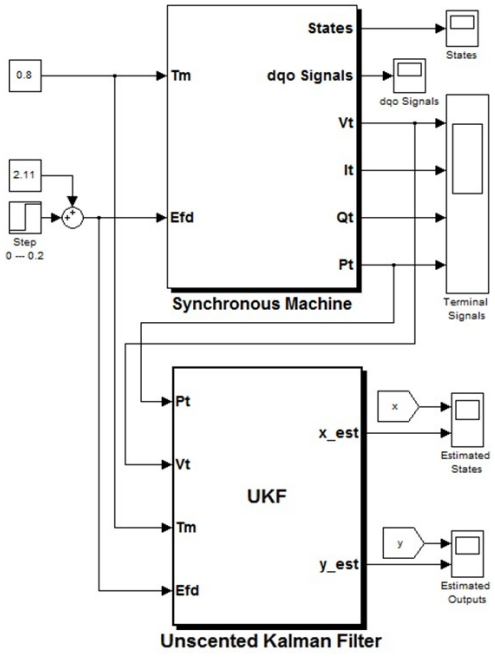

Figure 2.6: Implementation of UKF algorithm: Using the embedded Matlab function block which uses T_m, E_{fd}, V_t and P_t as its input signals.

V_t and the system observation signal P_t $(=y_1)$, taken from the machine model, have been used as inputs of the UKF block. The latter thus has access to these input-output signals at each time step in order to generate the state estimation based on the algorithm described in the previous section. Further details about Matlab implementation are described in Appendix 5.2.

The initial values for states and state covariance matrix are $\mathbf{x}_0 = [0.4; 0; 0; 0]$ and $\mathbf{P}_0 = diag([10, 10, 10, 10])$ respectively. The noise-free results of the state estimation of the UKF method are depicted in Figure 2.7(a), based on excitation voltage step responses. The corresponding estimated output signal $\hat{y}_k$ compared with the actual output signal y_k is also shown in Figure 2.7(a).

Also, the process and measurement noise covariance matrices are set as $\mathbf{w}_k \sim(0,\mathbf{Q}_k) = (0, 0.001^2 \times \mathbf{I}_{4\times4})$ and $\mathbf{v}_k \sim(0,\mathbf{R}_k)=(0, 0.01^2 \times \mathbf{I})$. For simulation near real system conditions, white-noise sequences with covariance $(0,0.08^2)$ and $(0,0.1^2)$ were added to the state process and output measurement respectively. The results in the presence of noise are presented in Figure 2.7(b).

As is clear from Figure 2.7(b) and when we compare the state estimation results in this figure with Figure 2.4(b) which was related to EKF estimation results in the presence of noise, the UKF approach definitely outperforms the EKF in term of accuracy and smoothness. In fact, at the same level of process and measurement noise, the EKF estimator results are noisier, like the rotor speed $\Delta\omega$, and have also DC component, like the rotor angle δ, e_q and e_d voltages while the UKF results are smoother and do not have DC

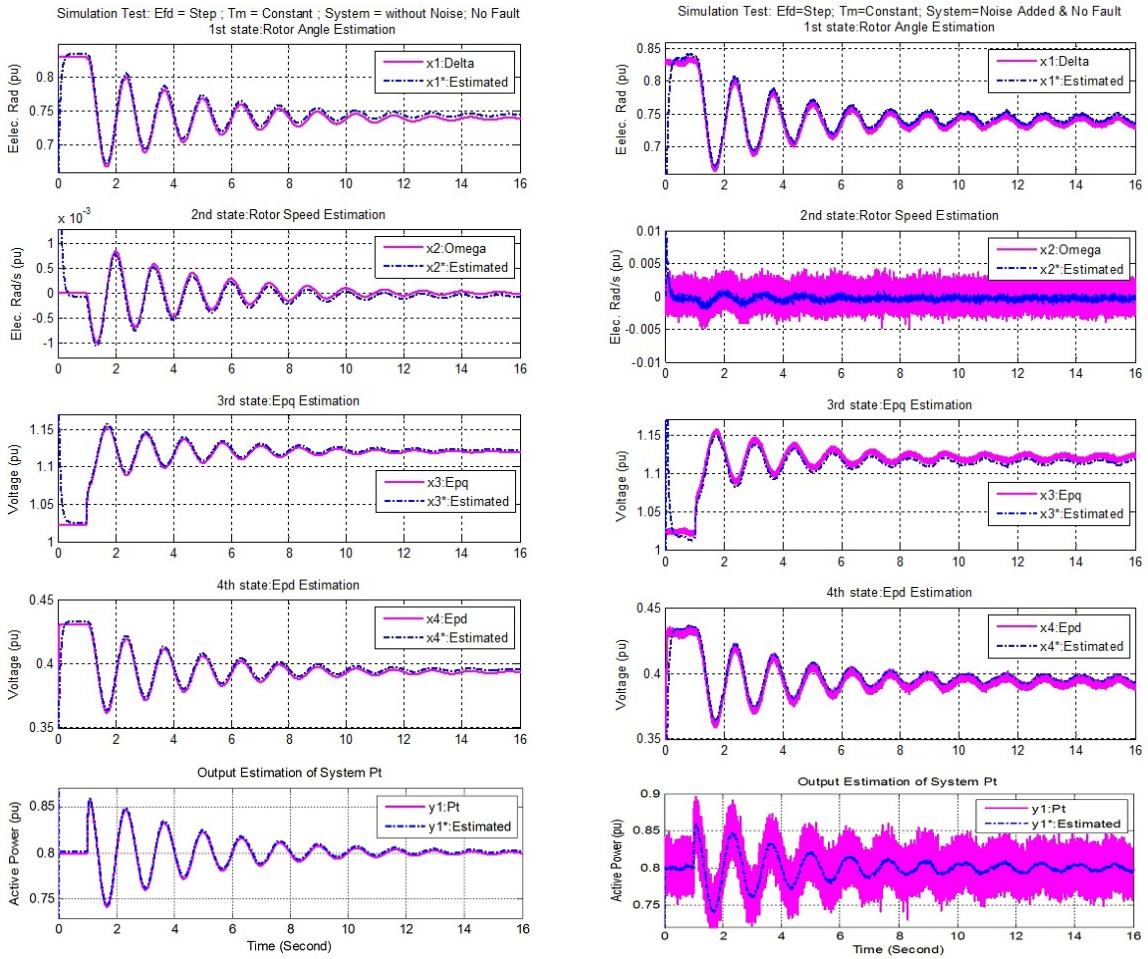

(a) (b)

Figure 2.7: UKF estimation results for states and output signals in two condition: (a) Noise-free results. (b) Noise-added results.

component.

2.4.4 Fault Analysis

In this part, the effectiveness of the UKF method was checked in the presence of a network fault. The general configuration of the power system can be reduced to the form of Figure 2.1 using Thévenin's equivalent theory [1].

Based on this equivalent circuit, we will consider that the fault occurred in the mid-point of the transmission line, as shown in Figure 2.8, with the system in the steady state at T=20 (s). The analysis will focus on two scenarios following a disturbance: (i) stable and (ii) unstable.

In the first scenario, the fault needs to be cleared after 0.1 (s), at T=20.1 (s), for the

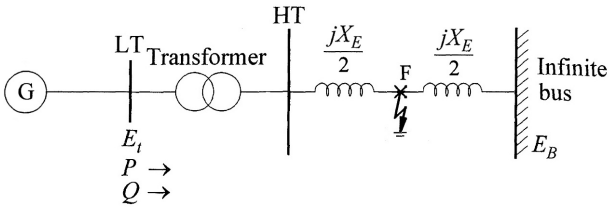

Figure 2.8: Mid-point short-circuit fault.

system to remain stable. The results of the state estimation process during and following the contingency in this case are shown in Figure 2.9(a). From these results, it is clear that broadly speaking, the UKF state estimator generates very accurate states right after fault clearing. However, some variables, notably the angle and speed, are temporarily wrong during the fault due to the abrupt change in the external reactance.

For the second scenario, the fault was cleared after 0.3 (s), at T=20.3 (s) and the system transitioned into an unstable condition. In this case also, the UKF state estimator generates the estimated states with an appropriate accuracy once the fault is cleared (Figure 2.9(b)). Generally, it takes several milliseconds for the state estimator to track the real signal after a sudden change in the network reactance and there is a large error between the real and the estimated signals within the fault time-frame. This error may be reduced by blocking the slow-changing states to their pre-fault values during the fault occurrence.

Finally, we have repeated the fault simulations (Figure 2.9) in the presence of noise. The noise sequences were set to have the same magnitudes as in Figure 2.9. We again obtained satisfactory results from the UKF state estimation process in the presence of noise, similarly to Figure 2.9. In order to have clarity in the results and be able to track the performance of the state estimator at the time of fault occurrence, we just present the fault simulations in the noise-free condition.

Based on the good performance achieved with these two fault scenarios, it could be concluded that the UKF approach will be able to estimate the state of a synchronous machine whatever the stability condition of the power system to which it is connected, even when the process and measurement noises are significant.

2.4.5 Discussion on UKF State Estimation Results

The results presented in Figures 2.8 and 2.9 assume that the input signal E_{fd} is a step function while T_m is a constant input. To confirm the UKF effectiveness under more general conditions, we tested it with different kinds of input. Hence, the simulation was repeated for two other configurations: the first for T_m=**ramp** and E_{fd}=**constant** and the second for T_m=**constant** and E_{fd}=**ramp**. In both simulation studies, the results of the UKF approach showed that the UKF block estimated the states properly and with enough accuracy. These scenarios were repeated for the system in the presence of noise and the results were accurate again.

Also, the state estimation process was repeated for different values of the external line

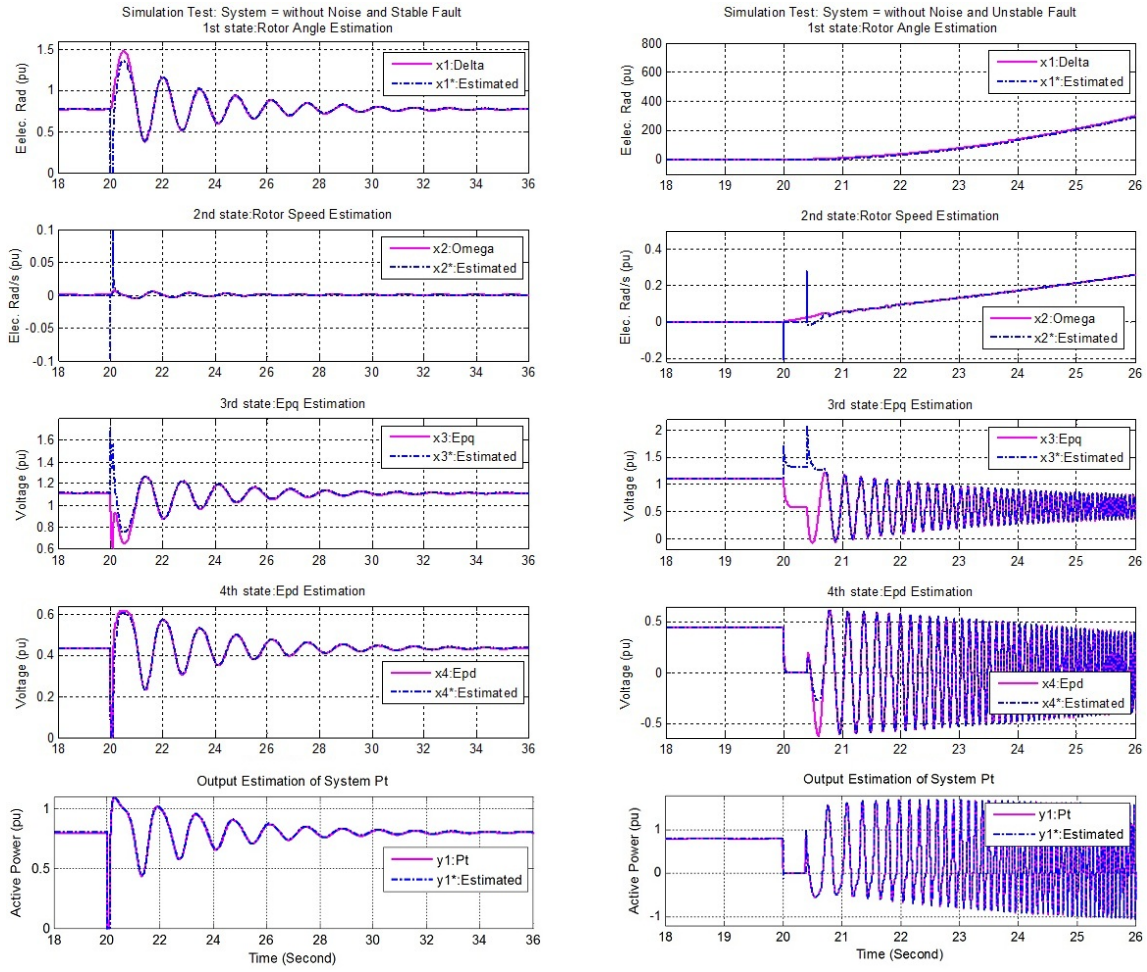

(a) (b)

Figure 2.9: UKF state estimation results in short-circuit faults for two post-fault conditions: (a) Stable. (b) Unstable.

reactance and for different values of the synchronous machine parameters. In all different simulation studies, we obtained results that showed the robustness and effectiveness of the proposed method.

Interestingly, it turns out that the UKF method is not so dependent on the initial value of the states. For example, if we run the UKF simulation with δ_0=0.4 (while the nominal value of rotor angle is δ=0.82), we still obtain accurate results. By contrast, the standard EKF algorithm is more dependent on the initial value of the rotor angle. For the same procedure, with a nominal value of rotor angle at δ=0.82, if we run the EKF simulation file with a δ_0 less than 0.6, the state estimator loses its ability to track the actual states. It could therefore be concluded that the UKF method is less dependent on the initial values than the EKF method.

As is clear from Figures 2.2 and 2.6, in addition to the phasor measurements of voltages and currents (V_{abc}, I_{abc}), which are required to determine P_t, V_t and I_t, the UKF approach (like the EKF method) needs to access E_{fd} and T_m as two other input quantities. In order to record and measure E_{fd} and T_m near the machine phasor signals, the Phasor Measurement Unit (PMU) should be located in the power plant.

From this point of view, as it was mentioned before, we are therefore present the Extended Kalman Filter with Unknown Inputs (EKF-UI) to remove these limitations (specially recording the E_{fd} signal) for dynamic state estimation of a synchronous machine. After that, the PMU could be installed on the transmission line but the transformer reactance would then have to be added to the machine reactance.

2.5 The Extended Kalman Filter with Unknown Inputs (EKF-UI)

2.5.1 Background

The EKF method of the previous section requires that both the deterministic inputs in the model and the measurement equations are known, which sometimes may not be the case in reality. The presence of unknown inputs could severely restrict the performance of classical nonlinear filters since a high bias will be introduced into the state estimation due to uncertainties from the unknown inputs. On the other hand, it is not always appropriate to treat unknown inputs as random noise to fit those traditional nonlinear filter approaches because (i) the unknown inputs could be signals with an arbitrary type and magnitude so it is not acceptable to assume them to be stationary and zero-mean random noise; and (ii) some unknown inputs need to be estimated for process control and optimization purposes.

In this regard, joint estimation of the states and unknown inputs for nonlinear stochastic systems becomes a meaningful task [32], which is often addressed as a constrained optimization problem [33, 34, 35, 36] where the state unbiasedness is the constraint and a joint global optimization of states and unknown inputs cannot be guaranteed [20]. To avoid the shortcomings of those approaches, an Extended Kalman Filter with Unknown Inputs (EKF-UI) [37] was proposed in the field of civil engineering for earthquake damage estimation studies. Its major novelty is that the unknown inputs are regarded as part of the states instead of disturbances (see [33, 34, 35, 36]). As a result, the EKF-UI approach can be directly derived from the unconstrained objective function of the traditional EKF (weighted least-squares objective function) and thus becomes a more general version of EKF. Since no prior information about unknown inputs is required, the proposed EKF-UI is quite suitable for the state estimation of a nonlinear system in the presence of unknown inputs. Therefore, it could be employed in state estimation of a synchronous machine with the unknown E_{fd} input signal.

2.5.2 Algorithm Description

An analytical solution for the proposed EKF-UI approach derived and presented in [37] for earthquake damage estimation studies will be modified and applied here based on the nonlinear synchronous machine system. This proposed EKF-UI technique [32] is applicable to both linear and nonlinear structures. Let the continuous-time nonlinear system (2.13) be represented in the discrete domain by the following equation (2.46), in which the subscripts k and k-1 is used to indicate t=$k.\Delta t$ and t=(k-1).Δt respectively:

$$\begin{aligned} \mathbf{x}_k &= \mathbf{f}(\mathbf{x}_{k-1}, \mathbf{u}_{k-1}, \mathbf{u}^*_{k-1}) + \mathbf{w}_{k-1} \\ \mathbf{y}_k &= \mathbf{h}(\mathbf{x}_k, \mathbf{u}_k) + \mathbf{v}_k \end{aligned} \tag{2.46}$$

where $\mathbf{f}$ denotes an n-dimensional nonlinear system function; $\mathbf{h}$, a p-dimensional output function; $\mathbf{x}_k$ and $\mathbf{x}_{k-1}$ are the n-state vector of the system; $\mathbf{u}_k$ and $\mathbf{u}_{k-1}$ are s-known input vectors; $\mathbf{u}^*_{k-1}$ is the r-unknown input vector; $\mathbf{y}_k$ is the p-observation (measured) output vector; $\mathbf{w}_{k-1}$ and $\mathbf{v}_k$ are n-model noise (uncertainty) and p-measurement noise vectors assumed to be mutually independent Gaussian white with the same characteristic presented in (2.18) to (2.21).

Based on the above system, the EKF-UI approach can be used to estimate unknown state and unknown input vectors $\mathbf{x}_k$ and $\mathbf{u}^*_k$ at t=$k.\Delta t$ given the observation (y_1, y_2, ..., y_k) denoted as $\mathbf{x}_{k|k}$ and $\mathbf{u}^*_{k-1|k}$ respectively. The derivations of the system which are essential for the EKF-UI method [32, 37] are briefly explained below from (2.47) to (2.53):

$$\mathbf{f}_{k-1} \approx \hat{\mathbf{f}}_{k-1|k-1} + \mathbf{F}_{k-1|k-1}(\mathbf{x}_{k-1} - \hat{\mathbf{x}}_{k-1|k-1}) + \mathbf{B}^*_{k-1|k-1}(\mathbf{u}^*_{k-1} - \hat{\mathbf{u}}^*_{k-1|k-1}) \tag{2.47}$$

$$\mathbf{h}_{k-1} \approx \hat{\mathbf{h}}_{k|k-1} + \mathbf{H}_{k|k-1}(\mathbf{x}_k - \hat{\mathbf{x}}_{k|k-1}) \tag{2.48}$$

where:

$$\hat{\mathbf{f}}_{k-1|k-1} = \mathbf{f}(\hat{\mathbf{x}}_{k-1|k-1}, \mathbf{u}_{k-1}, \hat{\mathbf{u}}^*_{k-2|k-1}) \tag{2.49}$$

$$\hat{\mathbf{h}}_{k|k-1} = \mathbf{h}(\hat{\mathbf{x}}_{k-1|k-1}, \mathbf{u}_k) \tag{2.50}$$

$$\mathbf{F}_{k-1|k-1} = \left.\frac{\partial \mathbf{f}_{k-1}}{\partial \mathbf{x}_{k-1}}\right|_{\mathbf{x}_{k-1}=\hat{\mathbf{x}}_{k-1|k-1}, \mathbf{u}^*_{k-1}=\hat{\mathbf{u}}^*_{k-2|k-1}} \tag{2.51}$$

$$\mathbf{B}^*_{k-1|k-1} = \left.\frac{\partial \mathbf{f}_{k-1}}{\partial \mathbf{u}^*_{k-1}}\right|_{\mathbf{x}_{k-1}=\hat{\mathbf{x}}_{k-1|k-1}, \mathbf{u}^*_{k-1}=\hat{\mathbf{u}}^*_{k-2|k-1}} \tag{2.52}$$

$$\mathbf{H}_{k|k-1} = \left.\frac{\partial \mathbf{h}_k}{\partial \mathbf{x}_k}\right|_{\mathbf{x}_k=\hat{\mathbf{x}}_{k|k-1}} . \tag{2.53}$$

The estimates $\mathbf{x}_{k|k-1}$ and $\mathbf{u}^*_{k-2|k-1}$ can be determined by minimizing the objective function of the summed square error between y_i and h_i (i=1, 2, ..., k) as follows:

$$\mathbf{J}_k = \bar{\Delta}_k^T \, \mathbf{W}_k \, \bar{\Delta}_k \tag{2.54}$$

where $\mathbf{W}_k$ is a $(pk \times pk)$ weighting matrix defined as the inverse of the covariance matrix for model and measurement noise; $(\Delta_i = y_i - h_i)$ is a p-output error vector at t=$i.\Delta t$ (i=1, 2, ... , k) and $\bar{\Delta}_k$ is defined as follows:

$$\bar{\Delta}_k = \left[\begin{array}{cccc} \bar{\Delta}_1^T & \bar{\Delta}_2^T & ... & \bar{\Delta}_k^T \end{array} \right] \tag{2.55}$$

where $\bar{\Delta}_k$ in (2.55) is a pk-vector [32, 37]. By minimizing $\mathbf{J}$ with respect to the unknown extended state vector $\mathbf{X}_{e,k}$ (subscript e denotes extended):

$$\mathbf{X}_{e,k} = \left[\begin{array}{ccccccc} \mathbf{x}_k^T & | & \mathbf{u}_{1|k}^{*T} & | & \mathbf{u}_{2|k}^{*T} & | \; ... \; | & \mathbf{u}_{k-1|k}^{*T} \end{array} \right]^T \tag{2.56}$$

to obtain the least-squares estimation (LSE) $\hat{\mathbf{X}}_{e,k|k}$ of $\mathbf{X}_{e,k}$ at t=$k.\Delta t$ we should use the following partial derivative formula:

$$\left.\frac{\partial \mathbf{J}_k}{\partial \mathbf{X}_{e,k}}\right|_{\mathbf{X}_{e,k}=\hat{\mathbf{x}}_{e,k}} = 0 \tag{2.57}$$

and then we will have:

$$\begin{aligned} \hat{\mathbf{X}}_{e,k|k} &= \mathbf{P}_{e,k} \left[\begin{array}{cc} \mathbf{A}_{e,k}^T \, \mathbf{W}_k & \mathbf{Y}_k \end{array} \right] \\ \mathbf{P}_{e,k} &= \left[\begin{array}{cc} \mathbf{A}_{e,k}^T \, \mathbf{W}_k & \mathbf{A}_{e,k} \end{array} \right]^{-1} \end{aligned} \tag{2.58}$$

and in turn:

$$\hat{\mathbf{X}}_{e,k|k} = \left[\begin{array}{ccccccc} \hat{\mathbf{x}}_{k|k}^T & | & \hat{\mathbf{u}}_{1|k}^{*T} & | & \hat{\mathbf{u}}_{2|k}^{*T} & | \; ... \; | & \hat{\mathbf{u}}_{k-1|k}^{*T} \end{array} \right]^T \tag{2.59}$$

where $\mathbf{Y}_k$ is a $[pk]$ known vector and $\mathbf{A}_{e,k}$ is a $[pk \times (n+(k\text{-}1)r)]$ known matrix. After some algebra, the recursive solution for $\hat{\mathbf{x}}_{k|k-1}$ and $\hat{\mathbf{u}}^*_{k-1|k}$ is obtained by the following steps [32, 37]:

Step 0: Initialization of the filter at k=0:

$$\begin{aligned}
\hat{\mathbf{x}}_0 &= E[\mathbf{x}_0] \\
\hat{\mathbf{u}}_0^* &= E[\mathbf{u}_0^*] \\
\mathbf{P}_{\mathbf{x},0} &= E[(\mathbf{x}_0 - \hat{\mathbf{x}}_0)(\mathbf{x}_0 - \hat{\mathbf{x}}_0)^T] \\
\mathbf{S}_{\mathbf{u}^*,0} &= E[(\mathbf{u}_0^* - \hat{\mathbf{u}}_0^*)(\mathbf{x}_0^* - \hat{\mathbf{u}}_0^*)^T]
\end{aligned} \tag{2.60}$$

where $\mathbf{S}_{\mathbf{u}^*}$ is a gain factor for the unknown input.

Step I: Prediction:

$$\hat{\mathbf{x}}_{k|k-1} = \mathbf{f}(\hat{\mathbf{x}}_{k-1|k-1}, \mathbf{u}_{k-1}, \hat{\mathbf{u}}^*_{k-2|k-1}) \tag{2.61}$$

where $\hat{\mathbf{x}}_{k-1|k-1}$ and $\hat{\mathbf{u}}^*_{k-2|k-1}$ are the estimation of states and unknown inputs at t=(k-1).Δt.

Step II: Gain Computation:

The computation at t=$k.\Delta t$ of the gain matrix for estimation of the states is given by:

$$\mathbf{K}_{x,k} = \mathbf{P}_{x,k|k-1}\mathbf{H}^T_{k|k-1}\left[\mathbf{R}_k + \mathbf{H}_{k|k-1}\mathbf{P}_{x,k|k-1}\mathbf{H}^T_{k|k-1}\right]^{-1} \tag{2.62}$$

and for the estimation of unknown inputs is respectively:

$$\mathbf{S}_{\mathbf{u}^*,k} = \left[\mathbf{B}^{*T}_{k-1|k-1}\mathbf{H}^T_{k|k-1}\mathbf{R}_k^{-1} \times (\mathbf{I}_p - \mathbf{H}^T_{k|k-1}\mathbf{K}_{x,k}) \times \mathbf{H}_{k|k-1}\mathbf{B}^*_{k-1|k-1}\right]^{-1} \tag{2.63}$$

where:

$$\mathbf{P}_{x,k|k-1} = \mathbf{F}_{k-1|k-1}\mathbf{P}_{x,k-1|k-1}\mathbf{F}^T_{k-1|k-1} + \mathbf{Q}_{k-1} \tag{2.64}$$

and $\mathbf{Q}_{k-1}$ is the autocovariance function of the model noise process vector $\mathbf{w}_{k-1}$.

Step III: Update:

In this step, the estimation of state and unknown inputs at t=$k.\Delta t$, $\hat{\mathbf{x}}_{k|k}$ and $\hat{\mathbf{u}}^*_{k-1|k}$ are updated from the combination of the state prediction and current measurement:

$$\hat{\mathbf{x}}_{k|k} = \hat{\mathbf{x}}_{k|k-1} + \mathbf{K}_{x,k}\left[\mathbf{y}_k - \mathbf{h}(\hat{\mathbf{x}}_{k|k-1}, \mathbf{u}_k)\right] \tag{2.65}$$

and:

$$\begin{aligned}
\hat{\mathbf{u}}^*_{k-1|k} = \mathbf{S}_{\mathbf{u}^*,k}\mathbf{B}^{*T}_{k-1|k-1}\mathbf{H}^T_{k|k-1}\mathbf{R}_k^{-1}(\mathbf{I}_p - \mathbf{H}^T_{k|k-1}\mathbf{K}_{x,k})\times \\
\left[\mathbf{y}_k - \mathbf{h}(\hat{\mathbf{x}}_{k|k-1}, \mathbf{u}_k) + \mathbf{H}^T_{k|k-1}\mathbf{B}^{*T}_{k-1|k-1}\hat{\mathbf{u}}^*_{k-2|k-1}.\right]
\end{aligned} \tag{2.66}$$

The covariance matrix $\mathbf{P}_{k-1|k-1}$ in (2.64) is updated at t=(k-1).Δt using (2.67):

$$\begin{aligned}
\mathbf{P}_{x,k-1|k-1} = (\mathbf{I}_n - \mathbf{K}_{x,k-1}\mathbf{H}_{k-1|k-2})\mathbf{P}_{x,k-1|k-2} + (\mathbf{I}_n - \mathbf{K}_{x,k-1}\mathbf{H}_{k-1|k-2})\times \\
\mathbf{B}^*_{k-2|k-2}\mathbf{S}_{\mathbf{u}^*,k-1}\mathbf{B}^{*T}_{k-2|k-2}(\mathbf{I}_n - \mathbf{K}_{x,k-1}\mathbf{H}_{k-1|k-2})^T
\end{aligned} \tag{2.67}$$

where $\mathbf{K}_{x,k-1}$, $\mathbf{S}_{\mathbf{u}^*,k-1}$ and $\mathbf{P}_{x,k-1|k-2}$ can be calculated from (2.62) to (2.64) by replacing k by k-1, respectively [32, 37].

Note that by checking the existence condition for $\mathbf{P}_{e,k}=\left[\ \mathbf{A}_{e,k}^T\ \mathbf{W}_k\ \mathbf{A}_{e,k}\ \right]^{-1}$ in (2.58), it can be concluded that **the major restriction of EKF-UI is that the number of output measurements (p) should be larger than the number of unknown inputs (r)**. Based on this, and because our system has just one unknown input, we need to add a new output from possible candidates accessible from PMU measurements not yet involved in the EKF-UI: I_t and Q_t. Since we have chosen to compute the gradients in (2.23), (2.25) and also in (2.50) to (2.53) analytically, as presented in next section, using I_t as the second output would require an appropriate and explicit equation of I_t with respect to the states and inputs to be able to compute its gradient for $\mathbf{H}_k$ matrix. By replacing (2.7) in (2.8) the equation can be calculated as:

$$I_t = \sqrt{\frac{x_3^2 + V_t^2 cos^2 x_1 - 2x_3 V_t cos x_1}{x'^2_d} + \frac{V_t^2 sin^2 x_1}{x_q^2}}. \tag{2.68}$$

It appears that such an equation for I_t with respect to the states and inputs is highly nonlinear and time consuming for analytical gradient calculation. Therefore, the reactive power of synchronous machine Q_t has been added to the active power P_t for a total of two system outputs. Similarly the active power equation, the reactive power equation, Q_t=$e_q i_d - e_d i_q$ with the state variables x_1 and x_3 can be derived as (2.69):

$$Q_t = y_2 = \frac{V_t}{x'_d} x_3 cos x_1 - V_t^2 (\frac{cos^2 x_1}{x'_d} + \frac{sin^2 x_1}{x_q}). \tag{2.69}$$

Thus, with the greater number of system outputs (p=2) than the number of unknown inputs (r=1), we can implement the described EKF-UI on the fourth-order synchronous generator model.

2.5.3 Gradient Calculations

The gradients in in (2.23), (2.25) and also in (2.50) to (2.53) are computed analytically. We now show the mathematical procedure of the calculations.

$$\mathbf{F}_{k-1} = \frac{\partial \mathbf{f}_{k-1}}{\partial \mathbf{x}} = \frac{\partial \mathbf{x}_k}{\partial \mathbf{x}} = \frac{\partial}{\partial \mathbf{x}} (\Delta t \times \mathbf{f}(\mathbf{f}, \mathbf{u}, \mathbf{w}) + \mathbf{x}_{k-1}) \tag{2.70}$$

which deliver us the following matrix:

$$\mathbf{F}_{k-1} = \left[\ \frac{\partial x_1(k)}{\partial \mathbf{x}}\ \ \frac{\partial x_2(k)}{\partial \mathbf{x}}\ \ \frac{\partial x_3(k)}{\partial \mathbf{x}}\ \ \frac{\partial x_4(k)}{\partial \mathbf{x}}\ \right]^T \tag{2.71}$$

and therefore, taking the first state equation from (2.12), f_1=($\mathbf{x}$,$\mathbf{u}$,$\mathbf{w}$)=($\omega_0 x_2$), the $\mathbf{F}_{k-1}$ elements [F_{11} and F_{21}] can be calculated as (2.72):

$$\begin{aligned} x_1(k) &= \Delta t \times f_1(\mathbf{x},\mathbf{u},\mathbf{w}) + x_1(k-1) \\ x_1(k) &= \Delta t \times (\omega_0 x_2) + x_1(k-1) \\ \Rightarrow \frac{\partial x_1(k)}{\partial \mathbf{x}} &= \left[\begin{array}{cccc} \frac{\partial x_1(k)}{\partial x_1} & \frac{\partial x_1(k)}{\partial x_2} & \frac{\partial x_1(k)}{\partial x_3} & \frac{\partial x_1(k)}{\partial x_4} \end{array} \right] \\ &= [\, F_{11} \quad F_{21} \quad 0 \quad 0 \,] \\ &= [\, 1 \quad \Delta t.\omega_0 \quad 0 \quad 0 \,]. \end{aligned} \tag{2.72}$$

Similarly, using the second state equation f_2=($\mathbf{x}$,$\mathbf{u}$,$\mathbf{w}$) from (2.12), second row elements of $\mathbf{F}_{k-1}$ matrix can be calculated as (2.73) and (2.74) respectively:

$$\begin{aligned} x_2(k) &= \Delta t \times f_2(\mathbf{x},\mathbf{u},\mathbf{w}) + x_2(k-1) \\ x_2(k) &= \Delta t \times \left[\frac{1}{J}(T_m - (\frac{V_t}{x'_d} x_3 sinx_1 + \frac{V_t^2}{2}(\frac{1}{x_q} - \frac{1}{x'_d}) sin2x_1) - Dx_2) \right] + x_2(k-1) \end{aligned} \tag{2.73}$$

and therefore we will have:

$$\begin{aligned} \frac{\partial x_2(k)}{\partial \mathbf{x}} &= \left[\begin{array}{cccc} \frac{\partial x_2(k)}{\partial x_1} & \frac{\partial x_2(k)}{\partial x_2} & \frac{\partial x_2(k)}{\partial x_3} & \frac{\partial x_2(k)}{\partial x_4} \end{array} \right] \\ &= [\, F_{21} \quad F_{22} \quad F_{23} \quad 0 \,] \\ F_{21} &= -\frac{\Delta t}{J} \left(\frac{V_t x_3}{x'_d} cosx_1 - V_t^2 (\frac{1}{x'_d} - \frac{1}{x_q}) cos2x_1 \right) \\ F_{22} &= -\Delta t \, \frac{D}{J} + 1 \text{ and } F_{23} = -\frac{\Delta t}{J} \, \frac{V_t}{x'_d} \, sinx_1 \end{aligned} \tag{2.74}$$

where the value of F_{24} is zero (F_{24}=0). Also, for the third state equation the elements of the $\mathbf{F}_{k-1}$ matrix with F_{32}=0 and F_{34}=0, can be calculated as (2.75):

$$\begin{aligned} x_3(k) &= \Delta t \times f_3(\mathbf{x},\mathbf{u},\mathbf{w}) + x_3(k-1) \\ x_3(k) &= \Delta t \times \left[\frac{1}{T'_{do}} (E_{fd} - x_3 - (x_d - x'_d)(\frac{x_3 - V_t cosx_1}{x'_d})) \right] + x_3(k-1) \\ \Rightarrow \frac{\partial x_3(k)}{\partial \mathbf{x}} &= \left[\begin{array}{cccc} \frac{\partial x_3(k)}{\partial x_1} & \frac{\partial x_3(k)}{\partial x_2} & \frac{\partial x_3(k)}{\partial x_3} & \frac{\partial x_3(k)}{\partial x_4} \end{array} \right] \\ &= [\, F_{31} \quad 0 \quad F_{33} \quad 0 \,] \\ F_{31} &= -\frac{\Delta t}{T'_{do}} \frac{V_t sinx_1}{x'_d} (x_d - x'_d) \text{ and } F_{33} = 1 - \frac{\Delta t}{T'_{do}} \left[1 + (\frac{x_d - x'_d}{x'_d}) \right] \end{aligned} \tag{2.75}$$

Finally for the fourth state equation (2.76) express the fourth row of $\mathbf{F}_{k-1}$ in which the values of F_{42} and F_{43} are zero (F_{42}=0 and F_{43}=0).

For calculating the $\mathbf{H}_k$ matrix in (2.25) and also in (2.53) we could do the same as we did for $\mathbf{F}_{k-1}$, except that in the output matrix, we do not have the Δt factor in the discrete form of the equations. So, we can easily calculate the gradients based on the main equations in (2.12).

$$\begin{aligned}
&x_4(k) = \Delta t \times f_4(\mathbf{x}, \mathbf{u}, \mathbf{w}) + x_4(k-1) \\
&x_4(k) = \Delta t \times \left[\frac{1}{T'_{qo}} (-x_4 - (x_q - x'_q)(\frac{V_t sin x_1}{x_q})) \right] + x_4(k-1) \\
&\Rightarrow \frac{\partial x_4(k)}{\partial \mathbf{x}} = \begin{bmatrix} \frac{\partial x_4(k)}{\partial x_1} & \frac{\partial x_4(k)}{\partial x_2} & \frac{\partial x_4(k)}{\partial x_3} & \frac{\partial x_4(k)}{\partial x_4} \end{bmatrix} \\
&\qquad\qquad = \begin{bmatrix} F_{41} & 0 & 0 & F_{44} \end{bmatrix} \\
&F_{41} = \frac{\Delta t}{T'_{qo}} \frac{V_t cos x_1}{x_q} (x_q - x'_q) \\
&F_{44} = 1 - \frac{\Delta t}{T'_{qo}} + 1.
\end{aligned} \tag{2.76}$$

Therefore from (2.46) the first output equation of the system is:

$$\mathbf{y}_k = \mathbf{h}(\mathbf{x}_k, \mathbf{u}_k, \mathbf{v}_k) \tag{2.77}$$

and for calculating $\mathbf{H}_k$ in (2.53), we will have:

$$\begin{aligned}
\mathbf{H}_k &= \begin{bmatrix} \frac{\partial h_1(k)}{\partial \mathbf{x}} & \frac{\partial h_2(k)}{\partial \mathbf{x}} \end{bmatrix}^T \\
&= \begin{bmatrix} H_{11} & 0 & H_{13} & 0 \\ H_{21} & 0 & H_{23} & 0 \end{bmatrix}.
\end{aligned} \tag{2.78}$$

Replacing ($y_1 = h_1(\mathbf{x}, \mathbf{u}, \mathbf{v})$ from (2.12) in (2.78), the first row of the gradient matrix $\mathbf{H}_k$ can be calculated as (2.79).

$$\begin{aligned}
&y_1(k) = h_1(\mathbf{x}_k, \mathbf{u}_k, \mathbf{v}_k) = \frac{V_t}{x'_d} x_3 sin x_1 + \frac{V_t^2}{2} (\frac{1}{x_q} - \frac{1}{x'_d}) sin 2x_1 \\
&\Rightarrow \frac{\partial h_1(k)}{\partial \mathbf{x}} = \begin{bmatrix} \frac{\partial h_1(k)}{\partial x_1} & \frac{\partial h_1(k)}{\partial x_2} & \frac{\partial h_1(k)}{\partial x_3} & \frac{\partial h_1(k)}{\partial x_4} \end{bmatrix} \\
&\qquad\qquad = \begin{bmatrix} H_{11} & 0 & H_{13} & 0 \end{bmatrix}
\end{aligned} \tag{2.79}$$

where the H_{11} and H_{13} can be replaced by:

$$\begin{aligned} H_{11} &= \frac{V_t}{x'_d}\, x_3\, cosx_1 + \frac{V_t^2}{2}(\frac{1}{x'_d} - \frac{1}{x_d}) \times 2 \times cos2x_1 \\ H_{13} &= \frac{V_t}{x'_d}\, x_3\, sinx_1. \end{aligned} \tag{2.80}$$

Similarly, we could compute the second-row elements of the $\mathbf{H}_k$ matrix by substituting (2.69) in (2.78) to obtain H_{21} and H_{23} as (2.81):

$$\begin{aligned} y_2(k) = h_1(\mathbf{x}_k, \mathbf{u}_k, \mathbf{v}_k) &= \frac{V_t}{x'_d} x_3 cosx_1 - V_t^2(\frac{cos^2 x_1}{x'_d} + \frac{sin^2 x_1}{x_q}) \\ \Rightarrow \frac{\partial h_2(k)}{\partial \mathbf{x}} &= \left[\begin{array}{cccc} \frac{\partial h_2(k)}{\partial x_1} & \frac{\partial h_2(k)}{\partial x_2} & \frac{\partial h_2(k)}{\partial x_3} & \frac{\partial h_2(k)}{\partial x_4} \end{array} \right] \\ &= [\, H_{21} \quad 0 \quad H_{23} \quad 0\,] \\ H_{21} &= -\frac{V_t}{x'_d}\, x_3\, sinx_1 - 2V_t^2(\frac{1}{x_q} - \frac{1}{x'_d})\, sinx_1\, cosx_1 \\ H_{23} &= \frac{V_t}{x'_d}\, cosx_1. \end{aligned} \tag{2.81}$$

Finally, using the state equations from (2.12) for calculating the matrix B*k-1 in (2.26), the elements of the $\mathbf{B}^*_{k-1}$ matrix can be computed as (2.82):

$$\begin{aligned} \mathbf{B}^*_{k-1} = \left[\frac{\partial x_k}{\partial \mathbf{u}^*_{k-1}}\right] &= \left[\begin{array}{cccc} \frac{\partial x_1(k)}{\partial \mathbf{u}^*_{k-1}} & \frac{\partial x_2(k)}{\partial \mathbf{u}^*_{k-1}} & \frac{\partial x_3(k)}{\partial \mathbf{u}^*_{k-1}} & \frac{\partial x_4(k)}{\partial \mathbf{u}^*_{k-1}} \end{array} \right]^T \\ &= [\, 0 \quad 0 \quad B_{31} \quad 0\,]^T \\ &= \left[\begin{array}{cccc} 0 & 0 & \frac{\Delta t}{T'_{do}} & 0 \end{array} \right]^T \end{aligned} \tag{2.82}$$

The $\mathbf{B}^*_{k-1}$ vector in (2.82) is related to the unknown input estimation, and it has a single nonzero element because we have just one unknown input in the equation of the third state.

2.5.4 Simulation Results

The EKF-UI algorithm was developed in Simulink using the embedded function block, just as we did for the EKF method. In the latter case, P_t was the only measurable output signal and E_{fd}, T_m and V_t were the three input signals. But in the EKF-UI method, P_t and Q_t are the two output measurements and the input signals T_m and V_t are still necessary. The input E_{fd} is now assumed to be inaccessible or unknown. The time step sets through the Simulink configuration panel as (T=1 ms). The values for the E_{fd} and T_m signals are the

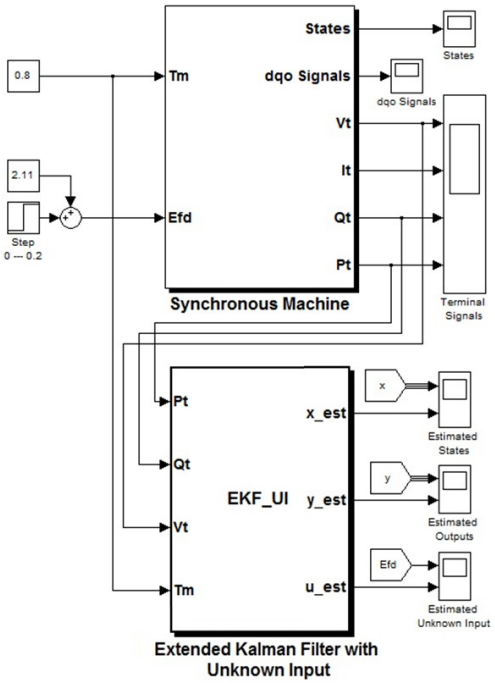

Figure 2.10: Implementation of EKF-UI algorithm: Using the embedded Matlab function block which uses T_m, V_t, P_t and Q_t as its input signals.

same as for the EKF method, which was presented in the section 2.3. The implementation of the EKF-UI method in Simulink is depicted in Figure 2.10.

The initial values vector for states is $\mathbf{x}_0 = [0; 0; 0; 0]$ and for the gain factor matrix $\mathbf{P}$ is $\mathbf{P}_0 = diag([10^2, 10^2, 10^2, 10^2])$. Also, the mean and covariance of the state and output noise matrices are as: $\mathbf{w}_k \sim(0,\mathbf{Q}_k) = (0, 0.01^2 \times \mathbf{I}_{4\times4})$ and $\mathbf{v}_k \sim(0,\mathbf{R}_k)=(0, 0.01^2 \times \mathbf{I}_{2\times2})$. The noise-free results are presented in Figure 2.11.

To better reflect real system conditions, white noise was added to the state with (mean, covariance)= $(0,0.001^2)$ and to the measured output with (mean, covariance)= $(0,0.01^2)$. Under these assumptions, the results of the EKF-UI algorithm for on-line state estimation of the fourth-order nonlinear model of the synchronous generator subjected to a step on E_{fd} are presented in Figure 2.12. The estimated output signals and the unknown input estimate E_{fd} are also shown in Figure 2.12(b).

2.5.5 Robustness Checking of EKF-UI State Estimator

For checking the effectiveness and robustness of the EKF-UI method, especially under **time variant unknown input**, the state estimation process will be performed with different kinds of E_{fd} input (constant and ramp) and different kinds of mechanical input T_m (constant and ramp). Also, the performance of the state estimator will be analyzed in the presence of network fault disturbances.

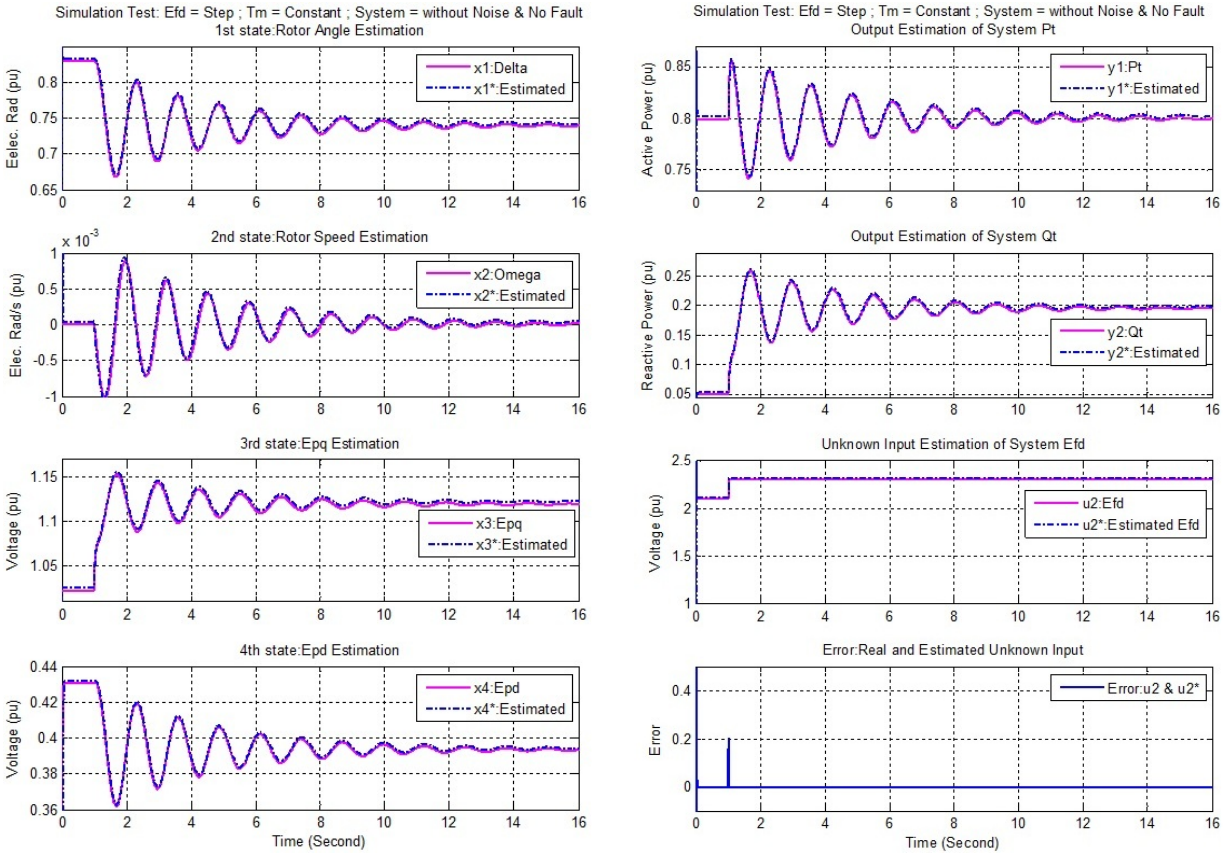

(a) (b)

Figure 2.11: EKF-UI state estimation results without noise: (a) Estimated states. (b) Estimated outputs and estimated unknown input.

2.5.5.1 T_m Input Signal: Ramp

In the simulations of this section, all settings including the initial values, time steps and noise characteristics are the same as in the previous section except that we replaced the constant Tm with a ramp signal. This ramp signal changes from T=1 to T=12 with a slope=1%/s and then remains constant from T=12 to T=16. The simulation results for this kind of T_m input signal demonstrate the accuracy of the estimated states, outputs and unknown input, which are presented in Figure 2.13.

2.5.5.2 E_{fd} Input Signal: Ramp

As another stringent robustness test of the EKF-UI method, the unknown input, E_{fd}, as a ramp signal. There is no difference in the simulation settings compared to the previous section, except that we replaced the step input for E_{fd} with a ramp signal having a slope=5%/s. The simulation results for the E_{fd} ramp signal are illustrated in Figure 2.14.

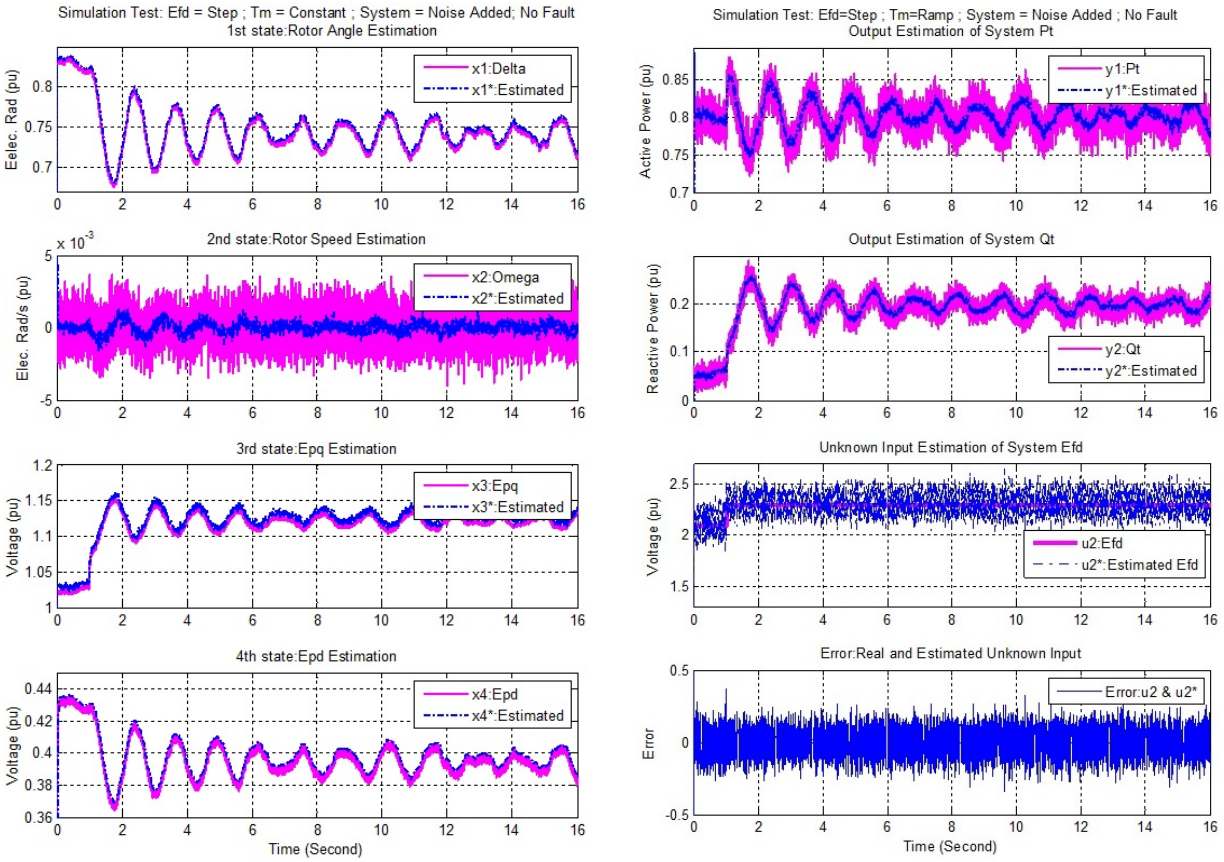

(a) (b)

Figure 2.12: EKF-UI state estimation results with noise: (a) Estimated states. (b) Estimated outputs and estimated unknown input.

They confirm that the proposed method is capable of tracking a time-variant unknown input, while estimating the sates correctly.

2.5.5.3 Fault Analysis

Based on the equivalent circuit in Figure 2.1, network disturbances impacts on the EKF-UI state estimator is studied by applying a short-circuit contingency at the mid-point of the transmission line at T=20 (s) as shown in Figure 2.8 previously in UKF state estimation fault analysis. The fault analysis relied on the fourth-order synchronous machine described in section 2.2. The synchronous machine model used in the fault simulation includes a two-factor saturation model with the parameters given in Appendix 5.2.

The analysis will be based on two post-disturbance scenarios: (i) stable and (ii) unstable. For the first scenario, the fault is cleared after 0.1 (s) at T=20.1 (s) and the system remained stable and for the second one it goes to an unstable condition.

The Simulink SMIB model settings and estimator initial values are the same as in

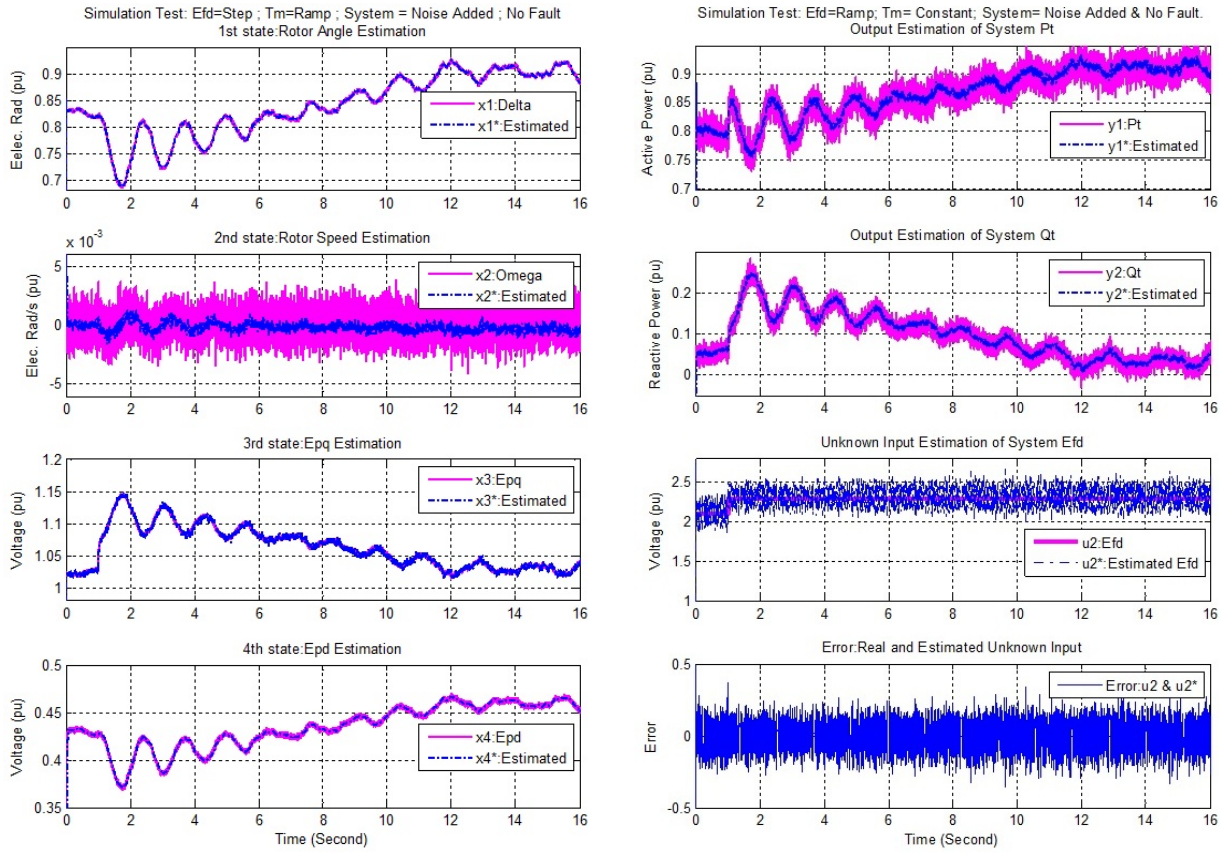

(a) (b)

Figure 2.13: EKF-UI state estimation results with T_m=**Ramp** and E_{fd}=**Step**: (a) Estimated states. (b) Estimated outputs and estimated unknown input.

previous simulations studies in Figures 2.13 and 2.14, except that we removed the noise in order to have clarity in the results and be able to track the performance of the state estimator at the time of fault occurrence. For this reason, we show the first 4 s after the fault only. The results in the stable case are presented in Figure 2.15.

From these results, it is clear that the EKF-UI estimator generates the correct estimates under network fault disturbance. However, attentive verification of the fault time-period revealed that, just after the fault occurrence, the estimator produces discontinuous responses and will track the actual outputs only after fault clearing.

In the second scenario, the fault was cleared after 0.3 (s) only, at T=20.3 (s) and the system therefore went into an unstable condition. Like for the stable case, the state estimator generated the estimated states with appropriate accuracy as shown in Figures 2.16. Based on these two scenarios, we conclude that the EKF-UI approach is capable of estimating the dynamic state of the power system independently of the stability condition. Also when the fault simulations were repeated with the noise added of the same magnitudes

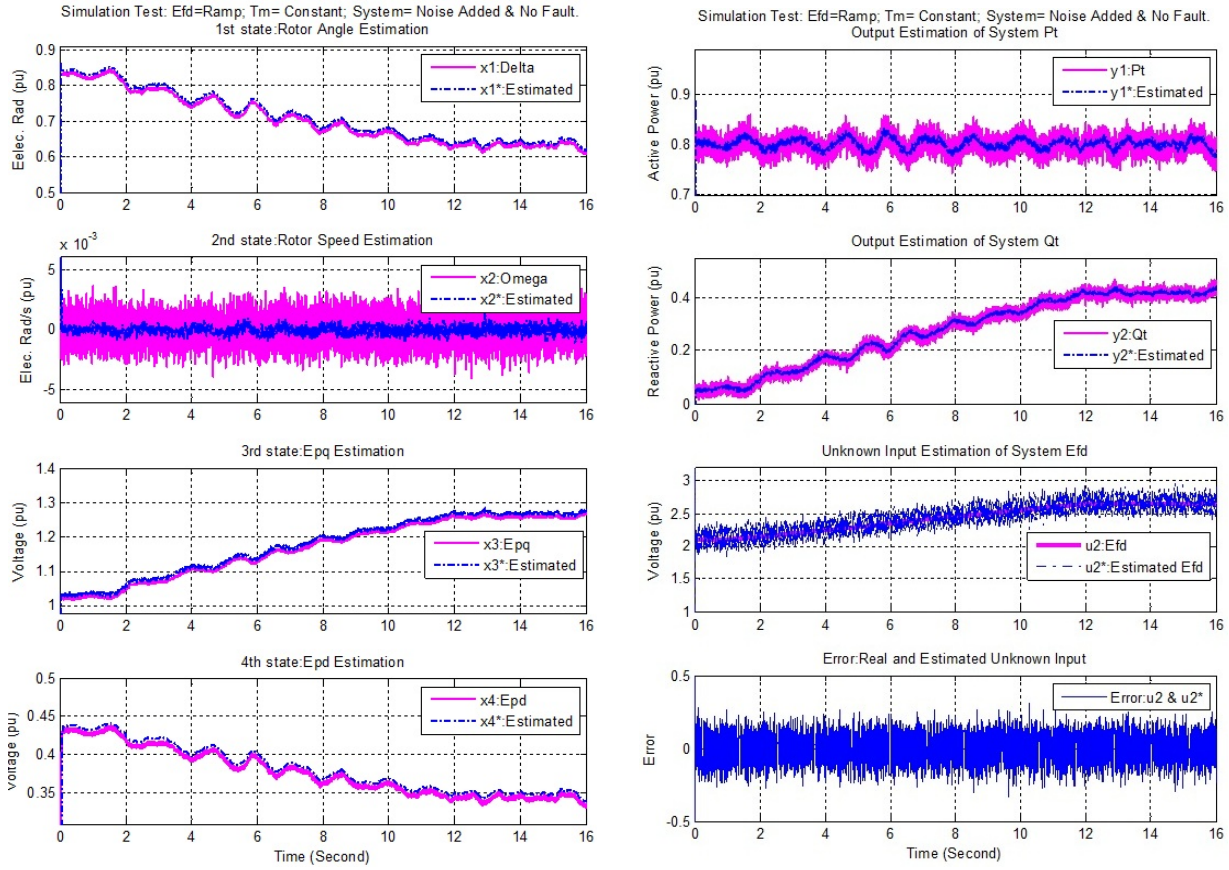

Figure 2.14: EKF-UI state estimation results with T_m=**Constant** and E_{fd}=**Ramp**: (a) Estimated states. (b) Estimated outputs and estimated unknown input.

as in Figures 2.14, the results were satisfactory, similar to Figures 2.15 and 2.16 in terms of accuracy.

2.5.6 EKF-UI Capability in Parameter Estimation

State estimation theory can be used to not only estimate the states of a system, but also to estimate the unknown parameters of a system. Suppose that we have a system model, but the system equations depend in a nonlinear way on an unknown parameter vector $\mathbf{p}$ [29]. The characteristic of the vector $\mathbf{p}$ in the continuous time format is $\dot{\mathbf{p}} = 0$. By using this characteristic in (2.13) we could have:

$$\begin{aligned} \begin{bmatrix} \dot{\mathbf{x}} \\ \dot{\mathbf{p}} \end{bmatrix} &= \begin{bmatrix} \mathbf{f}(\mathbf{x}, \mathbf{p}, \mathbf{u}, \mathbf{w}) \\ 0 \end{bmatrix} \\ \mathbf{y} &= \mathbf{h}(\mathbf{x}, \mathbf{p}, \mathbf{u}, \mathbf{v}) \end{aligned} \tag{2.83}$$

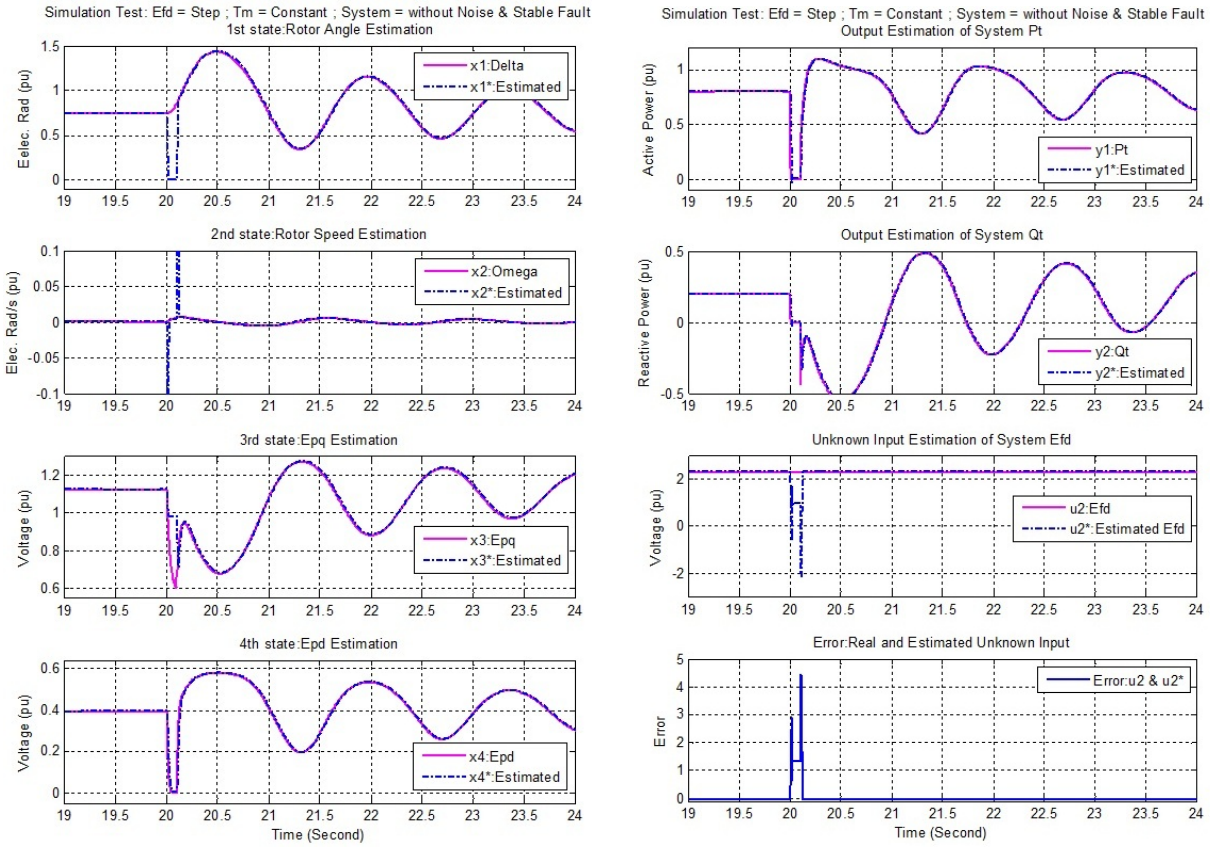

(a) (b)

Figure 2.15: EKF-UI state estimation results in stable short-circuit fault: (a) Estimated states. (b) Estimated outputs and estimated unknown input.

where $\mathbf{p}$ is the unknown parameter vector which is supposed to be estimated with the states of the system. Therfore, we can rewrite the extended state vector as:

$$\mathbf{x}' = \begin{bmatrix} \mathbf{x} \\ \mathbf{p} \end{bmatrix} \tag{2.84}$$

where $\mathbf{x}$ is the old state vector of the system, $\mathbf{p}$ is the unknown parameter of the system and $\mathbf{x}'$ is the extended state vector. To achieve the discrete-form of (2.83) we will have the following equations in (2.85) and (2.86). For vector $\mathbf{p}$:

$$\mathbf{p}_k = \mathbf{p}_{k-1} \tag{2.85}$$

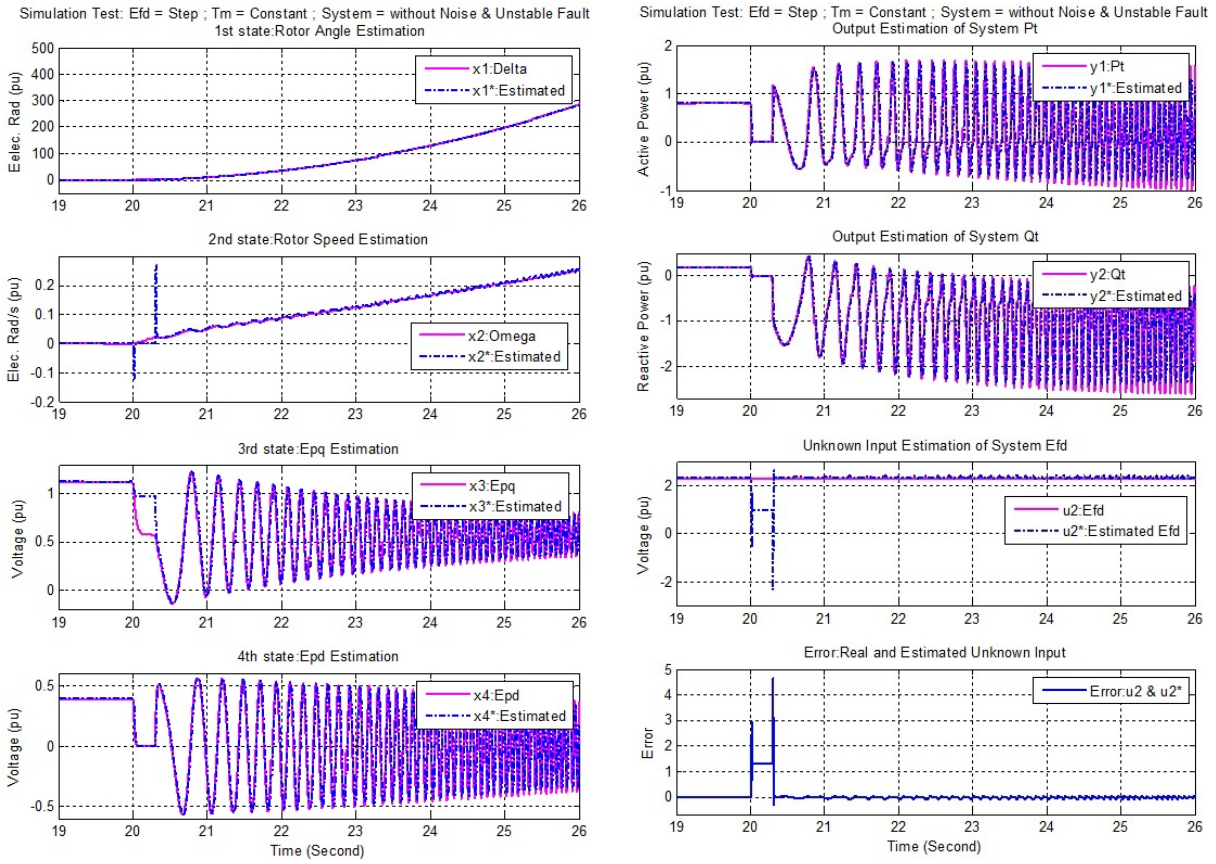

(a) (b)

Figure 2.16: EKF-UI state estimation results in unstable short-circuit fault: (a) Estimated states. (b) Estimated outputs and estimated unknown input.

and for the system equations (in case of presence unknown input in the system):

$$\begin{aligned} \begin{bmatrix} \mathbf{x}_k \\ \mathbf{p}_k \end{bmatrix} &= \begin{bmatrix} \mathbf{f}(\mathbf{x}_{k-1}, \mathbf{p}_{k-1}, \mathbf{u}_{k-1}, \mathbf{u}^*_{k-1}) + \mathbf{w}_{k-1} \\ \mathbf{p}_{k-1} + \mathbf{w}'_{k-1} \end{bmatrix} \\ \mathbf{y}_k &= \mathbf{h}(\mathbf{x}_k, \mathbf{p}_k, \mathbf{u}_k) + \mathbf{v}_k \end{aligned} \tag{2.86}$$

where the quantities definitions are the same as (2.46) and the discrete form of extended states vector is as:

$$\mathbf{x}'_k = \begin{bmatrix} \mathbf{x}_k \\ \mathbf{p}_k \end{bmatrix}. \tag{2.87}$$

Now, we can consider parameter estimation in the framework of our nonlinear fourth-order state space model of a synchronous machine. From theoretical point of view, we could define the vector p such as it includes all the parameters of machine presented in (10). But

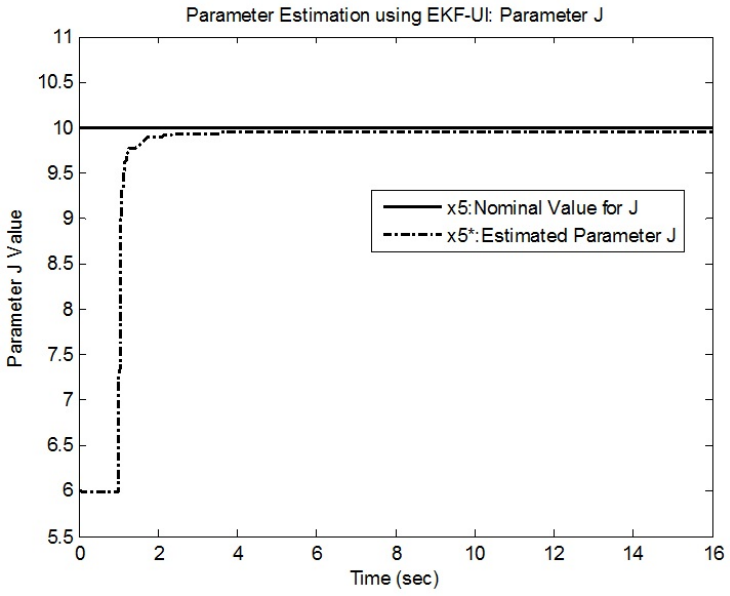

Figure 2.17: Parameter estimation using EKF-UI method for inertia constant J.

the fact is that in that case the state estimation process could not converge to a unique and acceptable response for the estimated states and as well for the estimated parameters. This situation could be worse for the EKF-UI method while we need to estimate the unknown input in addition of the states and parameters. Therefore, it is unrealistic to ask the estimation process to find the states, the unknown input and all the parameters of the system simultaneously while remaining robustly convergent. As a result, when extending EKF or EKF-UI methods to cope with parameter estimation, we will assume that just one or two parameters of the system are unknown. In our case, after checking the EKF-UI based parameter estimation procedure, described in this section, for some parameters of the machine, the inertia constant of the machine J was selected as the unknown parameter of the machine.

The setting values for the simulation file were similar to the setting values presented in previous simulations in Figures 2.11. Except now we have five state to be estimated, four system states and one unknown parameter as the extended fifth state. The initial values for the states were $\mathbf{x}_0 = [0.82; 0; 0; 0]$ which shows that we need to set the nominal rotor angle as the initial first state. The initial value for the gain factor matrix $\mathbf{P}$ was $\mathbf{P}_0 = diag([10, 10, 10, 10, 10^7])$. Also, the values of $\mathbf{Q}_k$ and $\mathbf{R}_k$ were: $\mathbf{w}_k \sim(0,\mathbf{Q}_k) = (0, 10^{-7} \times \mathbf{I}_{5\times5})$ and $\mathbf{v}_k \sim(0,\mathbf{R}_k)=(0, 0.1^2 \times \mathbf{I}_{2\times2})$. The estimated parameter for J compared with the nominal value as the fifth state is shown in Figure 2.17. The estimated states and estimated unknown input results, which were same as the results in 2.11, showed the accuracy in parameter, states and unknown input estimation process simultaneously.

As it is clear from the initial values and if we compared them with initial values in the previous simulation in Figures 2.11, it could be concluded that when we involve the

state estimation process with parameter estimation we need to set the nominal rotor angle as the initial first state. Also, we need to mention that the parameter estimation result using the EKF-UI method is very sensitive with respect to the initial rotor angle value and initial gain factor matrix. If we set the initial rotor angle less than 0.82, we could not get appropriate results.

2.5.7 Discussion on EKF-UI State Estimation Results

By comparing the initial values of the states in the EKF method $\mathbf{x}_0 = [0.6; 0; 0; 0]$ and the EKF-UI method $\mathbf{x}_0 = [0; 0; 0; 0]$, it is noticed that the latter is more robust against a poor initial value of the rotor angle δ_0 than the EKF method, for which we cannot set δ_0 far from the nominal rotor angle.

Noticing in Figures 2.15 and 2.16 that some state estimates are wrong during the fault, it could make sense to block the slow-changing states at their pre-fault values during the fault, in order to reduce the discontinuity-induced errors.

The simulation studies were repeated for different sets of machine and external system parameters to verify the EKF-UI method capability with respect to different sets of parameters and to analyze the influence of changing parameters on the proposed method. As expected, we obtained acceptable results in the simulations when we had different test machines (such as salient versus round rotor) and external systems with varying reactance. Lastly we performed additional simulation studies at different operating points considering saturation factors, in order to check the accuracy of the proposed EKF-UI method while varying the synchronous machine operating point. In all these sets of simulations, we again obtained accurate estimation of the states, outputs and unknown input.

Another interesting result, based on the estimated states of synchronous machine, would consist to estimate the capability curve of machine. First, let us define the internal generator voltage, E_I, as the voltage proportional to the field current i_{fd}:

$$E_I = x_{ad}\, i_{fd}. \tag{2.88}$$

Then, the relation between E_I and third state of machine e'_q can be expressed as:

$$e'_q = E_I - (x_d - x'_d)\, i_d. \tag{2.89}$$

Based on e'_q and i_d, which are now available through the EKF-UI method estimation results, the value of E_I and in turn i_{fd} can be estimated. Then using the field current i_{fd} estimated as above, and assuming x_{ad} and x_s to be known (including eventually the impact of a saturation model), the following equations can be derived [1]:

$$\begin{aligned} P &= \frac{x_{ad}}{x_s}\, V_t\, i_{fd}\, sin\delta \\ Q &= \frac{x_{ad}}{x_s}\, V_t\, i_{fd}\, cos\delta - \frac{V_t^2}{x_s} \end{aligned} \tag{2.90}$$

where x_s is the synchronous reactance, V_t is the terminal voltage and i_{fd} is the field current. The equations in (2.90) can be used to estimate one part of capability curve which is known as field current heating limit [1].

2.6 Summary

In this chapter, three different approaches were presented for dynamic state estimation of a power system including the synchronous generator rotor angle and rotor speed. The first approach was the traditional nonlinear state estimator, the Extended Kalman Filtering (EKF) method, which includes linearization steps in its algorithm. Simulation results of the EKF estimator showed appropriate accuracy in estimating the dynamic states of a saturated fourth-order generator connected to an infinite-bus, under noisy processes and measurements.

The second approach, the UKF state estimation, allows overcoming the limitations of the linearization process required by the traditional EKF method, and also to increase the operational range of the system variables around the operating point by not using the linearization in the state estimation algorithm. The implemented UKF based scheme produced high quality results and also showed greater accuracy of the state estimates in the presence of noise, compared to the traditional EKF method.

Finally the EKF-UI method was presented. As it was mentioned before, the EKF method requires that all input data be measured or available, which may not be the case in some configurations (e.g. with brushless exciters) where the field voltage E_{fd} is not easily measured from the power plant control room. The EKF with Unknown Inputs (EKF-UI) was consequently proposed for addressing this issue. We implemented it to simultaneously estimate the states of the system and the unknown input voltage E_{fd}. The robustness and effectiveness of the proposed EKF-UI approach was checked by successfully applying it to various kinds of field voltage and mechanical torque T_m inputs, ranging from step to ramp signals. The developed EKF-based estimators were effective as well under network fault conditions with process and measurement noise included.

Chapter 3

Optimal Placement of FACTS Devices in Power System Networks

After estimating the states of the synchronous machine in step 1, which will be used for the FACTS-based wide-area controller in step 3, the location of the FACTS device is determined using the method presented in this chapter as second step of thesis. In this step, the optimal process of FACTS placement to maximize the power system loadability and minimize the transmission line losses is presented.

Flexible AC Transmission Systems, so-called FACTS devices, can help reduce power flow on overloaded lines, which would result in an increased loadability of the power system, lower transmission line losses, improved stability and security and, ultimately, a more energy-efficient transmission system. In addition, with FACTS devices installed at suitable locations, wide area control strategies for power flow controls and oscillation damping could be implemented more effectively. In order to find suitable FACTS locations more easily and with more flexibility, in this chapter we present a Graphical User Interface (GUI) based on a genetic algorithm (GA) which is shown able to find the optimal locations and sizing parameters of multi-type FACTS devices in large power systems. This user-friendly tool, called **FACTS Placement Toolbox**, allows the user to pick a power system network, determine the GA settings and select the number and types of FACTS devices to be allocated in the network. The GA-based optimization process is then applied to obtain optimal locations and ratings of the selected FACTS to maximize the system static loadability. Six different FACTS devices are implemented: SVC (or STATCOM), TCSC (or SSSC), TCVR, TCPST, UPFC and STATCOM with Energy Storage(SMES). The simulation results on IEEE test networks with up to 300 buses show that the FACTS placement toolbox is effective and flexible enough for analyzing a large number of scenarios with mixed types of FACTS to be optimally sited at multiple locations simultaneously.

3.1 Literature Review

The limitation of energy resources and, also, a number of economic constraints increasingly force the power system to operate near its stability and loadability margins. In order to use the maximum capacity of power transmission lines while avoiding overloaded lines, utilities have expensive and time-consuming solutions such as building new lines. Alternatively, there are operational measures aimed at the same goal, such as: (i) topological changes through line switching and (ii) active and reactive power flow control [38].

FACTS devices fit in with the alternative approach as they improve the efficiency of existing networks by re-dispatching line flow patterns in such a way that the thermal limits are not exceeded, while fulfilling contractual requirements between grid stakeholders and increasing system loadability [39]. From the steady-state point of view, FACTS devices operate by supplying or absorbing reactive power, increasing or reducing voltage and controlling the series impedance of transmission lines or phase angle [40].

However, the benefits of these devices are severely dependent on their type, size, number and location in the transmission system. Many research projects and studies have been conducted in the area of FACTS device placement to improve power system operations. Considering the allocation technique or the optimization algorithm, we end up with the

following two categories:

A. Heuristic Optimization Algorithms

In this category, heuristic methods are used to find the best number, type, location and value for a given objective function. Among those used specifically in FACTS placement studies, the most popular are: Genetic Algorithm (GA) [40, 41, 42, 43, 44, 45], Tabu Search (TA) [46, 47], Simulated Annealing (SA) [47], Particle Swarm Optimization (PSO) [48, 49, 50], Evolutionary Algorithm (EA) [51, 52, 53, 54], Bacterial Swarming Algorithm (BSA) [55], Group Search Optimizer with Multiple Producer (GSOMP) [56], Harmony Search Algorithm (HSA) [57], and Bees Algorithm (BA) [58].

B. Analytical Techniques

Contrasting with the previous heuristic approaches, analytical methods are preferred by some authors to allocate the FACTS devices. For example, in [59, 60] singular analyses of the power system Jacobian matrix was used. Also, in [61, 62, 63] the authors used the Line Flow Index (LFI) as their allocation criterion. In [64] the power-angle characteristic was used to locate the FACTS devices. The Extended Voltage Phasors Approach (EVPA) [65], Mixed Integer Linear Programming (MILP) [66, 67, 68] and Locational Marginal Price (LMP) [69] are yet other methods in the second category.

Another categorization can be made as follows, based on the number and variety of devices involved:

A. Single-Type FACTS Device Allocation

The assumption here is that a single type of device is to be sited at a given number of optimally chosen locations. The FACTS placement procedure then starts to find the optimal locations and optimal values for the selected device such as: SVC [42, 60, 67], STATCOM [50, 64], TCSC [43, 70] and UPFC [44, 45, 49, 52, 64, 59, 63, 71].

B. Multiple-Type FACTS Devices Allocation

Adopting a mix of different type of FACTS devices allows the benefits of each singular type to be included. For example, in some papers three or four types of FACTS device such as, TCSC, TCVR, TCPST, SVC [41, 51, 55, 56] were used together. In [46, 47] the UPFC is also included near three of the four of other FACTS. In this context, the optimization procedure usually finds the optimal types, locations and values of the various FACTS devices simultaneously. All FACTS devices have one optimal location and one optimal rating number except the UPFC. Based on the UPFC modeling, which will be recapitulated in next section, this device has three operating values. In contrast with previous researches [46, 47], this study effectively includes the UPFC with three operating values together with other devices that have one operating value. Some papers also discussed the optimal number of FACTS devices in addition to the above variables [40, 41, 70, 72].

After these introductory remarks, we will now proceed to give an overall description of this chapter. A Matlab based Graphical User Interface (GUI), called **FACTS Placement Toolbox**, which uses the genetic algorithm as its optimization method, is presented. The tunable parameters of the genetic algorithm should be determined by the user. Using GA puts our method in the first category of allocation methods discussed above. Regarding the second categorization, we will perform the placement procedure for five types of FACTS

devices simultaneously: SVC (or STATCOM), TCSC (or SSSC), TCVR, TCPST, UPFC and STATCOM with Energy Storage(SMES). The user has the opportunity to select the desired number and types among them. The power network also should be selected by the user from a large number of IEEE test networks. The optimization process will then find the optimal locations and values of the given number of FACTS in the selected power system network in order to increase the power transmitted by the network or maximize the power system loadability [40, 42, 50, 67].

This chapter is organized as follows. The details of FACTS device modeling for power flow studies using Matpower [73] is given in section 3.2. In section 3.3, the influences of FACTS devices on the power network variables will be presented. Section 3.4 includes the general concepts of the genetic algorithm, definition of objective function and also the details of the optimization process. Section 3.5 describes the concept implementation using a generic graphical user interface which facilitates assessment of a wide-range of situations. To demonstrate the performance of the toolbox and to verify its performance, detailed simulation studies are presented in Section 3.6. Section 3.7 presents detailed simulations for analyzing the effects of different FACTS devices on Hydro-Québec network. Section 3.8 discusses the obtained results and section 3.9 presents a summary of the chapter.

3.2 FACTS Devices Modeling

In the two past decades, different types of FACTS devices have been developed and used in power system networks. Based on the type of compensation we could have three different categories for different types of FACTS devises:

- **Shunt Controllers** like: **SVC**, **STATCOM** and **STATCOM with SMES**.
- **Series Controllers** like: **TCSC**, **SSSC**, **TCPST** and **TCVR**.
- **Combined Shunt-Series Controllers** like: **UPFC**.

Each of the above FACTS devices has its own properties and could be used for a specific goal [74]. The modeling of the FACTS devices, which would be used for our power flow calculations in Matpower [73], could be done with two different techniques:

- **Operational Modeling**: based on the equivalent injected power at buses.
- **Analytical Modeling**: based on the admittance matrix modification.

In following the details of each technique will be presented.

3.2.1 Operational Modeling

The idea of operational modeling is related to this fact that we can model the FACTS devices by the equivalent injected active or reactive power at buses. At first, the schematic

of a typical transmission line for this kind of modeling is presented as Figure 3.1.

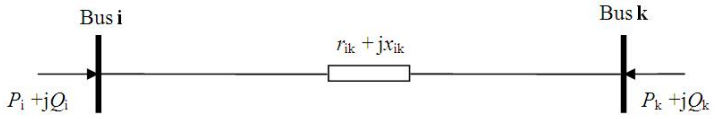

Figure 3.1: The schematic of transmission line.

In following the operational model of series and shunt FACTS devices will be presented briefly.

3.2.1.1 Series FACTS Device

The configuration of operational modeling of series FACTS devices like TCSC, SSSC, TCVR and TCPST can be presented as Figure 3.2.

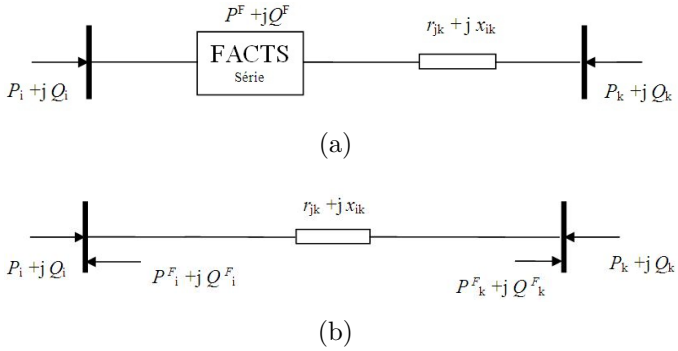

Figure 3.2: Operational modeling of series FACTS devices: (a) The line with FACTS devices. (b) The line with injected equivalent power.

The principle concept of operational modeling is replacing the effect of FACTS device on transmitted power in the line by equivalent injected power at terminal buses of that line, as presented in Figure 3.2. The injected equivalent active and reactive power at bus i can be calculated by:

$$\begin{aligned} P_i^F &= P_{ik} - P_{ik}^F \\ Q_i^F &= Q_{ik} - Q_{ik}^F \end{aligned} \tag{3.1}$$

where:

- P_i^F and Q_i^F: equivalent injected active and reactive power at bus i;
- P_{ik} and Q_{ik}: transmitted active and reactive power without FACTS devices;
- P_{ik}^F and Q_{ik}^F: transmitted active and reactive power with FACTS devices in the line.

There are two similar equations for node k. The total four equations, which present the operational modeling of series FACTS devices, could be used for load flow analysis in Matpower.

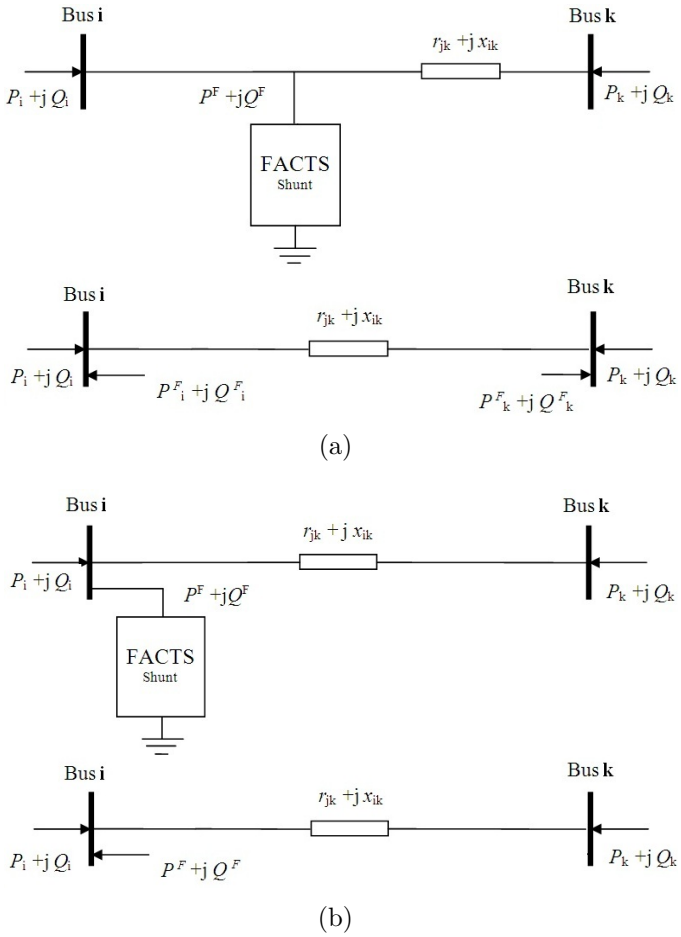

Figure 3.3: Operational modeling of shunt FACTS devices: (a) The line with shunt FACTS devices between two buses. (b) The line with shunt FACTS devices at one bus.

3.2.1.2 Shunt FACTS Device

For the operational modeling of shunt FACTS devices such as SVC, STATCOM and STATCOM with SMES, we have two possibilities for positions. If the shunt FACTS device is allocated in the line (between two buses), we would have the configuration presented in Figure 3.3(a).

But, if the device is allocated at one alone bus, the modeling configuration would be like Figure 3.3(b). The modeling equations of shunt FACTS devices are similar to series, which were presented in (3.1).

3.2.2 Analytical Modeling

As it was mentioned before, the analytical modeling of FACTS devices is implemented by modifying the admittance matrix of branch. Therefore, before presenting the analytical modeling of each FACTS device, we should at first present the branch modeling and ad-

mittance matrix equations. The schematic of classic π model of branch is presented in Figure 3.4.

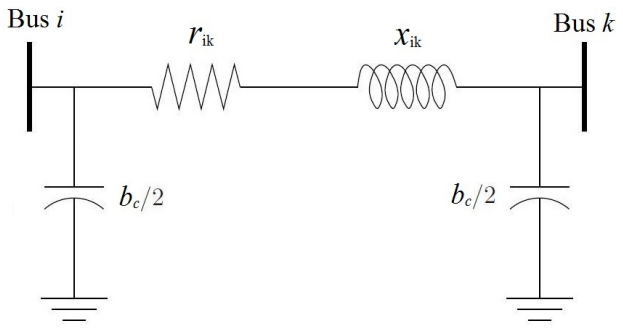

Figure 3.4: The schematic of classic π model of branch.

The admittance matrix for the classic π model of branch is given by following equations in (3.2) and (3.3).

$$\mathbf{Y} = \begin{bmatrix} y_{ik} + \frac{y_c}{2} & -y_{ik} \\ -y_{ik} & y_{ik} + \frac{y_c}{2} \end{bmatrix} \tag{3.2}$$

where the line admittance y_{ik} and the shunt admittance y_c are:

$$\begin{aligned} y_{ik} &= \frac{1}{r_{ik} + jx_{ik}} \\ y_c &= jb_c \end{aligned} \tag{3.3}$$

where r_{ik} is the line resistance, x_{ik} is the line reactance and b_c is the charging capacitance.

In analytical modeling when the FACTS device is inserted in the line (Figure 3.5), the admittance matrix will be modified in following form as equation (3.4). In following sections, the details of analytical modeling for all FACTS devices will be presented as:

$$\mathbf{Y}' = \begin{bmatrix} Y'_{ii} & Y'_{ik} \\ Y'_{ki} & Y'_{kk} \end{bmatrix} = \underbrace{\begin{bmatrix} Y_{ii} & Y_{ik} \\ Y_{ki} & Y_{kk} \end{bmatrix}}_{\text{Line}} + \underbrace{\begin{bmatrix} Y^F_{ii} & Y^F_{ik} \\ Y^F_{ki} & Y^F_{kk} \end{bmatrix}}_{\text{FACTS}}. \tag{3.4}$$

3.2.3 SVC

The SVC (*Static Var Compensator*) can operate at both inductive and capacitive compensation. In inductive case, the device absorbs reactive power and in capacitive case it supplies reactive power. The SVC is modeled by a shunt susceptance which includes two ideal switched elements in parallel: a capacitance for capacitive compensation and inductance for inductive compensation [41]. The SVC is the only device which could be installed in the buses of the network in addition the branches. All the other FACTS devices in this

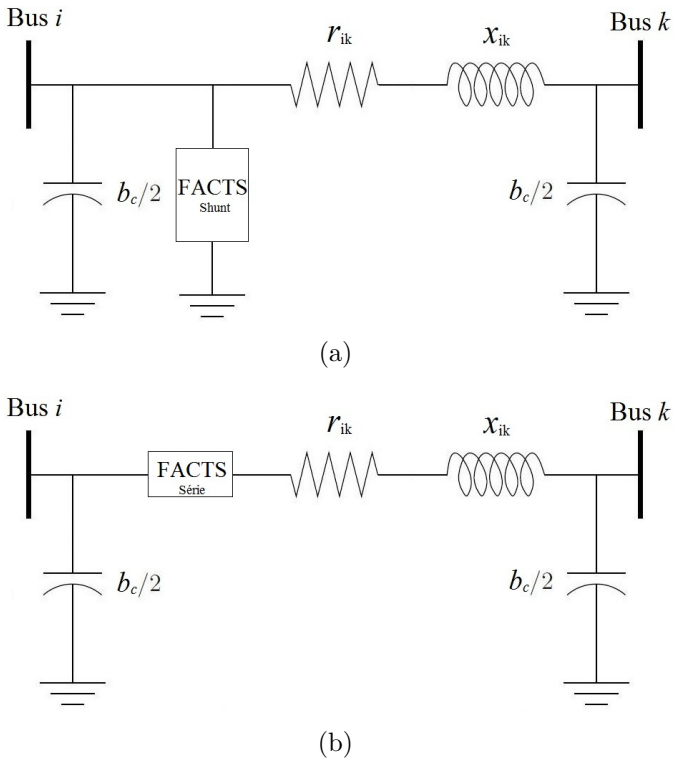

Figure 3.5: Two configurations for allocating of FACTS device in analytical modeling: (a) Shunt FACTS device. (b) Series FACTS device.

study are located just in the branches. The circuit structure of SVC and the typical V-I operating area are presented in Figure 3.6. The symbol and the model of SVC are also presented in Figure 3.7.

If the allocation process inserts the SVC in the buses, in this case the SVC just modeled only as reactive power injected at bus as presented in operational modeling. The reactive power injected or absorbed by the SVC at the nominal voltage of installed bus V_n could be calculated using (3.5) with the corresponding ranges for Q_{SVC} as:

$$\begin{gathered} Q_{SVC} = -\frac{V_n^2}{x_{SVC}} = -y_{SVC}V_n^2 = -b_{SVC}V_n^2 \\ -300 \ \text{ MVar} \leq Q_{SVC} \leq +300 \ \text{ MVar}. \end{gathered} \tag{3.5}$$

By inserting the SVC in the branches of network, the parameters of the classic equivalent π-model will be modified based on the value of the SVC susceptance.

In this case, the line is split into two equal parts and the SVC is inserted in the middle as it is shown in Figure 3.8.

Next, the procedure of finding the modified parameters of classic π-model of branch, as presented in Figure 3.9, is discussed. First of all, we should start with defining y_p and

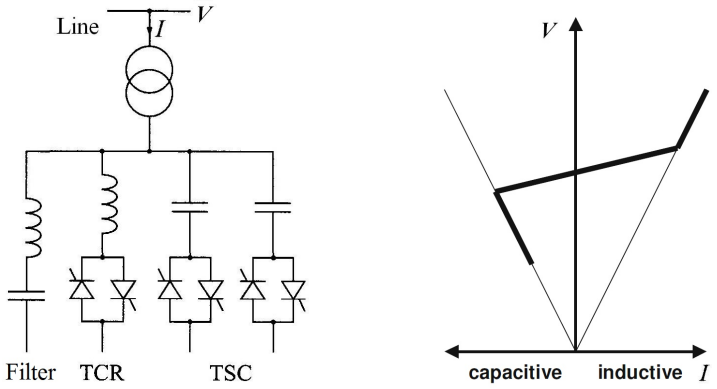

(a) (b)

Figure 3.6: The Static Var Compensator (SVC) : (a) The circuit structure. (b) The V-I operating area.

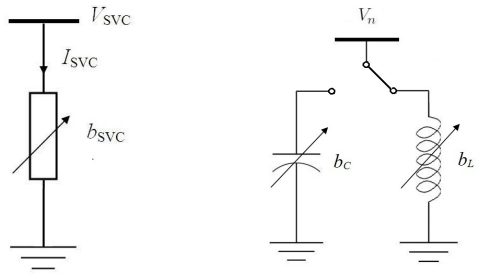

(a) (b)

Figure 3.7: The Static Var Compensator : (a) The symbol of SVC. (b) The model of SVC.

z_{ik} in Figure 3.9(a) as:

$$\begin{aligned} y_p &= \frac{y_c}{4} + \frac{y_c}{4} + y_{SVC} = \frac{y_c}{2} + y_{SVC} \\ \frac{z_{ik}}{2} &= \frac{1}{2y_{ik}} \end{aligned} \tag{3.6}$$

where $z_{ik} = r_{ik} + jx_{ik}$, $y_c = jb_c$ and $y_{SVC} = jb_{SVC}$.

Then, using the star-triangle transformation, for transformation from Figure 3.9(a) to

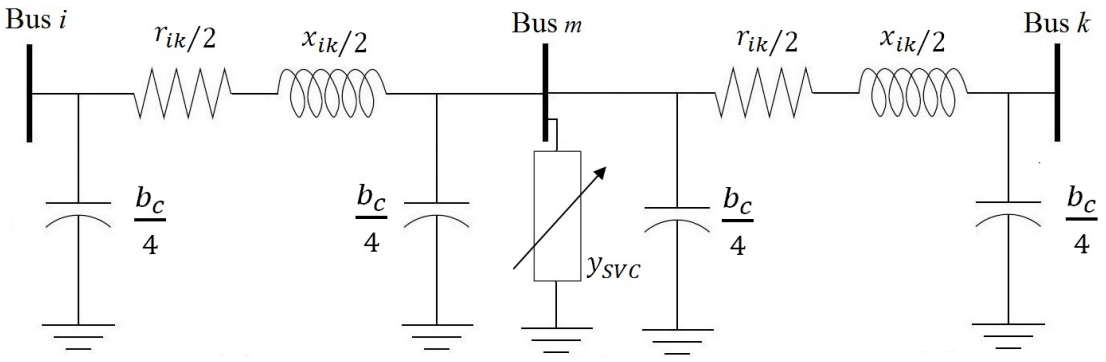

Figure 3.8: The modified configuration of a branch with SVC at the middle of the line.

Figure 3.9(b), the following equations will be written:

$$\begin{aligned} z'_{ik} &= \frac{\frac{1}{2y_{ik}} \times \frac{1}{2y_{ik}} + 2\left(\frac{1}{2y_{ik}} \times \frac{1}{y_p}\right)}{\frac{1}{y_p}} = \frac{\frac{1}{4y_{ik}^2} + \frac{1}{y_{ik}y_p}}{\frac{1}{y_p}} \\ z'_{ik} &= \frac{\frac{y_p + 4y_{ik}}{4y_{ik}^2 y_p}}{\frac{1}{y_p}} = \frac{4y_{ik} + y_p}{4y_{ik}^2} = \frac{1}{y_{ik}} + \frac{y_p}{4y_{ik}^2} \\ \Rightarrow z'_{ik} &= z_{ik} + \frac{1}{4} z_{ik}^2 \left(\frac{y_c}{2} + y_{SVC}\right). \end{aligned} \tag{3.7}$$

Then, by using $z_{ik} = r_{ik} + jx_{ik}$, $y_c = jb_c$ and $y_{SVC} = jb_{SVC}$ in (3.7) we will have (3.8):

$$z'_{ik} = (r_{ik} + jx_{ik}) + \frac{1}{4}(r_{ik} + jx_{ik})^2 \left(\frac{jb_c}{2} + jb_{SVC}\right). \tag{3.8}$$

After some mathematic simplification we could have the modified values of branch (r'_{ik} and x'_{ik}) in Figure 3.9(d) as:

$$\begin{aligned} r'_{ik} &= r_{ik} - \frac{1}{2} r_{ik} x_{ik} \left(\frac{b_c}{2} + b_{SVC}\right) \\ x'_{ik} &= x_{ik} + \frac{1}{4}\left(r_{ik}^2 - x_{ik}^2\right)\left(\frac{b_c}{2} + b_{SVC}\right). \end{aligned} \tag{3.9}$$

To calculate other parameters of Figure 3.9(d), $y'_{ii} = y'_{kk}$ and b'_c, we should start from

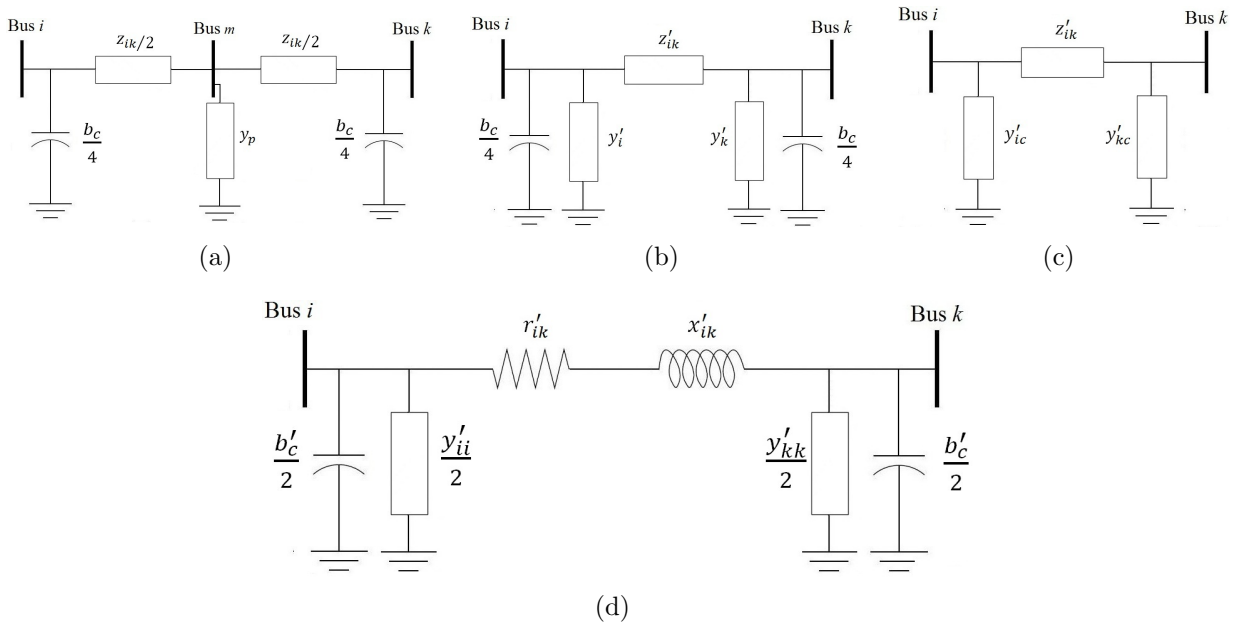

Figure 3.9: The star-triangle transformation for modeling the middle-line inserted SVC.

y'_{ic} and y'_{kc} in Figure 3.9(c) as:

$$\frac{y'_{ic}}{2} = \frac{y'_{kc}}{2} = \frac{y_c}{4} + \frac{2y_{ik}y_p}{4y_{ik} + y_p} = \frac{y_c}{4} + \frac{\left(\frac{y_c}{2} + y_{SVC}\right)}{2 + \frac{1}{2}z_{ik}\left(\frac{y_c}{2} + y_{SVC}\right)}. \tag{3.10}$$

Then again by using $z_{ik} = r_{ik} + jx_{ik}$, $y_c = jb_c$ and $y_{SVC} = jb_{SVC}$ in (3.10) we will have:

$$\frac{y'_{ii}}{2} = \frac{y'_{kk}}{2} = \frac{\frac{1}{2}r_{ik}\left(\frac{b_c}{2} + b_{SVC}\right)^2}{4 - 2x_{ik}\left(\frac{b_c}{2} + y_{SVC}\right) + \frac{1}{4}\left(r_{ik}^2 + x_{ik}^2\right)\left(\frac{b_c}{2} + b_{SVC}\right)^2}. \tag{3.11}$$

and the value of b'_c could be calculated by:

$$\frac{b'_c}{2} = \frac{b_c}{4} + \frac{2\left(\frac{b_c}{2} + b_{SVC}\right) - \frac{1}{2}x_{ik}\left(\frac{b_c}{2} + b_{SVC}\right)^2}{4 - 2x_{ik}\left(\frac{b_c}{2} + y_{SVC}\right) + \frac{1}{4}\left(r_{ik}^2 + x_{ik}^2\right)\left(\frac{b_c}{2} + b_{SVC}\right)^2}. \tag{3.12}$$

Now, when the SVC is allocated in the mid-point of a branch, we can easily use the equations (3.9), (3.11) and (3.12) to modify the branch parameters in Matpower to calculate power flow of the network.

Also we can analyze the influences of the SVC value Q_{SVC}, on the modified parameters of the branch (r'_{ik}, x'_{ik}, $y'_{ii} = y'_{kk}$ and b'_c) which are presented in Figure 3.9(a) and (b). As can be seen from this figure, the value of $y'_{ii} = y'_{kk}$ is effectively close to zero and so we can then neglect $y'_{ii} = y'_{kk}$ from final modeling of SVC device to decrease the process

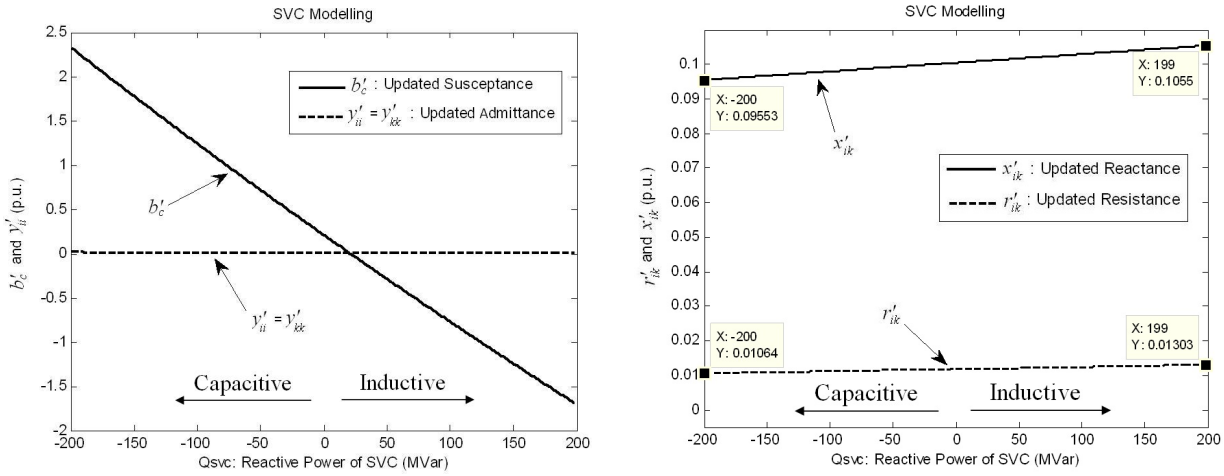

(a) (b)

Figure 3.10: The modified parameters of branch in function of Q_{SVC}:(a) The modified parameters: $y'_{ii} = y'_{kk}$ and b'_c. (b) The modified parameters: r'_{ik} and x'_{ik}.

calculation.

3.2.4 STATCOM

In 1999 the first SVC with Voltage Source Converter called STATCOM (*Static Synchronous Compensator*), went into operation. The STATCOM has a characteristic similar to the synchronous condenser, but as an electronic device it has no inertia and is superior to the synchronous condenser in several ways, such as better dynamics, a lower investment cost and lower operating and maintenance costs. The structure and operational characteristic is shown in Figure 3.11. The static line between the current limitations has a certain steepness determining the control characteristic for the voltage.

The advantage of a STATCOM is that the reactive power provision is independent from the actual voltage on the connection point. This can be seen in the diagram for the maximum currents being independent of the voltage in comparison to the SVC [39, 74].

Considering the modeling of STATCOM in this chapter, since our optimization method is based on the power flow calculation in steady-state condition, the STATCOM and the SVC both have the same characteristics in our optimization algorithm. Therefore, the analytical modeling of STATCOM is the same as SVC which is presented in previous section.

3.2.5 STATCOM with Energy Storage (SMES)

The STATCOM with SMES (*Superconducting Magnetic Energy Storage*) is a device which could be used to absorb or produce both active and reactive powers. The STATCOM part,

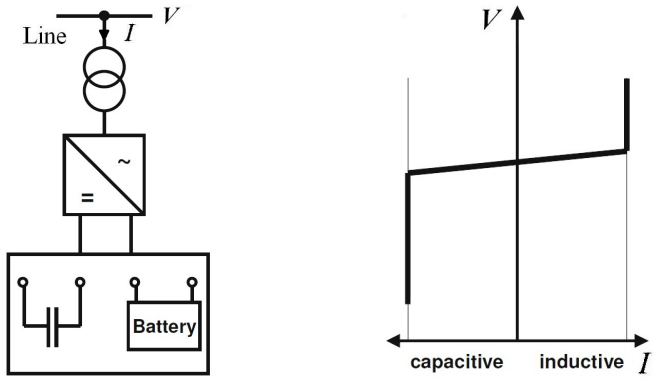

(a) (b)

Figure 3.11: The Static Synchronous Compensator: (a) The STATCOM structure. (b) The voltage-current characteristic.

which is presented in previous section, is related to the reactive power and the SMES part is for active power. The SMES system stores energy in the magnetic field created by the flow of direct current in a superconducting coil which has been cryogenically cooled to a temperature below its superconducting critical temperature [39, 74].

A typical SMES system includes three parts: superconducting coil, power conditioning system and cryogenically cooled refrigerator. Once the superconducting coil is charged, the current will not decay and the magnetic energy can be stored indefinitely. The stored energy can be released back to the network by discharging the coil. The power conditioning system uses an inverter/rectifier to transform alternating current (AC) power to direct current or convert DC back to AC power. Due to the energy requirements of refrigeration and the high cost of superconducting wire, SMES is currently used for short duration energy storage. Therefore, SMES is most commonly devoted to improving power quality [39, 74]. The internal control loop of a STATCOM with Energy Storage (SMES) is presented in Figure 3.12.

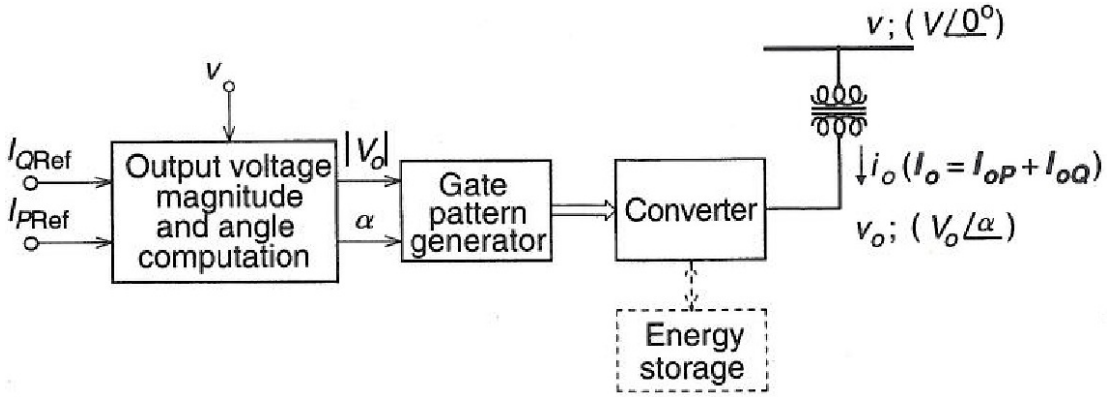

Figure 3.12: The internal control loop of a STATCOM with Energy Storage (SMES).

The symbol and the model of STATCOM with SMES is presented in Figure 3.13(a) and (b) respectively. As can be seen from Figure 3.13(b) the model of this device consists two parts: a variable inductance for absorbing or producing reactive power (STATCOM part) and a variable resistance for absorbing or producing the active power (SMES part). The SMES resistance has two operating modes: negative resistance ($-r_{SMES}$) for modeling the active power production and positive resistance ($+r_{SMES}$) for modeling the active power consumption.

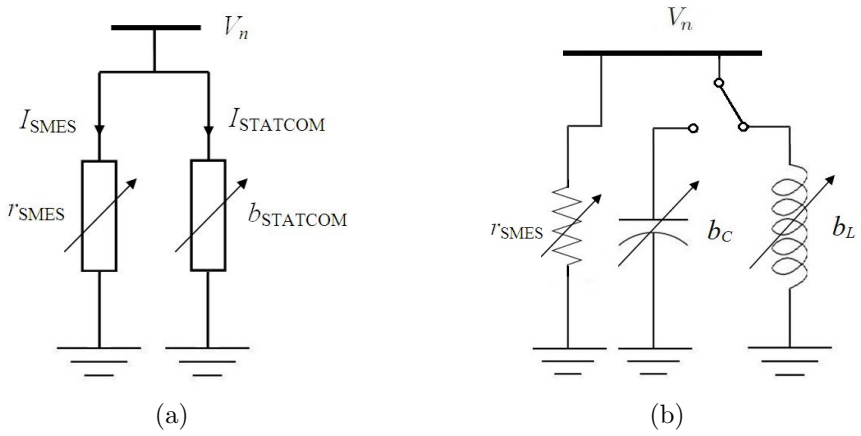

Figure 3.13: The STATCOM with SMES: (a) The symbol of device. (b) The model of device.

The injected or absorbed power, active and reactive, by the STATCOM with SMES at the nominal voltage of installed bus V_n could be calculated by following equations:

$$\begin{aligned} Q_{STATCOM} &= -\frac{V_n^2}{x_{STATCOM}} = -y_{STATCOM}V_n^2 = -b_{STATCOM}V_n^2 \\ P_{SMES} &= \frac{V_n^2}{r_{SMES}} = y_{SMES}V_n^2 \end{aligned} \tag{3.13}$$

where the ranges for $Q_{STATCOM}$ and P_{SMES} are :

$$\begin{aligned} -300 \ \text{MVar} \leq Q_{STATCOM} \leq +300 \ \text{MVar} \\ -300 \ \text{MW} \leq P_{SMES} \leq +300 \ \text{MW}. \end{aligned} \tag{3.14}$$

The analytical modeling of STATCOM with SMES is similar to the SVC with the same procedure. By inserting the STATCOM with SMES in the middle of line, the parameters of classic equivalent π-model will be modified based on the value of $Q_{STATCOM}$ and P_{SMES}. In this case, the line is split into two equal parts and the STATCOM with SMES is inserted in the middle as it is shown in Figure 3.14.

Using the steps in Figure 3.9 for the procedure of finding the modified parameters of classic π-model of branch, as presented in previous section for SVC, we will have the

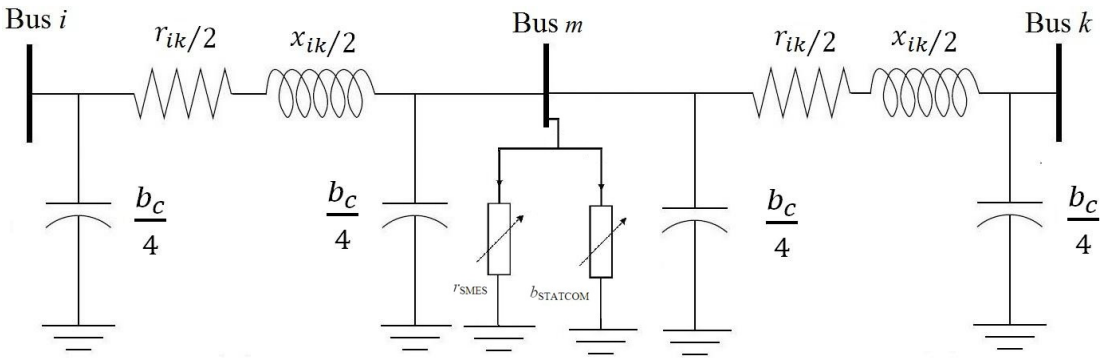

Figure 3.14: The modified configuration of a branch with the STATCOM with SMES at the middle of the line.

following definition for y_p as:

$$\begin{aligned} y_p &= \frac{y_c}{4} + \frac{y_c}{4} + y_{STATCOM} + y_{SMES} = \frac{y_c}{2} + y_{STATCOM} + \frac{1}{r_{SMES}} \\ \frac{z_{ik}}{2} &= \frac{1}{2y_{ik}} \end{aligned} \tag{3.15}$$

where:

$$\begin{aligned} z_{ik} &= r_{ik} + jx_{ik} \\ y_c &= jb_c \\ y_{STATCOM} &= jb_{STATCOM} \\ \frac{1}{r_{SMES}} &= y_{SMES}. \end{aligned} \tag{3.16}$$

Then, as we have done for SVC, using the star-triangle transformation from Figure 3.9(a) to Figure 3.9(b), the following equation could be written:

$$z'_{ik} = z_{ik} + \frac{1}{4} z_{ik}^2 \left(\frac{y_c}{2} + y_{STATCOM} + \frac{1}{r_{SMES}} \right). \tag{3.17}$$

Using (3.16) in (3.17) we will have:

$$z'_{ik} = (r_{ik} + jx_{ik}) + \frac{1}{4} (r_{ik} + jx_{ik})^2 \left(\frac{jb_c}{2} + jb_{STATCOM} + y_{SMES} \right). \tag{3.18}$$

After some mathematic simplification we could have the modified values of branch (r'_{ik}

and x'_{ik}) in Figure 3.9(d) as:

$$\begin{aligned} r'_{ik} &= r_{ik} - \frac{1}{2} r_{ik} x_{ik} \left(\frac{b_c}{2} + b_{STATCOM} \right) + \frac{1}{4} \left(r_{ik}^2 - x_{ik}^2 \right) y_{SMES} \\ x'_{ik} &= x_{ik} + \frac{1}{4} \left(r_{ik}^2 - x_{ik}^2 \right) \left(\frac{b_c}{2} + b_{STATCOM} \right) + \frac{1}{4} r_{ik} x_{ik} y_{SMES}. \end{aligned} \tag{3.19}$$

To calculate the other parameters of Figure 3.9(d), $y'_{ii} = y'_{kk}$ and b'_c, we should use the equations of y'_{ic} and y'_{kc} in Figure 3.9(c) as:

$$\frac{y'_{ic}}{2} = \frac{y'_{kc}}{2} = \frac{y_c}{4} + \frac{2 y_{ik} y_p}{4 y_{ik} + y_p} = \frac{y_c}{4} + \frac{\frac{y_c}{2} + y_{STATCOM} + y_{SMES}}{2 + \frac{1}{2} z_{ik} \left(\frac{y_c}{2} + y_{STATCOM} + y_{SMES} \right)}. \tag{3.20}$$

Then again, by using (3.16) in (3.20) we will have:

$$\frac{y'_{ic}}{2} = \frac{y'_{kc}}{2} = \frac{j b_c}{4} + \frac{y_{SMES} + j \left(\frac{b_c}{2} + b_{STATCOM} \right)}{2 + \frac{1}{2} \left(r_{ik} + j x_{ik} \right) \left(y_{SMES} + j \left(\frac{y_c}{2} + y_{STATCOM} \right) \right)}. \tag{3.21}$$

To simplify the mathematic procedure, we have the following definitions for real and imaginary part of divisor of (3.21):

$$\begin{aligned} R &= 2 + \frac{1}{2} r_{ik} y_{SMES} - \frac{1}{2} x_{ik} \left(\frac{b_c}{2} + b_{STATCOM} \right) \\ I &= \frac{1}{2} r_{ik} \left(\frac{b_c}{2} + b_{STATCOM} \right) + \frac{1}{2} x_{ik} y_{SMES}. \end{aligned} \tag{3.22}$$

Using the above definitions in (3.22), we could re-write equation (3.23) in following form:

$$\frac{y'_{ic}}{2} = \frac{y'_{kc}}{2} = \frac{j b_c}{4} + \frac{y_{SMES} + j \left(\frac{b_c}{2} + b_{STATCOM} \right)}{R + jI} \tag{3.23}$$

or:

$$\begin{aligned} \frac{y'_{ic}}{2} = \frac{y'_{kc}}{2} &= \frac{j b_c}{4} + \frac{y_{SMES} + j \left(\frac{b_c}{2} + b_{STATCOM} \right)}{R + jI} \times \frac{R - jI}{R - jI} \\ &= \frac{j b_c}{4} + \frac{y_{SMES} + j \left(\frac{b_c}{2} + b_{STATCOM} \right) \times (R - jI)}{R^2 - I^2}. \end{aligned} \tag{3.24}$$

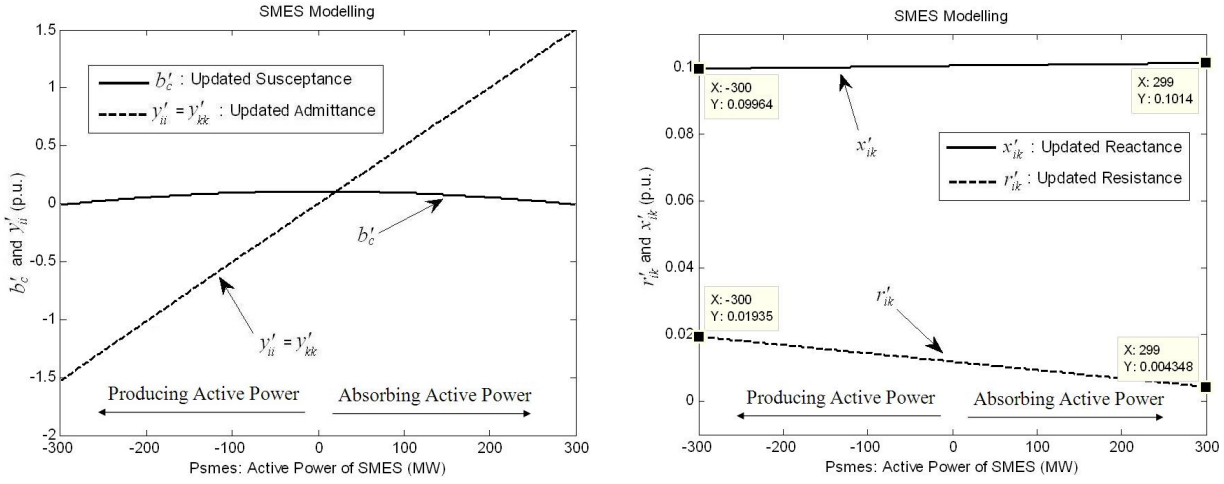

(a) (b)

Figure 3.15: The modified parameters of branch in function of P_{SMES}:(a) The modified parameters: $y'_{ii} = y'_{kk}$ and b'_c. (b) The modified parameters: r'_{ik} and x'_{ik}.

After some mathematic simplification for $y'_{ii} = y'_{kk}$ we will have:

$$\frac{y'_{ii}}{2} = \frac{y_{SMES} \times R + \left(\frac{b_c}{2} + y_{STATCOM}\right) \times I}{R^2 - I^2} \tag{3.25}$$

and in turn the value of b'_c is:

$$\frac{b'_c}{2} = \frac{b_c}{4} + \frac{\left(\frac{b_c}{2} + y_{STATCOM}\right) \times R - y_{SMES} \times I}{R^2 - I^2}. \tag{3.26}$$

Now, when the STATCOM with SMES is placed in the mid-point of a line, we can easily use the equations (3.19), (3.25) and (3.26) to modify the branch parameters in Matpower to be used in power flow calculation.

Also we can analyze the influence of $Q_{STATCOM}$ and P_{SMES}, on the modified parameters of branch (r'_{ik}, x'_{ik}, $y'_{ii} = y'_{kk}$ and b'_c) which are presented in Figures 3.15 and 3.16.

3.2.6 TCSC

The TCSC (*Thyristor-Controlled Series Capacitor*) can perform capacitive or inductive compensation by modifying the line reactance, decreasing it in capacitive mode and increasing it in inductive mode. The structure and voltage-current characteristic and the operating area are presented in Figure 3.17(a), (b) and (c) respectively.

The TCSC is modeled by three elements in parallel: a capacitance, an inductance and a zero-resistance wire. In the latter case, there would be no compensation in the line and the

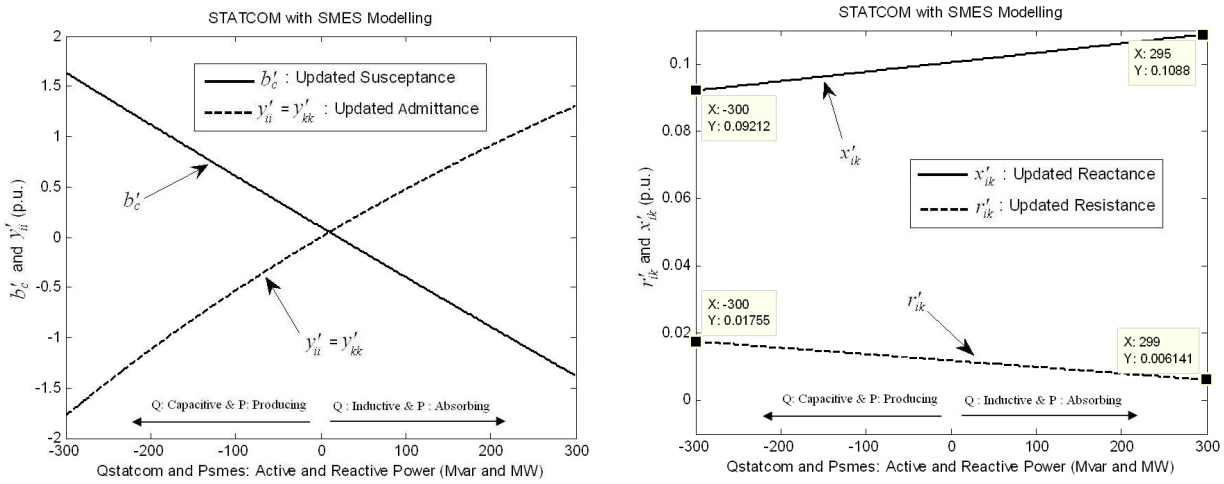

(a) (b)

Figure 3.16: The modified parameters of branch in function of $Q_{STATCOM}$ and P_{SMES} simultaneously:(a) The modified parameters: $y'_{ii} = y'_{kk}$ and b'_c. (b) The modified parameters: r'_{ik} and x'_{ik}.

TCSC will have the value of zero [41]. The model and the symbol of TCSC are presented in Figure 3.18.

The reactance value of TCSC in Figure 3.17(c) in function of α, $X_{TCSC}(\alpha)$, is given by following equation:

$$X_{TCSC}(\alpha) = \frac{X_C X_L(\alpha)}{X_L(\alpha) - X_C} \tag{3.27}$$

where the value of variable inductive reactance $X_L(\alpha)$ is given by:

$$X_L(\alpha) = X_L \frac{\pi}{\pi - 2\alpha - \sin\alpha} \qquad X_L \leq X_L(\alpha) \leq \infty. \tag{3.28}$$

For the power flow calculation, the value of TCSC is determined by a coefficient k_{TCSC} as (3.29):

$$\begin{aligned} x_{TCSC} &= k_{TCSC}\, x_{line} \\ -0.8 &\leq k_{TCSC} \leq 0.2. \end{aligned} \tag{3.29}$$

When the TCSC is inserted in the line, as presented in Figure 3.19, we could calculate the the modified value for the reactance of the line for power flow studies in Matpower as (3.29):

$$\begin{aligned} x'_{ik} &= x_{ik} + x_{TCSC} = x_{ik} + k_{TCSC}\, x_{ik} \\ &= (1 + k_{TCSC}) x_{ik} \end{aligned} \tag{3.30}$$

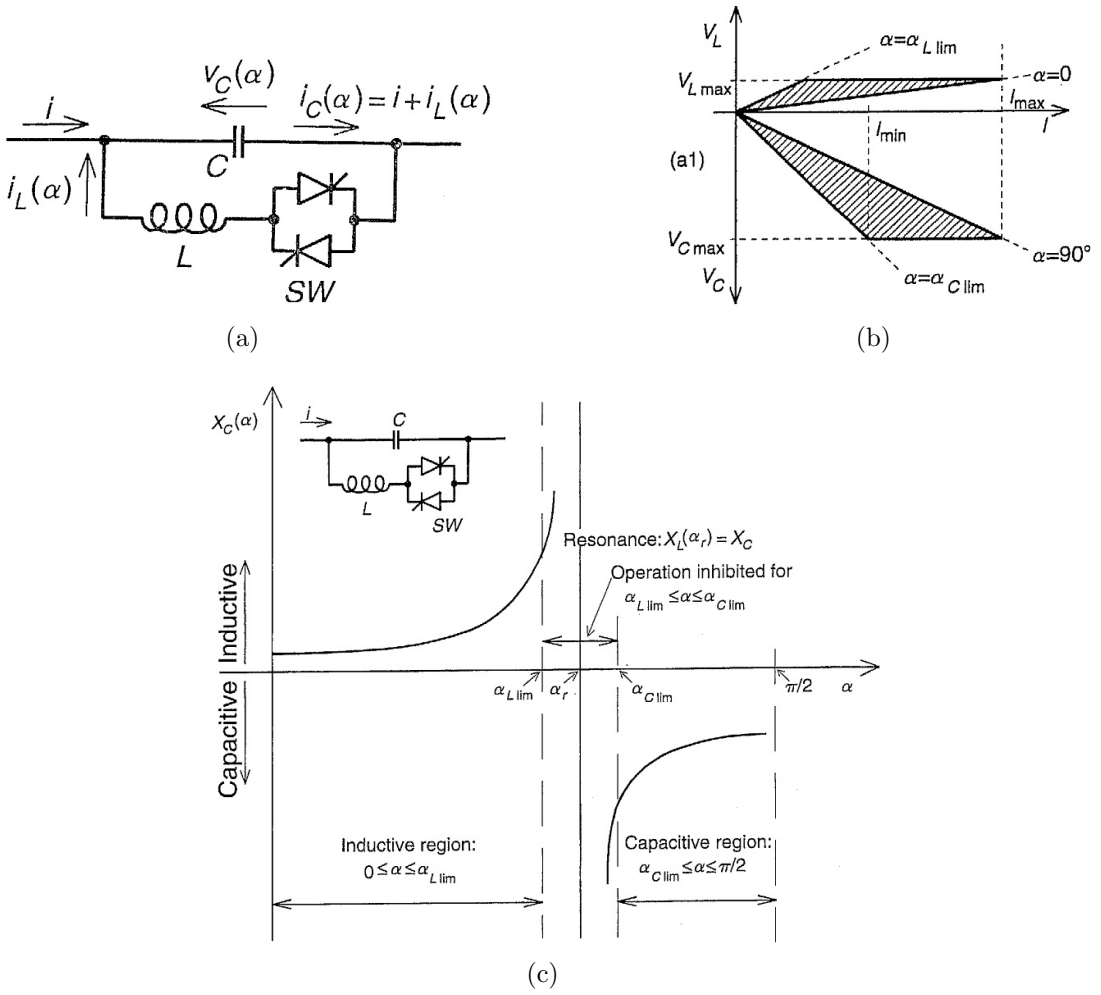

Figure 3.17: The Thyristor-Controlled Series Capacitor: (a) The TCSC structure. (b) The TCSC voltage-current characteristic. (c) The TCSC operating area.

where x'_{ik} is the modified value of the line reactance in the presence of TCSC device.

3.2.7 TCVR

The TCVR (*Thyristor-Controlled Voltage Regulator*) is used to change the magnitude of the bus voltage by inserting an in-phase voltage to the adjacent branch. The TCVR structure and the configuration of an inserted device is presented in Figure 3.20(a) and (b) respectively. For modeling, we can represent this device by an ideal tap changer transformer without series impedance [41, 74].

The voltage of the bus i in the presence of TCVR could be calculated by (3.31):

$$V'_i = (1 + k_{TCVR})V_i \qquad \text{where} \qquad -0.15 \le k_{TCVR} \le 0.15. \tag{3.31}$$

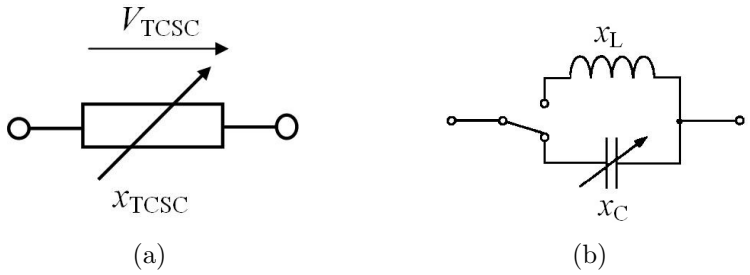

Figure 3.18: The TCSC: (a) The symbol of device. (b) The model of device.

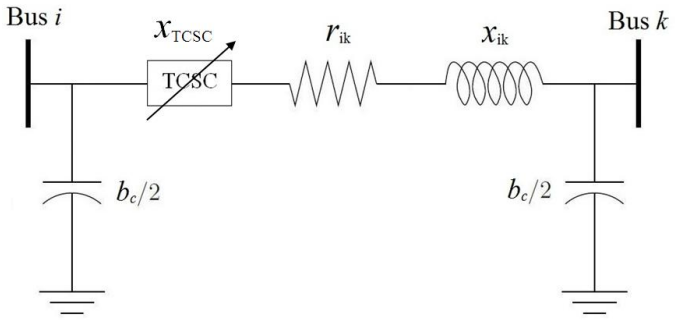

Figure 3.19: The TCSC inserted in the line.

For power flow calculation, we can set the value of tap ratio τ (see section 3.2.10) as:

$$\tau = 1 + k_{TCVR} \tag{3.32}$$

As it is clear from (3.32) the value of turns ratio ranges from 0.85 to 1.15. The value 1.0 means zero value for TCVR ($k_{TCVR} = 0$) and no transformation on voltage.

3.2.8 TSPST

The TCPST (*Thyristor-Controlled Phase Shifting Transformer*) which is presented in Figure 3.21 is used to regulate the voltage angle between the sending end and receiving end of the transmission line.

Therefore, by using this device we can easily increase or decrease the angles of bus voltages. The TCPST is modeled by an ideal phase shifter with series impedance equal to zero [41, 74]. The ranges for the angles of TCPST are as (3.33):

$$-20^\circ \leq \alpha_{TCPST} \leq 20^\circ \tag{3.33}$$

For power flow calculation we could easily set $\theta_{\text{shift}} = \alpha_{TCVR}$ (see section 3.2.10).

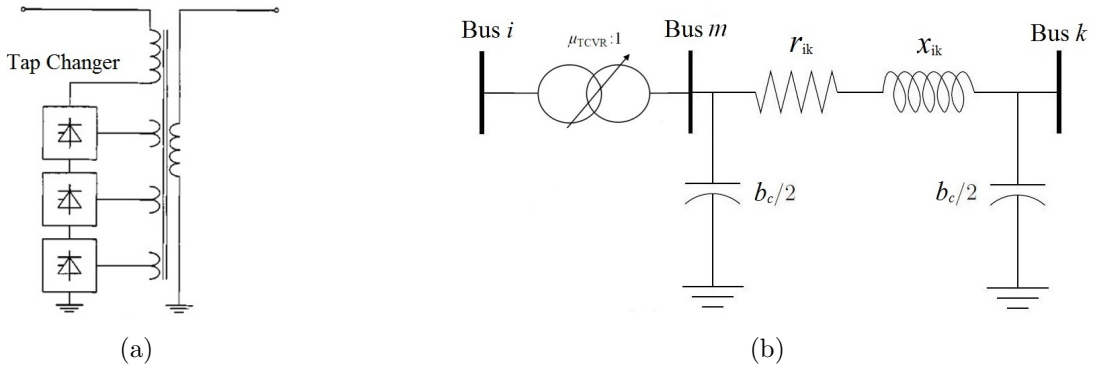

Figure 3.20: The Thyristor-Controlled Voltage Regulator:(a) The TCVR structure. (b) The TCVR configuration in the line.

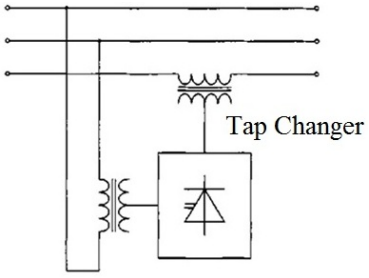

Figure 3.21: The TCPST structure.

3.2.9 UPFC

The UPFC (*Unified Power Flow Controller*) is a device from the third type of FACTS devices above, i.e. a combined shunt-series device. UPFC is a combination of a static compensator (STATCOM) and static series compensation (SSSC) as presented in Figure 3.22(a). It is therefore possible to control simultaneously all the parameters affecting power flow in the transmission line i.e., voltage, impedance and phase angle. Stated otherwise, it can independently control both the real and reactive power flow in the line and voltage magnitude at the UPFC terminals [10, 74].

A simplified schematic representation of the UPFC is given in Figure 3.22(a). The active power required by the series converter is drawn by the shunt converter from AC network and supplied to the bus k through the DC link. The output voltage of the series converter is added to the nodal voltage of bus k to boost the nodal voltage at bus k. So, neglecting the loss, the total power exchanged between the UPFC and the power system is zero ($P_{ex.} = 0$) [10, 74, 75, 76].

The equivalent circuit of UPFC is presented in Figure 3.22(b). As it is clear from this figure, the series part of UPFC could be modeled by a controllable voltage source ($\underline{V}_{SE}$), the shunt part with a controllable current source ($\underline{I}_{SH}$). The voltage magnitude of the output $\underline{V}_{SE}$ provides voltage regulation and the angle is used for phase regulation.

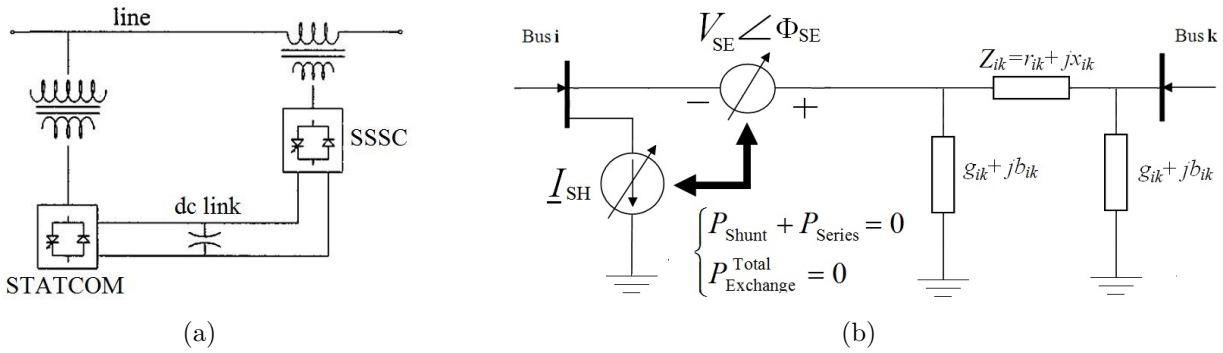

Figure 3.22: The Unified Power Flow Controller:(a) The UPFC structure. (b) The equivalent circuit of UPFC.

The three controllable parameters of the UPFC are V_{SE}, Φ_{SE} and I_{SH} where V_{SE} denotes the magnitude of the voltage injected in series with the transmission line with the ranges [0,V_{SEmax}], Φ_{SE} is the phase angle of this voltage with the ranges [0,2π] and I_{SH} is the shunt reactive current source of UPFC with the ranges [-I_{SHmax},I_{SHmax}] [10, 76, 77].

The computational results indicate that when the UPFC parameters V_{SE} and/or I_{SE} are set with too large values, load flow convergence is difficult due to the flat voltage starting method chosen. Practically, because of other physical limitations, such as insulation level of the apparatus in power system and the cost of the UPFC itself, V_{SEmax} and I_{SHmax} cannot assumed too large values. In our studies that follows, they we have set I_{SHmax}=0.15 p.u. and V_{SEmax}=0.3 p.u [77].

Based on the equivalent circuit presented in Figure 3.23(b), the two power injection in buses i (P_i^{inj}, Q_i^{inj}) and k (P_k^{inj}, Q_k^{inj}) for load flow analysis can be calculated according to the following expressions in (3.34):

$$\begin{aligned}
P_i^{inj} &= -V_k V_{SE}[Gcos(\delta_k - \Phi_{SE}) - Bsin(\delta_k - \Phi_{SE})] + G_F V_{SE}^2 + 2V_i V_{SE} G_F cos(\delta_i - \Phi_{SE}) \\
Q_i^{inj} &= V_i V_{SE}[G_F cos(\delta_i - \Phi_{SE}) - B_F sin(\delta_i - \Phi_{SE})] - V_i I_{SE} \\
P_k^{inj} &= -V_k V_{SE}[Gcos(\delta_k - \Phi_{SE}) + Bsin(\delta_k - \Phi_{SE})] \\
Q_k^{inj} &= -V_k V_{SE}[Gcos(\delta_k - \Phi_{SE}) - B_F sin(\delta_k - \Phi_{SE})]
\end{aligned} \tag{3.34}$$

where $G + jB = 1/Z_{ik}$, and $B_F = b_{ik} + B$. Also, in (6) the value of $V_i I_{SH}$ represents the reactive power injected by shunt current source (Q_{Shunt}) in bus i. In our case, since we have used the Matpower branch model, the value of g_{ik} is equal to zero, which makes G_F equals to G. Thus, using (3.35) it is possible to calculate the power flow when the allocation process includes the UPFC [10, 74, 75, 76, 77].

3.2.10 Using MatPower Package

In this chapter, MatPower software is used for power flow calculation. Every time the optimization process allocates a FACTS device to a network location (branch or line), we have to modify the admittance matrix accordingly, based on the FACTS value and its analytical model given in this section. This means that we have to modify the branch structure in the Matpower software and then use the modified network for power flow calculation.

The admittance matrix convention in MatPower software is better explained using the corresponding network schematic presented in Figure 3.23.

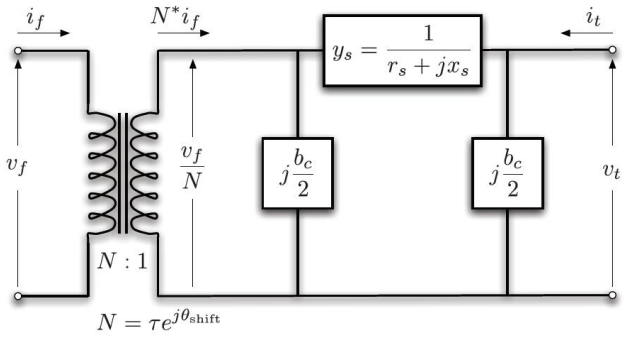

Figure 3.23: Branch model in Matpower software for power flow analysis.

Based on this figure, the admittance matrix in MatPower software could be expressed as (3.35):

$$\mathbf{Y}_{\text{Branch}} = \begin{bmatrix} \left(y_s + j\frac{b_c}{2}\right)\frac{1}{\tau^2} & -y_s\frac{1}{\tau e^{-j\theta_{\text{shift}}}} \\ -y_s\frac{1}{\tau e^{j\theta_{\text{shift}}}} & y_s + j\frac{b_c}{2} \end{bmatrix} \tag{3.35}$$

where $y_s = r_s + jx_s$, r_s is the line resistance, x_s is the line reactance, b_c is shunt susceptance, τ is the tap ratio and θ_{shift} is the phase shift angle. Based on the analytical modeling of the FACTS device, each branch parameter will be modified as well.

By way of example, for a SVC allocated in the middle of a line r_s , x_s and b_c , for TCSC x_s, for TCVR τ, and for TCPST θ_{shift} will be modified. For modeling a SVC allocated at the bus and for modeling a UPFC, we used the injected equivalent active and reactive power at the buses. Thereupon, we can calculate the power flow of the network using the appropriate commands.

3.3 FACTS Devices Influences on Network Variables

Having explained how the FACTS devices are modeled, which would be essential for power flow studies, now let us consider their influence separately on the power transmitted through a line between two buses 1 and 2. The active and reactive power flow equations

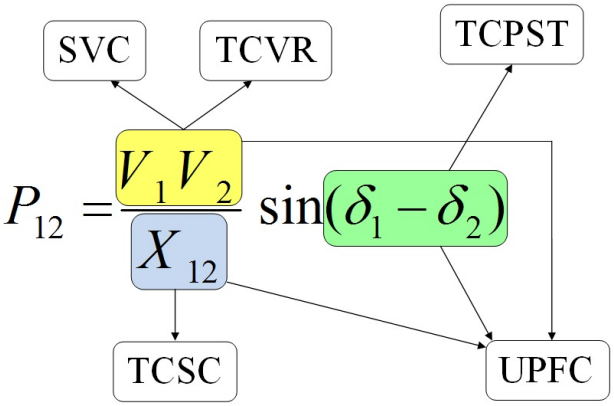

Figure 3.24: FACTS devices effects on variables of active power flow equation.

can be presented as (3.36):

$$\begin{aligned} P_{12} &= -P_{21} = \frac{V_1 V_2}{x_{12}} \sin(\delta_1 - \delta_2) \\ Q_{12} &= \frac{1}{x_{12}} \left(V_1^2 - V_1 V_2 \cos(\delta_1 - \delta_2) \right) \end{aligned} \tag{3.36}$$

where V_1 and V_2 are the voltages magnitudes of buses 1 and 2, x_{12} is the line reactance and $(\delta_1 - \delta_2 = \delta_{12})$ is the difference angle between phasors $\underline{V}_1$ and $\underline{V}_2$. Under normal operating condition we will have $V_1 = V_2 = 1.00$ p.u. and δ_{12} is small. Therefore we can decouple the active and reactive power control form each other as presented in (3.37):

$$\begin{aligned} P_{12} &\propto \frac{1}{x_{12}} \sin(\delta_{12}) \\ Q_{12} &\propto \frac{1}{x_{12}} \left(V_1 - V_2 \right). \end{aligned} \tag{3.37}$$

While the active power flow is coupled with δ_{12}, the reactive power flow is related to value of $(V_1 - V_2)$. By changing the value of x_{12}, both active and reactive power flows can be modified. Figure 3.24 shows the active power flow equation between two buses 1 and 2 and its controllable variables by each FACTS device [74].

Also, the impact of each FACTS device presented in previous section could be analyzed by inserting them in a small network such as 9 bus test system are presented in following sections. The schematic and bus data of 9 bus test system are presented in Appendix E.1.

3.3.1 SVC

At first, we consider the SVC's impact on the network variables by inserting this device in the branch 5 which is between buses 6 and 7. The results are shown in Figure 3.25. As can be seen from this figure, the SVC increases the voltages of all buses in capacitive mode

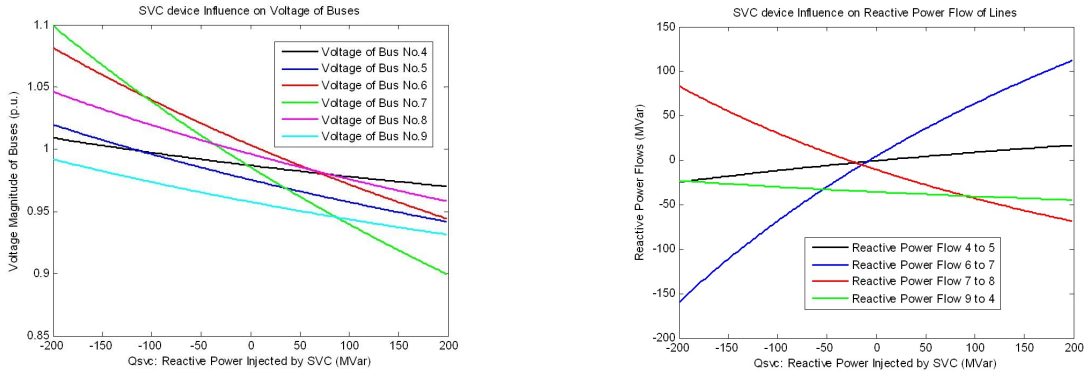

(a) (b)

Figure 3.25: Effect of SVC inserted in branch 5 on: (a) The voltage of buses. (b) The reactive power flow of lines.

and decreases them in inductive mode.

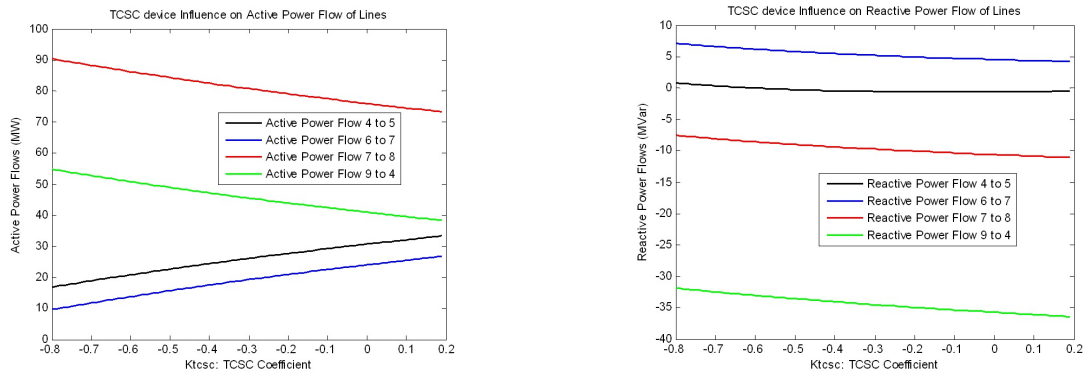

(a) (b)

Figure 3.26: Effect of TCSC inserted in branch 3 on: (a) The active power flow of lines. (b) The reactive power flow of lines.

3.3.2 TCSC

The second simulation is presented for TCSC's influence on branch power flows. The TCSC is inserted in the branch 3 which is between buses 5 and 6. The results are shown in Figure 3.26. As it is clear in this figure, the influence of TCSC in branch 3 is just limited on the neighborhood branches such as branch between buses 4 and 5 or buses 6 and 7.

3.3.3 TCVR

For the TCVR device, we inserted this device in branch number 9 which is between buses 4 and 9. The impact of TCVR device on the system bus voltages isshown in Figure 3.27. As it is clear in this figure, the influence of TCVR in branch 9 is just limited on the adjacent bus (bus No. 9), while the SVC has effect on all buses of the network.

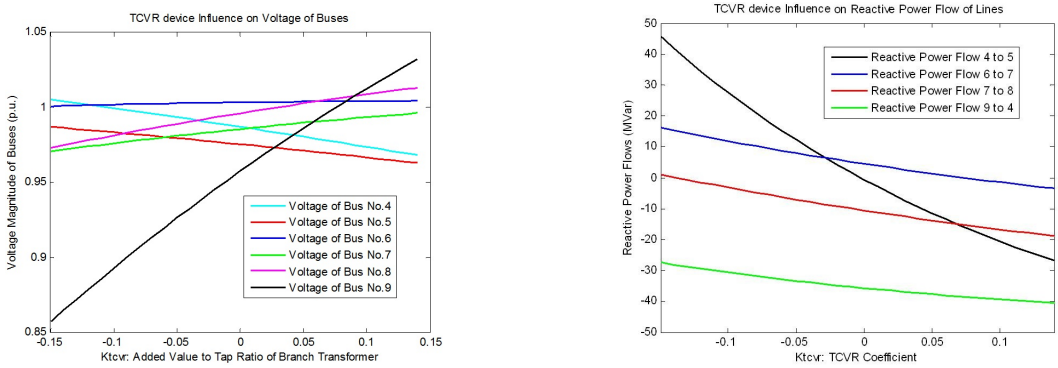

(a) (b)

Figure 3.27: The effect of inserted TCVR on: (a) The voltage of buses. (b) The reactive power flow of lines.

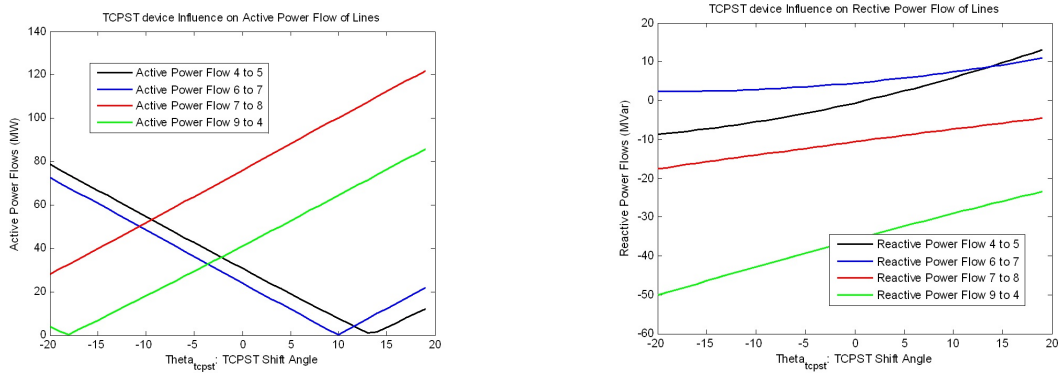

(a) (b)

Figure 3.28: The effect of inserted TCPST on: (a) The voltage of buses. (b) The reactive power flow of lines.

3.3.4 TSPST

Another simulation was performed for TCPST device, by inserting this device in the branch 3, between buses 5 and 6. The power flows of the system branches are shown in Figure 3.28.

Similar to TCSC, the influence of TCSC in branch 3 is just limited on the neighborhood branches such as branch between buses 4 and 5 or buses 6 and 7.

3.3.5 STATCOM with Energy Storage

For the last simulation, we consider the impact of STATCOM with SMES on the network variables by inserting this device in the branch 5, between buses 6 and 7, which is the same position as SVC. The results are presented in two mode: active power absorption and active power consumption. For the active power production mode, the P_{SMES} changes from -300 MW to zero and for absorption mode it changes from zero to +300 MW. The results for absorption mode are presented in Figures 3.29(a) and (c) and the results for production mode are presented in Figures 3.29(b) and (d). As it is clear in this figure similar to SVC, the device has influence on all buses of the network in both production and absorption modes.

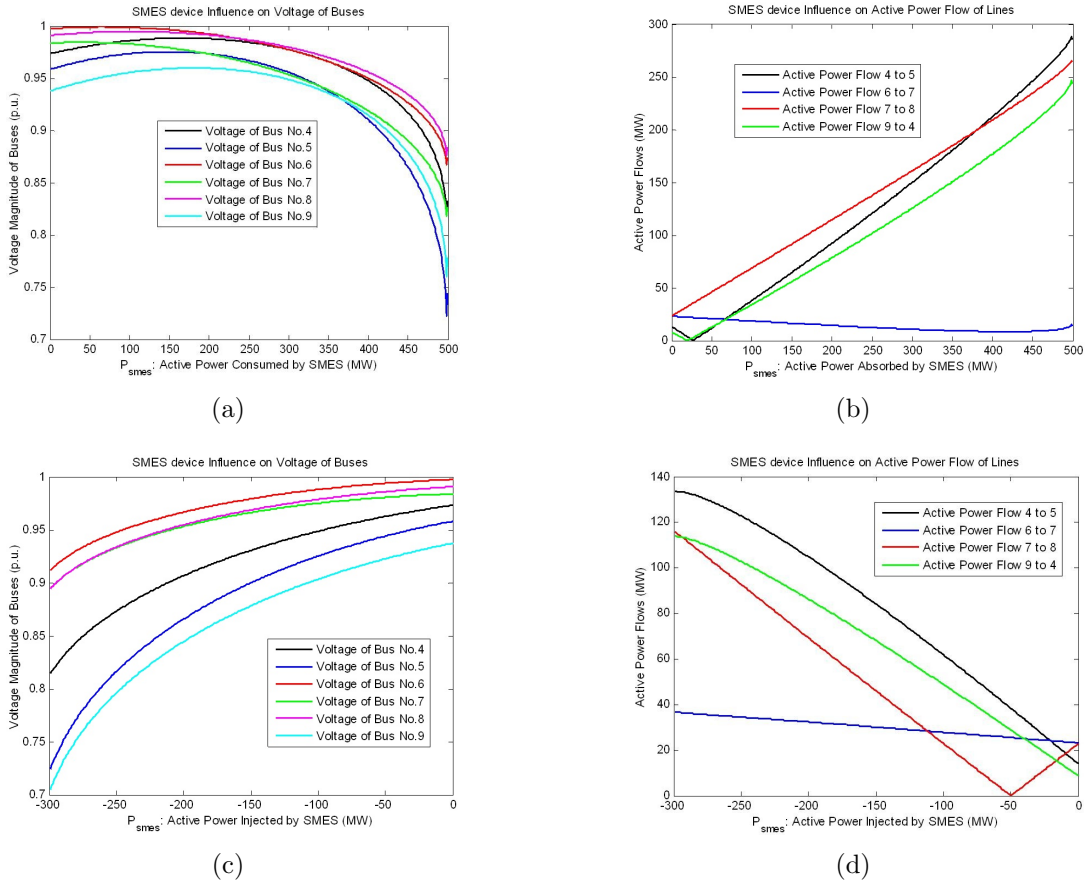

Figure 3.29: Effect of inserted STATCOM with SMES on: (a) and (c) The voltage of buses. (b) and (d) The active power flow of lines.

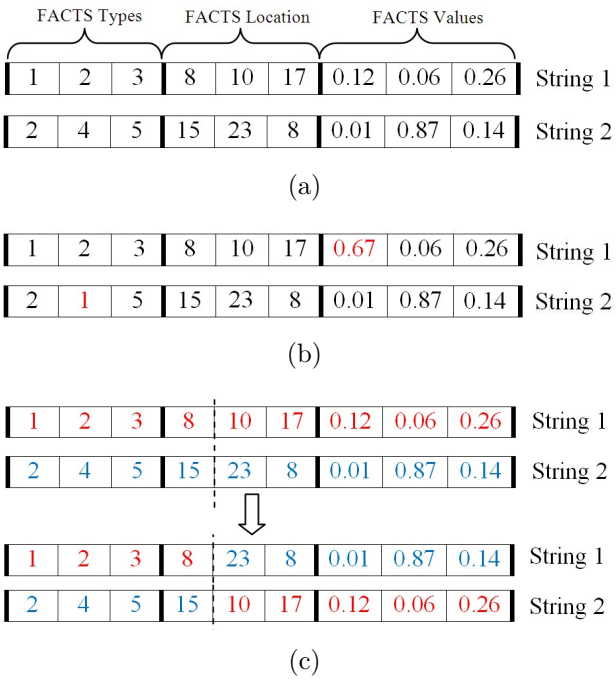

Figure 3.30: Genetic Algorithm: (a) Original individuals. (b) Mutation on each single individual. (c) Crossover between two original individuals.

3.4 Optimization Process

3.4.1 Optimization Method: Genetic Algorithm

The genetic algorithm is a kind of stochastic method for solving both constrained and unconstrained optimization problems based on mechanism of natural selection. The genetic algorithm repeatedly modifies a population of individual solutions. At each step, the genetic algorithm selects individuals at random from the current population to be parents and uses them to produce the children for the next generation. Over successive generations, the population "evolves" toward an optimal solution. It is possible to apply genetic algorithm to solve a variety of optimization problems that are not well suited for standard optimization algorithms, including problems in which the objective function is discontinuous, non-differentiable, and stochastic [78, 79].

As it was mentioned, there are several researches in the area of FACTS placement by using the genetic algorithm as optimization method that the reader can refer to them for more details [41, 78, 79]. Here, we just present a short description about how the genetic algorithm finds the best solution in an optimization problem. The following outline summarizes how the genetic algorithm works [79]:

1. Initial Population Generation: The algorithm begins by creating a random initial population. As a simple example, assume two presented individual in Figure 3.30(a) for the initial populations to follow the genetic operations.

2. Creating Next Generation: The algorithm then creates a sequence of new populations. At each step, the algorithm uses the individuals in the current generation to create the next population. To create the new population, the algorithm performs the following steps:

2.1. Scores each member of the current population by computing its fitness value. The fitness function for our case will be presented in next part of this section. The goal of algorithm will be minimizing the fitness value.

2.2. Scales the raw fitness scores to convert them into a more usable range of values.

2.3. Selects members, called parents, based on their fitness.

2.4. Some of the individuals in the current population that have best fitness value are chosen as **elite children**. These elite individuals are passed to the next population. They are the first type of children in genetic algorithm.

2.5. Genetic Operations: Produces children from the parents. Children are produced either by two methods:

2.5.1. Mutation: The algorithm creates mutation children as, the second type of children; by randomly changing the genes of a single individual parent (Figure 3.30(b)).

2.5.2. Crossover: The algorithm creates crossover children by combining pairs of parents in the current population (third type of children). At each coordinate of the child vector, the default crossover function randomly selects an entry, or gene, at the same coordinate from one of the two parents and assigns it to the child (Figure 3.30(c)). The dot line in Figure 3.30(c) shows the cross point or crossover factor.

2.6. Replaces the current population with the children to form the next generation.

3. Stop Criteria: The algorithm stops when one of the stopping criteria is met. The genetic algorithm uses some conditions to determine when to stop such as: number of generations, time limit and fitness limit [78, 79].

3.4.2 Objective Function Definition

The goal of our optimization process is to maximize the system loadability (transmitted power) on the network without any bus voltage violation or branch loading [41, 48, 49]. In order to achieve this objective, the load factor (λ) of the network will be increased in an iterative optimization process as follows.

First of all, the generating powers in generation buses (PG buses) are modified as (3.38):

$$P_{Gi} = (\lambda)\, P_{G0i} \tag{3.38}$$

where P_{G0i} is the initial power generation at bus i and P_{Gi} is the modified power generation.

Then, for the load buses (PQ buses) the active and reactive demands P_L and Q_L are modified as (3.39):

$$\begin{aligned} P_{Li} &= (\lambda)\, P_{L0i} \\ Q_{Li} &= (\lambda)\, Q_{L0i} \end{aligned} \tag{3.39}$$

where P_{L0i} and Q_{L0i} are the initial active and reactive load power at bus i and P_{Li} and Q_{Li} are the modified values.

At initial condition λ is equal to 1 (λ_0=1). Then, at each iteration, according to (3.38) and (3.39), the load factor is increased and the optimization constraints, which are bus voltage violation and branch loading, are verified. When it is no longer possible to satisfy the constraints, it is concluded that the maximum loadability has been reached. This is in fact a multi-stage greedy algorithm that follows the solving heuristic of making the locally optimal choice at each stage in the hope of finding a global optimum. On some problems, a greedy sequential strategy need not produce an optimal solution, but nonetheless a greedy heuristic may yield locally optimal solutions that approximate a global optimal solution.

The corresponding objective function which maximizes the power system loadability (ρ) to find the maximum load factor (λ_{max}) could be formalized as follows:

$$J = \text{Max}\,\{\rho\} \tag{3.40}$$

subject to the following security constraints:

$$\begin{array}{ll} S_l \leq S_{lmax} & \text{:for all branches of the network} \\ \Delta V_{bi} \leq 0.05 & \text{:for all buses of the network} \\ P_{gi}^{min} \leq P_{gi} \leq P_{gi}^{max} & \text{:for all generation buses of the network} \end{array} \tag{3.41}$$

where S_{lmax} is the maximum value for apparent power of the line l; S_l is the is the current apparent power of the line l; $\Delta V_{bi} = V_{bn} - V_{bi}$ is the difference between nominal and current voltage of bus i; $\Delta V_{bi} = 0.05$ is the maximum acceptable difference between V_{bn} and V_{bi} for all buses; P_{gi} is the generation at bus i, P_{gi}^{min} and P_{gi}^{max} are minimum and maximum bounds on P_{gi} respectively. Another security constrain which also could be considered is the difference angle between buses δ_{12}. The acceptable range for the value of this constrain in normal operation of power system is less than 35 degree.

The maximum system loadability will be determined by increasing the load factor λ at each zero-fitness value generation by monitoring the constraints presented in (3.41). If these constraints are not satisfied in a specific generation, then the previous increased load factor will be chosen as the maximum loading factor λ_{max}. In [41] it is shown that for each specific network there are a maximum number of FACTS device and more than that numbers of devices the network loadability cannot be further improved.

In order to simplify enforcement of the process constraints while placing FACTS at random locations, let us define a fitness function (Fit) that penalizes the configuration of FACTS devices which cause overloaded in transmission lines and over- or under- voltages at buses. This fitness function includes two terms targeting separately, branch overloading (OVL) and second term is related to bus voltage violations (VLB):

$$\text{Fit} = 2 - \left(\prod_{\text{Buses}} \text{VBL}_i + \prod_{\text{Branches}} \text{OVL}_l \right) \tag{3.42}$$

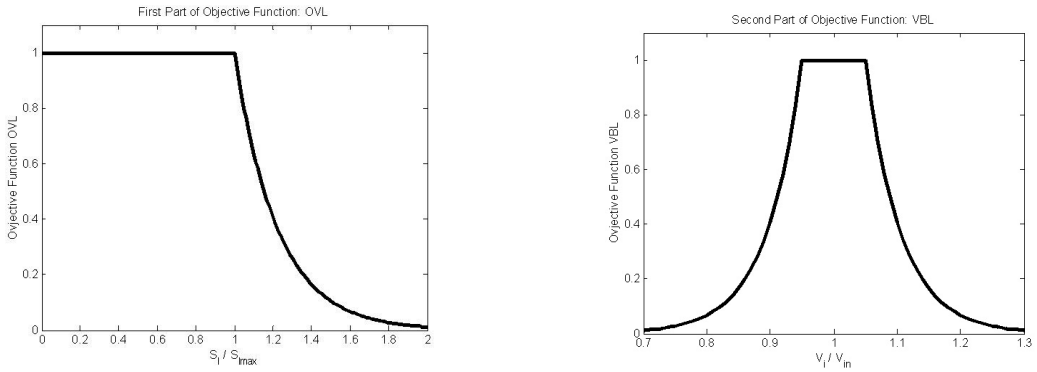

(a) (b)

Figure 3.31: The two terms of fitness function: (a) The OVL term related to over-loaded lines. (b) The VBL term related to voltage level of buses.

with first term of fitness function (OVL) which penalizes over-loaded lines as (3.43) and in Figure 3.31(a):

$$\mathrm{OVL}_l = \begin{cases} 1 & \text{if} \quad S_l \leq S_{lmax} \\ \exp\left(\mu_1 \left| 1 - \frac{S_1}{S_{lmax}} \right|\right) & \text{if} \quad S_l > S_{lmax} \end{cases} \tag{3.43}$$

and second term (VBL) penalizes the bus voltages which are not between 0.95 and 1.05 as (3.44) and in Figure 3.31(b):

$$\mathrm{VBL}_l = \begin{cases} 1 & \text{if} \quad \Delta V_{bi} \leq 0.05 \\ \exp\left(\mu_2 \left| 0.05 - \Delta V_{bi} \right|\right) & \text{if} \quad \Delta V_{bi} > 0.05 \end{cases} \tag{3.44}$$

where μ_1 and μ_1 are constant coefficient.

This means that, if the constraints are fulfilled, each term of the fitness function in (10) (OVL and VBL) will be equal to 1 and the value of the fitness function (Fit) in (3.42) will be equal to zero. On the other hand, if the constraints are not met, the above-defined fitness function penalizes overloaded branches and over- or under-voltage buses. In summary, the optimization process of the GUI implemented to find the maximum loading factor λ_{max} (maximum system loadability) could be presented as follows:

• **Step 1:** Initialize λ_0=1, select the number and types of FACTS device and load selected network.

• **Step 2:** Increase λ=λ+ 0.1, create an initial population of genetic algorithms and then verify the constraint satisfaction for each individual by means of the fitness function (Fit) presented in (3.42). If there is any individual with Fit=0, it means that at current load factor λ we have a configuration that satisfies the security constraints and as a results we should increase the load factor.

• **Step 3:** If there is any individual with fitness function (Fit) equal to zero repeat step 2. This loop continues until we reach to a load factor for which there is no individual with a fitness function equal to zero. This means that at this load factor, there is no configuration of FACTS device which can bring the network voltage level and loading constraints into acceptable ranges. At this point, we should report the previous load factor corresponding to maximum load factor (λ_{max}) and previous individual with zero value of (Fit) which includes optimal locations and values of selected FACTS device. (see Figure 3.34)

In summary, the global optimization (3.40) is a complex, possibly untrackable problem which is converted into several simpler sequential optimization problems. In fact, the global problem solving requires a continuation OPF to find the objective function while the greedy problem solving only relies on ordinary power flows to enforce security constraints (3.41) at each stress level. The pitfall is that there is no guaranty of global optimum, only the certainty to obtain one solution, at a giving stress level.

3.5 GUI Description: FACTS Placement Toolbox

After setting the Matlab path to the folder which includes the m-files programs of FACTS Placement Toolbox and running the main program, the main graphical user interface will be launched as it is shown in Figure 3.32. In the implemented GUI, which uses genetic algorithm as its optimization method, the user could choose the type and number of FACTS devices, the power system network and also determine the setting parameters of genetic algorithm. Then, the optimization process will find the optimal locations and values of the selected FACTS device in the selected power system network in order to maximize the power system loadability. In following, each section of this GUI will be presented briefly.

A. FACTS Device Selection

The first step of using the FACTS Placement Toolbox is to select the type and number of the FACTS devices. There are two categories for the user to select:

• Single Type FACTS Device Allocation.

• Multiple Type FACTS Devices Allocation.

After checking one of the boxes related to the above categories and pushing the "FACTS Selection" bottom, the related table will open as it is shown in Figure 3.33(a). Then, the user can select the type and number of FACTS devices which should be allocated in the network.

B. Genetic Algorithm Setting

The next step of the allocation process is to determine the settings parameters of genetic algorithm. These setting parameters are: number of generations, initial population size, number of elite child, the ratio of crossover fraction, fitness limit and time limit. The definition and explanation of these setting parameters are presented in the "Help" menu of the GUI. The table of setting parameters of genetic algorithm is shown in Figure 3.33(b).

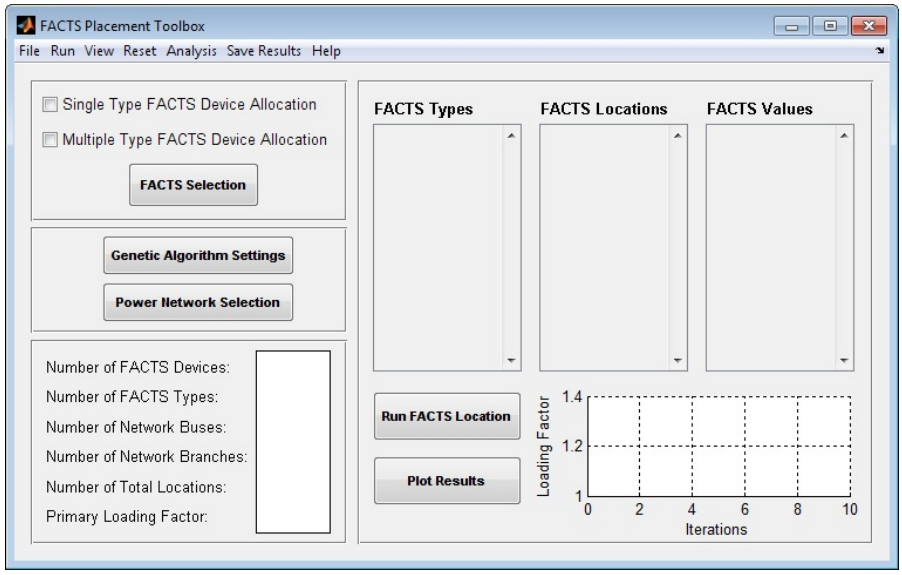

Figure 3.32: Main graphical user interface of FACTS Placement Toolbox.

This table is set by some default values for tunable parameters and if the user wants to modify them, new values should be inserted following the "Save" bottom.

C. Power Network Selection

In the third step, the user can pick a network among several IEEE test systems whose complexity ranges from 4 to 300 buses and also a full Hydro-Québec PSS/E based network. The related graphical user interface is shown in Figure 3.33(c).

D. Summaries Table

In this table the summaries of previous information about selected FACTS devices and power system are presented. Regarding the total location As it was mentioned before, the SVC (or STATCOM) and the STATCOM with SMES are the only devices that could be installed in both branches or buses. Therefore, if the user includes the SVC or STATCOM with SMES in the selected FACTS devices, the number of total location would be equal to the sum of buses and branches ($n_{\text{Locations}} = n_{\text{Branch}} + n_{\text{Bus}}$). Otherwise, the number of total location would be equal to the number of branches ($n_{\text{Locations}} = n_{\text{Branch}}$).

E. Running FACTS Placement Procedure

The flowchart of the FACTS placement procedure using the implemented GUI is depicted in Figure 3.34. Since the UFPC device has three controllable variables and STATCOM with SMES has two while the other FACTS devices have just one; we should classify the coding program into six different categories based on selecting or not selecting the UPFC or the STATCOM with SMES:

1. Single type allocation except both UPFC and STATCOM with SMES.
2. Single UPFC allocation.
3. Single STATCOM with SMES allocation.
4. Multiple type allocation without both UPFC and STATCOM with SMES.

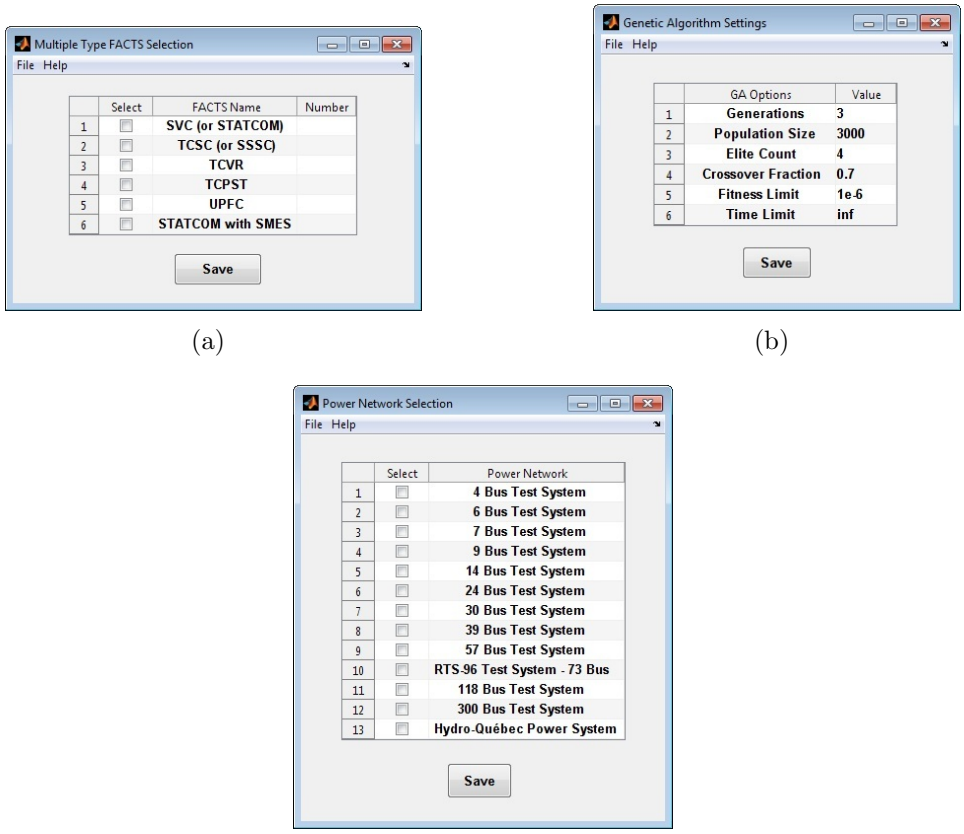

Figure 3.33: The graphical user interface for: (a) FACTS selection. (b) Genetic algorithm settings. (c) Power network selection.

5. Multiple type allocation including UPFC.
6. Multiple type allocation including both UPFC and STATCOM with SMES.

Based on above different categories, we will have different type of individuals for the genetic algorithm optimization process. For example, typical individuals for the third and fourth categories are shown in Figure 3.35(a), (b) and (c) respectively.

As it is clear in Figure 3.35, the first part of each individual's string is related to the FACTS type. For each specific FACTS device there is a specific code, namely: 1 for SVC, 2 for TCSC, 3 for TCVR, 4 for TCPST, 5 for UPFC and 6 for STATCOM with SMES. In the examples of Figure 3.35, since we have five FACTS devices ($n_{\text{FACTS}} = 5$), the FACTS types slot shown in the individual's string has five columns. The number of total columns of each individual's string ($n_{\text{individual}}$) can be calculated by following equation:

$$n_{\text{individual}} = 3n_{\text{FACTS}} + 2n_{\text{UPFC}} + n_{\text{SMES}}. \tag{3.45}$$

The second slot of each individual's string corresponds to the locations associated with

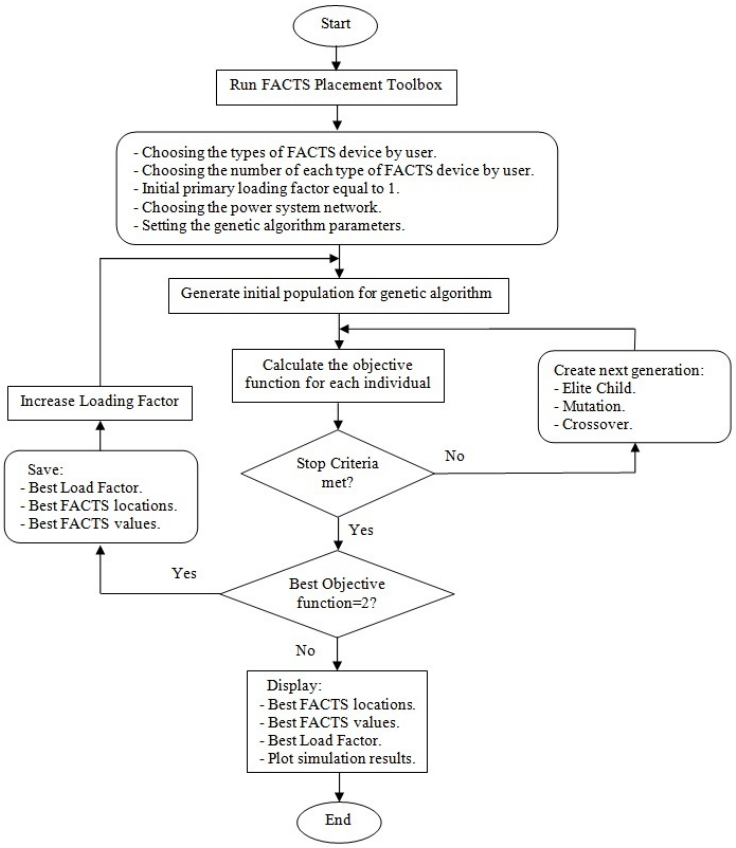

Figure 3.34: Flow chart of overall procedure of FACTS Placement Toolbox.

the first slot in the string. Each specific FACTS device has its own location. Repeated locations are not allowed in our optimization process and each line or bus should appear only once in the string.

The third and last part of the individual's string includes the rating values of the FACTS devices which are normalized between 0 and 1; 0 corresponding to the minimum value of the device and 1 to the maximum. To use these normalized values in the power flow calculations, we need to convert them to the physical real value of the device as follows:

$$v_{\text{real}} = v_{\min} + (v_{\min} - v_{\max})\, v_{\text{normalized}} \tag{3.46}$$

where $v_{\min}$ and $v_{\min}$ are the minimum and maximum value for each specific device which were presented in FACTS device modeling.

The optimization algorithm (GA) randomly selects the locations and values for all given FACTS devices after setting them in the power system network at each generation. The fitness function (Fit) is then calculated for each individual. If the constraints are met, the value of the fitness function (Fit) in (3.42) will be equal to 0; otherwise it will be

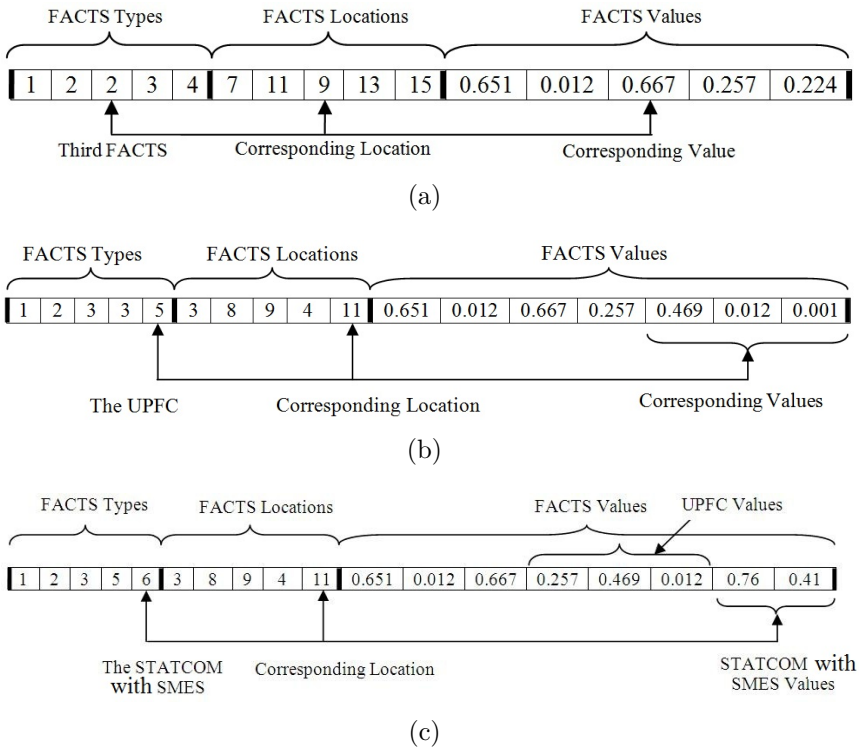

Figure 3.35: Typical example of an individual of multi-type FACTS device allocation: (a) Category 4. (b) Category 5. (c) Category 6.

greater than 0. Based on the fitness function value, the genetic algorithm performs the GA operations such as elite generation, mutation and crossover for creating next generation.These operations continue based on the algorithm presented in section 3.4.2. Then in a specific generation, the maximum system loadability (λ_{max}) will be determined while the security constraints are fulfilled. In [41] it is shown that for each specific network there are a maximum number of FACTS device and more than that numbers of devices the network loadability cannot be further improved.

3.6 Results of FACTS Placement Toolbox

In order to verify the performance of the implemented GUI, several combinations of FACTS devices were sited optimally on different IEEE test networks. The allocation results of a selected subset of the many scenarios studied are presented in this section.

3.6.1 30-Bus Test System

For the first case study the 30-bus test system is chosen for a detailed presentation to demonstrate how the different modules of the GUI work. The schematic and the network

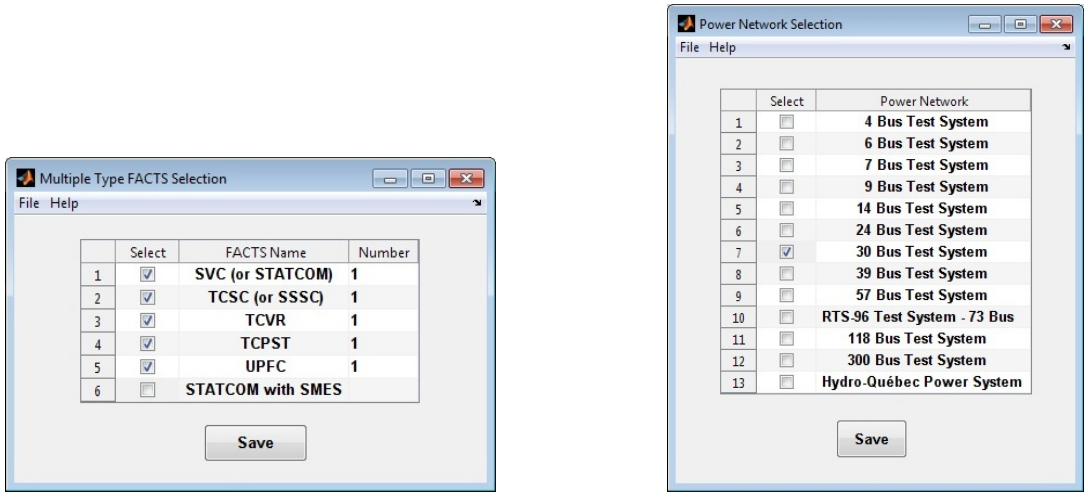

(a) (b)

Figure 3.36: The graphical user interface for the first case study the 30-bus test system: (a) Selected FACTS devices. (b) Selected power network.

data of 30-bus test system is presented in Appendix E.3. In this simulation, the following combination was selected by the GUI user as the input FACTS device types with corresponding numbers: SVC (1), TCSC (1), TCVR (1), TCPST (1) and UPFC (1) as shown in Figure 3.36(a).

After selection of the FACTS combination, the parameters of the genetic algorithm are set as shown in Figure 3.33(b) and and the 30-bus test system is selected as presented in 3.36(b). As mentioned before, the SVC is the only device that can be allocated in both buses and branches. Since we have the SVC in our selection, the total locations would be equal to 71 (30 buses plus 41 branches) which is presented in summaries in Figure 3.37.

Pushing the "*Run FACTS Location*" button starts the allocation process and we would see the FACTS placement results presented in Figure 3.37. Also the maximum loading factor for this given set of FACTS devices in the 30-bus test system was determined as $\lambda_{max} = 1.61$, which means that by installing the above set of devices at those optimal locations with those rated values, we will have a 61% improvement in the system loadability while fulfilling all the security constraints presented in (3.41). The physical meanings of the normalized values in Figure 3.37 are presented in Table 3.1.

Finally, pushing the "*Plot Results*" button in Figure 3.37, produces some more comparative figures. First, let consider the bus voltages of the networks with and without FACTS devices at the maximum load factor and also for a load factor chosen by user using the module presented in Figure 3.38. For the 30-bus test system, this graphs are presented for the load factors $\lambda_{max} = 1.61$ and $\lambda_{user} = 1.90$ in Figure 3.39(a) and (b) respectively.

As it is clear from these plots in Figure 3.39, at the same loadability condition, the network without FACTS devices has a greater voltage drop in the buses. This confirms

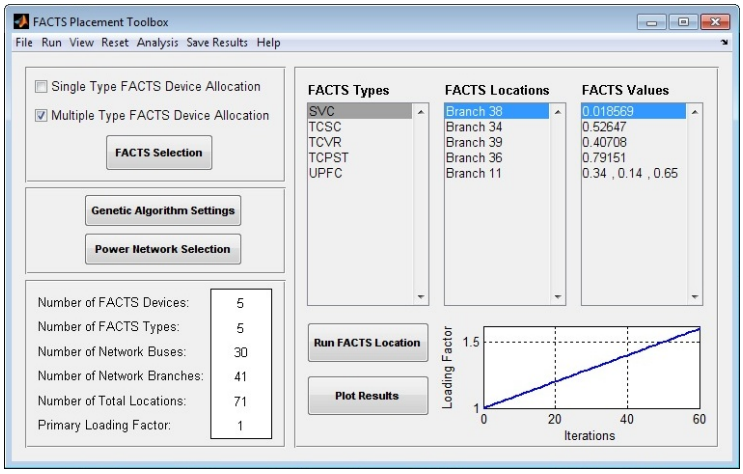

Figure 3.37: The results of FACTS placement toolbox in 30-bus test system for the selected FACTS devices by user.

Table 3.1: Physical values of the results for the 30-bus test system.

No.	**FACTS Type**	**FACTS Location**	**Normalized Value**	**Real Value**	
1	SVC	Branch 38	0.01584	-288.859	MVar
2	TCSC	Branch 34	0.52674	-j0.274	Reactance
3	TCVR	Branch 39	0.40708	1.029	Ratio
4	TCPST	Branch 36	0.79151	11.66	Degree
5	UPFC	Branch 11	0.34425 0.13525 0.64996	V_{SE} =0.100 Φ_{SE} =50 I_{SH} =0.045	p.u. Degree p.u.

the significant influence of FACTS devices on keeping the bus voltage in the acceptable ranges. Also, from these graphs we can compare the absolute deviation for all voltages of buses which could be calculated using following equation in (3.47):

$$\text{TVD} = \sum_{i=1}^{n_{bus}} |V_{bi} - V_{bn}| \tag{3.47}$$

where TVD is Total Voltage Deviation, V_{bn} is the nominal voltage and V_{bi} is the current voltage of bus i.

Another plot is the V-P graph for one specific bus which should be a PQ-bus (load bus), again chosen by user randomly, to check the system loadability improvement. This graph is traced based on CPF analysis. Here, the bus number 10 and 22 are selected for the V-P graph as presented in Figure 3.40(a) and (b) respectively.

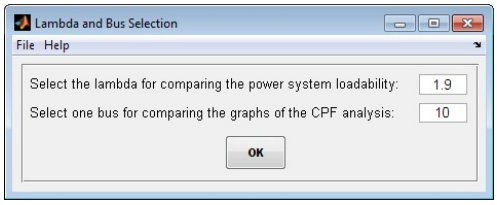

Figure 3.38: The module for selecting the user load factor and bus for plotting V-P graph.

The third presented graph is for the effects of FACTS devices on active power flow in transmission lines. The power flows of each branch for the network with and without FACTS device at $\lambda_{max} = 1.61$ are presented in Figure 3.41(a). As it is clear in this figure, at the presence of FACTS devices, we would totally have 2 MW (1.06%) lower amounts in active power flows. For the next graph the transmission line losses, again at $\lambda_{max} = 1.61$, are presented as Figure 3.41(b). Based on this graph, the line loss reduction at maximum loadability in the network with FACTS devices is around 1 MW (0.53%).

Also, we can monitor the total loss of the network for different load factor to find the threshold load factor named as λ_{LRI} (LRI: Loss Reduction Improvement). For each network, there is a load threshold factor (λ_{LRI}) (LRI: Loss Reduction Improvement) above which we observe a reduction in transmission line losses. This means that there is no guarantee to always reduce power system losses using FACTS devices if the main target of FACTS placement is to increase loadability.

Figure 3.42 presents the total loss associated with the 30-bus test system as a function of the load factor. The LRI load factor λ_{LRI} for the 30-bus test system is equal to 1.17,which is the first indication that we have an improvement in system losses. For example in the 30-bus test system, at $\lambda = 1.61$ and $\lambda = 1.90$, which are bigger than $\lambda_{LRI} = 1.17$, we will have 0.68 MW (0.71%) and 1.34 MW (0.36%) loss reduction on the transmission lines.

Figure 3.43 illustrates the influence of the located FACTS devices on the VBL and OVL terms of fitness function. At λ_{max}, the value of VBL term for all buses is 1 in the network with FACTS, while in the network without FACTS we have many over- or under voltages buses. Also, we can verify the FACTS influence on the OVL term of fitness function in Figure 3.43(b). These graphs help us to identify the overloaded lines as well as the over- or under-voltage buses at the maximum load factor.

3.6.2 57-Bus Test System

For the second case study the 57-bus test system is chosen to verify the performance of FACTS Placement Toolbox. The schematic and the network data of the 57-bus test system is presented in Appendix E.5. The following combination was selected by the GUI user as the input FACTS device types with the corresponding numbers: SVC (1), TCSC (2), TCPST (1) and UPFC (1). The results of FACTS placement process are presented in Table 3.2. For the 57-bus test system, with the given FACTS device, the maximum load factor was determined as $\lambda_{max} = 1.21$; which means that by installing the above set of devices in

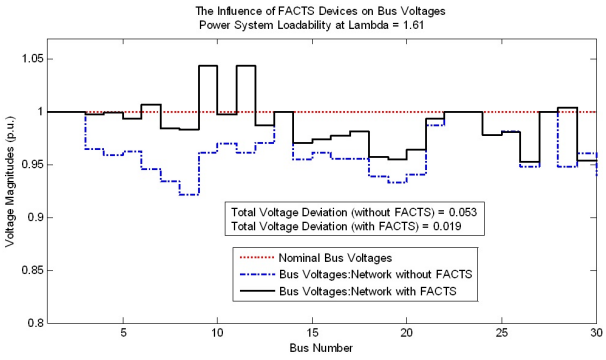

(a)

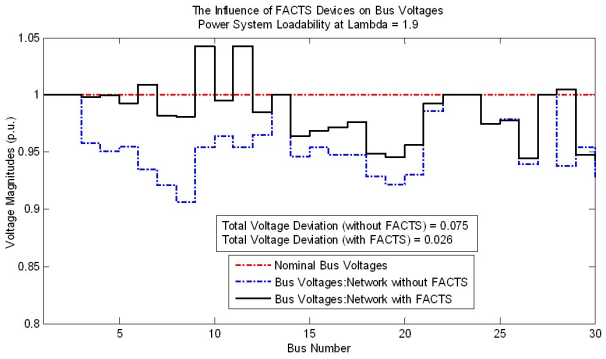

(b)

Figure 3.39: Comparing voltages magnitudes of all buses of the 30-bus test system at: (a) Maximum load factor $\lambda_{max} = 1.61$. (b) For user-selected load factor $\lambda_{user} = 1.90$.

those optimal locations with those rated values, we will have a 21% improvement in the system loadability while fulfilling all the security constraints presented in equation (3.41).

The voltages of buses for the networks with and without FACTS devices for $\lambda_{max} = 1.21$ is presented in Figure 3.44.

Also, based on the CPF analysis the V-P graph for the buses number 22 and 40 are presented in Figure 3.45(a) and (b) respectively.

The influence of FACTS devices allocated in the 57-bus test system on power flows and line losses are presented in Table 3.3. As it is shown in this table, at $\lambda = 1.41$ there is 7 (MW) (0.51%) lower amount in losses in persence of FACTS devices.

The total loss of the network for different load factors also presented in Figure 3.46 from which we determine the value of λ_{LRI} with the given set of FACTS devices as equal to 1.08.

Also, the influence of the allocated FACTS devices on VBL and OVL terms of fitness function are presented in Figure 3.47(a) and (b) respectively.

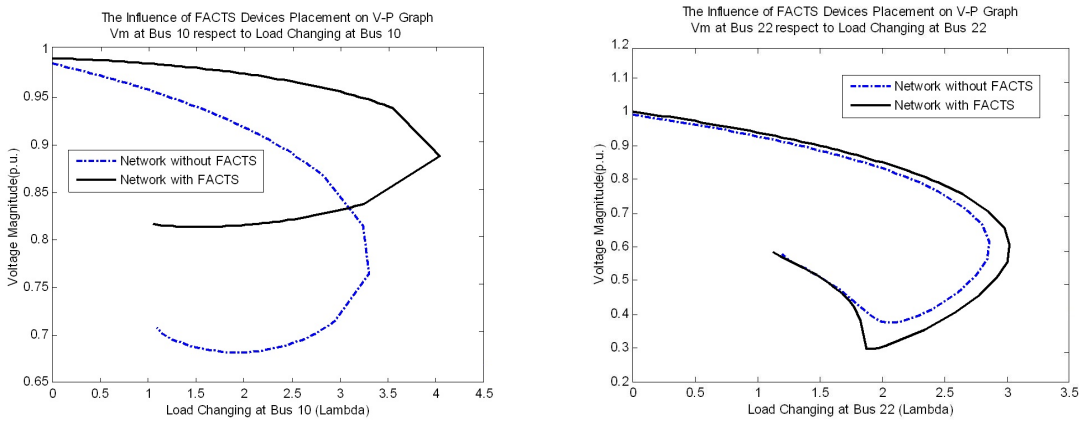

(a) (b)

Figure 3.40: Comparing the V-P graph for verifying the loadability improvement in the 30-bus power network with FACTS: (a) Bus number 10. (b) Bus number 22.

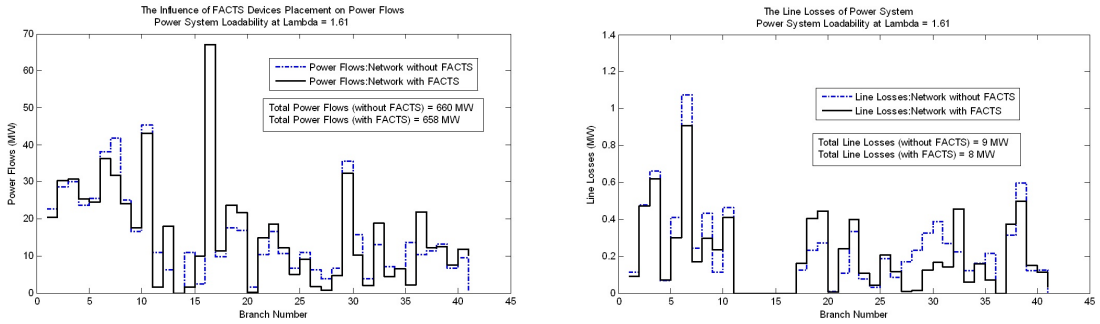

(a) (b)

Figure 3.41: Effects of FACTS devices in the 30-bus test system on: (a) Power flow transmitted in branches. (b) Transmission line losses in branches.

3.6.3 300-Bus Test System

For the third case study the 300-bus test system is chosen to verify the performance of FACTS Placement Toolbox. The schematic and the network data of the 300-bus test system is available on-line in [80]. For this network, the following combination was selected by the GUI user as the input FACTS device types with the corresponding numbers: SVC (2), TCSC (2), TCVR (1), TCPST (1) and UPFC (1). The results of FACTS placement process are presented in Table 3.4. For the 300-bus test system, with the given FACTS device, the maximum load factor was determined as $\lambda_{max} = 1.13$; which means we have 13% improvement in the system loadability.

The voltages of buses for the networks with and without FACTS devices for $\lambda_{max} = 1.13$ is presented in Figure 3.48.

The influence of FACTS devices allocated in the 300-bus test system on power flows

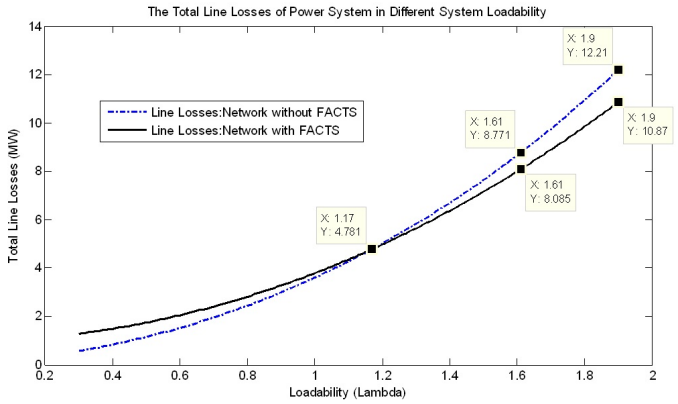

Figure 3.42: Comparing total loss of transmission lines of 30-bus test system with and without FACTS devices.

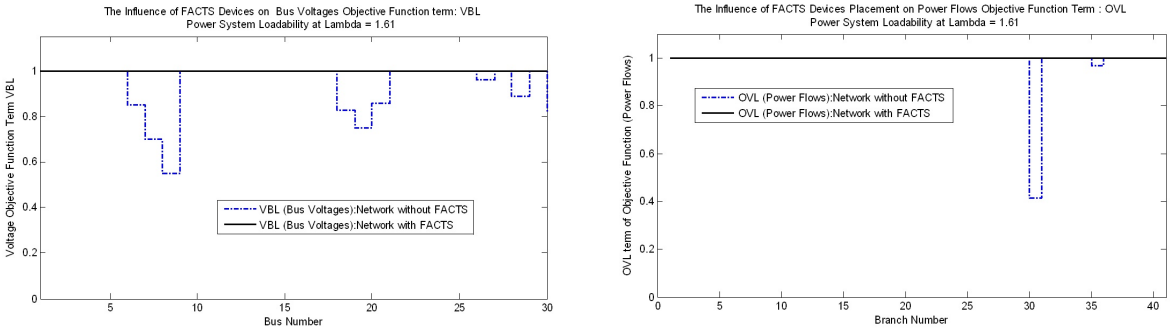

(a) (b)

Figure 3.43: Effects of FACTS devices in the 30-bus test system on fitness function (Fit) terms: (a) The VBL term. (b) The OVL term.

and line losses are presented in Table 3.5. As it is shown in this table, $\lambda_{max} = 1.13$ there is 2 (MW) (0.01%) lower amount in losses in persence of FACTS devices.

Also, the total loss of the network for different load factors presented in Figure 3.49 from which the value of λ_{LRI} with the given set of FACTS devices is determined equal to 1.08. For example, the loss reduction in the 300-bus test system at $\lambda = 1.20$ is 7 (MW) and for $\lambda = 1.32$ is 23 (MW).

3.6.4 The Analysis of Different Combination of FACTS Devices on One Network

The results presented in previous sections shows that the user can analyze different combinations of FACTS devices on different networks using the implemented FACTS placement toolbox. Actually, this toolbox presents a generic method which could help the user do more studies for a specific goal. For example, we can analyze the influence of any configu-

Table 3.2: FACTS placement results for the 57-bus test system.

Test System	**Selected FACTS and GUI Results**				λ_{max}	λ_{LRI}	**Loss Reduction**	
	Type	Location	Value				at $\lambda =$	Reduction
57 Bus	SVC	Bus 7	-90.401	MVar	1.21	1.24	1.41	7 MW (0.51%)
	TCSC	Branch 72	-j0.326	Reactance				
	TCSC	Branch 36	-j0.643	Reactance				
	TCPST	Branch 11	-13.403	Degree				
	UPFC	Branch 78	V_{SE} =0.25 Φ_{SE} =145 I_{SH} =-0.12	p.u. Degree p.u.				

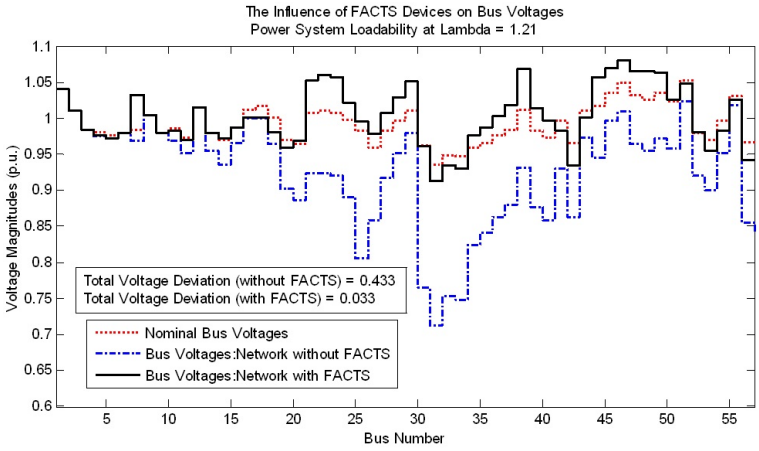

Figure 3.44: Comparing voltages magnitudes of all buses of the 57-bus test system at maximum load factor $\lambda_{max} = 1.21$.

ration of FACTS devices (single or multiple) on the power system loadability for a specific power system network. Here in this section, we have performed such a study for the 39-bus test system. The schematic and the network data of the 39-bus test system is presented in Appendix E.4. The same analysis could have been done on other networks using the implemented toolbox.

In this section, the influence of different combinations of FACTS devices, multiple or single type, with different numbers of each, is verified using the toolbox. The results for the 39-bus test system are presented in Table 3.6. By analyzing the selected FACTS devices and the corresponding results in Table 3.6, we can better understand the influence of each device on the network. For example we could state following conclusions:

• Considering the loss reduction, 1 UPFC is the most effective device compared to other FACTS devices.

• Also, 2 SVC in comparison of 1 SVC cannot improve the system loadability significantly. It means that even if we increase the number (or the size) of SVC it is not possible technically to improve the system loadability furthermore.

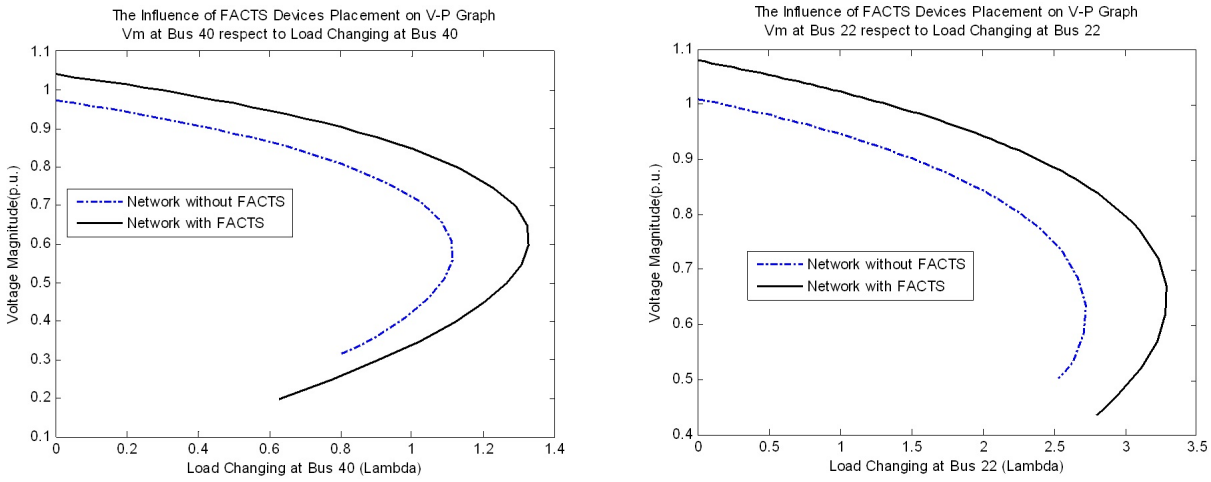

(a) (b)

Figure 3.45: The V-P graph based on CPF analysis for verifying the loadability improvement in the 57-bus power network: (a) Bus number 40. (b) Bus number 22.

• Comparing the result of 1 TCVR and 1 TCPST, it could be seen that in this network, the TCVR would be more effective than TCPST.

• In addition, based on the last column of Table 3.6, we can observe that the impact of TCPST and TCVR on the loss reduction is less than other devices.

• Also, we notice that increasing the number of UPFC from 1 to 2, result in not further improvement in system loadability.

• Finally, for the 39-bus test system the maximum load factor, achievable through FACTS devices placement, is 7%. It means that, even if we increase the number of FACTS devices (or size of them), we cannot improve the loadability by more than 8%.

Table 3.3: FACTS devices influence on power flows and line losses in the 57-bus test system.

Load Factor	$\lambda_{max} = 1.21$		$\lambda_{user} = 1.41$	
Network Condition	**Without FACTS**	**With FACTS**	**Without FACTS**	**With FACTS**
Total Active Power Flow (MW)	3365	3535	3963	4052
Total Line Losses (MW)	85	86	116.1	109.1
Loss Reduction Improvement (MW)		—		7 MW (0.51%)

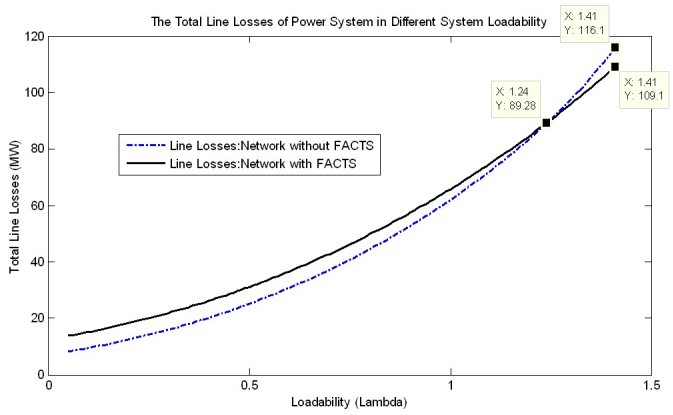

Figure 3.46: Comparing total loss of transmission lines of the 57-bus test system with and without FACTS devices.

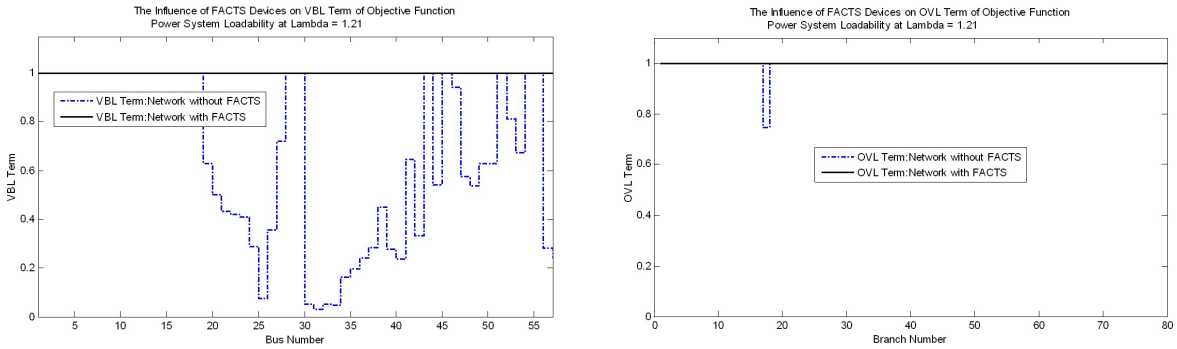

(a) (b)

Figure 3.47: Effects of FACTS devices in 57-bus test system on fitness function terms: (a) The VBL term. (b) The OVL term.

3.6.5 The Analysis of One Combination of FACTS device on Different Power System Networks

For another usefulness of the implemented GUI, the influence of one multiple-type combination of FACTS device including: SVC (1), TCSC (1), TCVR (1), TCPST (1) and UPFC (1) is verified on different power system networks. The results are presented in Table 3.7.

By considering the data in this table, it can be concluded that for the larger networks we need more devices to have significant loadability improvement. For example, if we compare Table 3.4 and Table 3.7 for the 300-bus network, we see that by using 7 FACTS devices we have 16% loadability improvement while with 5 devices the rate is 8%. A similar observation holds for the 118-bus test system. Using the GUI, the simulations of this table can be repeated for different set of FACTS devices.

Table 3.4: FACTS placement results for the 300-bus test system.

Test System	**Selected FACTS and GUI Results**				λ_{max}	λ_{LRI}	**Loss Reduction**	
	Type	Location	Value				at $\lambda =$	Reduction
300 Bus	SVC	Bus 8	-250.11	MVar	1.13	1.08	1.20	10 MW (0.05%)
	SVC	Bus 152	-54.493	MVar				
	TCSC	Branch 368	-j0.273	Reactance				
	TCSC	Branch 61	-j0.764	Reactance				
	TCVR	Branch 104	0.964	Ratio				
	TCPST	Branch 381	13.386	Degree				
	UPFC	Branch 80	V_{SE} =0.24 Φ_{SE} = 113 I_{SH} = -0.08	p.u. Degree p.u.				

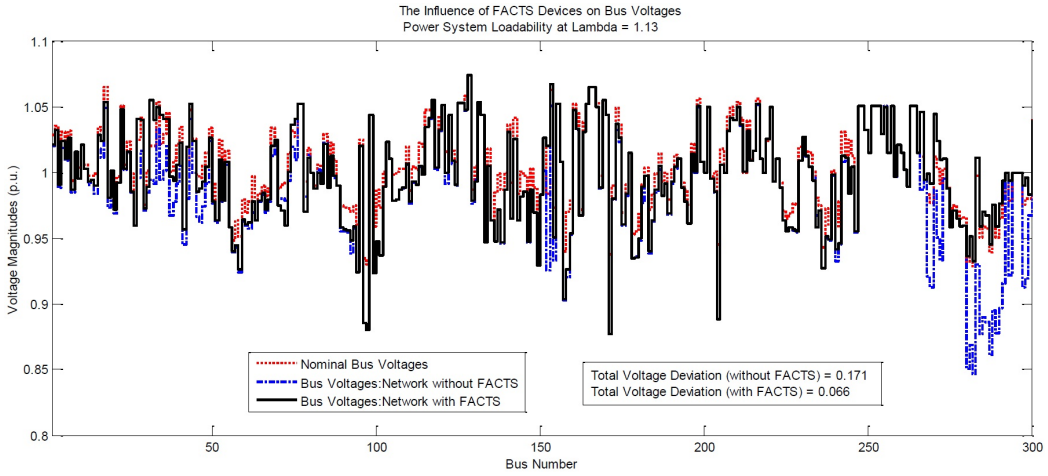

Figure 3.48: Comparing voltages magnitudes of all buses of the 300-bus test system at maximum load factor $\lambda_{max} = 1.13$.

3.6.6 The Analysis for Influence of Energy Storages (SMES) in Power System

In this section, the influence of energy storages (SMES) on power system performance for different networks is presented.

To better understand the effect of SMES (associated with STATCOM), we compare this device with an alone STATCOM. Here in this section, the analysis for one alone STATCOM and one STATCOM with SMES have been done for different power systems. The results are presented in Tables 3.8 and 3.9.

As it is clear from the results of these tables, when the STATCOM device is associated with energy storages (SMES), there is more improvement in loss reduction and maximizing the power system loadability.

Table 3.5: FACTS devices influence on power flows and line losses in the 300-bus test system.

Load Factor	$\lambda_{max} = 1.13$		$\lambda_{user} = 1.34$	
Network Condition	**Without FACTS**	**With FACTS**	**Without FACTS**	**With FACTS**
Total Active Power Flow (MW)	67343	67406	9712	79705
Total Line Losses (MW)	639	637	1032	1003
Loss Reduction Improvement (MW)		2 MW (0.01%)		30 MW (1.5%)

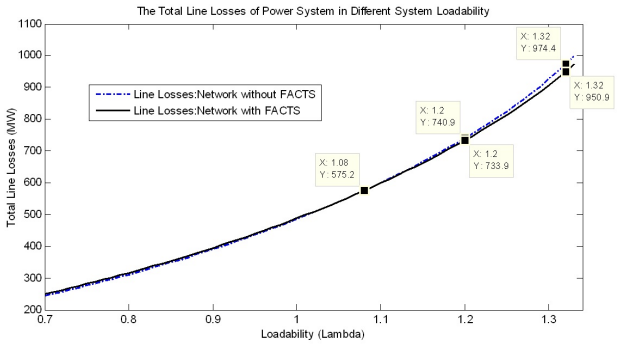

Figure 3.49: Comparing total loss of transmission lines in the 300-bus test system with and without FACTS devices.

3.7 FACTS Devices Placement in Hydro-Québec Network

To demonstrate the capability of the implemented GUI in practical real-world networks, we selected Hydro-Québec network with 884 buses and 650 branches as our final case study. The schematic of the Hydro-Québec network are presented in Figure 3.50.

The MatPower format of this network, which was used for power flow calculations, was obtained from the PSS/E version of the Hydro-Québec network (HQ network) dated January 29, 2010. The total load of this network is 33,654 (MW) and the total power production is 35,474 (MW).

Using the implemented GUI, the effects of different type of FACTS devices on Hydro-Québec network is presented. Since, the SVC is the common-used FACTS device in reality, the analysis will be at first focused on the effect of different number of SVC on HQ network.

Table 3.6: 39-Bus test system with different combination of FACTS devices.

Selected FACTS	**Device Number**	**Values and Locations**			**Loadability**		**Loss Reduction at $\lambda = 1.19$**
		Location	Value		λ_{max}	%	
SVC	1	Bus 20	-70.616	MVar	1.035	3.5%	1 MW (0.015%)
TCSC	1	Branch 14	-j0.67	Reactance	1.04	4%	2 MW (0.031%)
SVC	1	Branch 14	1.026	Ratio	1.04	4%	0 MW (0.0%)
TCSC	1	Branch 44	3.347	Degree	1.02	2%	0 MW (0.0%)
UPFC	1	Branch 16	V_{SE} =0.189 Φ_{SE} =185 I_{SH} =-0.097	p.u. Degree p.u.	1.04	4%	8 MW (0.13%)
SVC	2	Bus 3	-195.613	MVar	1.04	4%	3 MW (0.047%)
		Bus 8	-169.788	MVar			
TCSC	2	Branch 16	-j0.68	Reactance	1.05	5%	3 MW (0.047%)
		Branch 12	-j0.70	Reactance			
TCVR	2	Branch 14	0.880	Ratio	1.04	4%	1 MW (0.015%)
		Branch 10	0.962	Ratio			
TCPST	2	Branch 12	-2.710	Degree	1.02	2%	0 MW (0.0%)
		Branch 29	-3.480	Degree			
UPFC	2	Branch 14	V_{SE} =0.039 Φ_{SE} =80.6 I_{SH} =-0.058	p.u. Degree p.u.	1.04	4%	11.2 MW (0.17%)
		Branch 17	V_{SE} =0.192 Φ_{SE} =267 I_{SH} =-0.065	p.u. Degree p.u.			
All FACTS	5	Branch 12	-133.174	MVar	1.08	8%	4 MW (0.06%)
		Branch 14	-j0.62	Reactance			
		Branch 38	1.107	Ratio			
		Branch 32	13.368	Degree			
		Branch 16	V_{SE} =0.29 Φ_{SE} =210 I_{SH} =0.129	p.u. Degree p.u.			

3.7.1 The Allocation of One SVC in Hydro-Québec Network

For the analysis in this section, since the Hydro-Québec network is a large power system, we set the ranges of the SVC between -600 MVar and +600 MVar while before it was between -300 MVar and +300 MVar. Also, we modified the step size of the load factor (λ) from 0.1 to 0.01. The result of allocation of one SVC is presented in Table 3.10.

For Hydro-Québec network, with ons SVC with the capacity -592.248 MVar allocated in bus number 10 (BCV315) which is located at *Boucherville* city (see Figure 3.50) in *LSERiveSud* area (near Montréal), the maximum load factor was determined as $\lambda_{max} = 1.024$. This means that, with one SVC having the above-mentioned capacity allocated to bus 10, we have 2.4% improvement in the system loadability which is equal to (33654 MW $\times$ 0.024 =) **807.69 MW**.

Table 3.7: The influence of one combination of FACTS devices on different power system.

Test System	**Selected FACTS and GUI Results**				λ_{max}	λ_{LRI}	**Loss Reduction**	
	Type	Location	Value				at $\lambda =$	Reduction
30 Bus	SVC	Branch 23	14.175	MVar	1.42	1.25	1.60	2 MW (1.06%)
	TCSC	Branch 8	-j0.12	Reactance				
	TCVR	Branch 38	1.033	Ratio				
	TCPST	Branch 24	2.119	Degree				
	UPFC	Branch 9	V_{SE} =0.21	p.u.				
			Φ_{SE} = 110	Degree				
			I_{SH} =0.085	p.u.				
57 Bus	SVC	Branch 9	-107.301	MVar	1.16	1.03	1.45	8 MW (0.64%)
	TCSC	Branch 50	-j0.51	Reactance				
	TCVR	Branch 6	1.013	Ratio				
	TCPST	Branch 7	14.650	Degree				
	UPFC	Branch 79	V_{SE} =0.18	p.u.				
			Φ_{SE} =250	Degree				
			I_{SH} =0.123	p.u.				
118 Bus	SVC	Bus 113	-145.529	MVar	1.12	1.17	1.20	5 MW (0.12%)
	TCSC	Branch 60	-j0.56	Reactance				
	TCVR	Branch 155	1.046	Ratio				
	TCPST	Branch 104	-17.659	Degree				
	UPFC	Branch 166	V_{SE} =0.23	p.u.				
			Φ_{SE} =187	Degree				
			I_{SH} =0.075	p.u.				
300 Bus	SVC	Bus 151	-19.023	MVar	1.08	1.09	1.17	2 MW (0.008%)
	TCSC	Branch 148	-j0.27	Reactance				
	TCVR	Branch 244	0.922	ratio				
	TCPST	Branch 81	-6.648	Degree				
	UPFC	Branch 345	V_{SE} =0.24	p.u.				
			Φ_{SE} =156	Degree				
			I_{SH} =0.101	p.u.				

The voltages of buses for the networks with and without FACTS devices at $\lambda_{max} = 1.024$ and $\lambda_{user} = 1.08$ are presented in Figure 3.51(a) and (b). As can be seen from the plots in this Figure, at the same loadability condition, the network without FACTS devices has more voltage drop on the buses. It is an effective demonstration of the significant influence of FACTS devices on keeping the steady-state voltage of buses in the acceptable ranges.

Also, the influence of allocated SVC in Hydro-Québec network on power flow of lines and transmission line losses are presented in Table 3.11.

The total loss of the Hydro-Québec network for different load factors also is presented in Figure 3.52 from which the value of λ_{LRI} with the given set of FACTS devices is determined equal to 0.90 ($\lambda_{LRI} = 0.90$). As it is clear from this figure, at initial condition with the $\lambda = 1.00$ we have 16 MW (0.047%) loss reduction in the network.

Table 3.8: The influence of one STATCOM (or SVC) on different power system.

Device	**One STATCOM (or SVC)**					
Test System	**Location**	**Value**	λ_{max}	λ_{LRI}	**Loss Reduction**	
					λ	Red.
9 Bus	Bus 4	-130 MVar	1.45	1.05	1.40	0.4 MW
					1.80	1.5 MW
24 Bus	Bus 10	-205 MVar	1.20	1.03	1.20	1 MW
					1.60	6 MW
30 Bus	Bus 6	-111 MVar	1.32	1.64	1.90	0.31 MW
					2.00	0.50 MW
57 Bus	Bus 38	-86 MVar	1.11	0.43	1.00	3 MW
					1.40	14 MW
300 Bus	Bus 266	-283 MVar	1.05	0.88	1.00	2 MW
					1.20	9 MW
Hydro-Québec Network	Bus 10	-592 MVar	1.024	0.90	1.00	16 MW
					1.024	27 MW

Finally, the influence of the allocated SVC on the VBL term of the fitness function is also presented in Figure 3.53.

We have repeated the allocation of one SVC device several times and in all of them the optimal location was determined in the areas around Montréal city. To show how far the result of the implemented GUI for one SVC is acceptable, let us compare the effects of the GUI-allocated SVC with the two most recent SVC locations determined by Hydro Québec experts. These locations are near the Montréal area at *Chénier* (bus 23:CHE315) and *Bout-de-lile* (bus 51:BDL315) with ratings of -600 MVar for each. The number 315 refers to the nominal voltage of local buses. For a more specific comparison of the results, we set the value of the actual SVCs at -592.48 MVar instead of -600 MVar. The results are presented in Table 3.12. As can be seen from this table, the influence of the actual SVCs at buses 23 and 51 physically installed (*Chénier*) or planned (*Bout-de-lile*) in the Hydro-Québec network is very much the same and similar to the results of the GUI-allocated SVC at bus 10. While the maximum loadability for real SVCs is $\lambda_{max} = 1.022$ and $\lambda_{max} = 1.023$, for the GUI allocated SVC this value is $\lambda_{max} = 1.024$. We have close results also on λ_{LRI} values and loss reduction improvements.

The results presented in this table show that the implemented GUI is effective in real-world problems. It was clever enough to find a suitable location for an SVC of approximately -600 MVar near a big load such as the city of Montréal in which we already had the same size of SVC physically installed.

Table 3.9: The influence of one STATCOM with SMES on different power system.

Device	**One STATCOM with SMES**					
Test System	**Location**	**Value**	λ_{max}	λ_{LRI}	**Loss Reduction**	
					λ	Red.
9 Bus	Bus 9	-62 MVar	1.49	0.4	1.40	1.5 MW
		-175 MW			1.80	4 MW
24 Bus	Bramch 2	-187 MVar	1.34	1.00	1.20	0.1 MW
		-86 MW			1.60	1 MW
30 Bus	Bus 6	-69 MVar	1.35	0.34	1.00	0.5 MW
		-152 MW			2.00	2.5 MW
57 Bus	Bus 18	-67 MVar	1.14	0.10	1.00	12 MW
		-34 MW			1.40	29 MW
300 Bus	Bus 140	-74 MVar	1.10	1.08	1.20	4 MW
		-63 MW			1.30	10 MW
Hydro-Québec Network	Bus 538	-531 MVar	1.024	0.90	1.00	13 MW
		-208 MW			1.024	23 MW

Table 3.10: FACTS placement results for one SVC in Hydro-Québec network.

Test System	**Selected FACTS and GUI Results**			λ_{max}	λ_{LRI}	**Loss Reduction**	
	Type	Location (Area)	Value			at $\lambda =$	Reduction
Hydro-Québec Network	SVC	Bus 10 (BCV315) (LSERiveSud)	-592 MVar	1.024	0.90	1.00	16 MW
						1.024	26.5 MW

3.7.2 The Allocation of Two SVC in Hydro-Québec Network

In this section, as the second case study for Hydro-Québec network we will perform the allocation process for two SVC's. The results are presented in Table 3.13.

As it is shown in Table 3.13, with two SVC's with allocated in buses 11 and 552 which are in *LSELaval* and *LSEMontréal* area, the maximum load factor was determined as $\lambda_{max} = 1.033$. This means that we have 3.3% improvement in the system loadability which is equal to (33654 MW $\times$ 0.033 =) **1110.6 MW**.

The effects of allocated SVCs in Hydro-Québec network on power flows of lines and transmission line losses are also presented in Table 3.14.

From the information of Tables 3.13 and 3.14 we could mention that in initial condition with the $\lambda = 1.00$ we have 26 MW (0.08%) and in the $\lambda = 1.033$ we have 49 MW (0.015%) loss reduction in the network.

The voltages of buses for the networks with- and without FACTS devices for $\lambda_{max} =$

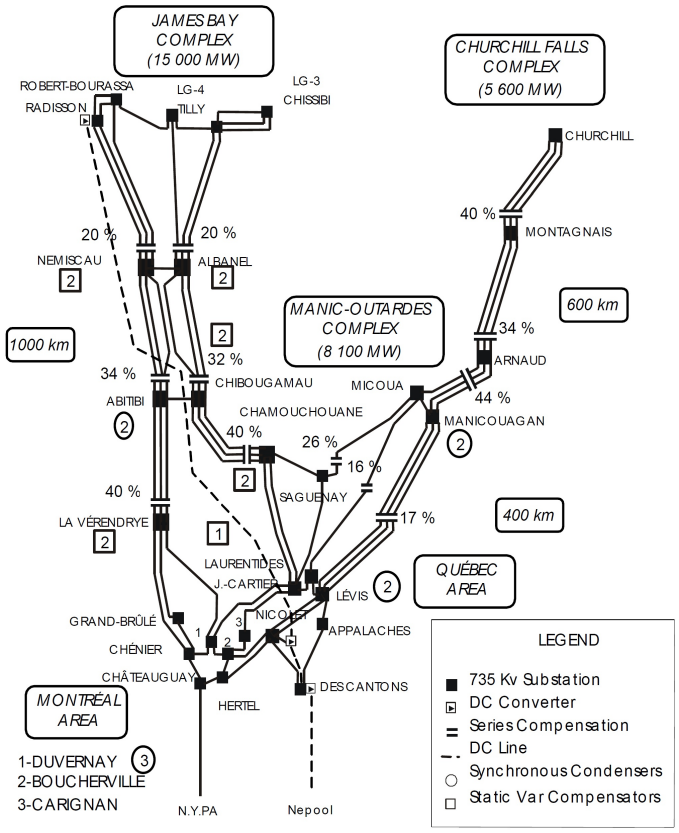

Figure 3.50: The schematic of Hydro-Québec network.

1.033 is presented in Figure 3.54. Again, it is shown the influence of FACTS devices on keeping the voltage of buses in the acceptable ranges. At the same loadability condition, the network without FACTS devices has a greater voltage drop on buses.

3.7.3 The Allocation Results of Different Number of SVC's in Hydro-Québec Network

In this section, by repeating the similar simulations as we have done in previous sections, the effects of different number of SVC in Hydro-Québec network are analyzed and compared. The comparison between different number of SVC for power system loadability is presented in Figure 3.55(a). As it can been from this figure, by inserting 3, 4 or 5 SVC comparing with 2 SVC, there is not any significant improvement in system loadability. Therefore, the optimum number of SVC for Hydro-Québec network is 2 devices.

The improvement on the voltage deviation reduction at maximum loadability condition is also presented in 3.55(b) from which it is clear that by increasing the number of SVC, there would be more reduction in voltage deviation of buses. The definition of absolute voltage deviation was presented in (3.47).

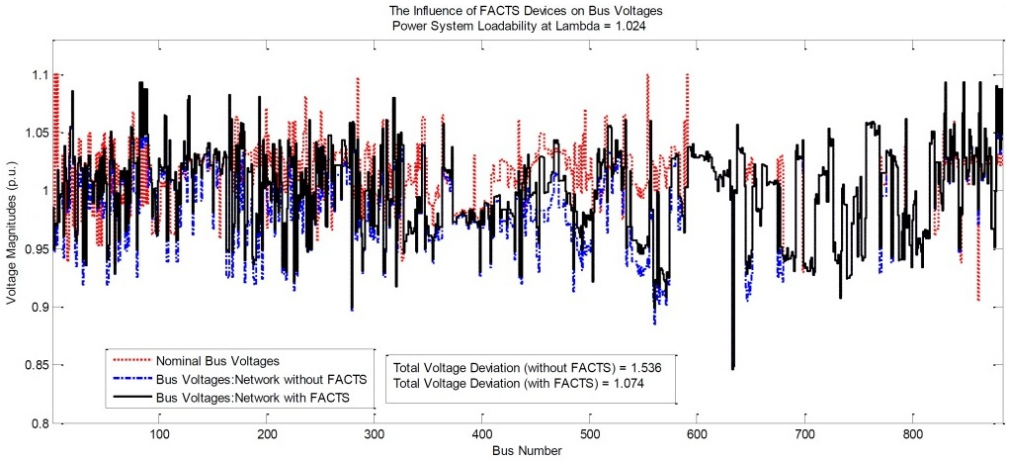

(a)

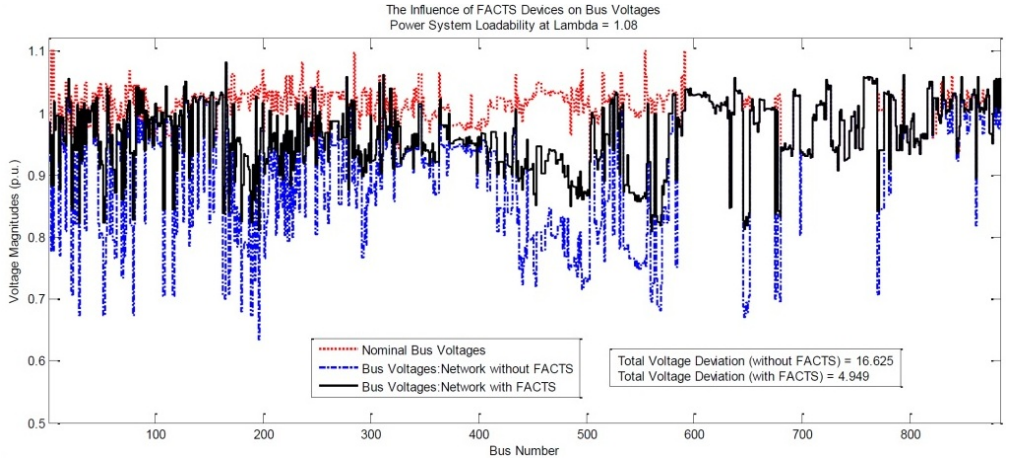

(b)

Figure 3.51: Comparing voltages magnitudes of all buses of Hydro-Québec network at: (a) Maximum loadability condition $\lambda_{max} = 1.024$. (b) Load factor selected by user $\lambda_{user} = 1.08$.

Also, Figure 3.56 presents the effect of different number of SVC on loss reduction of transmission lines. Figure 3.56(a) shows the loss reduction at initial load factor $\lambda = 1.00$, while Figure 3.56(b) shows it at maximum load factor. As we have observed for system loadability, here also considering the loss reduction of transmission lines, the optimum number of SVC in Hydro-Québec network is 2 devices.

3.7.4 The Allocation of Different Type of FACTS Devices in Hydro-Québec Network

In this section the effects of different type of FACTS devices, comparing one and two devices for each of them, are presented in Hydro-Québec network. These simulation are

Table 3.11: Effects of One SVC on power flows and line losses in Hydro-Québec network.

Load Factor	$\lambda_{max} = 1.024$		$\lambda_{user} = 1.08$	
Network Condition	**Without FACTS**	**With FACTS**	**Without FACTS**	**With FACTS**
Total Voltage Deviation	1.536	1.046	16.625	4.828
Total Active Power Flow (MW)	287761	287784	301177	303103
Total Line Losses (MW)	1761	1739	2316	2080
Loss Reduction Improvement (MW)		22 MW (0.06%)		236 MW (0.7%)

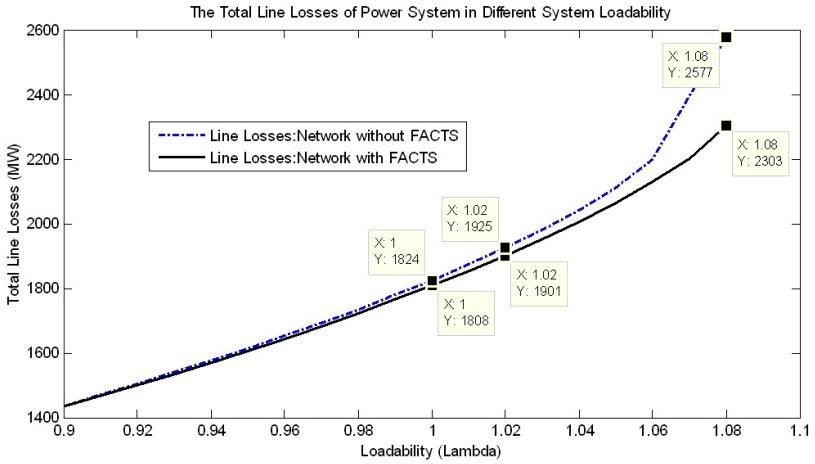

Figure 3.52: Comparing total loss of transmission lines of Hydro-Québec network with and without SVC.

executed to analyze the effects of different FACTS devices on system loadability and loss reduction.

For example, comparing the effects of different FACTS devices on maximizing the power system loadability is presented in Figure 3.57(a). As it is clear from this plot, with allocating the UPFC the maximum load factor is $\lambda_{max}^{\text{UPFC}} = 1.028$ while for the SVC it is $\lambda_{max}^{\text{SVC}} = 1.024$. The TCPST has minimum effect on maximizing the system loadability comparing with other FACTS devices.

Comparing the influence of different type of FACTS devices on reduction of voltage deviation, at maximum load factor λ_{max}, is also presented in 3.57(b). It can be seen from this figure that both the UPFC and the TCVR are the most effective devices to reduce the voltage deviation of buses.

The effects of different type of FACTS devices on loss reduction of transmission lines are presented in Figure 3.59. Figure 3.58(a) shows the loss reduction at initial load factor

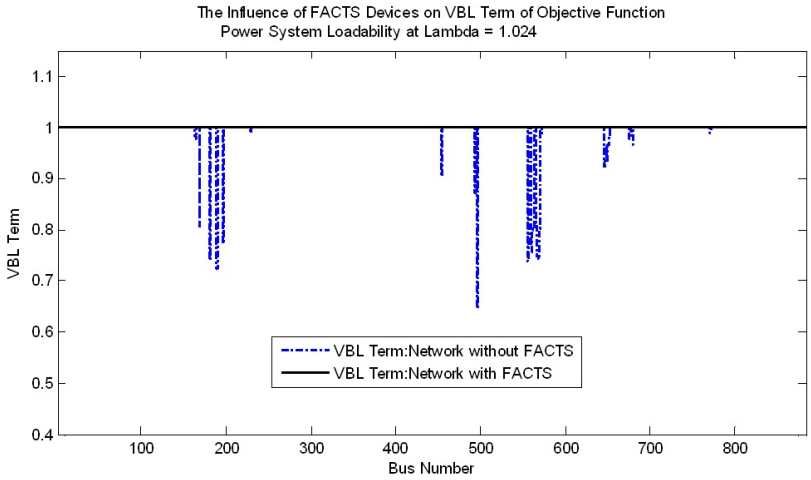

Figure 3.53: Effects of SVC on VBL term of fitness function for Hydro-Québec network.

Table 3.12: FACTS placement results for one SVC in Hydro-Québec network.

Test System	**Selected FACTS and GUI Results**			λ_{max}	λ_{LRI}	**Loss Reduction**	
	Type	Location (Area)	Value			at $\lambda =$	Reduction
Hydro-Québec Network	SVC	Bus 10 (BCV315) (LSERiveSud)	-592 MVar	1.024	0.90	1.00	16 MW
						1.024	26.5 MW
Hydro-Québec Network	SVC	Bus 51 (BDL315) (LSEMontréal)	-592 MVar	1.022	0.90	1.00	14 MW
						1.024	24.5 MW
Hydro-Québec Network	SVC	Bus 23 (CHE315) (LSELaval)	-592 MVar	1.023	0.85	1.00	21 MW
						1.024	33.5 MW

$\lambda = 1.00$, while Figure 3.58(b) shows the same objective at maximum load factor λ_{max}. As it is clear from these plots, considering the loss reduction, the UPFC is the most effective device and it comes back to this fact that the UPFC device is actually consists both shunt and series FACTS devices.

The above plots and analysis were related to comparing between one device of each FACTS. In following, the same analysis will be presented for two devices of different type of FACTS. Using the analysis in this part, not only we can compare the effects of a two-devices set for all FACTS, but also for each specific FACTS device we can compare the influence between one and two device. For example, near the comparing 2 UPFC with 2 SVC, we can analyze also the effects of 1 UPFC and 2 UPFC at the same graph. After this description, we can now present comparing the effects of different FACTS devices (with two devices) on maximizing the power system loadability in Figure 3.59(a).

As it is clear from this graph, the maximum load factor with allocating the 2 UPFC is $\lambda_{max}^{\text{UPFC}} = 1.036$ while for the 2 SVC it is $\lambda_{max}^{\text{SVC}} = 1.033$. It is interesting that with increasing the number of TCPST from 1 to 2, there is not any improvement in the power system loadability. Also, the graph related to the reduction of voltage deviation at maximum load

Table 3.13: FACTS placement results for two SVC in Hydro-Québec network.

Test System	**Selected FACTS and GUI Results**			λ_{max}	λ_{LRI}	**Loss Reduction**	
	Type	Location (Area)	Value			at $\lambda =$	Reduction
Hydro-Québec	SVC	Bus 11 (LSELaval)	-581 MVar	1.033	0.88	1.00	26 MW
Network	SVC	Bus 552 (LSEMontréal)	-538 MVar	1110 (MW)		1.033	49 MW

Table 3.14: Effects of two SVCs on power flows and line losses in Hydro-Québec network.

Load Factor	$\lambda_{max} = 1.033$		$\lambda_{user} = 1.08$	
Network Condition	**Without FACTS**	**With FACTS**	**Without FACTS**	**With FACTS**
Total Voltage Deviation	1.90	0.84	16.625	2.512
Total Active Power Flow (MW)	290225	290147	301177	302959
Total Line Losses (MW)	1998	1949	2577	2231
Loss Reduction Improvement (MW)		49 MW (0.15%)		346 MW (1.03%)

factor is presented in 3.59(b).

The effects of different type of FACTS devices on loss reduction of transmission lines are presented in Figure 3.60. While Figure 3.60(a) shows the loss reduction at initial load factor $\lambda = 1.00$, Figure 3.60(b) presents it at maximum load factor λ_{max}. As we have seen before, considering the loss reduction the UPFC is the most effective device between all different type of FACTS. We should also mention that, by increasing the number of UPFC from 1 to 2 there is not any improvement in reducing the losses in transmission lines. Finally it is clear, the TCVR has the most improvement in loss reduction by adding the number of device from 1 to 2. Considering loss reduction, there is not any difference between 1 or 2 devices for TCPST.

3.8 Discussion

The step size of the load factor at each iteration of the optimization process is equal to 0.01. This means that, after finding a successful configuration at a specific load factor with the zero value for (Fit) in (3.42), the algorithm increases the current load factor by the value of 0.01.

The total simulation run time for a given set of FACTS device in a specific power

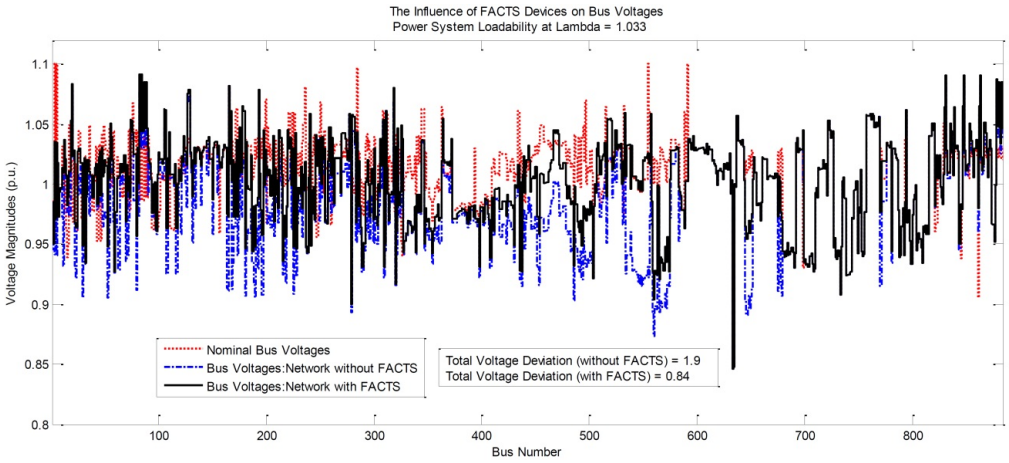

Figure 3.54: Comparing voltages magnitudes of all buses of Hydro-Québec network at Maximum loadability condition $\lambda_{max} = 1.033$.

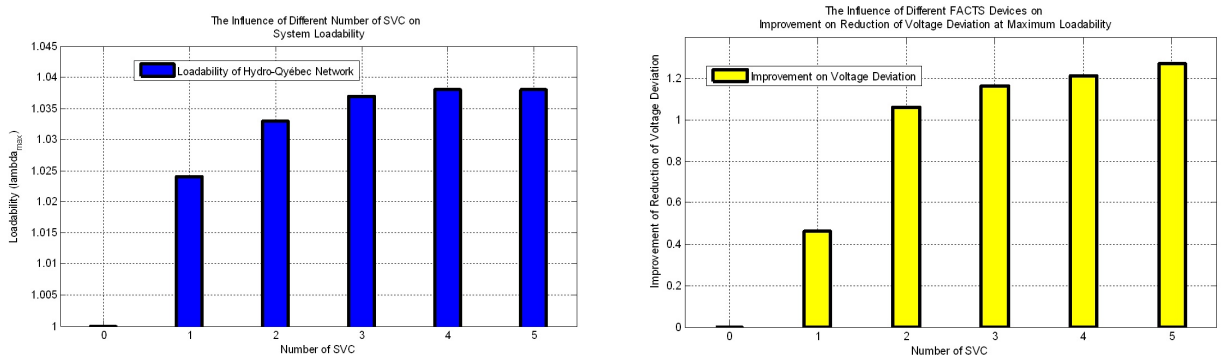

(a) (b)

Figure 3.55: Comparing the influence of different number of SVC on: (a) Maximizing power system loadability. (b) Reduction of total voltage deviation (TVD).

network depends on the initial load factor and is the total combination of all iterations. Also, the simulation run time at each iteration is related to different parameters such as the size of the network, the number of genetic algorithm generations (GA) and the initial population of GA.

The size of the network (number of buses as well as number of branches) has a large influence on the simulation run time since the optimization process needs to calculate the fitness function for each individual at each generation. This is particularly true since the size of the matrix (Fit) defined in (3.42) is related to the number of buses and branches. At each iteration of the allocation process, the fitness value should be calculated for all individuals of the current generations.

As an example, let us compare two case studies presented in the chapter. With an initial GA population equal to 1000, for the 57-bus test system, the simulation running

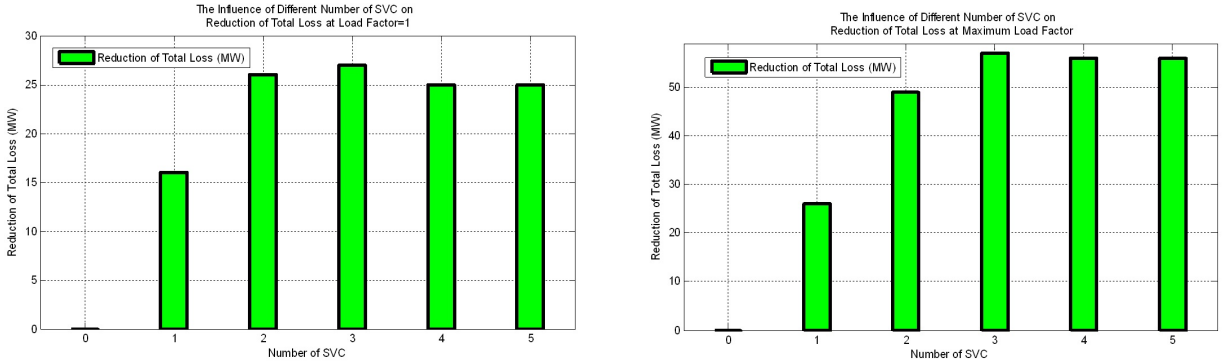

(a) (b)

Figure 3.56: Comparing the influence of different number of SVC on loss reduction of transmission lines at: (a) Initial load factor $\lambda = 1$. (b) Maximum load factor λ_{max}.

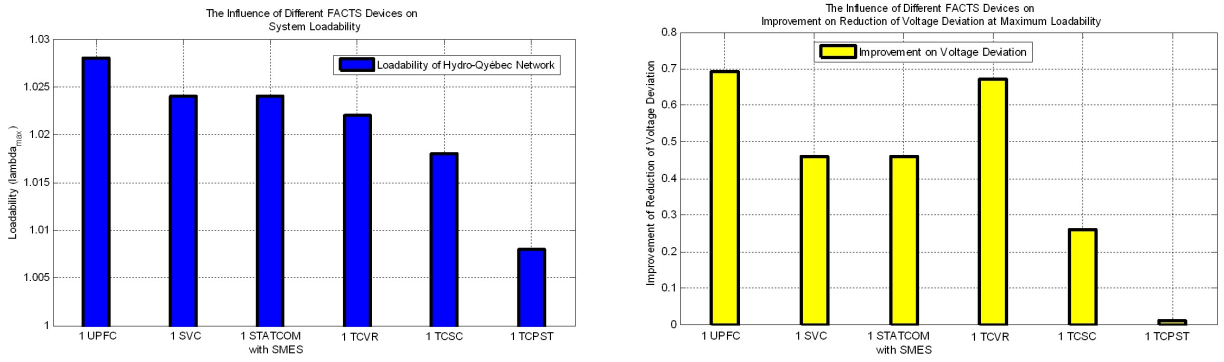

(a) (b)

Figure 3.57: Comparing the influence of different type of FACTS devices on: (a) Maximizing power system loadability. (b) Reduction of total voltage deviation.

time takes around 5 minutes while for the 300-bus test system it is 24 minutes. All the simulations were done on a two-core Intel Toshiba laptop running at 2.53 GHz with 4.00 GB of RAM memory.

Regarding the objective function, we should mention that in the first version of GUI, we only considered maximizing power system loadability as our objective function. However, as presented in the results of this chapter, we observed loss reduction in some cases even when the objective function was maximizing loadability. But for the next version of GUI, we could consider other objective functions such as minimizing the transmission line losses or minimizing the cost of FACTS devices at a given load factor or under a maximum loadability condition. In this case, the implemented GUI could be modified in such a way that the user can select the desired objective function before starting the allocation process.

The benefits of the optimal placement of FACTS devices in dynamic issues could be expressed as follows. Normally, the decision to install a FACTS device is often taken at

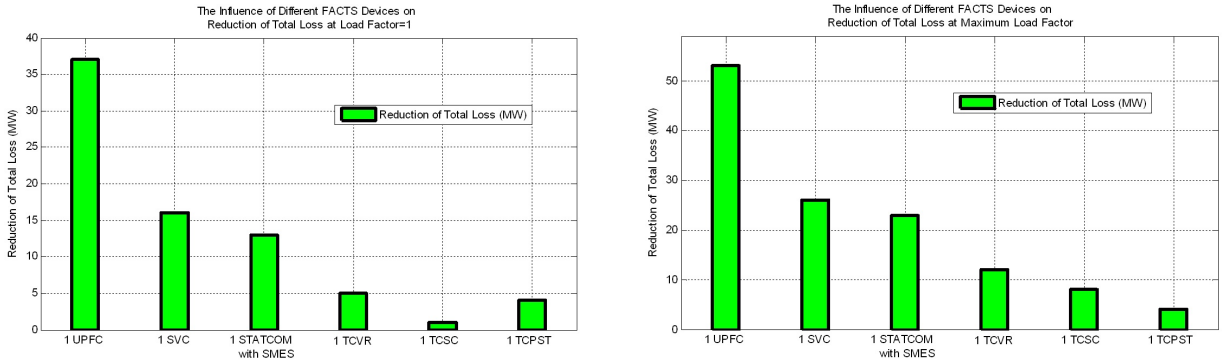

(a) (b)

Figure 3.58: Comparing the influence of different type of FACTS devices on loss reduction of transmission lines at: (a) Initial load factor $\lambda = 1$. (b) Maximum load factor λ_{max}.

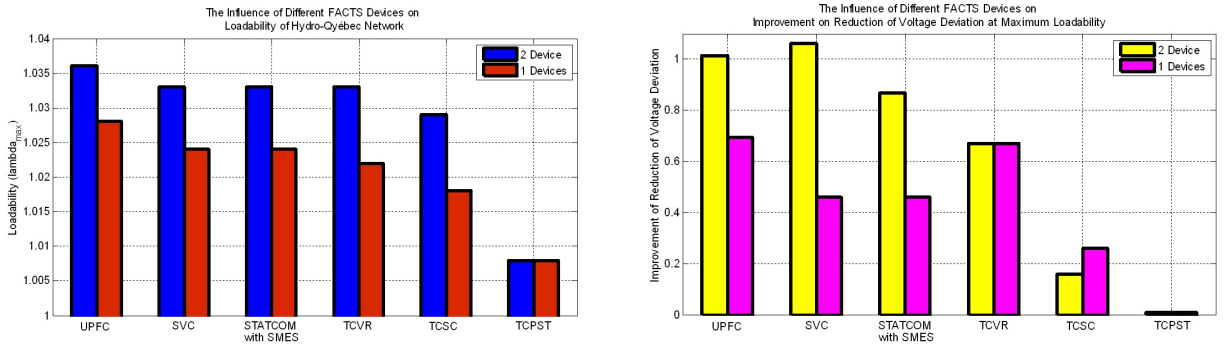

(a) (b)

Figure 3.59: Comparing the influences of different type of FACTS devices on: (a) Maximizing power system loadability. (b) Reduction of total voltage deviation (TVD).

a planning stage when the system planner needs to accommodate load growth and power plant integration. Therefore, the natural question will be as follows: Do we need to build a line or can we do it with a FACTS device? This is why we initially focused on FACTS as a loadability tool.

However, if the goal is to improve the system‘s dynamic performance, we can use the proposed GUI as a screening tool to first select m suitable locations which are optimal from the steady-state viewpoint. Then a more focused study is performed on this subset of m FACTS to select a reduced number of n locations which are well suited for both loadability and dynamic performance.

More generally, the first step in wide-area control design could be finding the suitable location for a FACTS device using this toolbox. The next step would be to design and implement the supplementary controller for power oscillation damping involving those FACTS as we have done in this thesis.

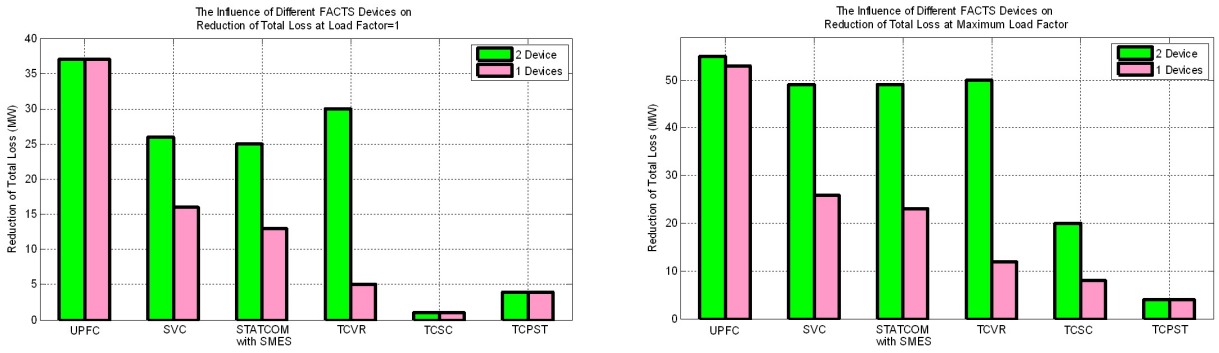

(a) (b)

Figure 3.60: Comparing the influence of different type of FACTS devices on loss reduction of transmission lines at: (a) Initial load factor $\lambda = 1$. (b) Maximum load factor λ_{max}.

3.9 Summary

This chapter presented a Graphical User Interface (GUI) based on genetic algorithm (GA) to seek the optimal locations and values of a given set of FACTS devices for more efficient use of power system assets. In this user-friendly framework, called the FACTS Placement Toolbox, the user has the opportunity to choose the power system network, determine the GA settings and select the number and types of FACTS device to be allocated in the network. Six different FACTS devices are used in this GUI: SVC, TCSC, TCVR, TCPST, UPFC and STATCOM with SMES. The simulation results show that the FACTS placement toolbox is effectively applicable to find the optimal locations and values of the given multi-type FACTS devices mix in a given power system so as to maximize the system loadability under security constraints. Quite expectedly, the UPFC turned out to be the most effective FACTS if we want to increase the loadability while reducing the losses at the same time, even though the latter criterion was not part of the optimization process. Finally, to show the capability of the implemented GUI in practical real-world case studies, the results of FACTS devices allocation in the Hydro-Québec network were presented.

Chapter 4

Implementing a FACTS-based Power Oscillation Damping Controller Using Wide-Area Signals

This chapter as the final step of thesis, presents the implementing of the FACTS-based power oscillation damping controller using wide-area signals. This wide-area controller receives the estimated rotor angles, available from the results of step 1, and other information from all over the network, and then modifies the set points of optimized local FACTS device controllers. The location of the FACTS device will be determined using the method presented in step 2 in chapter 3.

One of the most important issues for power system security is to effectively damp the power system oscillations in order to enhance transient stability and improve dynamic performance. Traditionally, oscillations have been damped by Power System Stabilizer (PSS). In recent years, FACTS devices combined with a supplementary controller, known as a Power Oscillation Damper (POD), have been also used to damp low-frequency oscillations in power systems. In this paper, a multi-step plan is developed to implement a Wide-Area Power Oscillation Damping (WA-POD) controller of a UPFC in 14-bus test system. The first step of this plan is to find the optimal location for the UPFC to maximize power system loadability; the second step is to estimate the dynamic states of the synchronous generators; and the third step is to implement the WA-POD controller using the states estimated in step two. The estimated rotor angles are used to provide the input signal of the WA-POD controller while the estimated rotor speed deviations will be used for an off-line parameter tuning of both PSS and WA-POD using the genetic algorithm. Different types of faults are applied to the network to compare the performance of the traditional PSS and the WA-POD controller in the 14-bus test system. Simulation results show the effectiveness of the implemented WA-POD controller in damping low-frequency oscillations and improving the dynamic performance of the system.

4.1 Literature Review

Rapid growth in power demand, combined with the need to reduce generating costs, are making power systems increasingly complex to operate and less secure against contingencies. To enhance and improve power system security, in addition to traditional local controllers such as PSSs and AVRs, FACTS devices are employed to control power systems more effectively and also to maximize their capability [1].

Flexible AC Transmission Systems (FACTS) devices firstly could help to enhance power system security under steady-state conditions. Secondly, they would also improve dynamic and/or transient stability by using a supplementary controller, called a Power Oscillation Damper (POD). While local oscillations are damped by a local controller such as a PSS, inter-area oscillation could be damped by FACTS devices. Because of their fast response, FACTS controllers can improve the stability of the power network by helping the critical generators give away the excess energy gained through acceleration during a fault [10, 81].

In recent years, wide-area measurement systems (WAMS), which include Phasor Measurement Units (PMUs) installed in suitable locations and synchronized by a Global Positioning System (GPS), are being adopted rapidly worldwide to monitor and control large power systems and improve their security [2, 81, 82, 83]. Technological improvements

in phasor measurement and data communication have enabled utilities to employ remote feedback signals for effective damping of power oscillation. As a result, by using wide-area measurement signals, wide-area power oscillation damping (WA-POD) control would be more effective and capable in damping local and inter-area oscillations [82, 84, 85, 86]. For example, in [86] and [87] it is shown that for the Hydro-Québec network, wide-area control is very effective in stabilizing a large power system under various operating conditions.

Many researchers have achieved good results by applying wide-area measurements to the POD controller for oscillation damping. In [88] an adaptive phasor power oscillation damping controller (ADPOD), which uses wide-area measurement signals considering time-delay in remote feedback control signals, is presented. In [89] a robust TCSC wide-area damping controller (WADC) is designed to enhance power system stability. Also, the authors in [90] developed a systematic procedure of designing a centralized WADC system for inter-area oscillation damping by putting emphasis on signal selection and control system structure assignment. In [91] a power oscillation damping controller is presented using wide-area measurements applied to a single static var compensator (SVC). Another contribution in this area has been done in [92] for developing a wide-area phasor power oscillation damping controller for TCSC,taking into account the time-delay in the wide-area measurement signals. In [93] the design and implementation of an optimal neuro-controller for a UPFC is presented and the wide-area signals in the power system are used to provide auxiliary control to a UPFC in order to achieve enhanced damping of system oscillations.

We should also mention that in some researches studies the idea of using wide-area measurement signals is developed for global or supervisory PSS (SPSS). An SPSS is employed for oscillatory damping in an area that includes multiple generators by using wide-area measurement signals over the entire network (or in a specific area), while a local PSS is used in a power plant for local oscillation damping [94]. For example in [85, 95] an SPSS that uses global signals in addition to local control signals is designed for damping inter-area oscillations. In [82] a similar technique is applied by incorporating additional remote signals into a selected number of PSSs in Hydro-Quebec's network in a decentralized/ hierarchical structure for a wide-area control system. In addition, in [96] an SPSS is designed based on the robust fuzzy logic using wide-area measurement signals.

The goal of this chapter is to present a multi-stage plan for setting up a UPFC-based wide-area power oscillation damping controller to enhance power system stability. The first step of this plan is to find the optimal location for the UPFC to maximize power system loadability. The second step is to estimate the local dynamic state of the generators' internal signals using the phasor measurement units installed in their terminal buses. The third and final step is to develop the WA-POD controller using the previously estimated signals of rotor speed deviations and rotor angles.

This chapter is organized as follows. A short description of the 14-bus test system, i.e. the power system under study, is given in section 4.2. In section 4.3, the structure and parameter tuning of both the PSS and the WA-POD will be presented. In section 4.4, a brief description about the implemented multi-stage plan is given. Section 4.5 presents a brief explanation about the procedure of optimal allocation of UPFC to maximize the power

system loadability. The dynamic state estimation of the power system for generating the estimated states of the synchronous machines is presented in Section 4.6. Section 4.7 gives a short description about the implemented wide-area power oscillation damping (WA-POD) controller in the 14-bus test system using PSAT software. Section 4.8 and 4.9 includes the simulation results and eigenvalue analysis respectively. Section 4.10 presents a summary of the chapter.

4.2 Multi-Machine Power System

The behavior of a dynamic system, such as a power system networks, may be represented by set of n first order non-linear ordinary differential equations (DAE) in the following form as (4.1) [1, 97, 98]:

$$\begin{aligned} \dot{\mathbf{x}} &= \mathbf{f}(\mathbf{x}, \mathbf{y}, \mathbf{u}) \\ \mathbf{0} &= \mathbf{g}(\mathbf{x}, \mathbf{y}, \mathbf{u}) \\ \mathbf{w} &= \mathbf{h}(\mathbf{x}, \mathbf{y}, \mathbf{u}) \end{aligned} \tag{4.1}$$

where $\mathbf{x} \in R^n$ is the vector of the state variable associated with the dynamic states of the generators, loads, and other system controllers; $\mathbf{y} \in R^m$ is the vector of algebraic variables such as bus voltage magnitudes and phase angles; $\mathbf{u} \in R^l$ is a set of controllable parameters such as tap and AVR settings, or controller reference signals; $\mathbf{w}$ is a set of output variables such as line current flows; $\mathbf{f}$ is a set of differential equations that represents system and controller dynamics; $\mathbf{g}$ is a set of algebraic equations that represents the transmission network power flows; and $\mathbf{h}$ is a set of equations that represents output variables (e.g., measurements), such as line power flows and rotor angles speeds [1, 97, 98].

The modeling and structure of the POD and PSS controllers can be analyzed based on the linearized system of the power network. Therefore, the linearized system of equations given in (4.1) are presented as follows:

$$\begin{aligned} \Delta\dot{\mathbf{x}} &= \mathbf{A}\Delta\mathbf{x} + \mathbf{B}\Delta\mathbf{u} \\ \Delta\mathbf{w} &= \mathbf{C}\Delta\mathbf{x} + \mathbf{D}\Delta\mathbf{u} \end{aligned} \tag{4.2}$$

where $\mathbf{A}$ is the state or plant matrix, $\mathbf{B}$ is the control or input matrix, $\mathbf{C}$ is the output matrix and $\mathbf{D}$ is the feedforward matrix. The details of the linearization and the definition of matrices $\mathbf{A}$, $\mathbf{B}$, $\mathbf{C}$ and $\mathbf{D}$ are presented in [1].

The stability concepts of power system can be expressed based on linear system techniques such as Lyapunov's methods and eigenvalues analysis. As a result, the linear presentation of the power system presented in (4.2) is the base for the controller and stabilizer structure and design even if the test system devices, topology and/or the elements of $\mathbf{A}$, $\mathbf{B}$, $\mathbf{C}$ and $\mathbf{D}$ change in size or elements.

Here in this study, the 14-bus test system, presented in Figure 4.1, is the case study for the simulations analysis in PSAT [99] software. Detailed information about this network is

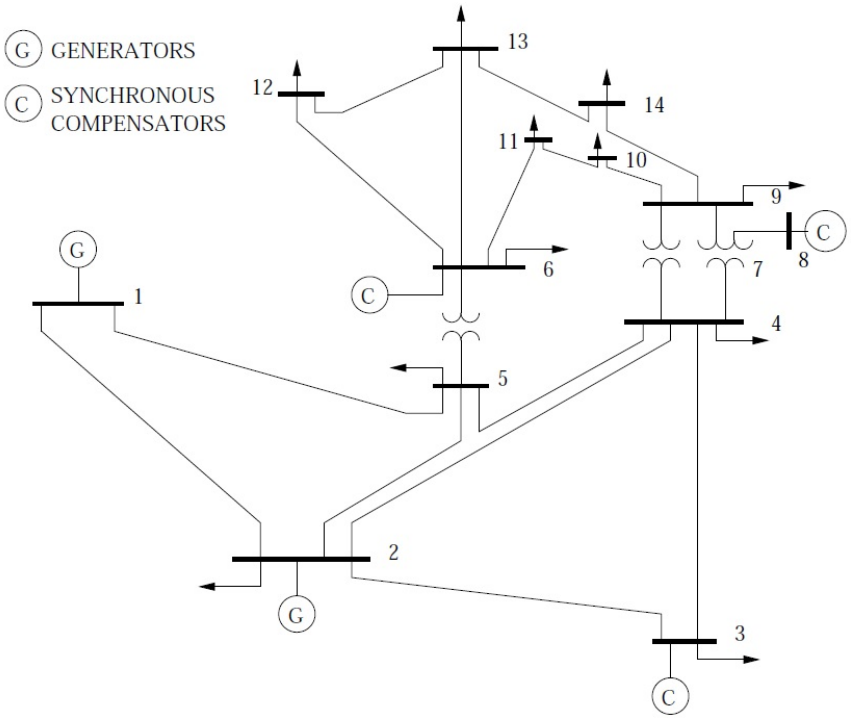

Figure 4.1: Multi-machine power network: the 14-bus test system.

available online [80] and presented in Appendix E.2. The total generating capacity of this network is 272 MW while the total load is 259 MW. This network includes two generation buses and three synchronous compensator with total compensation rates of 53 MVar. For the stability simulations, the network will include one PSS at bus 1 (slack bus) and one UPFC, allocated optimally in the network, associated with a POD as a supplementary controller.

4.3 Structure and Parameter Tuning of PSS and POD Controllers

The principal function of a power system stabilizer (PSS) is to add damping to the generator rotor oscillations by using auxiliary stabilizing signals to control excitation using auxiliary stabilizing signals. A PSS controller can be expressed as an additional block of generator excitation control (AVR), added to improve overall dynamic performance, especially by controlling electromechanical oscillations. The PSS uses supplementary stabilizing signals such as shaft speed, terminal frequency and/or power to change the input signal of the AVR [1].

The block diagram of the PSS controller is shown in Figure 4.2; it involves a gain block with gain K_{PSS}, a signal wash-out block with washout time constant T_w, two lead-lag

blocks with time constants T_1, T_2, T_3 and T_4 and an anti-windup limiter with time constant T_r. The lead-lag blocks supply the suitable phase-lead characteristics to compensate lag between the exciter input and the generator electrical torque [1].

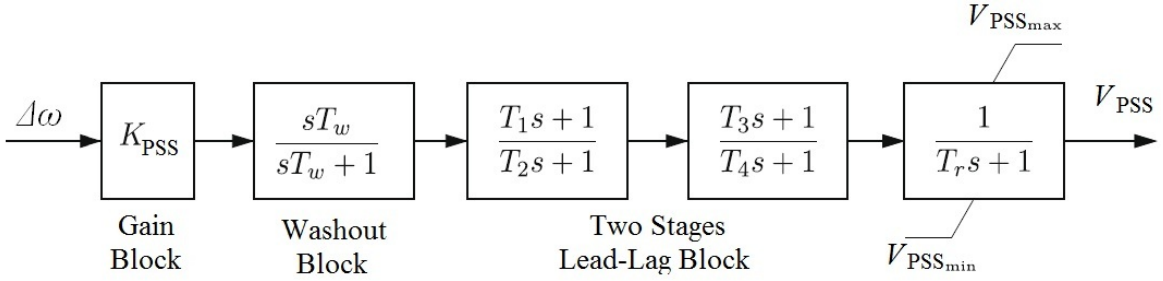

Figure 4.2: Block diagram of power system stabilizer (PSS) controller.

The structure of the POD controller of the UPFC is same as the PSS structure as shown in Figure 4.2 with similar parameters: gain K_{POD}, washout time constant T_{wf}, the time constants of lead-lag blocks T_{1f}, T_{2f}, T_{3f} and T_{4f} and the time constant of an anti-windup limiter T_{rf}.

As can be seen in Figure 4.5, the parameters of the POD and PSS controllers are tuned by an off-line genetic algorithm-based block using the estimated rotor speed deviations of generators 1 and 2. Therefore we have a total of 14 parameters which could be tuned using a genetic algorithm optimization process. In order to formulate the optimization process, the objective function of the genetic algorithm which should reflect small steady state error and oscillation damping could be presented as (4.3):

$$J = \int_{t=0}^{T} \left(|\Delta\omega_1| + |\Delta\omega_1|\right) t \tag{4.3}$$

where $\Delta\omega_1$ and $\Delta\omega_2$ are the speed deviations of generators 1 and 2 following a disturbance and T is the time range of simulation. The constraints of the above objective function, J in (4.3), are the bounds of the controller's parameters.

As it was explained in previous chapter, the genetic algorithm repeatedly modifies a population of individual solutions to minimize a pre-defined objective function. At each step, the genetic algorithm selects individuals randomly from the current population to be parents and uses them to produce the children for the next generation. The highly fit individuals that are those with higher fitness value have more opportunities to reproduce through recombination operation such as mutation, crossover and elite child. This routine continues until a stop criterion such as number of generations or fitness limit is achieved.

The final goal of the optimization process is to minimize the objective function J in (4.3) with respect to problem constraints in order to find the optimal values for parameters of PSS and POD controllers. The objective function is evaluated for each individual of the current generation of GA by simulating the developed dynamic system in PSAT software by applying a disturbance. When the minimum value for the objective function

Table 4.1: Setting parameters of genetic algorithm.

Setting Parameter	**Value/Type**
Maximum Generation	30
Population Size	50
Crossover Fraction	0.7
Termination	Maximum Generation
Number of Elite Child	6
Mutation Type	@mutationadaptfeasible
Crossover Type	@crossovertwopoint
Selection Type	@selectionroulette

is determined, the corresponding individual represents the optimal solution of the problem [75]. To calculate the objective function we should use the m-file converted version of the implemented Simulink file. The details of this conversion and using the converted m-file to calculate the objective function of genetic algorithm are presented in Appendix D.

By applying the genetic algorithm to the optimization problem, the setting parameters of the genetic algorithm should be also specified. For our simulations, the setting parameters of the genetic algorithm are presented in Table 4.1. The definitions and descriptions of these parameters can be found in [75, 76].

In addition of setting the parameters of the genetic algorithm, we must determine the bounds of the controller's parameters. The bounds of the WA-POD and PSS parameters (our unknown parameters) are presented in Table 4.2.

The total optimization procedure is terminated when the algorithm reaches the maximum number of generations. The best individual of the final generation is the optimal solution for the controller's parameters. The optimized parameters of the PSS and POD controller in the 14-bus test system are presented in Table 4.3.

In this study a three-phase short circuit is applied at bus 2 at t=1.00 (sec) and cleared at t=1.1 (sec) followed by a line-outage at line 16 (buses 2 and 4) at t=1.1 (sec). Using the equation (4.3) the objective function value is calculated in the network without any controller as 0.0417, in network with PSS as 0.0388 and with WA-POD controller it is

Table 4.2: Bounds of POD and PSS parameters.

Controller	**The Bounds of Parameters**				
Power System Stabilizer (PSS)	K_{PSS}	T_w	T_1&T_3	T_2&T_4	T_r
	$-5 \leq K_{PSS} \leq 5$	$0 \leq T_w \leq 10$	$0 \leq T_1 \leq 2$	$0 \leq T_2 \leq 2$	$0 \leq T_r \leq 0.1$
Power Oscillation Damper (POD)	K_{POD}	T_{wf}	T_{1f}&T_{3f}	T_{2f}&T_{4f}	T_{rf}
	$-5 \leq K_{PSS} \leq 5$	$0 \leq T_{wf} \leq 10$	$0 \leq T_{1f} \leq 2$	$0 \leq T_{2f} \leq 2$	$0 \leq T_{rf} \leq 0.1$

Table 4.3: Optimized parameters of POD and PSS using genetic algorithm.

Controller	**Tuned Parameters by Genetic Algorithm**						
Power System Stabilizer (PSS)	K_{PSS}	T_w	T_1	T_2	T_3	T_4	T_r
	2	5	0.31	0.05	0.31	0.05	0.01
Power Oscillation Damper (POD)	K_{POD}	T_{wf}	T_{1f}	T_{2f}	T_{3f}	T_{4f}	T_{rf}
	1.6	0.4	0.93	1.28	0.93	1.28	0.01

0.0134. By comparing the minimum values of the objective function in different condition, we may also conclude that by using the WA-POD controller we would have a lower value for the objective function defined in (4.3). This shows that use of the WA-POD controller yields more effective results in damping out low frequency oscillations. Based on the optimal solution the parameters of the network controllers (POD and PSS) will be set and the stability studies could be done.

4.4 Problem Formulation: The Multi-Stages Plan for Implementing the WA-POD Controller

Figure 4.3 shows the basic structure of the WAMS-based power oscillation damping controller associated with the UPFC device.

This structure is expressed with the dynamic control model and can be used to describe the basic control concept as applied to the wide-area power oscillation damping (WA-POD) controller to enhance the power system stability.

• **Stage 1:** As can be seen from Figure 4.3, in the supplementary control scheme of the UPFC device, the control output of the wide-area damping controller is one part of the control input of the UPFC device. This input could provide an additional damping control demand to adjust the UPFC output within a certain range to provide effective damping on low frequency oscillations. The location of the UPFC device would be determined under steady-state conditions to maximize power system loadability in Stage 1.

• **Stage 2:** Generally, the wide-area signals as the input signal of the WA-POD could be the remote generator rotor speed or angle, the bus angle, or the line active power flow. Basically, the selection on the wide-area signals can be performed by mode analysis and based on principles of observability and controllability [100]. Here in this study, the line active power flow between generators 1 and 2 has been selected as the wide-area input signal for the WA-POD controller. Since, the values of the rotor angles of generators 1 and 2 (see Figure 4.4) are necessary for the equations of the line active power flow, nonlinear state estimators are used in Stage 2 to generate the estimated rotor angles using PMU

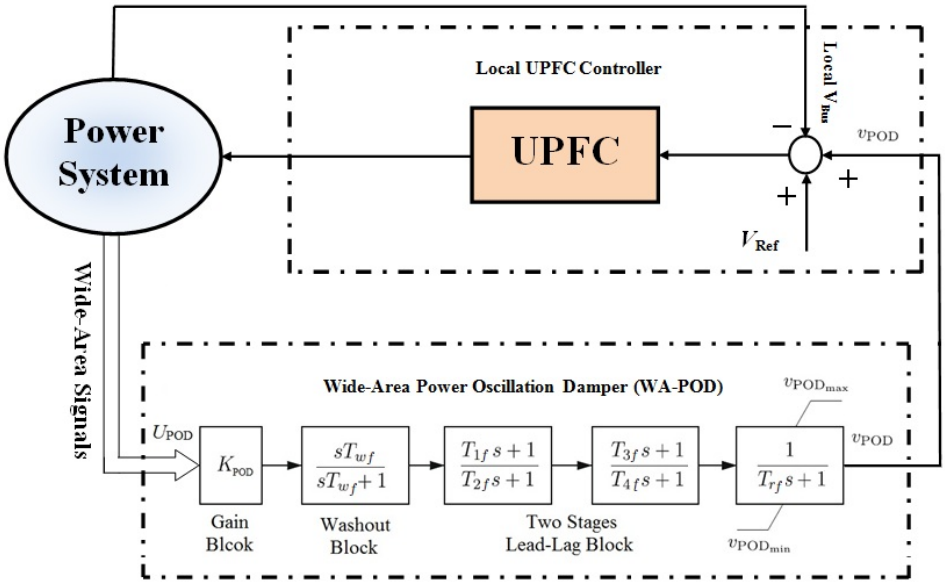

Figure 4.3: Block diagram of the wide-area power oscillation damper (WA-POD) controller.

measurement signals.

• **Stage 3:** Finally, in Stage 3 the WA-POD controller implemented in the PSAT software [99] using the previously estimated rotor speed deviations and rotor angles will be explained. In the next section, the procedure for the UPFC allocation as the first step of the multi-stage plan is presented.

4.5 Step 1: Optimal Placement of UPFC in the 14-Bus Test System

Another option for damping low-frequency oscillation is to use a FACTS device with a supplementary controller (POD). Obviously it costs more to use a FACTS device than PSS for oscillation damping, but there are some other benefits of FACTS controllers beside oscillation control such as the capability for local voltage control, increasing the power system loadability and also in some cases reducing transmission line losses [41, 77, 78].

In this study, the WA-POD controller sends the control set-point signal to a UPFC. This device offers several advantages for improving power system static and dynamic operations since it combines the feature of both STATCOM and SSSC as presented in Figure 3.23(a). The main objectives of placing a UPFC in a transmission line include controlling active and reactive power flow to achieve optimal power flow in the network and providing reactive support to maintain a constant voltage at the shunt bus. It can also be used to enhance several power system parameters such as system stability, power oscillation damping, and prevention of voltage collapse [74].

Table 4.4: The result of allocation process for UPFC device in the 14-bus test system.

Test System	**Device Number**	**Allocation Type**	**Selected FACTS and GUI Results**			λ_{max}	**Loadability Improvement**
			Type	Location	Values		
14 Bus	1	Single Type	UPFC	Branch 17	V_{SE} =0.188 p.u. Φ_{SE} =141 Deg. I_{SH} =0.034 p.u.	1.07	7% (18 MW)

Based on the modeling of UPFC device, as presented in section 3.2.9, the active power required by the series converter is drawn by the shunt converter from AC network and supplied to the bus k through the DC link. The equivalent circuit of the UPFC was presented in Figure 3.23(b). Based on this modeling, the series part of the UPFC is modeled by a controllable voltage source ($\underline{V}_{SE}$) while the shunt part is modeled with a controllable current source (I_{SH}). As a result, the UPFC device has three controllable variable: V_{SE}, Φ_{SE} and I_{SH}.

Using the implemented GUI in chapter 3, the results of optimal allocation of UPFC device in the 14-bus test system to maximize power system loadability are presented in Table 4.4. The location obtained by this method will improve the power system loadability without violating the security constraints presented in (3.46).

The results of allocation process, presented in Table 4.4, show that by optimal installation of one UPFC in branch 17 (between buses 9-14) with those optimal values, the maximum load factor of power system would be $\lambda_{max} = 1.07$ which means that we would have 7% (18.13 MW) improvement in power system loadability.

4.6 Step 2: State Estimation of Synchronous Generators

Availability of the synchronous machine angle and speed variables gives us an accurate picture of the overall condition of power networks leading therefore to an improved situational awareness by system operators. In addition, these variable are essential in developing local and global control schemes aimed at enhancing system stability and reliability [1].

As can be seen from Figure 4.5, the active power flow in line 1 is chosen as the input signal of the WA-POD controller. By using the nonlinear state estimators we can estimate the rotor angles and rotor speed deviations for generating the input signal of the WA-POD controller and for the offline parameter tuning of POD and PSS respectively. So, the fourth-degree model with E_{fd} and T_m as the input signals and electrical output power $y = P_e$ as the output signal, will be chosen for modeling the synchronous generators as

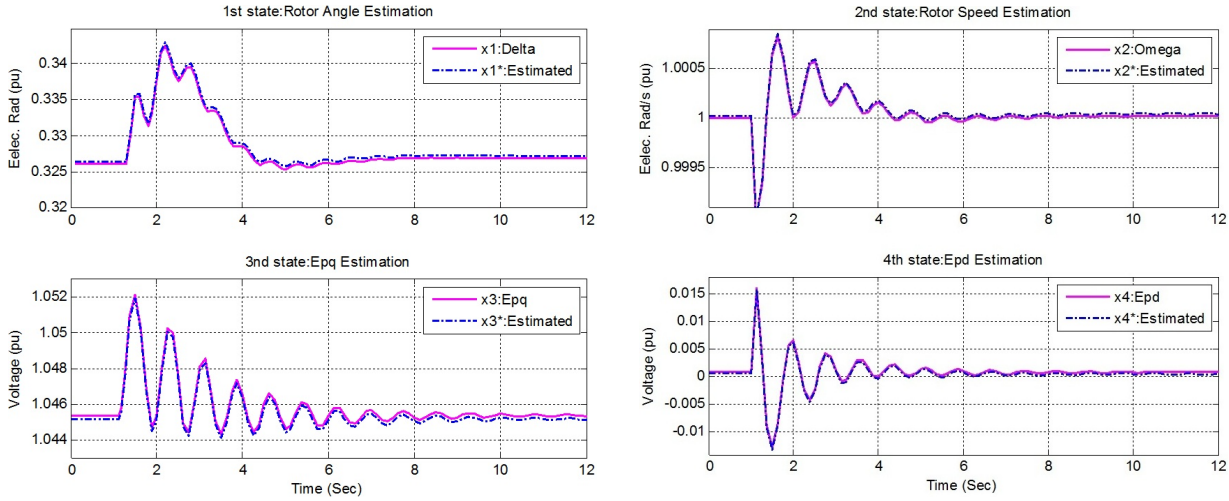

(a) (b)

Figure 4.4: The state estimation results: (a) First and third states of Generator 1. (b) Second and fourth states of Generator 2.

(4.4):

$$
\begin{aligned}
&\mathbf{x} = [\delta \quad \Delta\omega \quad e'_q \quad e'_d] = [x_1 \quad x_2 \quad x_3 \quad x_4] \\
&\mathbf{u} = [T_m \quad E_{fd}] = [u_1 \quad u_2] \\
&\dot{x}_1 = \omega_0 x_2 \\
&\dot{x}_2 = \frac{1}{J}(u_1 - T_e - Dx_2) \\
&\dot{x}_3 = \frac{1}{T'_{do}}(u_2 - x_3 - (x_d - x'_d)i_d) \\
&\dot{x}_4 = \frac{1}{T'_{qo}}(-x_4 - (x_q - x'_q)i_q)
\end{aligned}
\tag{4.4}
$$

where ω_0=$2\pi f_0$ is the nominal synchronous speed (elec. rad/s), ω is the rotor speed (p.u.), T_m is the mechanical input torque (p.u.), T_e is the air-gap torque or electrical output power (p.u.), E_{fd} is the exciter output voltage (p.u.) and δ is the rotor angle in (elec.rad). Other variables and constants are defined in List of Symbols in frontpages.

Using the method presented in chapter 2 we could generate the estimated states of the generators 1 and 2 following a severe disturbance. The results for a three-phase short circuit fault at bus 2 occured at t=1.00 (sec) and cleared t=1.1 (sec) followed by a line-outage at line 16 (between buses 2 and 4) at t=1.1 (sec) are presented in Figure 4.4. The simulation results, which include first and third states of generator 1 and the second and fourth states of generator 2, show high accuracy in the estimated states.

4.7 Step 3: Implementing the Wide-Area Power Oscillation Damping Controller

Finally, based on the results of the previous steps we can now implement the wide-area power oscillation damping controller, whose overall structure is presented in Figure 4.5.

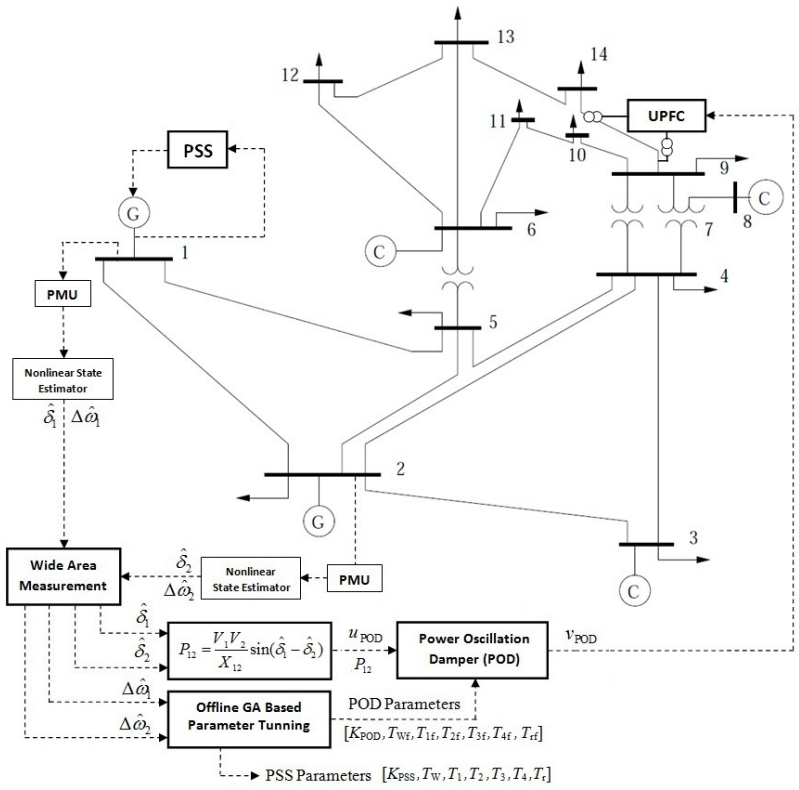

Figure 4.5: Overall structure of the WA-POD controller implemented in the 14-bus test system.

As mentioned before, the input signal of the WA-POD controller is the line active power flow between generators 1 and 2, which can be calculated by the rotor angles estimated in step two. The values of the voltage magnitudes are also available from the PMU phasor measured signals. All the simulations in this study including the parameter tuning of PSS and POD and stability studies were done in PSAT (Power System Analysis Toolbox) [99]. In PSAT, the input signal for the POD block can be chosen from the voltage magnitude of buses (V_i), the current flow of the lines (I_{ij}), the line active power flow (P_{ij}) and the line reactive power flow (Q_{ij}). Therefore, instead of directly choosing the value of ($\hat{\delta}_1 - \hat{\delta}_2$) as the input signal for the POD controller, which is not easily done in PSAT, we chose the line active power flow between buses 1 and 2 (P_{12}) which is a direct function of the estimated rotor angles ($\hat{\delta}_1 - \hat{\delta}_2$) as presented in Figure 4.5.

The overall structure of the implemented WA-POD controller in PSAT is shown in

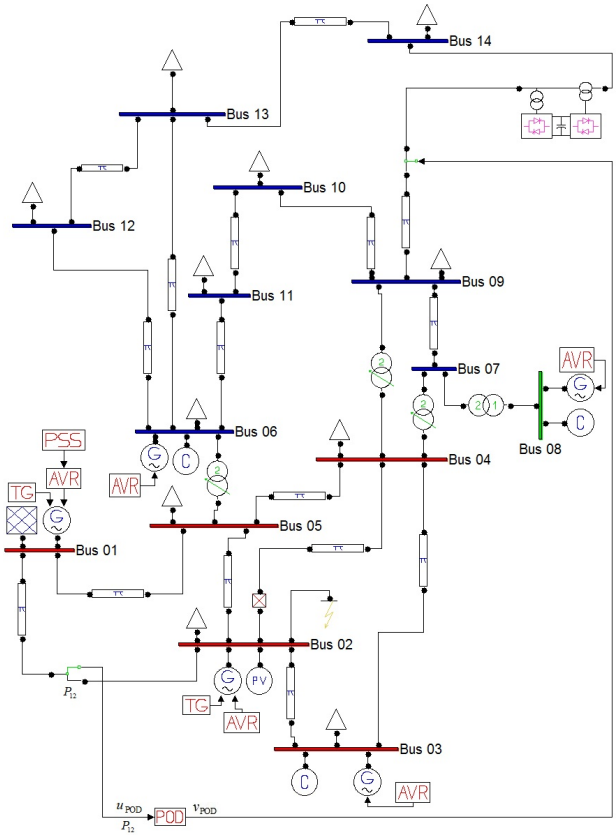

Figure 4.6: PSAT schematic of the WA-POD controller implemented for the 14-bus test system.

Figure 4.6. Since defining and using a new device in PSAT, such as our nonlinear state estimator, is a time-consuming process and because we have already shown that the estimated states of the generators have high accuracy compared with real signals, the active power flow in line 1 (P_{12}) was used directly as the input signal for the WA-POD controller as shown in Figure 4.6.

By setting the parameters of the PSS and WA-POD controllers by optimal solution of genetic algorithm, obtained in section 4.3, we can now analyze the simulation results to compare the effects of a WA-POD controller and a PSS controller on oscillation damping in the 14-bus test system.

4.8 Simulation Results

To show the effectiveness of the wide-area power oscillation damping (WA-POD) controller two types of disturbances are applied to the 14-bus test system:

(*a*) Three-phase short circuit followed by a line-outage.

(*b*) Load-demand imbalance contingency.

For each disturbance, the time-domain responses of generators variables such as rotor speeds, bus voltages, and output electrical power are presented in four conditions:

(*i*) Without any controller (No Controller: NC).

(*ii*) With just UPFC device (without WA-POD controller).

(*iii*) With power system stabilizer (PSS) installed at generator 1.

(*iv*) With WA-POD controller (combined with the UPFC device).

At first, the simulation results for three-phase short circuit fault followed by a line-outage are presented.

4.8.1 Case study-1: Three-phase short-circuit fault followed by a line-outage

In the first case study, a three phase short-circuit fault at bus 5 is applied to the system at t=1.00 (sec) and cleared after 5 (ms) at t=1.05(sec) followed by a line-outage for line 13 (between buses 4 and 5) at t=1.05(sec). The time-domain responses of generators variables are presented in Figures 4.7 and 4.8.

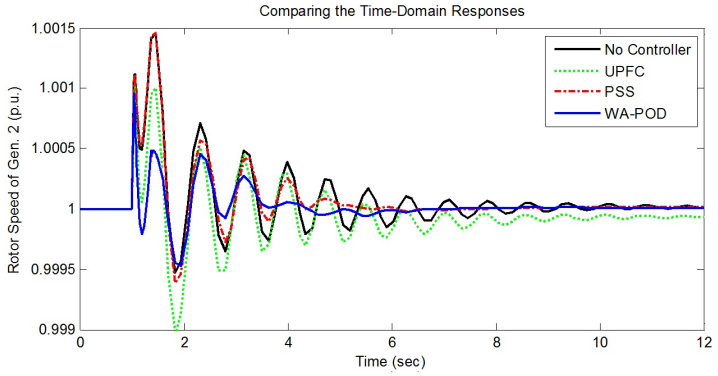

(a)

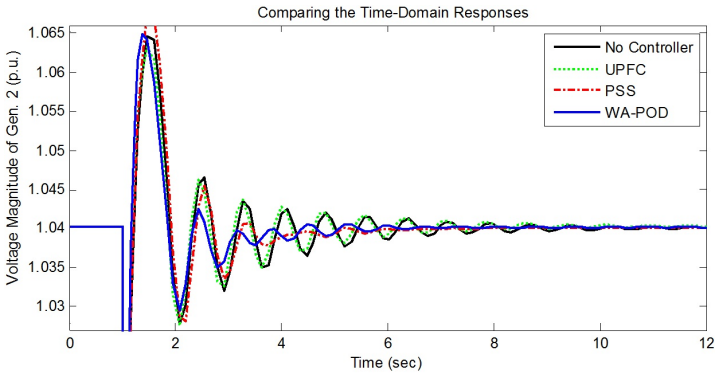

(b)

Figure 4.7: Time-domain responses of the first case study of generator 2: (a) Rotor speed (ω_2). (b) Voltage magnitude (V_2).

As can be seen from Figures 4.7 and 4.8, in the network without controller (NC), the system remains stable but the power system oscillations are not damped effectively while by using the PSS controller and also the WA-POD controller the damping of low-frequency oscillations is improved.

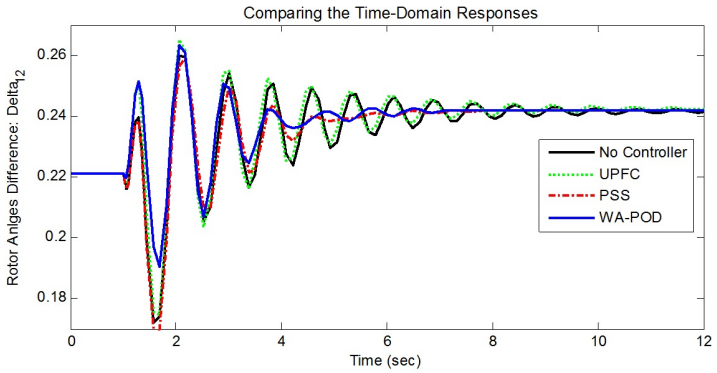

(a)

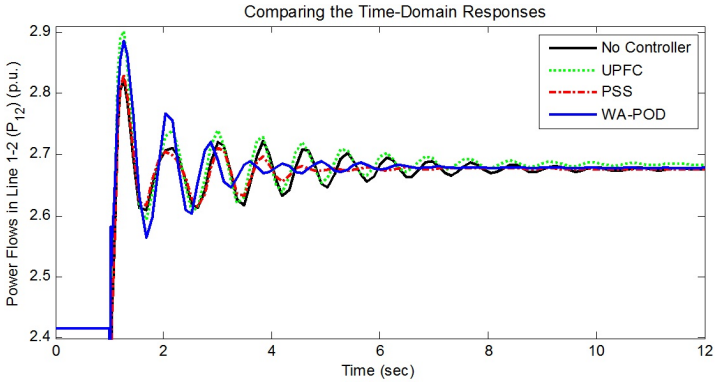

(b)

Figure 4.8: Time-domain responses of the first case study for: (a) Difference between rotor angles ($\delta_1 - \delta_2 = \delta_{12}$). (b) Active power flow between buses 1 and 2 (P_{12}).

Clearly in the results presented in Figure 4.7(a) and 4.8(a), specifically the rotor speed of generator 2 (ω_2) and the difference between rotor angles (δ_{12}), the WA-POD controller has better response in terms of overshoot and settling time. In other results such as bus voltage and output electrical power; the performance of WA-POD is clearly better than the PSS controller.

Therefore in the 14-bus test system, considering the improvement of dynamic performance and damping of low-frequency oscillations for all variables, the WA-POD controller is generally more effective than the PSS controller, both having been tuned using the same GA-based method. This benefit comes on top of a 7% loadability improvement already provided by the optimally located UPFC without supplementary control.

Finally for the first case study, the output signals for the WA-POD and PSS controllers are presented in Figure 4.9. As can be seen from this figure, the output control signals are

saturated in the appropriate time delay.

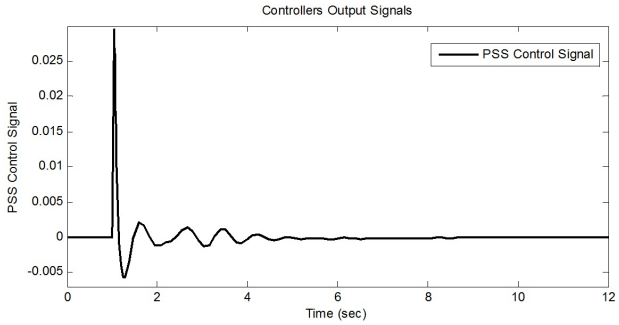

(a)

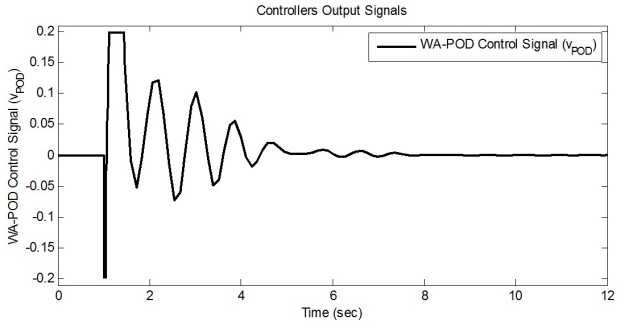

(b)

Figure 4.9: Output controller signals: (a) PSS controller output signal. (b) WA-POD controller output signal.

4.8.2 Case study-2: Load-demand contingency

In the second case study, a load-demand contingency with 5% increasing for both active and reactive loads for all PQ buses is applied to the 14-bus test system at t=1.00 (sec). The time-domain responses for generator variables such as rotor speeds and voltage magnitude are presented in Figsures 4.10 and 4.11. Considering the oscillation damping in the network, interestingly in this study, the influence of one UPFC alone is much better.

As can be seen in Figure 4.10 from the results presented for rotor speed responses, in the case of load-demand contingency the UPFC is more capable to damp low-frequency oscillations even better than PSS based on the objective function value. The value of objective function (from t=0 to T=20 in Figure 4.10) is calculated as 0.4605 for the network without controller, 0.4595 for the network with PSS controller, 0.4545 for the network with UPFC device and finally 0.4269 for the network with WA-POD controller.

Similar to the first case study, based on the results obtained in the second case study presented in Figures 4.10 and 4.11, the WA-POD controller combined with a UPFC device clearly has the best improvement in damping out the network oscillations.

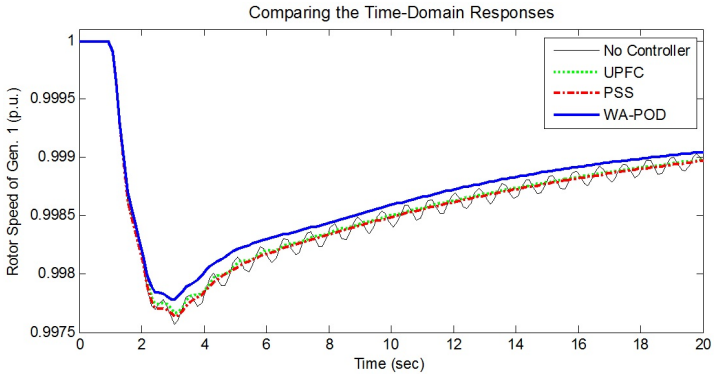

(a)

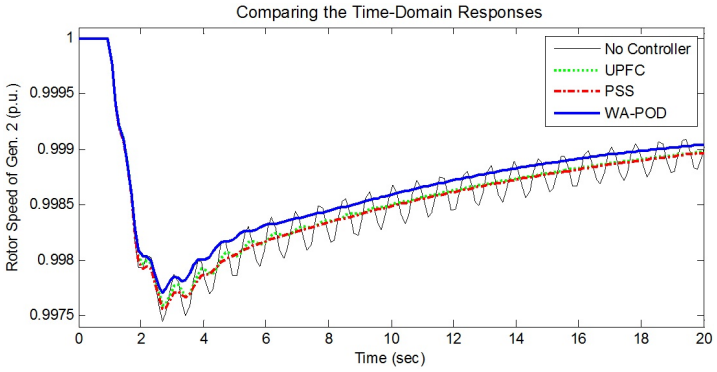

(b)

Figure 4.10: Time-domain responses of second case study for rotor speeds: (a) Generator 1 (ω_1). (b) Generator 2 (ω_2).

To present other variable responses in load-demand contingency, here the voltage magnitude of generator 2 and the active power flow between buses 1 and 2 are shown in Figure 4.11.

4.9 Discussion: Eigenvalue Analysis

In this section, the eigenvalue analyses of the 14-bus test system are summarized in Table 4.5 for the following configurations:

(i) Base network or the network without controller.

(ii) Network with the PSS controller.

(iii) Network with the UPFC device.

(iv) Network with UPFC combined with the WA-POD controller.

Based on the results in this table, we can compare the influence of each controller on damping out the main oscillation modes of the network.

As can be seen in Table 4.5, the influence of the UPFC device on damping the oscillation

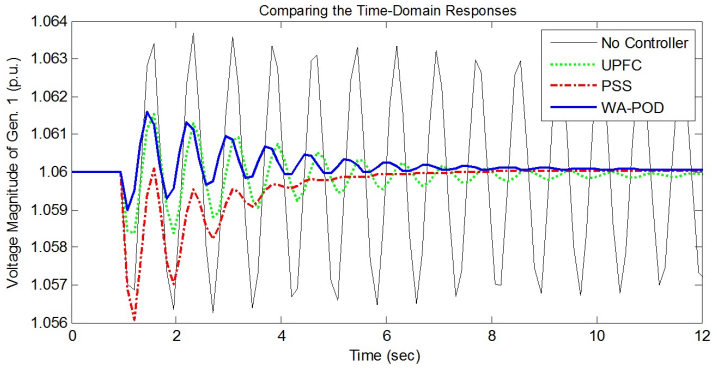

(a)

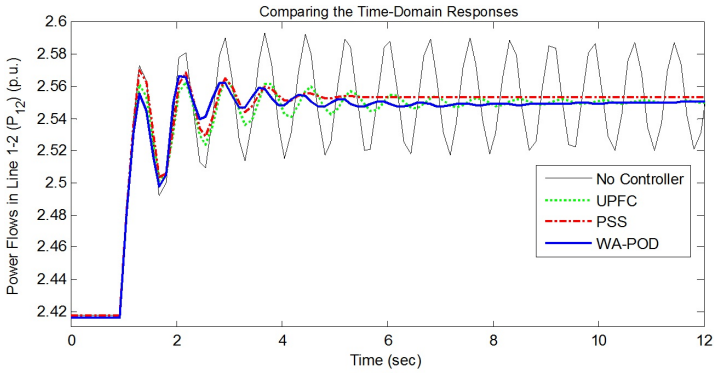

(b)

Figure 4.11: Time-domain responses of second case study for: (a) Voltage magnitude of generator 1 (V_1). (b) Active power flow between buses 1 and 2 (P_{12}).

modes is not significant. This device improves the damping ratio by only 1% on 1.72-Hz-mode ($\Delta\omega_5$), 1.24-Hz-mode ($\Delta\omega_2$) and 0.17-Hz-mode ($\Delta\omega_1$) and by only 2% for 0.21-Hz-mode (e'_{q4}).

In comparison with the UPFC device, the PSS controller achieves better improvement of the damping ratio on several oscillation modes. For example, for 1.41-Hz-mode (e'_{q1}) we have 2% improvement on damping ratio, for 1.24-Hz-mode ($\Delta\omega_2$) 4%, for 0.21-Hz-mode (e'_{q4}) 2% (similar to UPFC device), for 0.17-Hz-mode ($\Delta\omega_1$) 4% and finally for 0.10-Hz-mode (e'_{q2}) it is 1%.

Lastly, we can analyze the damping performance of the WA-POD controller in combination with the UPFC device. As it was clear in the results of the stability simulation in the previous section, the WA-POD controller has the best effects in damping out the low-frequency modes. As can be seen from the results presented in Table 4.5, the WA-POD controller improves the damping ratio for 7 low-frequency oscillation modes. The best achievements on damping performance are for 0.17-Hz-mode ($\Delta\omega_1$) with 9% and 1.24-Hz-mode ($\Delta\omega_2$) with 8% improvement. For other oscillation modes the damping ratio improvement varies from 1% to 5%: 1% for 1.72-Hz, 0.15-Hz and 0.10-Hz modes, 4% for

Table 4.5: Damping Performance of the 14-bus test system in 4 different categories.

Associated States	**Base Network**		**Network with PSS**		**Network with UPFC**		**Network with WA-POD**	
	f(Hz)	ζ Damping Ratio	**f**(Hz)	ζ Damping Ratio	**f**(Hz)	ζ Damping Ratio	**f**(Hz)	ζ Damping Ratio
$\Delta\omega_5, \delta_5$	1.72	0.33	1.68	0.33	1.72	0.34	1.72	**0.34**
$\Delta\omega_4, \delta_4$	1.55	0.29	1.55	0.29	1.55	0.29	1.55	0.29
$\Delta\omega_3, \delta_3$	1.44	0.27	1.44	0.27	1.44	0.27	1.44	0.27
e'_{q1}	1.41	0.06	1.42	0.08	1.41	0.06	1.43	**0.12**
$\Delta\omega_2, \delta_2$	1.24	0.26	1.23	0.30	1.24	0.27	1.23	**0.34**
e'_{q4}	0.21	0.61	0.21	0.63	0.21	0.63	0.20	**0.65**
$\Delta\omega_1, \delta_1$	0.17	0.67	0.17	0.71	0.17	0.68	0.17	**0.76**
e'_{q5}	0.15	0.78	0.15	0.78	0.15	0.78	0.15	**0.79**
e'_{q2}	0.10	0.66	0.10	0.68	0.10	0.66	0.10	**0.68**
e'_{q3}	0.05	0.87	0.05	0.87	0.05	0.87	0.05	0.87

0.21-Hz-mode and 6% for 1.41-Hz-mode.

4.10 Summary

This chapter presented a multi-stage plan for developing a wide-area power oscillation damping (WA-POD) controller in comparison with the conventional power system stabilizer (PSS) in the 14-bus test system. The implemented WA-POD controller sets an auxiliary stabilizing signal for a UPFC device. In the first step of the plan the optimal location of the UPFC was determined in order to maximize power system loadability. To calculate the input signal of the WA-POD controller, the rotor angles of the generators were estimated using the nonlinear state estimator in step 2. Finally in step 3, after parameter tuning of the PSS and WA-POD controllers using an off-line GA-based optimization process, the WA-POD controller was developed in PSAT. The simulation results showed the capability and effectiveness of the WA-POD controller in comparison with PSS to damp low-frequency oscillations and enhance the dynamic performance of power system. However, while the PSS controller is only capable of damping out low-frequency oscillations, by using the WA-POD controller in combination with a UPFC device, besides the improvement in transient stability and dynamic performance, we would have a 7% improvement in power system loadability, which is equal to 18.13 (MW).

Chapter 5

Conclusion

5.1 Summary and Contributions

In this thesis we had a multi-step plan for implementing a FACTS-based wide-area power oscillation damping controller. All these three steps were presented in chapter 2 to 4 of this thesis while covering the initial goals expressed in introduction. In following these goals and the achieved results are discussed separately for each step.

The goal of the first step of this plan, presented in chapter 2, was developing the dynamic state estimation of power system using the PMU measured signals. In chapter 2, three different approaches: traditional EKF method, UKF and EKF-UI, were applied for dynamic state estimation of a synchronous machine. The simulation results for all these three approaches were presented on two condition: with noise and without noise. Also, the robustness and effectiveness of the UKF and EKF-UI methods was checked successfully by applying it to the various kinds of field voltage E_{fd} and mechanical torque T_m inputs, ranging from step to ramp signals. Also, for the UKF and EKF-UI method, the developed state estimators were analyzed effective as well under network fault conditions with process and measurement noise included. The obtained results showed that we covered all the goals requested in step 1.

In chapter 3, the second step of thesis, the goal was implementing an optimization method to find the best location of FACTS controller. A Graphical User Interface (GUI) based on the genetic algorithm (GA) was presented to seek the optimal locations and optimal values of a given set of FACTS devices for more efficient use of power system assets. In the implemented GUI, called FACTS Placement Toolbox, the user had the opportunity to pick a power system network, determine GA settings and select the number and types of the FACTS device. Six different FACTS devices were used in the GUI: SVC, TCSC, TCVR, TCPST, UPFC and STATCOM with SMES. The simulation results showed that the FACTS placement toolbox is applicable to seek the optimal locations and rates of the given multi-type FACTS devices mix in a given power system, so as to maximize the system loadability under security constraints. The goals and objective of step 2 were addressed effectively using the presented method in chapter 3.

In step 3 which was our final step, presented in chapter 4, the FACTS-based wide-area power oscillation damping controller (WA-POD) was implemented as it was set in initial plan. For better understanding the benefits of previous steps, a multi-stage plan was presented for developing the wide-area controller in this chapter. The implemented WA-POD controller set an auxiliary stabilizing signal for the UPFC device. In the first stage, the optimal location of the UPFC was determined in order to maximize the power system loadability using the method presented in chapter 3 (step 2). To calculate the input signal of the WA-POD controller the rotor angles of the generators were estimated in stage 2 using the nonlinear state estimator presented in chapter 2 (step 1). Finally in the stage 3, after parameter tuning of the PSS and WA-POD controllers using an off-line GA-based optimization process, the WA-POD controller was developed in PSAT software. The simulation results showed the capability and effectiveness of the WA-POD controller in comparison with traditional power system stabilizer (PSS) to damp the low frequency

oscillations of the network and to enhance the dynamic performance of power system.

5.2 Directions for Future Works

Interesting directions for future works can be presented for each step of this thesis:

- In step 1, **Dynamic State Estimation in Power System Networks**, the EKF-UI presented method can be improved in such a form that the state estimator does not need the mechanical torque T_m (first input) near the second input E_{fd} signal. It means that, in this case we will have two unknown inputs and the states of the synchronous machine will be estimated with two unknown inputs. As it is presented in section 2.5, in the EKF-UI algorithm the unknown inputs of the system will be estimated with the states simultaneously.

- In step 2, **Optimal Placement of FACTS Devices in Power System Networks**, the implemented GUI can be improved by including different optimization algorithms such as Particle Swarm Optimization (PSO) and Evolutionary Algorithm (EA) in addition of Genetic Algorithm (GA). Also, beside maximizing the power system loadability, we can add more options for choosing as objective functions like: minimizing the transmission line losses or minimizing the production costs.

- In step 3, **Implementing a FACTS-based Power Oscillation Damping Controller Using Wide-Area Signals**, the developed study could be expanded by choosing different signals as the input signal of WA-POD controller. Also, we can implement the same study in other networks such as 24-bus, 39-bus or 57-bus test system. Another option could be comparing the influences of UPFC with other FACTS device such as STATCOM, SVC or TCSC in damping out the low-frequency oscillations.

Appendices

Appendix A

SMIB Model Presentation with Respect to the Infinite-Bus

A general power system configuration presented in Figure A.1(a) can be simplified to an equivalent circuit system with a single machine connected to an infinite-bus via transmission lines using using Thévenin's equivalent theory as presented in Figure A.1(b) [1].

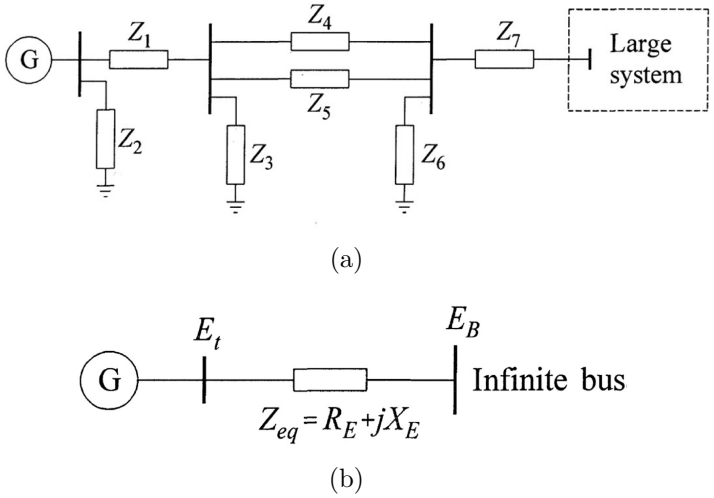

Figure A.1: Power system network: (a) General configuration. (b) Thévenin's equivalent.

The so-called single-machine infinite-bus (SMIB) power system, shown in Figure A.2, was the the basis for developing and validating the dynamic state estimation process in Chapter 3. In section 2.2 the SMIB model was presented with $V_t(=E_t)$ as the reference phasor while here, that presentation will be repeated by assuming the $V_B(=E_B)$ as the reference phasor.

This second presentation, could have some benefits rather than the first presentation in (2.1) to (2.12). The first fact that should be mentioned is, by defining the V_B or E_B as the reference phasor as presented in Figure A.3, all the local state estimator will generate

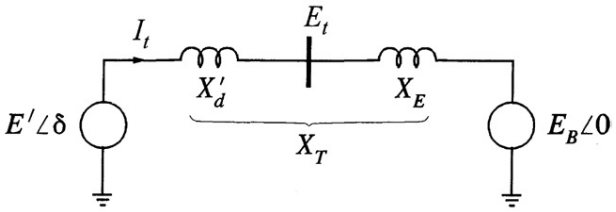

Figure A.2: Synchronous machine connected to infinite-bus.

the estimated states (specially the first state δ) of the synchronous machines entire the network with respect to one reference bus (Slack Bus). While by defining the V_t or E_t as the reference phasor, each local state estimator will estimate the states with respect to its own terminal bus which is a local reference. In first case, the estimated rotor angles of the entire network, which are estimated with respect to the same reference, could be more useful in wide area control operations.

Secondly, by defining the V_B or E_B as the reference phasor, the Phasor Measurement Unit (PMU) could be installed on the transmission lines (at the substation) instead of terminal bus but the transformer reactance would then have to be added to the machine reactance.

Finally, with having the V_B or E_B as the reference phasor , the quantity of V_t in equations (2.1) to (2.12) would be replaced by V_B which it is a constant value. It therefore leads us to not having V_t as the third input in the equations.

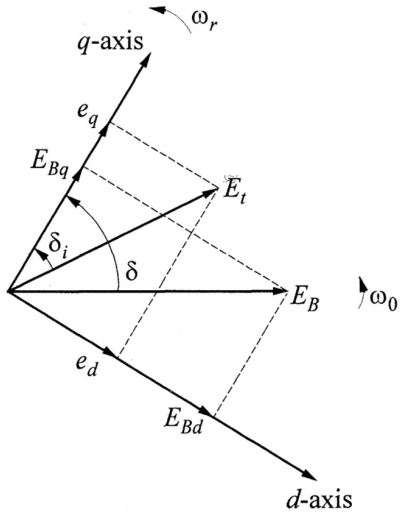

Figure A.3: Phasor diagram of synchronous machine.

Giving a classical model for the synchronous generator and neglecting the transmission line resistance (R_e=0), all the active power produced by generator P_t, is delivered to the infinite-bus (P_t=P_B). Also, δ is the angle by which e'_q, the q-axis component of the voltage behind transient reactance x'_d, leads the terminal bus of machine E_B (or V_B). With

assuming V_B as the reference phasor as shown in Figure A.3, the single-machine infinite-bus power system in Figure 2.1, can be represented in per unit (pu) by the fourth-order nonlinear equation in the *dqo* domain as (A.1):

$$\begin{aligned}
\dot{\delta} &= \omega_0 \Delta\omega \\
\Delta\dot{\omega} &= \frac{1}{J}(T_m - T_e - D\Delta\omega) \\
\dot{e}'_q &= \frac{1}{T'_{do}}(E_{fd} - e'_q - (x_d - x'_d)i_d) \\
\dot{e}'_d &= \frac{1}{T'_{qo}}(-e'_d - (x_q - x'_q)i_q).
\end{aligned} \tag{A.1}$$

which can be rewritten in the input-output, state-variable form as follows in (A.2):

$$\begin{aligned}
\mathbf{x} &= [\delta \quad \Delta\omega \quad e'_q \quad e'_d] = [x_1 \quad x_2 \quad x_3 \quad x_4] \\
\mathbf{u} &= [T_m \quad E_{fd}] = [u_1 \quad u_2] \\
\dot{x}_1 &= \omega_0 x_2 \\
\dot{x}_2 &= \frac{1}{J}(u_1 - T_e - Dx_2) \\
\dot{x}_3 &= \frac{1}{T'_{do}}(u_2 - x_3 - (x_d - x'_d)i_d) \\
\dot{x}_4 &= \frac{1}{T'_{qo}}(-x_4 - (x_q - x'_q)i_q).
\end{aligned} \tag{A.2}$$

where ω_0=$2\pi f_0$ is the nominal synchronous speed (elec. rad/s), ω the rotor speed (pu), T_m the mechanical input torque (pu), T_e the air-gap torque or electrical output power (pu), E_{fd} the exciter output voltage or the field voltage as seen from the armature (pu) and δ the rotor angle in (elec.rad). Other variables and constants are defined in List of Symbols in front-pages. Based on the phasor diagram presented in Figure A.3, the air-gap torque T_e will be equal to the terminal electrical power P_t (or P_e=$\omega_r T_e$) neglecting the stator resistance (R_a=0)and assuming ω_r=1.0 (pu):

$$T_e = P_t + R_a I_t^2 \quad \overset{R_a=0}{\rightarrow} \quad T_e \cong P_t = e_d i_d + e_q i_q \tag{A.3}$$

where the d-and q-axis voltages (e_d,e_q) can be expressed as:

$$\begin{aligned}
e_d &= e_{bd} - x_e i_q \\
e_q &= e_{bq} + x_e i_d
\end{aligned} \tag{A.4}$$

where e_{bd} and e_{bq} are presented as (A.5):

$$\begin{aligned} e_{bd} &= V_B\ sin\delta \\ e_{bq} &= V_B\ cos\delta \end{aligned} \tag{A.5}$$

and in turn we will have:

$$E_B = V_B = \sqrt{e_{bd}^2 + e_{bq}^2}. \tag{A.6}$$

Also, the d-and q-axis currents (i_d,i_q) are:

$$\begin{aligned} i_d &= I_t sin(\delta + \Phi) = \frac{e'_q - V_B\ cos\delta}{x'_d + x_e} \\ i_q &= I_t cos(\delta + \Phi) = \frac{V_B\ sin\delta}{x_q + x_e} \end{aligned} \tag{A.7}$$

and consequently for the terminal current we will have:

$$I_t = \sqrt{i_d^2 + i_q^2}. \tag{A.8}$$

where the presence of x_e in i_d and i_q formulas is related to δ definition with respect to V_B. By defining x_{td} and x_{tq} as:

$$\begin{aligned} x_{td} &= x'_d + x_e \\ x_{tq} &= x_q + x_e \end{aligned} \tag{A.9}$$

and with replacing the variables δ and e'_q by the state variables x_1 and x_3, we will have:

$$\begin{aligned} i_d &= \frac{x_3 - V_B\ cosx_1}{x_{td}} \\ i_q &= \frac{V_B\ sinx_1}{x_{tq}}. \end{aligned} \tag{A.10}$$

Using (A.5) and (A.7) in (A.10) and after mathematical simplification, the electrical output power P_e at the terminal bus (P_e= P_t) can be presented as (A.11):

$$y_1 = P_e = \frac{V_B}{x_{td}}\ e'_q\ sin\delta + \frac{V_B^2}{2}(\frac{1}{x_{tq}} - \frac{1}{x_{td}})sin2\delta \tag{A.11}$$

and in terms of states x_1 and x_3 we will have:

$$y_1 = P_e = \frac{V_B}{x_{td}}\ x_3\ sinx_1 + \frac{V_B^2}{2}(\frac{1}{x_{tq}} - \frac{1}{x_{td}})sin2x_1. \tag{A.12}$$

Similarly the active power equation, the reactive power equation can be calculated as:

$$Q_e = e_d\, i_q - e_q\, i_d \tag{A.13}$$

in which using (A.5) and (A.7) in (A.13) can we will have:

$$y_2 = Q_e = \frac{V_B}{x_{td}}\, e'_q\, sin\delta - V_B^2(\frac{sin^2\delta}{x_{tq}} + \frac{cos^2\delta}{x_{td}}) - 2x_e I_t^2 \tag{A.14}$$

or with substituting the variables δ and e'_q by the state variables x_1 and x_3, we will have:

$$y_2 = Q_e = \frac{V_B}{x_{td}}\, x_3\, sinx_1 - V_B^2(\frac{sin^2x_1}{x_{tq}} + \frac{cos^2x_1}{x_{td}}) - 2x_e I_t^2 \tag{A.15}$$

To summarize, using (A.12) and (A.15) in (A.2), the fourth-order nonlinear synchronous machine state space model is rewritten as (A.16) in a form suitable for state estimation purposes like EKF-UI, with the active and reactive electrical output power P_t and Q_t as the measurable system outputs. Since in this presentation in (A.16) we have V_B instead of V_t, therefore the terminal voltage V_t does not appear in the vector $\mathbf{u}$ in (A.16) while we had it before in (2.12):

$$\begin{aligned}
&\mathbf{x} = [\delta \quad \Delta\omega \quad e'_q \quad e'_d] = [x_1 \quad x_2 \quad x_3 \quad x_4]\\
&\mathbf{u} = [T_m \quad E_{fd}] = [u_1 \quad u_2]\\
&\dot{x}_1 = \omega_0 x_2\\
&\dot{x}_2 = \frac{1}{J}(T_m - (\frac{V_B}{x_{td}}\, x_3\, sinx_1 + \frac{V_B^2}{2}(\frac{1}{x_{tq}} - \frac{1}{x_{td}})sin2x_1) - Dx_2)\\
&\dot{x}_3 = \frac{1}{T'_{do}}(E_{fd} - x_3 - (x_d - x'_d)(\frac{x_3 - V_B\, cosx_1}{x_{td}}))\\
&\dot{x}_4 = \frac{1}{T'_{qo}}(-x_4 - (x_q - x'_q)(\frac{V_B\, sinx_1}{x_{tq}}))\\
&y_1 = \frac{V_B}{x_{td}}\, x_3\, sinx_1 + \frac{V_B^2}{2}(\frac{1}{x_{tq}} - \frac{1}{x_{td}})sin2x_1\\
&y_2 = \frac{V_B}{x_{td}}\, x_3\, sinx_1 - V_B^2(\frac{sin^2x_1}{x_{tq}} + \frac{cos^2x_1}{x_{td}}) - 2x_e I_t^2
\end{aligned} \tag{A.16}$$

where all the parameters and quantities other than state variables are (or assumed to be) known and measurable. We can therefore represent (A.16) in a global structure as equation (2.13).

Appendix B

Test Machine and External System Data

The main variables and constants of the system presented in (2.1) in (2.12) and their values are expressed here in Table B.1. The values for the parameters are in (p.u.) and the signals variables presented in their nominal values.

Table B.1: Variables and constants values.

Parameter	Description	Value (pu)
δ	Nominal rotor angle (Load angle)	0.82
ω_0	Nominal synchronous speed	377
Φ	Power factor angle	0.062
T_m	Mechanical input torque	0.8
D	Damping factor per unit	0.05
J	Inertia constant per unit	10
x_{adu}	Unsaturated direct axis mutual reactance	2.15
x_{aqu}	Unsaturated quadratic axis mutual reactance	1.36
x_{ad}	Direct axis mutual reactance	1.91
x_{aq}	Quadratic axis mutual reactance	1.06
x_d	Direct axis reactance	2.06
x_q	Quadratic axis reactance	1.21
k_{sd}	Direct saturation factors	0.88
k_{sq}	Quadratic saturation factors	.78
x'_d	Direct axis transient reactance	0.37
x'_q	Quadratic axis transient reactance	0.37
R_a	Stator resistance	0.0
X_e	Line reactance	0.193
R_e	Line resistance	0.0
T'_{do}	Direct transient open-circuit time constant	0.13
T'_{qo}	Quadratic transient open-circuit time constant	0.013
x_{fd}	Field circuit reactance	2.165
V_B	Infinite-bus voltage	0.98
E_{fd}	Steady-state internal voltage of armature	2.29
i_{fd}	Field current	1.09
E_I	Internal generator voltage proportional to field current	2.09
V_t	Terminal bus voltage	1.02
I_t	Terminal bus current	0.81
P_t	Terminal active power	0.80
Q_t	Terminal reactive power	0.05

Appendix C

Matlab Implementation for Dynamic State Estimation Processes

As it was mentioned in chapter 3, the embedded Matlab function, which is shown in Figure C.1, was used for implementation of the EKF, UKF and EKF-UI methods.

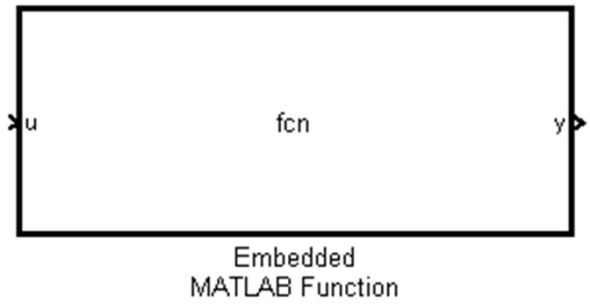

Figure C.1: Embedded MATLAB function block in Simulink/Matlab.

By running the Simulink file and receiving the signals from embedded MATLAB function block inputs, the block creates the outputs based on its internal commands. At the beginning of the m-file, we can use the commands "*persistent*", "*isempty*" and "*if-end*" for initializing the algorithm (EKF, UKF or EKF-UI) variables $\mathbf{x}_0$ and $\mathbf{P}_0$.

The following script allows the algorithm to be initialized matrix $\mathbf{P}$ and state vector $\mathbf{x}$ once at the start of the simulation and loads the initial value. In the next iterations, the command *isempty*($\mathbf{P}$) will not allow the matrix $\mathbf{P}$ to be reloaded again. After the second iteration, the matrix $\mathbf{P}$ will always have a value and it will not be null so the program will pass the loop "*if-end*".

```
% A m-file template for initialization the EKF, UKF and EKF-UI
% methods in embedded matlab function block
```

```
P_0=diag([10^2,10^2,10^2,10^2]);
x_0=[0;0;0;0];
Qk_0=0.5^2*eye(4);
Rk_0=0.1^2*eye(2);

persistent P;
persistent x;
persistent Qk;
persistent Rk;

if isempty(P)
   P=P_0;
end

if isempty(x)
   x=x_0;
end

if isempty(Qk)
   Qk=Qk_0;
end

if isempty(Rk)
   Rk=Rk_0;
end;
```

In following the m-files of the algorithms for EKF, UKF and EKF-UI methods used in the embedded matlab functions will be presented.

C.1 EKF algorithm

```
function [x_est  ,y_est ] =EKF(Pe,Tm,Efd)

%%%%%%%%%%%%%%%%%%%%%%%%%%%%%%%%%%%%%%%%%%%%%%%%%%%%%%%%%%%%%%%%%%%%
%%%%%%%%%%%%%%%%%%%%%%%%%%%%%%%%%%%%%%%%%%%%%%%%%%%%%%%%%%%%%%%%%%%%
% Initialization

       XADU=2.15;
       XAQU=1.365;
```

```
W0=2*60*3.14159;
H=4;
%H=4.75;
JJ=2.*H;
XL=0.15;
A=0.031;
B=6.93;
VT1=0.8;
XPD=0.375;
XPQ=0.375;
TPDO=0.131;
XE=0.193;
KD=0.05;
P=0.8;
QS=0.05;
VB=0.98;
PHI=atan2(QS,P);
IT=sqrt(P^2+QS^2)/VB;
VTT=sqrt((VB+XE*IT*sin(PHI))^2+(XE*IT*cos(PHI))^2);

if (VTT >= VT1),
   DV=A*exp(B*(VTT-VT1));
   ksd=VTT/(VTT+DV);
else,
   ksd=1.0;
end;
ksq=0.78;
XAD=ksd*XADU;
XAQ=ksq*XAQU;
XD=ksd*XADU+XL;
XQ=ksq*XAQU+XL;
XFFD=(XAD^2)/(W0*(XD-XPD));
XTD=XPD+XE;
XTQ=XQ+XE;
PF=cos(PHI);
QF=sin(PHI);
DELTA=atan2((XTQ*PF),((VB/IT)+XTQ*QF));
VBD=VB*sin(DELTA);
VBQ=VB*cos(DELTA);
TETA=DELTA+PHI;
ID=IT*sin(TETA);
IQ=IT*cos(TETA);
```

```
        VQ=VBQ+XE*ID;
        VD=VBD-XE*IQ;
        VT=sqrt(VD*VD+VQ*VQ);

        U1=XTD*ID+VBQ+(XD-XPD)*ID;  % Vf
        ME=VD*ID+VQ*IQ;
        U2=ME;   % Torque

        W0=2*60*3.14159;
        VB=0.98 ;
        x_prime_d=XPD;
        x_prime_q=XPQ;
        xe=XE;
        xq=XQ;
        D=KD;
        T_prime_do=TPDO;
        xd=XD;
        T_prime_qo=0.013;

        u1=Tm;
        u2=Efd;

%%%%%%%%%%%%%%%%%%%%%%%%%%%%%%%%%%%%%%%%%%%%%%%%%%%%%%%%%%%%%%%%%%%
%%%%%%%%%%%%%%%%%%%%%%%%%%%%%%%%%%%%%%%%%%%%%%%%%%%%%%%%%%%%%%%%%%%

persistent P
persistent Qk
persistent Rk
persistent x
persistent z

if isempty(P)    P=([10 0 0 0;0 10 0 0; 0 0 10 0; 0 0 0 10]).^2;end
if isempty(x)    x=[0.6;0;0;0];end
if isempty(Qk)   Qk=0.5^2*eye(4);end
if isempty(Rk)   Rk=0.5^2;end

n=4;     %number of state
q=1^2;r=1^2;
Q=q*eye(4);    % covariance of process
R=r*eye(1);        % covariance of measurement
z_out=Pe;
```

```
%nonlinear update and linearization at current state
[x_f,A]=jaccsd_f(x,u1,u2);

P=A*P*A'+Qk;                  %partial update
[z_h,Hx]=jaccsd_h(x_f);    %nonlinear measurement and linearization
P12=P*Hx';                    %cross covariance

K=P12*inv(Hx*P12+Rk);       %Kalman filter gain
x=x_f+K*(z_out-z_h);            %state estimate
P=P-K*P12';

x_est=x;
y_est=z_h;

%%%%%%%%%%%%%%%%%%%%%%%%%%%%%%%%%%%%%%%%%%%%%%%%%%%%%%%%%%%%%%%%
%%%%%%%%%%%%%%%%%%%%%%%%%%%%%%%%%%%%%%%%%%%%%%%%%%%%%%%%%%%%%%%%

function [x_f,A_f]=jaccsd_f(x,u1,u2)

Tm=u1;
Efd=u2;

Ts=0.001;

A_f=[1   Ts*W0    0    0;
     (-Ts/J)*((VB*x(3)*cos(x(1))/XTD)+VB*VB*((+1/XTD)+(-1/XTQ))...
     *(cos(x(1))^2-sin(x(1))^2))   (-(Ts/J)*D+1)  (-Ts/J)*(VB*sin(x(1))/XTD)   0;
     (Ts/T_prime_do)*(xd-x_prime_d)*VB*-1*sin(x(1))*(1/XTD)    0  ...
     (1+(-Ts/T_prime_do)*(1+((xd-x_prime_d)/XTD))) 0;
     (Ts/T_prime_qo)*(xq-x_prime_q)*VB*cos(x(1))*(1/XTQ)  0    0  ...
     (-(Ts/T_prime_qo)+1)];

id=[(x(3)-VB*cos(x(1)))*(1/(x_prime_d+xe))];
iq=[VB*sin(x(1))*(1/(xq+xe))];
Pe=VB*sin(x(1))*[(x(3)-VB*cos(x(1)))*(1/(x_prime_d+xe))]+ ...
VB*cos(x(1))*[VB*sin(x(1))*(1/(xq+xe))];

dx1=Ts*(W0*x(2))+x(1);
dx2=Ts*((1/J)*(Tm-Pe-D*x(2)))+x(2);
dx3=Ts*((1/T_prime_do)*(Efd-x(3)-(xd-x_prime_d)*id))+x(3);
dx4=Ts*((1/T_prime_qo)*(-x(4)+(xq-x_prime_q)*iq))+x(4);
```

```
x_f=[dx1;dx2;dx3;dx4];

%%%%%%%%%%%%%%%%%%%%%%%%%%%%%%%%%%%%%%%%%%%%%%%%%%%%%%%%%%%%%%%%
%%%%%%%%%%%%%%%%%%%%%%%%%%%%%%%%%%%%%%%%%%%%%%%%%%%%%%%%%%%%%%%%

function [z_h,Hx]=jaccsd_h(x)

Pest=VB*sin(x(1))*(x(3)-VB*cos(x(1)))*(1/(XTD))+...
VB*cos(x(1))*VB*sin(x(1))*(1/(XTQ));
Hx=[( (VB*x(3)*cos(x(1))/XTD) +  VB*VB*((-1/XTD)+...
(1/XTQ))*(cos(x(1))^2-sin(x(1))^2)) 0 (VB*sin(x(1))/XTD) 0];
z_h=Pest;

%%%%%%%%%%%%%%%%%%%%%%%%%%%%%%%%%%%%%%%%%%%%%%%%%%%%%%%%%%%%%%%%
%%%%%%%%%%%%%%%%%%%%%%%%%%%%%%%%%%%%%%%%%%%%%%%%%%%%%%%%%%%%%%%%
```

C.2 UKF algorithm

```
function [x_est,y_est] =UKF(Pe,Tm,Efd)

%%%%%%%%%%%%%%%%%%%%%%%%%%%%%%%%%%%%%%%%%%%%%%%%%%%%%%%%%%%%%%%%
%%%%%%%%%%%%%%%%%%%%%%%%%%%%%%%%%%%%%%%%%%%%%%%%%%%%%%%%%%%%%%%%
% Initialization

        XADU=2.15;
        XAQU=1.365;
        W0=2*60*3.14159;
        H=4;
        %H=4.75;
        JJ=2.*H;
        XL=0.15;
        A=0.031;
        B=6.93;
        VT1=0.8;
        XPD=0.375;
        XPQ=0.375;
        TPDO=0.131;
        XE=0.193;
        KD=0.05;
```

```
P=0.8;
QS=0.05;
VB=0.98;
PHI=atan2(QS,P);
IT=sqrt(P^2+QS^2)/VB;
VTT=sqrt((VB+XE*IT*sin(PHI))^2+(XE*IT*cos(PHI))^2);

if (VTT >= VT1),
   DV=A*exp(B*(VTT-VT1));
   ksd=VTT/(VTT+DV);
else,
   ksd=1.0;
end;
ksq=0.78;
XAD=ksd*XADU;
XAQ=ksq*XAQU;
XD=ksd*XADU+XL;
XQ=ksq*XAQU+XL;
XFFD=(XAD^2)/(W0*(XD-XPD));
XTD=XPD+XE;
XTQ=XQ+XE;
PF=cos(PHI);
QF=sin(PHI);
DELTA=atan2((XTQ*PF),((VB/IT)+XTQ*QF));
VBD=VB*sin(DELTA);
VBQ=VB*cos(DELTA);
TETA=DELTA+PHI;
ID=IT*sin(TETA);
IQ=IT*cos(TETA);
VQ=VBQ+XE*ID;
VD=VBD-XE*IQ;
VT=sqrt(VD*VD+VQ*VQ);

U1=XTD*ID+VBQ+(XD-XPD)*ID;  % Vf
ME=VD*ID+VQ*IQ;
U2=ME;   % Torque

W0=2*60*3.14159;
VB=0.98 ;
x_prime_d=XPD;
x_prime_q=XPQ;
xe=XE;
```

```
        xq=XQ;
        D=KD;
        T_prime_do=TPDO;
        xd=XD;
        T_prime_qo=0.013;

        u1=Tm;
        u2=Efd;

%%%%%%%%%%%%%%%%%%%%%%%%%%%%%%%%%%%%%%%%%%%%%%%%%%%%%%%%%%%%%%%%
%%%%%%%%%%%%%%%%%%%%%%%%%%%%%%%%%%%%%%%%%%%%%%%%%%%%%%%%%%%%%%%%

persistent x % State vector x = [roll; pitch]
persistent P % Error covariance matrix
persistent Qk % Driving noise covariance matrix
persistent Rk % Measurement noise covariance matrix
persistent Xm % Temporary buffer for predicted state sigma points
persistent Z % Temporary buffer for predicted measurement sigma points
persistent zk_g

if isempty(x)
    x=[0.4;0;0;0];
end

if isempty(P)
    P = ([10 0 0 0;0 10 0 0; 0 0 10 0; 0 0 0 10]);
end

if isempty(Qk)
      % must be modified to match your model.
      Qk = [1e-6 0 0 0; 0 1e-6 0 0; 0 0 1e-6 0; 0 0 0 1e-6];
end

if isempty(Rk)
    Rk = [1e-2].^2;  % must be modified to match your model.
end

if isempty(Xm)
    Xm = zeros(4,8);    % must be modified to match your model.
end

if isempty(Z)
```

```
    Z = zeros(1,8);  % must be modified to match your model.
end

%%%%%%%%%%%%%%%%%%%%%%%%%%%%%%%%%%%%%%%%%%%%%%%%%%%%%%%%%%%%
%%%%%%%%%%%%%%%%%%%%%%%%%%%%%%%%%%%%%%%%%%%%%%%%%%%%%%%%%%%%

zk_g=Pe;

X = ukf_sigmapoints(x,P);
n2 = size(X,2); % Size of the state vector multiplied by 2

for k = 1:n2
     Xm(:,k) = updatex(X(:,k),u1,u2);
end

[xm, Pm] = ukf_mean_covariance(Xm);
Pm = Pm + Qk;

% must be modified to match your model
%(only if the h function has more input or output parameters).
for k = 1:n2
    Z(:,k) = h(Xm(:,k));
end

[z, Pz] = ukf_mean_covariance(Z);
Pz = Pz + Rk;

Pxz = ukf_covariance(Xm, Z); % Cross covariance matrix

Kk = Pxz/Pz; % Kalman gain matrix
x = xm + Kk*(zk_g - z); % Find the state estimates
P = Pm - Kk*Pz*Kk'; % Estimation error covariance matrix
P = 0.5*(P+P'); % Prevent numerical problem

x_est = x;
y_est=z;

%%%%%%%%%%%%%%%%%%%%%%%%%%%%%%%%%%%%%%%%%%%%%%%%%%%%%%%%%%%%
%%%%%%%%%%%%%%%%%%%%%%%%%%%%%%%%%%%%%%%%%%%%%%%%%%%%%%%%%%%%
function xo = updatex(x,u1,u2)

Pe=[(VB/x_prime_d)*x(3)*sin(x(1))+(VB/2)*((1/xq)-(1/x_prime_d)*sin(2*x(1)))];
```

```
id=[(x(3)-VB*cos(x(1)))*(1/(XTD))];
iq=[VB*sin(x(1))*(1/(XTQ))];
%Pe=VB*sin(x(1))*id+VB*cos(x(1))*iq;

Ts=0.0001;

dx1=Ts*(W0*x(2))+x(1);
dx2=Ts*((1/JJ)*(u1-Pe-D*x(2)))+x(2);
dx3=Ts*((1/T_prime_do)*(u2-x(3)-(xd-x_prime_d)*id))+x(3);
dx4=Ts*((1/T_prime_qo)*(-x(4)+(xq-x_prime_q)*iq))+x(4);

xo=[dx1;dx2;dx3;dx4];

%%%%%%%%%%%%%%%%%%%%%%%%%%%%%%%%%%%%%%%%%%%%%%%%%%%%%%%%%%%%%%%%
%%%%%%%%%%%%%%%%%%%%%%%%%%%%%%%%%%%%%%%%%%%%%%%%%%%%%%%%%%%%%%%%

function z = h(x)

z=VB*sin(x(1))*[(x(3)-VB*cos(x(1)))*(1/(XTD))]+...
VB*cos(x(1))*[VB*sin(x(1))*(1/(XTQ))];

%%%%%%%%%%%%%%%%%%%%%%%%%%%%%%%%%%%%%%%%%%%%%%%%%%%%%%%%%%%%%%%%
%%%%%%%%%%%%%%%%%%%%%%%%%%%%%%%%%%%%%%%%%%%%%%%%%%%%%%%%%%%%%%%%

function X = ukf_sigmapoints(xbar,Pi)

n = size(xbar,1);
A = chol(n*Pi)'; % R = chol(A) where R'*R = A
X = [A -A] + repmat(xbar,1,n*2);

%%%%%%%%%%%%%%%%%%%%%%%%%%%%%%%%%%%%%%%%%%%%%%%%%%%%%%%%%%%%%%%%
%%%%%%%%%%%%%%%%%%%%%%%%%%%%%%%%%%%%%%%%%%%%%%%%%%%%%%%%%%%%%%%%

function [m, P] = ukf_mean_covariance(sigmaX)

n2 = size(sigmaX,2);
m = sum(sigmaX,2)/n2;
P = zeros(size(sigmaX,1)); % size n
for k = 1:n2
    P = P + ((sigmaX(:,k)-m)*(sigmaX(:,k)-m)');
end
P = P/n2;
```

```
%%%%%%%%%%%%%%%%%%%%%%%%%%%%%%%%%%%%%%%%%%%%%%%%%%%%%%%%%%%%%%%%
%%%%%%%%%%%%%%%%%%%%%%%%%%%%%%%%%%%%%%%%%%%%%%%%%%%%%%%%%%%%%%%%

function P = ukf_covariance(sigmaX, sigmaY)

n2 = size(sigmaX,2); % 2*n
mx = sum(sigmaX,2)/n2;
my = sum(sigmaY,2)/n2;
P = zeros(size(sigmaX,1),size(sigmaY,1)); % size n
for k = 1:n2
    P = P + ((sigmaX(:,k)-mx)*(sigmaY(:,k)-my)');
end
P = P/n2;

%%%%%%%%%%%%%%%%%%%%%%%%%%%%%%%%%%%%%%%%%%%%%%%%%%%%%%%%%%%%%%%%
%%%%%%%%%%%%%%%%%%%%%%%%%%%%%%%%%%%%%%%%%%%%%%%%%%%%%%%%%%%%%%%%
```

C.3 EKF-UI algorithm

```
function [x_est,y_est] =UKF(Pe,Tm,Efd)

%%%%%%%%%%%%%%%%%%%%%%%%%%%%%%%%%%%%%%%%%%%%%%%%%%%%%%%%%%%%%%%%
%%%%%%%%%%%%%%%%%%%%%%%%%%%%%%%%%%%%%%%%%%%%%%%%%%%%%%%%%%%%%%%%
% Initialization

       XADU=2.15;
       XAQU=1.365;
       W0=2*60*3.14159;
       H=4;
       %H=4.75;
       JJ=2.*H;
       XL=0.15;
       A=0.031;
       B=6.93;
       VT1=0.8;
       XPD=0.375;
       XPQ=0.375;
       TPDO=0.131;
```

```
XE=0.193;
KD=0.05;
P=0.8;
QS=0.05;
VB=0.98;
PHI=atan2(QS,P);
IT=sqrt(P^2+QS^2)/VB;
VTT=sqrt((VB+XE*IT*sin(PHI))^2+(XE*IT*cos(PHI))^2);

if (VTT >= VT1),
   DV=A*exp(B*(VTT-VT1));
   ksd=VTT/(VTT+DV);
else,
   ksd=1.0;
end;
ksq=0.78;
XAD=ksd*XADU;
XAQ=ksq*XAQU;
XD=ksd*XADU+XL;
XQ=ksq*XAQU+XL;
XFFD=(XAD^2)/(W0*(XD-XPD));
XTD=XPD+XE;
XTQ=XQ+XE;
PF=cos(PHI);
QF=sin(PHI);
DELTA=atan2((XTQ*PF),((VB/IT)+XTQ*QF));
VBD=VB*sin(DELTA);
VBQ=VB*cos(DELTA);
TETA=DELTA+PHI;
ID=IT*sin(TETA);
IQ=IT*cos(TETA);
VQ=VBQ+XE*ID;
VD=VBD-XE*IQ;
VT=sqrt(VD*VD+VQ*VQ);

U1=XTD*ID+VBQ+(XD-XPD)*ID;  % Vf
ME=VD*ID+VQ*IQ;
U2=ME;   % Torque

W0=2*60*3.14159;
VB=0.98 ;
x_prime_d=XPD;
```

```
        x_prime_q=XPQ;
        xe=XE;
        xq=XQ;
        D=KD;
        T_prime_do=TPDO;
        xd=XD;
        T_prime_qo=0.013;

        u1=Tm;
        u2=Efd;

%%%%%%%%%%%%%%%%%%%%%%%%%%%%%%%%%%%%%%%%%%%%%%%%%%%%%%%%%%%%%%%%
%%%%%%%%%%%%%%%%%%%%%%%%%%%%%%%%%%%%%%%%%%%%%%%%%%%%%%%%%%%%%%%%

function [x_est  ,y_est  ,u_est  ] =EKF_UI(Pe,Qe,Tm)

u1=Tm;
n=4;
yk=[Pe;Qe];

persistent Pk_1
persistent Qk_1
persistent Rk
persistent x
persistent u2x
persistent u2x_k_plus_1
persistent S_k

if isempty(Pk_1)  Pk_1=([10 0 0 0;0 10 0 0; 0 0 10 0; 0 0 0 10]).^2;end
if isempty(x)     x=[0;0;0;0];end
if isempty(Qk_1)  Qk_1=0.1^2*eye(4);end
if isempty(Rk)    Rk=0.1^2*eye(2);end
if isempty(u2x)   u2x=0;end
if isempty(u2x_k_plus_1)   u2x_k_plus_1=0;end
if isempty(S_k)   S_k=0;end

%%%%%%%%%%%%%%%%%%%%%%%%%%%%%%%%%%%%%%%%%%%%%%%%%%%%%%%%%%%%%%%%
%%%%%%%%%%%%%%%%%%%%%%%%%%%%%%%%%%%%%%%%%%%%%%%%%%%%%%%%%%%%%%%%
%%%% Step I : Prediction

[Gk_1,x_k,B_k_1]=sys(x,u1,u2x);
```

```
[h_est_k,H_k]=measurement(x_k);

%%%% Step II : Gain Computaion

P_k=Gk_1*Pk_1*Gk_1'+Qk_1;
K_k=P_k*H_k'*inv(Rk+H_k*P_k*H_k');
S_k=inv(B_k_1'*H_k'*inv(Rk)*(eye(2)-H_k*K_k)*H_k*B_k_1);

%%%% Step III : Update

u2x_k_plus_1=S_k*B_k_1'*H_k'*inv(Rk)*(eye(2)-H_k*K_k)*...
[yk-h_est_k+H_k*B_k_1*u2x];

x=x_k+K_k*(yk-h_est_k);

Pk_1=(eye(4)-K_k*H_k)*[P_k+B_k_1*S_k*B_k_1'*(eye(4)-K_k*H_k)'];

%%%%%%%%%%%%%%%%%%%%%%%%%%%%%%%%%%%%%%%%%%%%%%%%%%%%%%%%%%%%
%%%%%%%%%%%%%%%%%%%%%%%%%%%%%%%%%%%%%%%%%%%%%%%%%%%%%%%%%%%%

u2x=u2x_k_plus_1;
x_est=x;
u_est=u2x;
y_est=h_est_k;


%%%%%%%%%%%%%%%%%%%%%%%%%%%%%%%%%%%%%%%%%%%%%%%%%%%%%%%%%%%%
%%%%%%%%%%%%%%%%%%%%%%%%%%%%%%%%%%%%%%%%%%%%%%%%%%%%%%%%%%%%

function [Gk_1,x_k,B_k_1]=sys(x,u1,u2x)

Ts=0.001;

Gk_1=[1   (Ts*W0)    0    0;
     (-Ts/J)*((VB*x(3)*cos(x(1))/XTD)+VB*VB*((-1/XTD)+(+1/XTQ))*...
     (cos(x(1))^2-sin(x(1))^2))   (-(Ts/J)*D+1)  (-Ts/J)*(VB*sin(x(1))/XTD)   0;
     (Ts/T_prime_do)*(xd-x_prime_d)*VB*-1*sin(x(1))*(1/XTD)    0  ...
     (1+(-Ts/T_prime_do)*(1+((xd-x_prime_d)/XTD))) 0;
     (Ts/T_prime_qo)*(xq-x_prime_q)*VB*cos(x(1))*(1/XTQ)  0    0  ...
     (-(Ts/T_prime_qo)+1)];

Tm=u1;
```

```
Efd=u2x;

id=[(x(3)-VB*cos(x(1)))*(1/(x_prime_d+xe))];
iq=[VB*sin(x(1))*(1/(xq+xe))];
Pe=VB*sin(x(1))*[(x(3)-VB*cos(x(1)))*(1/(x_prime_d+xe))]+...
VB*cos(x(1))*[VB*sin(x(1))*(1/(xq+xe))];

dx1=Ts*(W0*x(2))+x(1);
dx2=Ts*((1/J)*(Tm-Pe-D*x(2)))+x(2);
dx3=Ts*((1/T_prime_do)*(Efd-x(3)-(xd-x_prime_d)*id))+x(3);
dx4=Ts*((1/T_prime_qo)*(-x(4)+(xq-x_prime_q)*iq))+x(4);

x_k=[dx1;dx2;dx3;dx4];

B_k_1=[0;0;(Ts/T_prime_do);0];

%%%%%%%%%%%%%%%%%%%%%%%%%%%%%%%%%%%%%%%%%%%%%%%%%%%%%%%%%%%%
%%%%%%%%%%%%%%%%%%%%%%%%%%%%%%%%%%%%%%%%%%%%%%%%%%%%%%%%%%%%

function [h_est_k,H_k]=measurement(x)

h_est_k1=VB*sin(x(1))*(x(3)-VB*cos(x(1)))*(1/(XTD))+...
VB*cos(x(1))*VB*sin(x(1))*(1/(XTQ));
h_est_k2=VB*cos(x(1))*((x(3)-VB*cos(x(1))))*(1/(XTD))-...
VB*sin(x(1))*VB*sin(x(1))*(1/(XTQ));
h_est_k=[h_est_k1;h_est_k2];

H_k=[((VB*x(3)*cos(x(1))/XTD)+VB*VB*((-1/XTD)+(1/XTQ))*...
(cos(x(1))^2-sin(x(1))^2)) 0 (VB*sin(x(1))/XTD) 0;
     ((-VB*x(3)*sin(x(1))/XTD)-2*VB*VB*sin(x(1))*cos(x(1))*...
     ((-1/XTD)+(1/XTQ))) 0 (VB*cos(x(1))/XTD) 0];
```

Appendix D

Running the PSAT Simulink files in m-file version

In this appendix a short description about the parameter tuning implementation using the genetic algorithm in PSAT toolbox will be given. As mentioned before, all the simulations in chapter 5 were done in PSAT [99]. In PSAT, for time-domain analysis the Simulink file formats must be converted to m-file formats. In the m-file format, each device or model in the Simulink file has a vector or matrix which represents that component in the m-file version.

For example the matrix Bus.con represents the buses and includes the bus data. In a similar way, we would have Line.con for the lines of power system, PV.con for the PV buses, PQ.con for the load buses (PQ buses), Syn.con for the synchronous machines, Exc.con for the excitation systems data and if the Simulink file includes FACTS devices we would have Upfc.con for UPFC, Svc.con for SVC and Statcom.con for STATCOM. For example for UPFC, PSS and POD we would have the afore-mentioned vector in the following forms:

```
Upfc.con = [ ...
   8  1  100  13.8  60  30  75  0.005  0.1  -0.1  ...
   0.1  -0.1  3  -1  0  0  1  1];

Pss.con = [ ...
  1  2  1  0.1  -0.1  5  10  0.38  0.02  0.38  0.02  ...
  25  0.5  20  5  0.045  0.045  0.045  -0.045  1  0.95  0 ];

Pod.con = [ ...
  11  1  4  5  0.12  -0.12  -1.37  3  0.2172  ...
  0.2928  0.2172  0.2928  0.001  1 ];
```

So by using the above vector in the m-file format, if we want to set new values for the parameters of the PSS or POD, we can easily update Pss.con and Pod.con in the m-file version (of the Simulink file) and then by running the updated version of m-file, we

can analyze the influence of those modifications on the network variables such as speed deviations of generators and voltage magnitudes of buses. Finally, we can calculate the objective function after each modification.

In summary, when we want to calculate the objective function for an individual of the genetic algorithm, we should modify the values of the PSS or POD in Pss.con and Pod.con using that individual as the new parameters. Then, by running the updated m-file, which now represents the updated network with new values for PSS (or POD), we can calculate the objective function defined in (3) using the speed deviations of generators. By calculating the objective function for each individual, we can rank all the individuals of the current generation to be used for generating the next population.

After installing the PSAT software in MATLAB directory and before running the m-file version of a Simulink file in PSAT, we must run PSAT to define the variables and initializations. Then we can easily run the m-file version of implemented Simulink file. Here, as an example we present the commands for running a Simulink (.mdl file) file in workspace:

```
>> psat % running PSAT
>> initpsat % initialize PSAT
>> clpsat.readfile = 0; % do not reload data file
>> runpsat('d_014_pss_mdl.m','data'); % set data file
>> Settings.t0=0; % set starting time for simulation
>> Settings.tf=20; % set ending time for simulation
>> runpsat('pf'); % running the power flow calculation
>> runpsat('td'); % running time-domain simulation
>> t=Varout.t;   %   time vector from output matrix
>> voltages=Varout.vars(:,DAE.n+Bus.n+1: DAE.n+2*Bus.n);
>> Bus_voltage_1=voltages(:,1); %   voltage of bus 1
>> Bus_voltage_2=voltages(:,2); %   voltage of bus 2
>> Power_1=Varout.vars(:,89); %   output power of bus 1
>> Power_2=Varout.vars(:,97); %   output power of bus 2
>> Rotor_Speed_1=Varout.vars(:,2); %  rotor speed of gen. 1
>> Rotor_Speed_2=Varout.vars(:,13); % rotor speed of gen. 2
>> figure; % plotting the rotor speeds of gen. 1 and gen. 2
>> plot(t,Rotor_Speed_1,t,Rotor_Speed_2);
>> figure; % plotting the output power of gen. 1 and gen. 2
>> plot(t,Power_1,t,Power_2);
>> figure; % plotting the bus voltages of gen. 1 and gen. 2
>> plot(t,Bus_voltage_1,t,Bus_voltage_2);
```

Appendix E

Test System Networks

E.1 9-Bus Test System

Figure E.1 depicts the 9-bus test system which represents three generators.

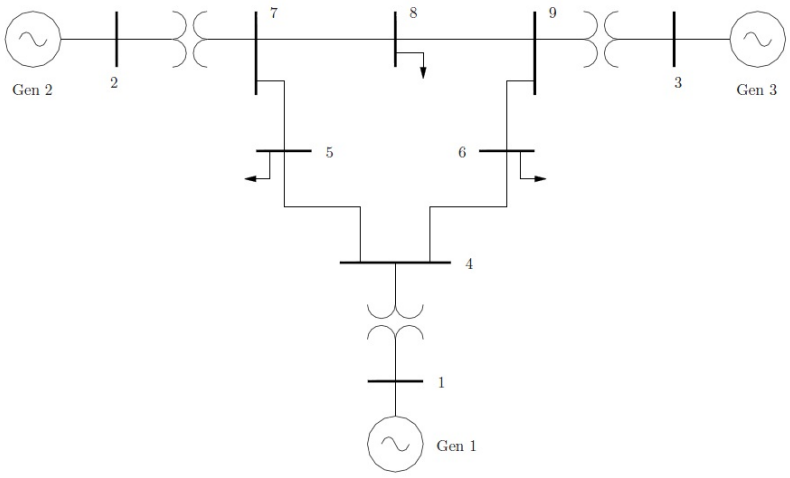

Figure E.1: The 9-bus test system.

The complete data of this network in Matpower format are as follows:

```
%% case stduy: case9

%%-----  Power Flow Data  -----%%
%% system MVA base
mpc.baseMVA = 100;

%% bus data
```

```
% bus_i type Pd Qd Gs Bs area Vm Va baseKV zone Vmax Vmin
mpc.bus = [
1 3 0 0 0 0 1 1 0 345 1 1.1 0.9;
2 2 0 0 0 0 1 1 0 345 1 1.1 0.9;
3 2 0 0 0 0 1 1 0 345 1 1.1 0.9;
4 1 0 0 0 0 1 1 0 345 1 1.1 0.9;
5 1 90 30 0 0 1 1 0 345 1 1.1 0.9;
6 1 0 0 0 0 1 1 0 345 1 1.1 0.9;
7 1 100 35 0 0 1 1 0 345 1 1.1 0.9;
8 1 0 0 0 0 1 1 0 345 1 1.1 0.9;
9 1 125 50 0 0 1 1 0 345 1 1.1 0.9;
];

%% generator data
% bus Pg Qg Qmax Qmin Vg mBase status Pmax Pmin Pc1 Pc2 Qc1min Qc1max Qc2min
Qc2max ramp_agc ramp_10 ramp_30 ramp_q apf
mpc.gen = [
1 0 0 300 -300 1 100 1 250 10 0 0 0 0 0 0 0 0 0 0 0;
2 163 0 300 -300 1 100 1 300 10 0 0 0 0 0 0 0 0 0 0 0;
3 85 0 300 -300 1 100 1 270 10 0 0 0 0 0 0 0 0 0 0 0;
];

%% branch data
% fbus tbus r x b rateA rateB rateC ratio angle status angmin angmax
mpc.branch = [
1 4 0 0.0576 0 250 250 250 0 0 1 -360 360;
4 5 0.017 0.092 0.158 250 250 250 0 0 1 -360 360;
5 6 0.039 0.17 0.358 150 150 150 0 0 1 -360 360;
3 6 0 0.0586 0 300 300 300 0 0 1 -360 360;
6 7 0.0119 0.1008 0.209 150 150 150 0 0 1 -360 360;
7 8 0.0085 0.072 0.149 250 250 250 0 0 1 -360 360;
8 2 0 0.0625 0 250 250 250 0 0 1 -360 360;
8 9 0.032 0.161 0.306 250 250 250 0 0 1 -360 360;
9 4 0.01 0.085 0.176 250 250 250 0 0 1 -360 360;
];
```

E.2 14-Bus Test System

The 14-bus test system is shown in Figure E.2.

The complete data of this network in Matpower format are as follows:

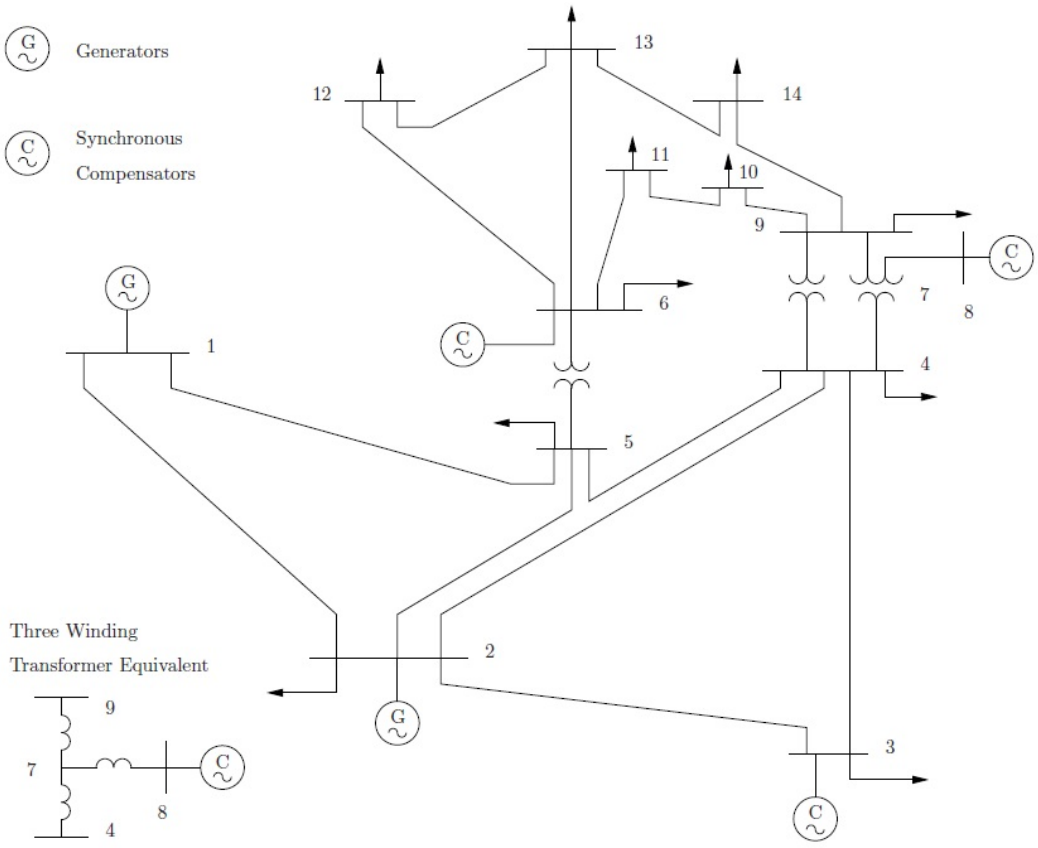

Figure E.2: The 14-bus test system.

```
%% case study: case14

%%-----  Power Flow Data  -----%%
%% system MVA base
mpc.baseMVA = 100;

%% bus data
% bus_i type Pd Qd Gs Bs area Vm Va baseKV zone Vmax Vmin
mpc.bus = [
1 3 0 0 0 0 1 1.06 0 69 1 1.06 0.94;
2 2 21.7 12.7 0 0 1 1.045 -4.98 69 1 1.06 0.94;
3 2 94.2 19 0 0 1 1.01 -12.72 69 1 1.06 0.94;
4 1 47.8 -3.9 0 0 1 1.019 -10.33 69 1 1.06 0.94;
5 1 7.6 1.6 0 0 1 1.02 -8.78 69 1 1.06 0.94;
6 2 11.2 7.5 0 0 1 1.07 -14.22 13.8 1 1.06 0.94;
7 1 0 0 0 0 1 1.062 -13.37 13.8 1 1.06 0.94;
8 2 0 0 0 0 1 1.09 -13.36 18 1 1.06 0.94;
```

```
9 1 29.5 16.6 0 19 1 1.056 -14.94 13.8 1 1.06 0.94;
10 1 9 5.8 0 0 1 1.051 -15.1 13.8 1 1.06 0.94;
11 1 3.5 1.8 0 0 1 1.057 -14.79 13.8 1 1.06 0.94;
12 1 6.1 1.6 0 0 1 1.055 -15.07 13.8 1 1.06 0.94;
13 1 13.5 5.8 0 0 1 1.05 -15.16 13.8 1 1.06 0.94;
14 1 14.9 5 0 0 1 1.036 -16.04 13.8 1 1.06 0.94;
];

%% generator data
% bus Pg Qg Qmax Qmin Vg mBase status Pmax Pmin Pc1 Pc2 Qc1min Qc1max Qc2min
Qc2max ramp_agc ramp_10 ramp_30 ramp_q apf
mpc.gen = [
1 232.4 -16.9 10 0 1.06 100 1 332.4 0 0 0 0 0 0 0 0 0 0 0 0;
2 40 42.4 50 -40 1.045 100 1 140 0 0 0 0 0 0 0 0 0 0 0 0;
3 0 23.4 40 0 1.01 100 1 100 0 0 0 0 0 0 0 0 0 0 0 0;
6 0 12.2 24 -6 1.07 100 1 100 0 0 0 0 0 0 0 0 0 0 0 0;
8 0 17.4 24 -6 1.09 100 1 100 0 0 0 0 0 0 0 0 0 0 0 0;
];

%% branch data
% fbus tbus r x b rateA rateB rateC ratio angle status angmin angmax
mpc.branch = [
1 2 0.01938 0.05917 0.0528 220 0 0 0 0 1 -360 360;
1 5 0.05403 0.22304 0.0492 220 0 0 0 0 1 -360 360;
2 3 0.04699 0.19797 0.0438 220 0 0 0 0 1 -360 360;
2 4 0.05811 0.17632 0.034 220 0 0 0 0 1 -360 360;
2 5 0.05695 0.17388 0.0346 220 0 0 0 0 1 -360 360;
3 4 0.06701 0.17103 0.0128 220 0 0 0 0 1 -360 360;
4 5 0.01335 0.04211 0 220 0 0 0 0 1 -360 360;
4 7 0 0.20912 0 220 0 0 0.978 0 1 -360 360;
4 9 0 0.55618 0 220 0 0 0.969 0 1 -360 360;
5 6 0 0.25202 0 220 0 0 0.932 0 1 -360 360;
6 11 0.09498 0.1989 0 220 0 0 0 0 1 -360 360;
6 12 0.12291 0.25581 0 220 0 0 0 0 1 -360 360;
6 13 0.06615 0.13027 0 220 0 0 0 0 1 -360 360;
7 8 0 0.17615 0 220 0 0 0 0 1 -360 360;
7 9 0 0.11001 0 220 0 0 0 0 1 -360 360;
9 10 0.03181 0.0845 0 220 0 0 0 0 1 -360 360;
9 14 0.12711 0.27038 0 220 0 0 0 0 1 -360 360;
10 11 0.08205 0.19207 0 220 0 0 0 0 1 -360 360;
12 13 0.22092 0.19988 0 220 0 0 0 0 1 -360 360;
13 14 0.17093 0.34802 0 220 0 0 0 0 1 -360 360;
```

```
];
```

E.3 30-Bus Test System

The 30-bus test system is shown in Figure E.3.

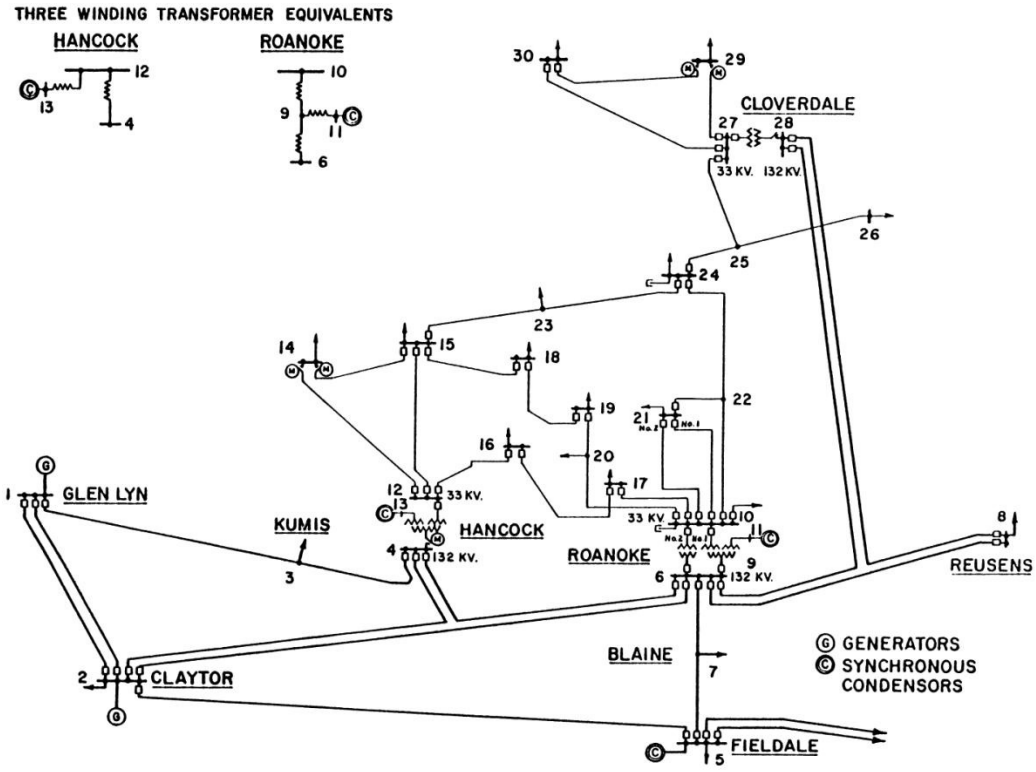

Figure E.3: The 30-bus test system.

The complete data of this network in Matpower format are as follows:

```
%% case study: case14

%%-----  Power Flow Data  -----%%
%% system MVA base
mpc.baseMVA = 100;

%% bus data
% bus_i type Pd Qd Gs Bs area Vm Va baseKV zone Vmax Vmin
mpc.bus = [
```

```
1 3 0 0 0 0 1 1 0 135 1 1.05 0.95;
2 2 21.7 12.7 0 0 1 1 0 135 1 1.1 0.95;
3 1 2.4 1.2 0 0 1 1 0 135 1 1.05 0.95;
4 1 7.6 1.6 0 0 1 1 0 135 1 1.05 0.95;
5 1 0 0 0 0.19 1 1 0 135 1 1.05 0.95;
6 1 0 0 0 0 1 1 0 135 1 1.05 0.95;
7 1 22.8 10.9 0 0 1 1 0 135 1 1.05 0.95;
8 1 30 30 0 0 1 1 0 135 1 1.05 0.95;
9 1 0 0 0 0 1 1 0 135 1 1.05 0.95;
10 1 5.8 2 0 0 3 1 0 135 1 1.05 0.95;
11 1 0 0 0 0 1 1 0 135 1 1.05 0.95;
12 1 11.2 7.5 0 0 2 1 0 135 1 1.05 0.95;
13 2 0 0 0 0 2 1 0 135 1 1.1 0.95;
14 1 6.2 1.6 0 0 2 1 0 135 1 1.05 0.95;
15 1 8.2 2.5 0 0 2 1 0 135 1 1.05 0.95;
16 1 3.5 1.8 0 0 2 1 0 135 1 1.05 0.95;
17 1 9 5.8 0 0 2 1 0 135 1 1.05 0.95;
18 1 3.2 0.9 0 0 2 1 0 135 1 1.05 0.95;
19 1 9.5 3.4 0 0 2 1 0 135 1 1.05 0.95;
20 1 2.2 0.7 0 0 2 1 0 135 1 1.05 0.95;
21 1 17.5 11.2 0 0 3 1 0 135 1 1.05 0.95;
22 2 0 0 0 0 3 1 0 135 1 1.1 0.95;
23 2 3.2 1.6 0 0 2 1 0 135 1 1.1 0.95;
24 1 8.7 6.7 0 0.04 3 1 0 135 1 1.05 0.95;
25 1 0 0 0 0 3 1 0 135 1 1.05 0.95;
26 1 3.5 2.3 0 0 3 1 0 135 1 1.05 0.95;
27 2 0 0 0 0 3 1 0 135 1 1.1 0.95;
28 1 0 0 0 0 1 1 0 135 1 1.05 0.95;
29 1 2.4 0.9 0 0 3 1 0 135 1 1.05 0.95;
30 1 10.6 1.9 0 0 3 1 0 135 1 1.05 0.95;
];

%% generator data
% bus Pg Qg Qmax Qmin Vg mBase status Pmax Pmin Pc1 Pc2 Qc1min Qc1max Qc2min
Qc2max ramp_agc ramp_10 ramp_30 ramp_q apf
mpc.gen = [
1 23.54 0 150 -20 1 100 1 80 0 0 0 0 0 0 0 0 0 0 0 0;
2 60.97 0 60 -20 1 100 1 80 0 0 0 0 0 0 0 0 0 0 0 0;
22 21.59 0 62.5 -15 1 100 1 50 0 0 0 0 0 0 0 0 0 0 0 0;
27 26.91 0 48.7 -15 1 100 1 55 0 0 0 0 0 0 0 0 0 0 0 0;
23 19.2 0 40 -10 1 100 1 30 0 0 0 0 0 0 0 0 0 0 0 0;
13 37 0 44.7 -15 1 100 1 40 0 0 0 0 0 0 0 0 0 0 0 0;
```

```
];


%% branch data
% fbus tbus r x b rateA rateB rateC ratio angle status angmin angmax
mpc.branch = [
1 2 0.02 0.06 0.03 130 130 130 0 0 1 -360 360;
1 3 0.05 0.19 0.02 130 130 130 0 0 1 -360 360;
2 4 0.06 0.17 0.02 65 65 65 0 0 1 -360 360;
3 4 0.01 0.04 0 130 130 130 0 0 1 -360 360;
2 5 0.05 0.2 0.02 130 130 130 0 0 1 -360 360;
2 6 0.06 0.18 0.02 65 65 65 0 0 1 -360 360;
4 6 0.01 0.04 0 90 90 90 0 0 1 -360 360;
5 7 0.05 0.12 0.01 70 70 70 0 0 1 -360 360;
6 7 0.03 0.08 0.01 130 130 130 0 0 1 -360 360;
6 8 0.01 0.04 0 65 65 65 0 0 1 -360 360;
6 9 0 0.21 0 65 65 65 0 0 1 -360 360;
6 10 0 0.56 0 32 32 32 0 0 1 -360 360;
9 11 0 0.21 0 65 65 65 0 0 1 -360 360;
9 10 0 0.11 0 65 65 65 0 0 1 -360 360;
4 12 0 0.26 0 65 65 65 0 0 1 -360 360;
12 13 0 0.14 0 65 65 65 0 0 1 -360 360;
12 14 0.12 0.26 0 32 32 32 0 0 1 -360 360;
12 15 0.07 0.13 0 32 32 32 0 0 1 -360 360;
12 16 0.09 0.2 0 32 32 32 0 0 1 -360 360;
14 15 0.22 0.2 0 16 16 16 0 0 1 -360 360;
16 17 0.08 0.19 0 16 16 16 0 0 1 -360 360;
15 18 0.11 0.22 0 16 16 16 0 0 1 -360 360;
18 19 0.06 0.13 0 16 16 16 0 0 1 -360 360;
19 20 0.03 0.07 0 32 32 32 0 0 1 -360 360;
10 20 0.09 0.21 0 32 32 32 0 0 1 -360 360;
10 17 0.03 0.08 0 32 32 32 0 0 1 -360 360;
10 21 0.03 0.07 0 32 32 32 0 0 1 -360 360;
10 22 0.07 0.15 0 32 32 32 0 0 1 -360 360;
21 22 0.01 0.02 0 65 65 65 0 0 1 -360 360;
15 23 0.1 0.2 0 16 16 16 0 0 1 -360 360;
22 24 0.12 0.18 0 16 16 16 0 0 1 -360 360;
23 24 0.13 0.27 0 16 16 16 0 0 1 -360 360;
24 25 0.19 0.33 0 16 16 16 0 0 1 -360 360;
25 26 0.25 0.38 0 16 16 16 0 0 1 -360 360;
25 27 0.11 0.21 0 16 16 16 0 0 1 -360 360;
28 27 0 0.4 0 65 65 65 0 0 1 -360 360;
```

```
27 29 0.22 0.42 0 16 16 16 0 0 1 -360 360;
27 30 0.32 0.6 0 16 16 16 0 0 1 -360 360;
29 30 0.24 0.45 0 16 16 16 0 0 1 -360 360;
8 28 0.06 0.2 0.02 32 32 32 0 0 1 -360 360;
6 28 0.02 0.06 0.01 32 32 32 0 0 1 -360 360;
];
```

E.4 39-Bus Test System

The 39-bus test system is presented in Figure E.4.

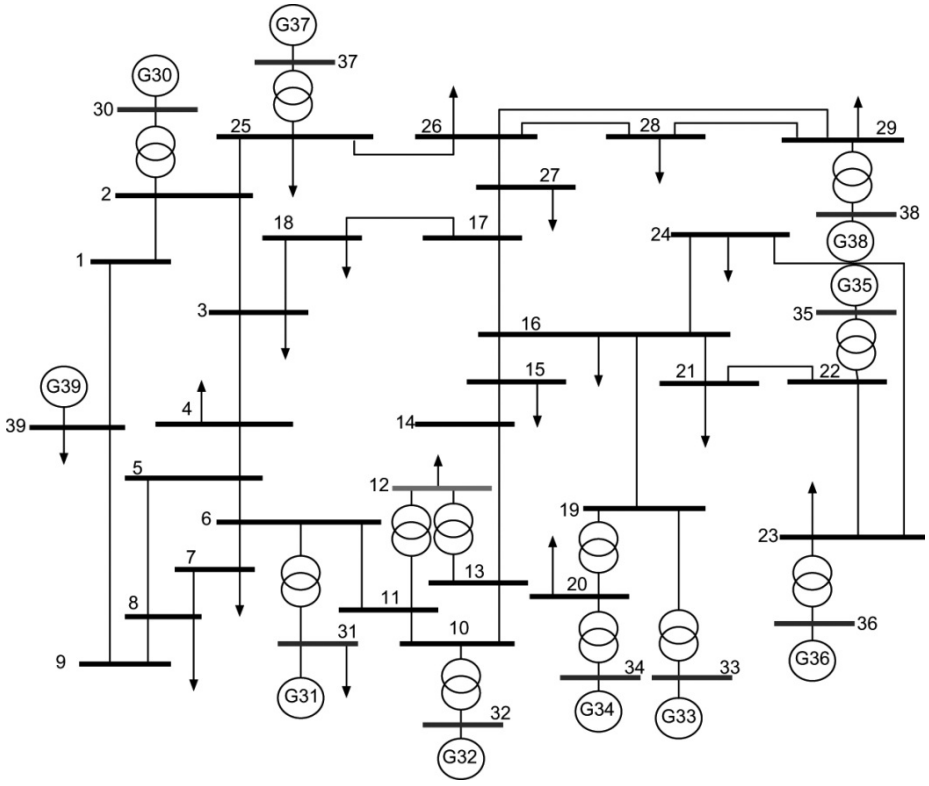

Figure E.4: The 39-bus test system.

The complete data of this network in Matpower format are as follows:

```
%% case study: case39
%% MATPOWER Case Format : Version 2
mpc.version = '2';
```

```
%%-----  Power Flow Data  -----%%
%% system MVA base
mpc.baseMVA = 100;

%% bus data
% bus_i type Pd Qd Gs Bs area Vm Va baseKV zone Vmax Vmin
mpc.bus = [
1 1 97.6 44.2 0 0 2 1.0393836 -13.536602 345 1 1.06 0.94;
2 1 0 0 0 0 2 1.0484941 -9.7852666 345 1 1.06 0.94;
3 1 322 2.4 0 0 2 1.0307077 -12.276384 345 1 1.06 0.94;
4 1 500 184 0 0 1 1.00446 -12.626734 345 1 1.06 0.94;
5 1 0 0 0 0 1 1.0060063 -11.192339 345 1 1.06 0.94;
6 1 0 0 0 0 1 1.0082256 -10.40833 345 1 1.06 0.94;
7 1 233.8 84 0 0 1 0.99839728 -12.755626 345 1 1.06 0.94;
8 1 522 176.6 0 0 1 0.99787232 -13.335844 345 1 1.06 0.94;
9 1 6.5 -66.6 0 0 1 1.038332 -14.178442 345 1 1.06 0.94;
10 1 0 0 0 0 1 1.0178431 -8.170875 345 1 1.06 0.94;
11 1 0 0 0 0 1 1.0133858 -8.9369663 345 1 1.06 0.94;
12 1 8.53 88 0 0 1 1.000815 -8.9988236 345 1 1.06 0.94;
13 1 0 0 0 0 1 1.014923 -8.9299272 345 1 1.06 0.94;
14 1 0 0 0 0 1 1.012319 -10.715295 345 1 1.06 0.94;
15 1 320 153 0 0 3 1.0161854 -11.345399 345 1 1.06 0.94;
16 1 329 32.3 0 0 3 1.0325203 -10.033348 345 1 1.06 0.94;
17 1 0 0 0 0 2 1.0342365 -11.116436 345 1 1.06 0.94;
18 1 158 30 0 0 2 1.0315726 -11.986168 345 1 1.06 0.94;
19 1 0 0 0 0 3 1.0501068 -5.4100729 345 1 1.06 0.94;
20 1 680 103 0 0 3 0.99101054 -6.8211783 345 1 1.06 0.94;
21 1 274 115 0 0 3 1.0323192 -7.6287461 345 1 1.06 0.94;
22 1 0 0 0 0 3 1.0501427 -3.1831199 345 1 1.06 0.94;
23 1 247.5 84.6 0 0 3 1.0451451 -3.3812763 345 1 1.06 0.94;
24 1 308.6 -92.2 0 0 3 1.038001 -9.9137585 345 1 1.06 0.94;
25 1 224 47.2 0 0 2 1.0576827 -8.3692354 345 1 1.06 0.94;
26 1 139 17 0 0 2 1.0525613 -9.4387696 345 1 1.06 0.94;
27 1 281 75.5 0 0 2 1.0383449 -11.362152 345 1 1.06 0.94;
28 1 206 27.6 0 0 3 1.0503737 -5.9283592 345 1 1.06 0.94;
29 1 283.5 26.9 0 0 3 1.0501149 -3.1698741 345 1 1.06 0.94;
30 2 0 0 0 0 2 1.0499 -7.3704746 345 1 1.06 0.94;
31 3 9.2 4.6 0 0 1 0.982 0 345 1 1.06 0.94;
32 2 0 0 0 0 1 0.9841 -0.1884374 345 1 1.06 0.94;
33 2 0 0 0 0 3 0.9972 -0.19317445 345 1 1.06 0.94;
34 2 0 0 0 0 3 1.0123 -1.631119 345 1 1.06 0.94;
35 2 0 0 0 0 3 1.0494 1.7765069 345 1 1.06 0.94;
```

```
36 2 0 0 0 0 3 1.0636 4.4684374 345 1 1.06 0.94;
37 2 0 0 0 0 2 1.0275 -1.5828988 345 1 1.06 0.94;
38 2 0 0 0 0 3 1.0265 3.8928177 345 1 1.06 0.94;
39 2 1104 250 0 0 1 1.03 -14.535256 345 1 1.06 0.94;
];

%% generator data
% bus Pg Qg Qmax Qmin Vg mBase status Pmax Pmin Pc1 Pc2 Qc1min Qc1max Qc2min
Qc2max ramp_agc ramp_10 ramp_30 ramp_q apf
mpc.gen = [
30 250 161.762 400 140 1.0499 100 1 1040 0 0 0 0 0 0 0 0 0 0 0 0;
31 677.871 221.574 300 -100 0.982 100 1 646 0 0 0 0 0 0 0 0 0 0 0 0;
32 650 206.965 300 150 0.9841 100 1 725 0 0 0 0 0 0 0 0 0 0 0 0;
33 632 108.293 250 0 0.9972 100 1 652 0 0 0 0 0 0 0 0 0 0 0 0;
34 508 166.688 167 0 1.0123 100 1 508 0 0 0 0 0 0 0 0 0 0 0 0;
35 650 210.661 300 -100 1.0494 100 1 687 0 0 0 0 0 0 0 0 0 0 0 0;
36 560 100.165 240 0 1.0636 100 1 580 0 0 0 0 0 0 0 0 0 0 0 0;
37 540 -1.36945 250 0 1.0275 100 1 564 0 0 0 0 0 0 0 0 0 0 0 0;
38 830 21.7327 300 -150 1.0265 100 1 865 0 0 0 0 0 0 0 0 0 0 0 0;
39 1000 78.4674 300 -100 1.03 100 1 1100 0 0 0 0 0 0 0 0 0 0 0 0;
];

%% branch data
% fbus tbus r x b rateA rateB rateC ratio angle status angmin angmax
mpc.branch = [
1 2 0.0035 0.0411 0.6987 600 600 600 0 0 1 -360 360;
1 39 0.001 0.025 0.75 1000 1000 1000 0 0 1 -360 360;
2 3 0.0013 0.0151 0.2572 500 500 500 0 0 1 -360 360;
2 25 0.007 0.0086 0.146 500 500 500 0 0 1 -360 360;
2 30 0 0.0181 0 900 900 2500 1.025 0 1 -360 360;
3 4 0.0013 0.0213 0.2214 500 500 500 0 0 1 -360 360;
3 18 0.0011 0.0133 0.2138 500 500 500 0 0 1 -360 360;
4 5 0.0008 0.0128 0.1342 600 600 600 0 0 1 -360 360;
4 14 0.0008 0.0129 0.1382 500 500 500 0 0 1 -360 360;
5 6 0.0002 0.0026 0.0434 1200 1200 1200 0 0 1 -360 360;
5 8 0.0008 0.0112 0.1476 900 900 900 0 0 1 -360 360;
6 7 0.0006 0.0092 0.113 900 900 900 0 0 1 -360 360;
6 11 0.0007 0.0082 0.1389 480 480 480 0 0 1 -360 360;
6 31 0 0.025 0 1800 1800 1800 1.07 0 1 -360 360;
7 8 0.0004 0.0046 0.078 900 900 900 0 0 1 -360 360;
8 9 0.0023 0.0363 0.3804 900 900 900 0 0 1 -360 360;
9 39 0.001 0.025 1.2 900 900 900 0 0 1 -360 360;
```

```
10 11 0.0004 0.0043 0.0729 600 600 600 0 0 1 -360 360;
10 13 0.0004 0.0043 0.0729 600 600 600 0 0 1 -360 360;
10 32 0 0.02 0 900 900 2500 1.07 0 1 -360 360;
12 11 0.0016 0.0435 0 500 500 500 1.006 0 1 -360 360;
12 13 0.0016 0.0435 0 500 500 500 1.006 0 1 -360 360;
13 14 0.0009 0.0101 0.1723 600 600 600 0 0 1 -360 360;
14 15 0.0018 0.0217 0.366 600 600 600 0 0 1 -360 360;
15 16 0.0009 0.0094 0.171 600 600 600 0 0 1 -360 360;
16 17 0.0007 0.0089 0.1342 600 600 600 0 0 1 -360 360;
16 19 0.0016 0.0195 0.304 600 600 2500 0 0 1 -360 360;
16 21 0.0008 0.0135 0.2548 600 600 600 0 0 1 -360 360;
16 24 0.0003 0.0059 0.068 600 600 600 0 0 1 -360 360;
17 18 0.0007 0.0082 0.1319 600 600 600 0 0 1 -360 360;
17 27 0.0013 0.0173 0.3216 600 600 600 0 0 1 -360 360;
19 20 0.0007 0.0138 0 900 900 2500 1.06 0 1 -360 360;
19 33 0.0007 0.0142 0 900 900 2500 1.07 0 1 -360 360;
20 34 0.0009 0.018 0 900 900 2500 1.009 0 1 -360 360;
21 22 0.0008 0.014 0.2565 900 900 900 0 0 1 -360 360;
22 23 0.0006 0.0096 0.1846 600 600 600 0 0 1 -360 360;
22 35 0 0.0143 0 900 900 2500 1.025 0 1 -360 360;
23 24 0.0022 0.035 0.361 600 600 600 0 0 1 -360 360;
23 36 0.0005 0.0272 0 900 900 2500 1 0 1 -360 360;
25 26 0.0032 0.0323 0.531 600 600 600 0 0 1 -360 360;
25 37 0.0006 0.0232 0 900 900 2500 1.025 0 1 -360 360;
26 27 0.0014 0.0147 0.2396 600 600 600 0 0 1 -360 360;
26 28 0.0043 0.0474 0.7802 600 600 600 0 0 1 -360 360;
26 29 0.0057 0.0625 1.029 600 600 600 0 0 1 -360 360;
28 29 0.0014 0.0151 0.249 600 600 600 0 0 1 -360 360;
29 38 0.0008 0.0156 0 1200 1200 2500 1.025 0 1 -360 360;
];
```

E.5 57-Bus Test System

Figure E.5 illustrates the 59-bus test system.

The complete data of this network in Matpower format are as follows:

```
%% case study: case57
%% MATPOWER Case Format : Version 2
mpc.version = '2';
```

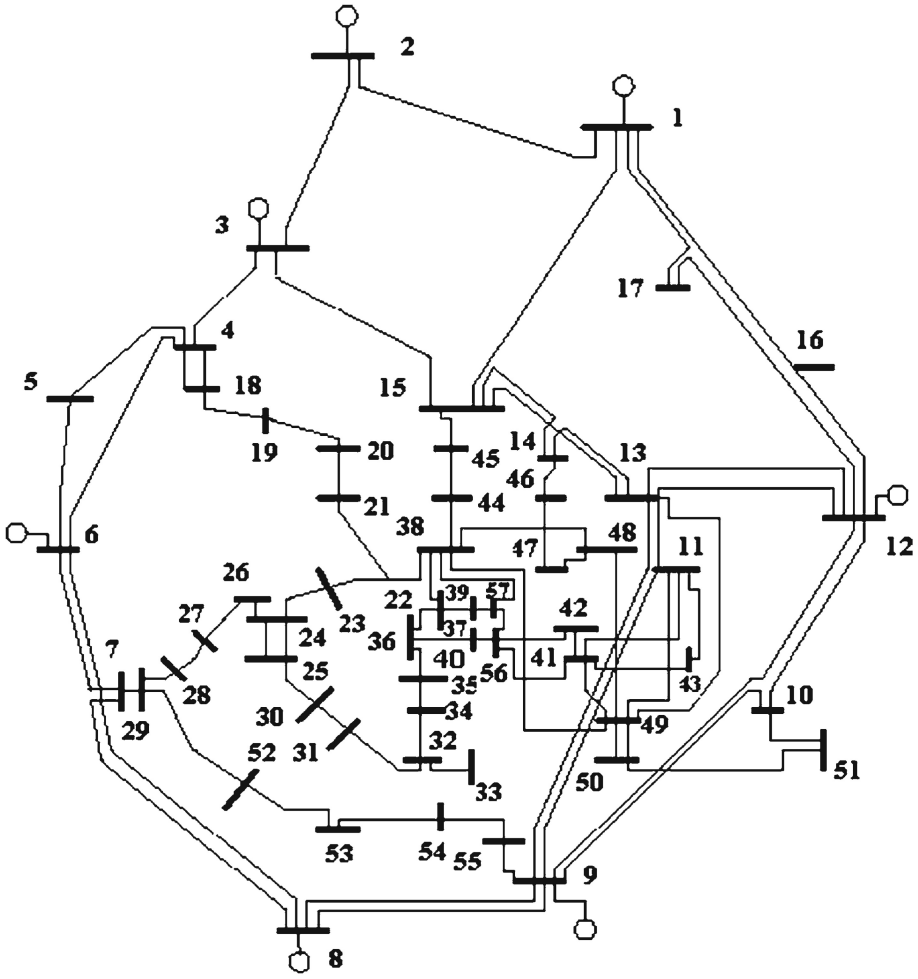

Figure E.5: The 59-bus test system.

```
%%-----  Power Flow Data  -----%%
%% system MVA base
mpc.baseMVA = 100;

%% bus data
% bus_i type Pd Qd Gs Bs area Vm Va baseKV zone Vmax Vmin
mpc.bus = [
1 3 55 17 0 0 1 1.04 0 345 1 1.06 0.94;
2 2 3 88 0 0 1 1.01 -1.18 345 1 1.06 0.94;
3 2 41 21 0 0 1 0.985 -5.97 345 1 1.06 0.94;
4 1 0 0 0 0 1 0.981 -7.32 345 1 1.06 0.94;
5 1 13 4 0 0 1 0.976 -8.52 345 1 1.06 0.94;
6 2 75 2 0 0 1 0.98 -8.65 345 1 1.06 0.94;
7 1 0 0 0 0 1 0.984 -7.58 345 1 1.06 0.94;
```

```
8 2 150 22 0 0 1 1.005 -4.45 345 1 1.06 0.94;
9 2 121 26 0 0 1 0.98 -9.56 345 1 1.06 0.94;
10 1 5 2 0 0 1 0.986 -11.43 345 1 1.06 0.94;
11 1 0 0 0 0 1 0.974 -10.17 345 1 1.06 0.94;
12 2 377 24 0 0 1 1.015 -10.46 345 1 1.06 0.94;
13 1 18 2.3 0 0 1 0.979 -9.79 345 1 1.06 0.94;
14 1 10.5 5.3 0 0 1 0.97 -9.33 345 1 1.06 0.94;
15 1 22 5 0 0 1 0.988 -7.18 345 1 1.06 0.94;
16 1 43 3 0 0 1 1.013 -8.85 345 1 1.06 0.94;
17 1 42 8 0 0 1 1.017 -5.39 345 1 1.06 0.94;
18 1 27.2 9.8 0 10 1 1.001 -11.71 345 1 1.06 0.94;
19 1 3.3 0.6 0 0 1 0.97 -13.2 345 1 1.06 0.94;
20 1 2.3 1 0 0 1 0.964 -13.41 345 1 1.06 0.94;
21 1 0 0 0 0 1 1.008 -12.89 345 1 1.06 0.94;
22 1 0 0 0 0 1 1.01 -12.84 345 1 1.06 0.94;
23 1 6.3 2.1 0 0 1 1.008 -12.91 345 1 1.06 0.94;
24 1 0 0 0 0 1 0.999 -13.25 345 1 1.06 0.94;
25 1 6.3 3.2 0 5.9 1 0.982 -18.13 345 1 1.06 0.94;
26 1 0 0 0 0 1 0.959 -12.95 345 1 1.06 0.94;
27 1 9.3 0.5 0 0 1 0.982 -11.48 345 1 1.06 0.94;
28 1 4.6 2.3 0 0 1 0.997 -10.45 345 1 1.06 0.94;
29 1 17 2.6 0 0 1 1.01 -9.75 345 1 1.06 0.94;
30 1 3.6 1.8 0 0 1 0.962 -18.68 345 1 1.06 0.94;
31 1 5.8 2.9 0 0 1 0.936 -19.34 345 1 1.06 0.94;
32 1 1.6 0.8 0 0 1 0.949 -18.46 345 1 1.06 0.94;
33 1 3.8 1.9 0 0 1 0.947 -18.5 345 1 1.06 0.94;
34 1 0 0 0 0 1 0.959 -14.1 345 1 1.06 0.94;
35 1 6 3 0 0 1 0.966 -13.86 345 1 1.06 0.94;
36 1 0 0 0 0 1 0.976 -13.59 345 1 1.06 0.94;
37 1 0 0 0 0 1 0.985 -13.41 345 1 1.06 0.94;
38 1 14 7 0 0 1 1.013 -12.71 345 1 1.06 0.94;
39 1 0 0 0 0 1 0.983 -13.46 345 1 1.06 0.94;
40 1 0 0 0 0 1 0.973 -13.62 345 1 1.06 0.94;
41 1 6.3 3 0 0 1 0.996 -14.05 345 1 1.06 0.94;
42 1 7.1 4.4 0 0 1 0.966 -15.5 345 1 1.06 0.94;
43 1 2 1 0 0 1 1.01 -11.33 345 1 1.06 0.94;
44 1 12 1.8 0 0 1 1.017 -11.86 345 1 1.06 0.94;
45 1 0 0 0 0 1 1.036 -9.25 345 1 1.06 0.94;
46 1 0 0 0 0 1 1.05 -11.89 345 1 1.06 0.94;
47 1 29.7 11.6 0 0 1 1.033 -12.49 345 1 1.06 0.94;
48 1 0 0 0 0 1 1.027 -12.59 345 1 1.06 0.94;
49 1 18 8.5 0 0 1 1.036 -12.92 345 1 1.06 0.94;
```

```
50 1 21 10.5 0 0 1 1.023 -13.39 345 1 1.06 0.94;
51 1 18 5.3 0 0 1 1.052 -12.52 345 1 1.06 0.94;
52 1 4.9 2.2 0 0 1 0.98 -11.47 345 1 1.06 0.94;
53 1 20 10 0 6.3 1 0.971 -12.23 345 1 1.06 0.94;
54 1 4.1 1.4 0 0 1 0.996 -11.69 345 1 1.06 0.94;
55 1 6.8 3.4 0 0 1 1.031 -10.78 345 1 1.06 0.94;
56 1 7.6 2.2 0 0 1 0.968 -16.04 345 1 1.06 0.94;
57 1 6.7 2 0 0 1 0.965 -16.56 345 1 1.06 0.94;
];

%% generator data
% bus Pg Qg Qmax Qmin Vg mBase status Pmax Pmin Pc1 Pc2 Qc1min Qc1max Qc2min
Qc2max ramp_agc ramp_10 ramp_30 ramp_q apf
mpc.gen = [
1 128.9 -16.1 200 -140 1.04 100 1 575.88 0 0 0 0 0 0 0 0 0 0 0 0;
2 0 -0.8 50 -17 1.01 100 1 100 0 0 0 0 0 0 0 0 0 0 0 0;
3 40 -1 60 -10 0.985 100 1 140 0 0 0 0 0 0 0 0 0 0 0 0;
6 0 0.8 25 -8 0.98 100 1 100 0 0 0 0 0 0 0 0 0 0 0 0;
8 450 62.1 200 -140 1.005 100 1 550 0 0 0 0 0 0 0 0 0 0 0 0;
9 0 2.2 9 -3 0.98 100 1 100 0 0 0 0 0 0 0 0 0 0 0 0;
12 310 128.5 155 -150 1.015 100 1 410 0 0 0 0 0 0 0 0 0 0 0 0;
];

%% branch data
% fbus tbus r x b rateA rateB rateC ratio angle status angmin angmax
mpc.branch = [
1 2 0.0083 0.028 0.129 440 0 0 0 0 1 -360 360;
2 3 0.0298 0.085 0.0818 440 0 0 0 0 1 -360 360;
3 4 0.0112 0.0366 0.038 220 0 0 0 0 1 -360 360;
4 5 0.0625 0.132 0.0258 220 0 0 0 0 1 -360 360;
4 6 0.043 0.148 0.0348 220 0 0 0 0 1 -360 360;
6 7 0.02 0.102 0.0276 220 0 0 0 0 1 -360 360;
6 8 0.0339 0.173 0.047 220 0 0 0 0 1 -360 360;
8 9 0.0099 0.0505 0.0548 440 0 0 0 0 1 -360 360;
9 10 0.0369 0.1679 0.044 220 0 0 0 0 1 -360 360;
9 11 0.0258 0.0848 0.0218 220 0 0 0 0 1 -360 360;
9 12 0.0648 0.295 0.0772 220 0 0 0 0 1 -360 360;
9 13 0.0481 0.158 0.0406 220 0 0 0 0 1 -360 360;
13 14 0.0132 0.0434 0.011 220 0 0 0 0 1 -360 360;
13 15 0.0269 0.0869 0.023 220 0 0 0 0 1 -360 360;
1 15 0.0178 0.091 0.0988 440 0 0 0 0 1 -360 360;
1 16 0.0454 0.206 0.0546 220 0 0 0 0 1 -360 360;
```

```
1 17 0.0238 0.108 0.0286 220 0 0 0 0 1 -360 360;
3 15 0.0162 0.053 0.0544 220 0 0 0 0 1 -360 360;
4 18 0 0.555 0 220 0 0 0.97 0 1 -360 360;
4 18 0 0.43 0 220 0 0 0.978 0 1 -360 360;
5 6 0.0302 0.0641 0.0124 220 0 0 0 0 1 -360 360;
7 8 0.0139 0.0712 0.0194 220 0 0 0 0 1 -360 360;
10 12 0.0277 0.1262 0.0328 220 0 0 0 0 1 -360 360;
11 13 0.0223 0.0732 0.0188 220 0 0 0 0 1 -360 360;
12 13 0.0178 0.058 0.0604 220 0 0 0 0 1 -360 360;
12 16 0.018 0.0813 0.0216 220 0 0 0 0 1 -360 360;
12 17 0.0397 0.179 0.0476 220 0 0 0 0 1 -360 360;
14 15 0.0171 0.0547 0.0148 220 0 0 0 0 1 -360 360;
18 19 0.461 0.685 0 220 0 0 0 0 1 -360 360;
19 20 0.283 0.434 0 220 0 0 0 0 1 -360 360;
21 20 0 0.7767 0 220 0 0 1.043 0 1 -360 360;
21 22 0.0736 0.117 0 220 0 0 0 0 1 -360 360;
22 23 0.0099 0.0152 0 220 0 0 0 0 1 -360 360;
23 24 0.166 0.256 0.0084 220 0 0 0 0 1 -360 360;
24 25 0 1.182 0 220 0 0 1 0 1 -360 360;
24 25 0 1.23 0 220 0 0 1 0 1 -360 360;
24 26 0 0.0473 0 220 0 0 1.043 0 1 -360 360;
26 27 0.165 0.254 0 220 0 0 0 0 1 -360 360;
27 28 0.0618 0.0954 0 220 0 0 0 0 1 -360 360;
28 29 0.0418 0.0587 0 220 0 0 0 0 1 -360 360;
7 29 0 0.0648 0 220 0 0 0.967 0 1 -360 360;
25 30 0.135 0.202 0 220 0 0 0 0 1 -360 360;
30 31 0.326 0.497 0 220 0 0 0 0 1 -360 360;
31 32 0.507 0.755 0 220 0 0 0 0 1 -360 360;
32 33 0.0392 0.036 0 220 0 0 0 0 1 -360 360;
34 32 0 0.953 0 220 0 0 0.975 0 1 -360 360;
34 35 0.052 0.078 0.0032 220 0 0 0 0 1 -360 360;
35 36 0.043 0.0537 0.0016 220 0 0 0 0 1 -360 360;
36 37 0.029 0.0366 0 220 0 0 0 0 1 -360 360;
37 38 0.0651 0.1009 0.002 220 0 0 0 0 1 -360 360;
37 39 0.0239 0.0379 0 220 0 0 0 0 1 -360 360;
36 40 0.03 0.0466 0 220 0 0 0 0 1 -360 360;
22 38 0.0192 0.0295 0 220 0 0 0 0 1 -360 360;
11 41 0 0.749 0 220 0 0 0.955 0 1 -360 360;
41 42 0.207 0.352 0 220 0 0 0 0 1 -360 360;
41 43 0 0.412 0 220 0 0 0 0 1 -360 360;
38 44 0.0289 0.0585 0.002 220 0 0 0 0 1 -360 360;
15 45 0 0.1042 0 220 0 0 0.955 0 1 -360 360;
```

```
14 46 0 0.0735 0 220 0 0 0.9 0 1 -360 360;
46 47 0.023 0.068 0.0032 220 0 0 0 0 1 -360 360;
47 48 0.0182 0.0233 0 220 0 0 0 0 1 -360 360;
48 49 0.0834 0.129 0.0048 220 0 0 0 0 1 -360 360;
49 50 0.0801 0.128 0 220 0 0 0 0 1 -360 360;
50 51 0.1386 0.22 0 220 0 0 0 0 1 -360 360;
10 51 0 0.0712 0 220 0 0 0.93 0 1 -360 360;
13 49 0 0.191 0 220 0 0 0.895 0 1 -360 360;
29 52 0.1442 0.187 0 220 0 0 0 0 1 -360 360;
52 53 0.0762 0.0984 0 220 0 0 0 0 1 -360 360;
53 54 0.1878 0.232 0 220 0 0 0 0 1 -360 360;
54 55 0.1732 0.2265 0 220 0 0 0 0 1 -360 360;
11 43 0 0.153 0 220 0 0 0.958 0 1 -360 360;
44 45 0.0624 0.1242 0.004 220 0 0 0 0 1 -360 360;
40 56 0 1.195 0 220 0 0 0.958 0 1 -360 360;
56 41 0.553 0.549 0 220 0 0 0 0 1 -360 360;
56 42 0.2125 0.354 0 220 0 0 0 0 1 -360 360;
39 57 0 1.355 0 220 0 0 0.98 0 1 -360 360;
57 56 0.174 0.26 0 220 0 0 0 0 1 -360 360;
38 49 0.115 0.177 0.003 220 0 0 0 0 1 -360 360;
38 48 0.0312 0.0482 0 220 0 0 0 0 1 -360 360;
9 55 0 0.1205 0 220 0 0 0.94 0 1 -360 360;
];
```

Appendix F

Published and Submitted Papers of Thesis

[1] E. Ghahremani, and I. Kamwa,"Dynamic State Estimation in Power System by Applying the Extended Kalman Filter With Unknown Inputs to Phasor Measurements," *IEEE Transactions on Power Systems*, vol. 26, no. 4, November 2011, pp. 2556-2566.

[2] E. Ghahremani, and I. Kamwa, "Online State Estimation of a Synchronous Machine Using Unscented Kalman Filter From Phasor Measurements Units,"*IEEE Transactions on Energy Conversion*, vol. 26, no. 4, December 2011, pp. 1099-1108.

[3] E. Ghahremani, and I. Kamwa, "Optimal Placement of Multiple-Type FACTS Devices to Maximize Power System Loadability Using a Generic Graphical User Interface," Accepted for *IEEE Transactions on Power Systems* on 19 July 2012.

[4] E. Ghahremani, and I. Kamwa, "Simultaneous State and Input Estimation of a Synchronous Machine Using the Extended Kalman Filter With Unknown Inputs," in *Proceedings of the IEEE International Electric Machines and Drives Conference (IEMDC 2011)*, Niagara Falls, Ontario, Canada, May 2011, pp. 1490-1495.

[5] E. Ghahremani, and I. Kamwa, "Maximizing Transmission Capacity through a Minimum Set of Distributed Multi-Type FACTS," in *Proceedings of IEEE Power and Energy Society General Meeting (PESGM 2012)*, San Diego, United States, July 2012.

[6] E. Ghahremani, and I. Kamwa, "Joint Improvement of System Loadability and Stability through a Multi-Stage Planning of a UPFC with a PMU Based Supplementary Damping Control," will be submitted for *IEEE Power and Energy Society General Meeting 2013 (PESGM 2013)* on 1 November 2012.

[7] E. Ghahremani, and I. Kamwa, "Optimal Allocation of STATCOM with Energy Storage to Improve the Power System Performance," will be submitted for *IEEE Power and*

Energy Society General Meeting 2013 (PESGM 2013) on 1 November 2012.

[8] E. Ghahremani, and I. Kamwa, "Analyzing the Effects of Different Type of FACTS Devices on Steady-State Performance of Hydro-Québec Network," will be submitted for *IET Generation, Transmission and Distribution journal (IET-GTD)* on 1 November 2012.

References

[1] P. Kundur, *Power System Stability and Control*. New York: McGraw Hill Publication Company, 1994.

[2] M. Zima, M. Larsson, P. Korba, C. Rehtanz, and G. Andersson, "Design Aspects for Wide-Area Monitoring and Control Systems," in *Proceedings of the IEEE*, vol. 93, pp. 980–996, May 2005.

[3] J. Bertsch, C. Carnal, D. Karlson, J. McDaniel, and K. Vu, "Wide-Area Protection and Power System Utilization," in *Proceedings of the IEEE*, vol. 93, pp. 997–1003, May 2005.

[4] M. Anjia, Y. Jiaxi, and G. Zhizhong, "PMU Placement and Data Processing in WAMS that Complement SCADA," in *Proceedings of IEEE Power Engineering Society General Meeting*, vol. 1, pp. 780–783, June 2005.

[5] D. Yan, "Wide Area Protection and Control System with WAMS Based," in *Proceedings of International Conference on Power System Technology*, vol. 1, pp. 1–5, October 2006.

[6] ABB, "Power System Guard: Wide Area Measurement, Monitoring, Protection and Control System," tech. rep., ABB Power Automation and Protection Division Ltd., Switzerland, 2003.

[7] A. Ghosh and G. Ledwich, "Opportunities in Wide Area Control and Measurements," in *Proceedingss of Australian Universities Power Engineering Conference (AUPEC)*, vol. 1, pp. 1–6, December 2006.

[8] C. W. Taylor, D. C. Erickson, K. E. Martin, R. E. Wilson, and V. Venkatasubramanian, "Wide-Area Stability and Voltage Control System: R & D and Online Demonstration," in *Proceedings of the IEEE*, vol. 93, pp. 892–906, May 2005.

[9] G. K. Venayagamoorthy, "A Neural Network Based Optimal Wide Area Control Scheme for a Power System," in *Proceedings of IEEE Industry Applications Conference*, vol. 1, pp. 700–706, October 2005.

[10] X. P. Zhang, C. Rehtanz, , and B. Pal, *Flexible AC Transmission Systems: Modeling and Control*. New York: Springer-Verlag Berlin Heidelberg, 2006.

[11] D. Karlson, M. Hemmingsson, and S. Lindahl, "Wide Area System Monitoring and Control," *IEEE Power & Energy Magazine*, vol. 93, pp. 892–906, September 2004.

[12] Y. N. Yu, *Electric Power System Dynamic*. New York: Academic Press, 1983.

[13] Z. Huang, K. Schneider, and J. Neplocha, "Feasibility Studies of Applying Kalman Filter Techniques to Power System Dynamic State Estimation," in *Proceedingss of International Power Engineering Conference (IPEC)*, pp. 376–382, 3-6 December 2007.

[14] I. Kamwa, B. Baraboi, and R. Wamkeue, "Sensorless ANN-Based Speed Estimation of Synchronous Generator: Improved Performance through Physically Motivated Pre-Filters," in *Proceedings of IEEE Neural Network Conference (IJCNN)*, pp. 1710–1718, 2006.

[15] A. D. Angel, P. Geurts, D. Ernst, M. Glavic, and L. Wehenkel, "Estimation of Rotor Angle of Synchronous Machines Using Artificial Neural Networks and Local PMU-Based Quantities," *Neurocomputing*, vol. 70, pp. 2668–2678, October 2007.

[16] A. S. Debs and R. E. Larson, "A Dynamic Estimation for Tracking the State of a Power system," *IEEE Transactions Power Apparatus and System*, vol. 89, pp. 1670–1678, September 1970.

[17] J. K. Mandal, A. K. Sinha, and L. Roy, "Incorporating Nonlinearity of Measurement Function in Power System Dynamic State Estimation," *IEE Generation, Transmission and Distribution*, vol. 142, pp. 289–296, May 1995.

[18] G. Valverde and V. Terzija, "Unscented Kalman Filter For Power System Dynamic State Estimation," *IET Generation, Transmission and Distribution*, vol. 5, no. 1, pp. 29–37, 2011.

[19] K. R. Shih and S. Huang, "Application of a Robust Algorithm for Dynamic State Estimation of a Power System," *IEEE Transactions on Power Systems*, vol. 17, pp. 141–147, February 2002.

[20] J. Chang, G. N. Taranto, and J. Chow, "Dynamic State Estimation in Power System using Gain-Scheduled Nonlinear Observer," in *Proceedings of IEEE Control Application Conference*, pp. 221–226, 28-29 September 1995.

[21] L. Lin, Linawati, L. Jasa, and E. Ambikairajah, "A Hybrid State Estimation Scheme for Power System," in *Proceedings of IEEE Circuits and Systems Conference (APCCAS'02)*, vol. 1, pp. 555–558, 2002.

[22] M. Huanga, W. Li, and W. Yana, "Estimating Parameters of Synchronous Generators Using Square-root Unscented Kalman Filter," *International Journal of Electric Power System Research*, vol. 80, pp. 1137–1144, September 2010.

[23] V. Venkatasubramanian and R. Kavasseri, "Direct Computation of Generator Internal Dynamic States from Terminal Measurements," in *Proceedings of 37th Hawaii International Conference on System Sciences*, pp. 1–6, 5-8 January 2004.

[24] E. Farantatos, G. K. Stefopoulos, G. J. Cokkinides, and A. P. Meliopoulos, "PMU-Based Dynamic State Estimation Electric Power Systems," in *Proceedings of Power & Energy Society Meeting (PES)*, pp. 1–8, 26-30 July 2009.

[25] S. Meliopoulos, G. Cokkinides, R. Huang, E. Farantatos, S. Choi, and Y. Lee, "Wide Area Dynamic Monitoring and Stability Controls," in *Proceedings of Bulk Power System Dynamic and Control*, pp. 1–8, 1-6 August 2010.

[26] I. Kamwa, M. Leclerc, , and D. McNabb, "Performance of Demodulation-Based Frequency Measurement Algorithms Used in Typical PMUs," *IEEE Transactions on Power Delivery*, vol. 19, pp. 505–514, April 2004.

[27] J. Warichet, T. Sezi, and J. C. Maun, "Considerations about Synchrophasors Measurements in Dynamic System Conditions," *International Journal of Electric Power Energy Systems*, vol. 31, pp. 452–464, October 2009.

[28] I. K. K.Pradhan and G. Joos, "Adaptive Phasor and Frequency-Tracking Schemes for Wide-Area Protection and Control," *IEEE Transactions on Power Delivery*, vol. 26, pp. 744–753, February 2011.

[29] D. Simon, *Optimal State estimation; Kalman, H-infinity, and Nonlinear Approaches*. New Jersey: John Wiley & Sons, 2006.

[30] S. J. Julier and J. K. Uhlmann, "Unscented Filtering and Nonlinear Estimation," in *Proceedings of IEEE*, vol. 92, pp. 744–753, March 2004.

[31] R. Kandepu, B. Foss, , and L. Imsland, "Applying the Unscented Kalman Filter for Nonlinear State Estimation," *International Journal of Process Control*, vol. 18, pp. 753–768, August 2008.

[32] S. Pan, H. Su, P. Li, and Y. Gu, "State Estimation for Batch Distillation Operation with A novel Extended Kalman Filter Approach," in *Proceedings of 48th IEEE Conference on Decision and Control*, pp. 1884–1889, 15-18 December 2009.

[33] P. K. Kitanidis, "Unbiased Minimum-Variance Linear State Estimation," *Automatica*, vol. 23, no. 6, pp. 775–778, 1987.

[34] M. Darouach and M. Zasadzinski, "Unbiased Minimum Variance Estimation for Systems with Unknown Exogenous Inputs," *Automatica*, vol. 33, no. 4, pp. 717–719, 1997.

[35] S. Gillijns and B. D. Moor, "Unbiased Minimum-Variance Input and State Estimation for Linear Discrete-Time Systems," *Automatica*, vol. 33, no. 4, pp. 111–116, 2007.

[36] Y. Cheng, Y. W. H. Ye, and D. Zhou, "Unbiased Minimum-Variance State Estimation for Linear Systems with Unknown Input," *Automatica*, vol. 45, no. 2, pp. 485–491, 2009.

[37] J. N. Yang, S. Pan, and H. Huang, "An Adaptive Extended Kalman Filter for Structural Damage Identification II: Unknown Inputs," *International Journal of Structure Control Health Monitoring*, vol. 14, pp. 497–521, April 2007.

[38] S. Bruno and M. L. Scala, "Unified Power Flow Controllers for Security-Constrained Transmission Management," *IEEE Transactions on Power Systems*, vol. 19, pp. 418–426, February 2004.

[39] N. Hingorani, "Flexible AC Transmission," *IEEE Spectrum*, vol. 30, pp. 40–45, April 1993.

[40] S. Rahimzadeh, M. T. Bina, and A. Viki, "Simultaneous Application of Multi-Type FACTS Devices to the Restructured Environment: Achieving Both Optimal Number and Location," *IET Generation, Transmission and Distribution*, vol. 4, pp. 349–362, September 2009.

[41] S. Gerbex, R. Cherkaoui, and A. J. Germond, "Optimal Placement of Multi-Type FACTS Devices in a Power System by Means of Genetic Algorithms," *IEEE Transactions on Power Systems*, vol. 16, pp. 537–544, August 2001.

[42] S. R. Najafi, M. Abedi, and S. H. Hosseinian, "A Novel Approach to Optimal Allocation of SVC Using Genetic Algorithms and Continuation Power Flow," in *Proceedings of IEEE International Power and Energy Conference*, pp. 202–206, 28-29 November 2006.

[43] G. I. Rashed, H. I. Shaheen, and S. J. Cheng, "Optimal Location and Parameter Setting of Multiple TCSCs for Increasing Power System Loadability Based on GA and PSO techniques," in *Proceedings of IEEE International Natural Computation Conference (ICNC'07)*, vol. 4, pp. 335–344, 24-27 August 2007.

[44] A. Kazemi, D. Arabkhabori, M. Yari, and J. Aghaei, "Optimal Location of UPFC in Power Systems for Increasing Loadability by Genetic Algorithm," in *Proceedings of IEEE Universities of Power Engineering Conference*, vol. 2, pp. 774–779, 6-8 September 2007.

[45] M. Behshad, A. Lashkarara, and A. H. Rahmani, "Optimal Location of UPFC Devices Considering System Loadability, Total Fuel Cost, Power Losses and Cost of Installation," in *Proceedings of IEEE International Conference on Power Electronics and Intelligent Transportation Systems*, vol. 2, pp. 1–7, 19-20 December 2009.

[46] P. Bhasaputra and W. Ongsakul, "Optimal Placement of Multi-Type FACTS Devices by Hybrid TS/SA Approach," in *Proceedings of IEEE Circuits and Systems (ISCAS'03)*, vol. 3, pp. 375–378, 25-28 May 2003.

[47] S. Gerbex, R. Cherkaoui, and A. J. Germond, "Optimal Placement of FACTS Devices to Enhance Power System Security," in *Proceedings of IEEE Power Tech Conference*, vol. 3, pp. 1–6, 23-26 June 2003.

[48] M. Saravanan, S. M. R. Slochanal, P. Venkatesh, and P. Abraham, "Application of PSO Technique for Optimal Location of FACTS Devices Considering Cost of Installation and System Loadability," *Electric Power Systems Research*, vol. 77, pp. 276–283, April 2007.

[49] S. T. J. Christa and P. Venkatesh, "Application of Particle Swarm Optimization for Optimal Placement of Unified Power Flow Controllers in Electrical Systems with Line Outages," in *Proceedings of IEEE International Conference on Computational Intelligence*, vol. 1, pp. 119–124, 13-15 December 2007.

[50] E. N. Azadani, S. H. Hosseinian, M. Janati, and P. Hasanpor, "Optimal Placement of Multiple STATCOM," in *Proceedings of IEEE International Middle-East Conference on Power System (MEPCON'08)*, pp. 523–528, 12-15 March 2008.

[51] M. Santiago-Luna and J. R. Cedeno-Maldonado, "Optimal Placement of FACTS Controllers in Power Systems via Evolution Strategies," in *Proceedings of IEEE Transmission and Distribution Conference and Exposition (ITDC 2006)*, pp. 1–6, 15-18 August 2006.

[52] R. P. Kalyani, M. L. Crow, and D. R. Tauritz, "Optimal Placement and Control of Unified Power Flow Control Devices using Evolutionary Computing and Sequential Quadratic Programming," in *Proceedings of IEEE Power Systems Conference and Exposition (PSCE'06)*, pp. 959–964, 29-30 November 2006.

[53] I. Marouani, T. Guesmi, H. H. Abdallah, and A. Quali, "Application of a Multi-Objective Evolutionary Algorithm for Optimal Location and Parameters of FACTS Devices Considering the Real Power Loss in Transmission Lines and Voltage Deviation Buses," in *Proceedings of IEEE System, Signals and Devices (SSD'09)*, pp. 1–6, 2009.

[54] H. I. Shaheen, G. I. Rashed, and S. J. Cheng, "Application of Evolutionary Optimization Techniques for Optimal Location and Parameters Setting of Multiple UPFC Devices," in *Proceedings of IEEE International Natural Computation Conference (ICNC'07)*, vol. 4, pp. 688–697, 24-27 August 2007.

[55] Z. Lu, M. S. Li, W. J. Tang, and Q. H. Wu, "Optimal Location of FACTS Devices by a Bacterial Swarming Algorithm for Reactive Power Planning," in *Proceedings of IEEE Evolutionary Computing (CEC'07)*, pp. 2344–2349, 25-28 September 2007.

[56] Q. H. Wu, Z. Lu, M. S. Li, and T. Y. Ji, "Optimal Placement of FACTS Devices by a Group Search Optimizer with Multiple Producer," in *Proceedings of IEEE Evolutionary Computing (CEC'07)*, pp. 1033–1039, 1-6 June 2007.

[57] A. Kazemi, A. Parizad, and H. R. Baghaee, "On the use of Harmony Search Algorithm in Optimal Placement of FACTS Devices to Improve Power System Security," in *Proceedings of IEEE Euro Conference*, pp. 540–576, 18-23 May 2009.

[58] R. M. Idris, A. Kharuddin, and M. W. Mustafa, "Optimal Choice of FACCTS Devices for ATC Enhancement using Bees Algorithm," in *Proceedings of IEEE Power Engineering Conference (AUPEC'09)*, pp. 1–6, 27-30 September 2009.

[59] A. Z. Gamm and I. I. Gloub, "Determination of Locations for FACTS and Energy Storage by the Singular Analysis," in *Proceedings of IEEE Power System Technology (POWERCON '98)*, pp. 411–414, 18-21 August 1998.

[60] A. D. Shakib and G. Balzer, "Optimal Location and Control of Shunt FACTS for Transmission of Renewable Energy in Large Power Systems," in *Proceedings of IEEE Mediterranean Electrotechnical Conference (MELECON 2010)*, pp. 890–895, 26-28 April 2010.

[61] S. Singh and A. David, "Optimal Location of FACTS Devices for Congestion Management," *Electric Power Systems Research*, vol. 58, no. 2, pp. 71–79, 2001.

[62] S. Singh and A. David, "Placement of FACTS device in Open Power Market," in *Proceedings of IEEE Power System Control, Operation and Management (APSCOM-2000)*, vol. 1, pp. 173–177, 30 November 2000.

[63] S. N. Singh and I. Erlich, "Locating Unified Power Flow Controller for Enhancing Power System Loadability," in *Proceedings of IEEE International Conference on Future Power Systems*, pp. 1–5, 18-21 November 2005.

[64] M. H. Haque, "Optimal Location of Shunt FACTS devices in Long Transmission Lines," *IET Generation Transmission and Distribution*, vol. 147, pp. 218–222, July 2000.

[65] N. K. Sharma, A. Ghosh, and R. K. Varma, "A Novel Placement Strategy for FACTS Controllers," *IEEE Transactions on Power Delivery*, vol. 18, pp. 982–987, July 2003.

[66] A. Sharma, S. Chanana, and S. Parida, "Combined Optimal Location of FACTS Controllers and Loadability Enhancement in Competitive Electricity Markets using MILP," in *Proceedings of IEEE Power Engineering Society General Meeting (PES'05)*, vol. 1, pp. 670–677, 12-16 July 2005.

[67] R. W. Chang and T. K. Saha, "Maximizing Power System Loadability by Optimal Allocation of SVC using Mixed Integer Linear Programming," in *Proceedings of IEEE Power Engineering Society General Meeting (PES'10)*, pp. 1–7, 25-29 July 2010.

[68] F. G. M. Lima, F. D. Galiana, I. Kockar, and J. Munoz, "Phase Shifter Placement in Large-Scale Systems via Mixed Integer Linear Programming," *IEEE Transactions on Power Systems*, vol. 18, pp. 1029–1034, August 2003.

[69] N. M. N. Acharya, "Locating Series FACTS Devices for Congestion Management in Deregulated Electricity Markets," *Electric Power System Research*, vol. 77, pp. 352–360, May 2006.

[70] L. J. Cai, I. Erlich, and G. Stamtsis, "Optimal Choice and Allocation of FACTS Devices in Deregulated Electricity Market Using Genetic Algorithm," in *Proceedings of IEEE Power System Conference and Exposition*, vol. 1, pp. 201–207, 10-13 October 2004.

[71] M. Noroozian, L. Angquist, M. Ghandhari, and G. Andersson, "Use of UPFC for Optimal Power Flow Control," *IEEE Transactions on Power Delivery*, vol. 12, pp. 1629–1634, October 1997.

[72] S. Rahimzadeh and M. T. Bina, "Looking for Optimal Number and Placement of FACTS Devices to Manage the Transmission Congestion," *Energy Conversion and Management*, vol. 52, pp. 437–446, January 2010.

[73] R. D. Zimmermann, C. E. M. Sanchez, and R. J. Thomas, "Matpower: Steady-State Operations, Planning and Analysis Tools for Power Systems Research and Education," *IEEE Transactions on Power System*, vol. 26, pp. 12–19, February 2011.

[74] N. G. Hingorani and L. Gyugyi, *Understanding FACTS Concepts and Technology of Flexible AC Transmission Systems*. New York: IEEE Press, 1999.

[75] A. Nabavi-Niaki and M. R. Iravani, "Steady-State and Dynamic Models of Unified Power Flow Controller (UPFC) for Power System Studies," *IEEE Transactions on Power System*, vol. 11, pp. 1937–1943, November 1996.

[76] E. Acha, C. R. Fuerte-Esquivel, H. Ambriz-Perez, and C. Angeles-Camacho, *FACTS: Modeling and Simulation in Power Networks*. Chichester: John Wiley and Sons, 2004.

[77] W. L. Fang and H. Ngan, "A Robust Load Flow Technique For Use in Power Systems with Unified Power Flow Controllers,," *Electric Power System Research Journal*, vol. 53, pp. 181–186, 2005.

[78] D. E. Golderberg, *Genetic Algorithm in Search Optimization and Machine Learning*. Boston-USA: Addison-Wesley Publishing Company Inc., 1989.

[79] MATLAB, "Matlab Help Documentation: Global Optimization Toolbox User's Guide," tech. rep., The MathWorks Inc., 2010.

[80] (On-line), "Power System Test Case Archives." available online at: http://www.ee.washington.edu/research/pstca/.

[81] D. P. Subramanian and R. P. K. Devi, "Application of TCSC power Oscillation Damping Controller to Enhance Power System Dynamic Performance," in *Proceedings of IEEE Power Electronics, Drive and Energy (PEDES)*, pp. 1–5, 20-23 December 2010.

[82] H. Wu and G. T. Heydt, "Design of Delayed-Input Wide-Area Power System Stabilizer Using the Gain Scheduling Method," in *Proceedings of IEEE Power Engineering Society General Meeting*, vol. 3, pp. 1704–l709, 13-17 July 2003.

[83] I. Kamwa, R. Grondin, and V. Hebert, "Wide-Area Measurement Based stabilizing Control of Large Power Systems-A Decentralized/Hierarchical Approach," *IEEE Transactions on Power System*, vol. 16, pp. 136–153, February 2001.

[84] D. Dotta, A. S. Silva, and I. C. Decker, "Wide-Area Measurements-Based Two-Level Control Design Considering Signal Transmission Delay," *IEEE Transactions on Power System*, vol. 24, pp. 208–216, February 2009.

[85] J. Chow, J. Sanchez-Gasca, H. Ren, and S. Wang, "Power System Damping Controller Design-Using Multiple Input Signals," *IEEE Control System Magazine*, vol. 20, pp. 82–90, August 2000.

[86] M. Aboul-Ela, A. Sallam, J. McCalley, and A. Fouad, "Damping Controller Design for Power System Oscillations Using Gobal Signals," *IEEE Transactions on Power System*, vol. 11, pp. 767–773, May 1996.

[87] I. Kamwa, A. Heniche, G. Trudel, M. Dobrescu, R. Grondin, and D. Lefebvre, "Assessing the Technical Value of FACTS-Based Wide-Area Damping Control Loops," in *Proceedings of IEEE Power Engineering Society General Meeting*, vol. 2, pp. 1734–1743, 12-16 June 2005.

[88] I. Kamwa, J. Bland, G. Trudel, R. Grondin, C. Lafond, and D. McNabb, "Wide-Area Monitoring and Control at Hydro-Québec: Past, Present and Future," in *Proceedings of IEEE Power Engineering Society General Meeting*, pp. 1–12, June 2006.

[89] N. R. Chaudhuri, S. Ray, R. Majumder, and B. Chaudhuri, "A New Approach to Continuous Latency Compensation with Adaptive Phasor Power Oscillation Damping Controller (POD)," *IEEE Transactions on Power System*, vol. 25, pp. 939–946, May 2010.

[90] F. Liu, R. Yokoyama, Y. C. Zhou, and M. Wu, "TCSC Wide-Area Damping Controller to Enhance the Damping of Inter-area Oscillation for Power Systems with Considering the Time Delay of Wide-Area Signals," in *Proceedings of IEEE Conference on Power System Technology*, pp. 1–6, 24-28 October 2005.

[91] Y. Zhang and A. Bose, "Design of Wide-Area Damping Controllers for Inter-area Oscillations," *IEEE Transactions on Power System*, vol. 23, pp. 1136–1143, August 2008.

[92] N. R. Chaudhuri, A. Domahidi, R. Majumder, B. Chaudhuri, P. Korba, S. Ray, and K. Uhlen, "Wide-Area Power Oscillation Damping Control in Nordic Equivalent System," *IET Generation, Transmission and Distribution*, vol. 4, pp. 1139–1150, October 2010.

[93] N. R. Chaudhuri, B. Chaudhuri, S. Ray, and R. Majumder, "Wide-area Phasor Power Oscillation Damping Controller: A New Approach to Handling Time-Varying Signal Latency," *IET Generation, Transmission and Distribution*, vol. 4, pp. 620–630, May 2010.

[94] S. Ray and G. K. Venagamoorthy, "Wide-Area Signal-Based Optimal Neuro-Controller for a UPFC," *IEEE Transactions on Power System*, vol. 23, pp. 1597–1605, July 2008.

[95] S. Mohagheghi, G. Venayagamoorthy, and R. Harley, "Optimal Wide-Area Controller and State Predictor for a Power System," *IEEE Transactions on Power System*, vol. 22, pp. 693–705, May 2007.

[96] H. Ni, G. T. Heydt, and L. Mili, "Power System Stability Agents Using Robust Wide-Area Control," *IEEE Transactions on Power System*, vol. 17, pp. 1123–1131, November 2002.

[97] P. Anderson and A. Fouad, *Power System Control and Stability*. Piscataway, New Jersey: IEEE Press: John Wiley and Sons, 2003.

[98] P. Sauer and M. Pai, *Power System Dynamics and Stability*. Upper Saddle River, New Jersey: Prentice Hall, 1998.

[99] F. Milano, "An Open Source Power System Analysis Toolbox (PSAT)," *IEEE Transactions on Power System*, vol. 20, pp. 1199–1206, November 2011.

[100] A. Heniche and I. Kamwa, "Assessment of Two Methods to Select Wide-Area Signals for Power System Damping Control," *IEEE Transactions on Power System*, vol. 23, pp. 572–581, May 2008.